Femtosecond Excitations in Metallic Nanostructures

From Ultrafast Light Confinement to a Local Electron Source

DISSERTATION

zur Erlangung des akademischen Grades
doctor rerum naturalium
(Dr. rer. nat.)
im Fach Physik

eingereicht an der
Mathematisch-Naturwissenschaftlichen Fakultät I
Humboldt-Universität zu Berlin

von
Herrn Dipl.-Phys. Claus Ropers
geboren am 18.04.1977 in Stade

Präsident der Humboldt-Universität zu Berlin:
Prof. Dr. Christoph Markschies

Dekan der Mathematisch-Naturwissenschaftlichen Fakultät I:
Prof. Dr. Christian Limberg

Gutachter:

1. Prof. Dr. Thomas Elsässer
2. Prof. Dr. Oliver Benson
3. Prof. Dr. Christoph Lienau

eingereicht am: 9. Mai 2007
Tag der mündlichen Prüfung: 11. Juli 2007

Abstract

This thesis contributes to the understanding of optical excitations in metallic nanostructures. In experiments on selected model structures, the dynamics of these excitations and their electromagnetic spatial modes are investigated with femtosecond temporal and nanometer spatial resolution, respectively.

Angle- and time-resolved transmission experiments on metallic thin film gratings demonstrate the dominant role resonant surface plasmon polaritons (SPPs) play in the optical properties of such structures. The lifetimes of these excitations are determined, and it is shown that coherent couplings among SPP-resonances result in drastic lifetime modifications. Near the visible part of the spectrum, subradiant SPP lifetimes of up to 200 femtoseconds are observed, which is considerably longer than previously expected for these structures.

The spatial SPP mode profiles are imaged using a custom-built near-field optical microscope. The experiments reveal a direct correlation between the spatial mode structure and the dynamics of different SPP resonances. Coupling-induced SPP band gaps are identified as splittings into symmetric and antisymmetric surface modes.

These findings allow for an interpretation of the near-field optical image contrast in terms of the contributions of different vectorial components of the electromagnetic near-field. A selective imaging of different electric and magnetic field components is demonstrated for various types of near-field probes.

Furthermore, the excitation of SPPs in periodic structures is employed in a novel type of near-field tip. The resonant excitation of SPPs in a nanofabricated grating on the shaft of a sharp metallic tip results in their concentration at the tip apex.

The final part of the thesis highlights the importance of optical field enhancements for the local generation of nonlinear optical signals at the apex of sharp metallic tips. Specifically, the observation of intense multiphoton electron emission after femtosecond excitation is a major result. This process is thoroughly characterized, and a novel scanning microscopy application based on this effect is presented. In this technique, an image contrast with nanometer resolution arises from spatially varying electron emission rates.

Keywords:
Surface Plasmon Polariton, Femtosecond, Near-Field Optics, Electron Pulses

Kurzfassung

Diese Arbeit leistet einen Beitrag zum Verständnis optischer Anregungen in kleinsten metallischen Strukturen, sogenannten Nanostrukturen. Am Beispiel ausgewählter Nanostrukturen werden experimentell die Dynamik dieser Anregungen mit Femtosekunden-Zeitauflösung und ihre elektromagnetischen Moden auf der Nanometer-Längenskala untersucht.

Anhand winkel- und zeitaufgelöster Transmissionsexperimente an metallischen Dünnfilmgittern wird gezeigt, dass resonante Oberflächenplasmon-Polaritonen (OPPen) wesentlich die optischen Eigenschaften dieser Strukturen beeinflussen. Die Lebensdauer solcher Anregungen wird ermittelt und damit nachgewiesen, dass Kopplungen zwischen OPP-Resonanzen drastische Lebensdauer-Modifikationen zur Folge haben. Als eine Konsequenz der Kopplungen werden nahe dem sichtbaren Spektralbereich subradiante OPP-Lebensdauern von bis zu 200 Femtosekunden beobachtet, welches weitaus länger ist, als bisher für diese Strukturen vermutet wurde.

Das räumliche Gegenstück der zeitlichen Aspekte bilden die elektromagnetischen Feldverteilungen nahe der metallischen Oberfläche. Diese werden in einem eigens konstruierten, spektral auflösenden optischen Nahfeldmikroskop direkt abgebildet. Derartige Experimente erlauben erstmals eine Zuordnung der räumlichen Moden zur zeitlichen Dynamik verschiedener OPP-Resonanzen. Speziell werden kopplungsinduzierte Bandlücken als Aufspaltungen in symmetrische und antisymmetrische Oberflächenmoden identifiziert. Dies stellt die unmittelbare Beobachtung einer optischen Realisierung fundamentaler Aussagen der Bloch-Theorie periodischer Medien dar.

Die so gewonnenen Erkenntnisse ermöglichen darüberhinaus eine Interpretation des nahfeldmikroskopischen Bildkontrasts bezüglich der Beiträge verschiedener vektorieller Komponenten des optischen Nahfeldes. Insbesondere wird die selektive Abbildung unterschiedlicher elektrischer und magnetischer Feldkomponenten in Abhängigkeit von dem gewählten Sondentyp demonstriert.

Die Erzeugung und Propagation von Oberflächenplasmon-Polaritonen in periodischen Systemen wird zudem in einer hier entwickelten Nanostruktur ausgenutzt. Dazu werden in einem Gitter auf dem Schaft einer Metallspitze resonant OPPen angeregt, die an den Apex der Spitze propagieren und dort eine räumlich stark konzentrierte Lichtquelle bilden.

Ein weiterer Teil der Arbeit nutzt elektrische Feldüberhöhungen an scharfen Metallspitzen für die lokalisierte Erzeugung nichtlinearer optischer Signale. Die Beobachtung intensiver Multiphoton-Elektronenemission nach Femtosekundenanregung stellt ein zentrales Ergebnis dar. Dieser Prozess wird umfangreich charakterisiert und findet seine erste Anwendung in einer neuartigen Rastersondentechnik, in der die örtlich variierende Elektronenemission der Bildgebung dient.

Schlagwörter:
Oberflächenplasmon, Femtosekunde, Nahfeldoptik, Elektronenimpulse

Contents

1 Introduction

The optical properties of metals are extraordinary in many respects. Their most apparent feature is certainly a high reflectivity, which, for some metals, spans from the far infrared to the ultraviolet spectral ranges. This reflectivity can be traced to the large density of mobile conduction electrons that react to incoming light fields and prevent them from penetrating the metal. Such exclusion effects take place very close to the surface, in a narrow region known as the "skin depth", a thin layer of approximately 10 nanometers in thickness.[1]

Induced by external radiation, charge and current oscillations within the skin depth in-turn create optical fields near the surface that act back on the charges. This can result in combined resonant modes of the electron motion with a surface-bound electromagnetic field. The relevant timescales of such resonances are usually exceedingly short, namely in the range of femtoseconds.[2]

Depending on the particular geometry, these excitations may have markedly different characteristics. For example, surface plasmon polaritons (SPPs) [1] are delocalized waves traveling along a metal surface and can possess spatial coherence lengths of several hundred micrometers for near-infrared light and a metal like silver. On the other hand, sharp edges or other highly curved geometries (nanometer scale metal clusters etc.) lead to localized surface plasmons, highly spatially concentrated resonances in which the electromagnetic fields may far exceed those illuminating the structure.

Thanks to a wide range of unique properties from localized field enhancements to surface-bound optical transport, the study of surface plasmons has developed from fundamental research into an important quest targeting technological applications in opto-electronics, biology and medicine. To name only a few, surface plasmons are used to enhance Raman scattering [2], molecular fluorescence [3] and the output efficiency of solid state light emitters [4]. Commercial surface plasmon resonance ellipsometers [5] are capable of tracing minute amounts of a substance and are used, e.g., to detect protein monolayers [6] or to monitor antibody reactions.

An exciting theme in "plasmonics" that is expected to make the leap to technological relevance in the near future is the control of light propagation and local-

[1] 1 nm (nanometer)= 10^{-9} m=1 millionth of a millimeter

[2] 1 fs (femtosecond)= 10^{-15} s=1 millionth of a billionth of a second

ization on the nanoscale [7–10]. A prominent early example was the achievement of very high optical transmissivity through periodic arrays of very small subwavelength apertures in thin metal sheets [11]. These periodically-patterned film structures are ideal model systems that merge the concepts known from photonic crystals [12] with the exceptional material properties of metals to form "plasmonic crystals".

The surface plasmon polaritons excited in these structures are strongly coupled to the optical far-field, which limits their lifetime to few tens of femtoseconds [13–15]. This will restrict their use in certain optical elements, if no pathways are found to control this lifetime. To this end, understanding the spatial distributions of the light fields near the surfaces of such metallic photonic crystals is of paramount importance.

This thesis is a study of metallic nanostructures under femtosecond optical excitation. In the main part of the work, the dynamics of delocalized SPP excitations in plasmonic crystals and the underlying microscopic field distributions are investigated by spatially and temporally resolved optical spectroscopy. The results establish a connection between surface plasmon lifetimes and their real-space mode structure.

Measurements performed with a newly constructed near-field optical microscope provide a microscopic view into the plasmonic crystal's unit cell. Comparison with numerical simulations allows for an identification of different electromagnetic field components contributing to the image formation. Specifically, it is shown that both electric and magnetic field components can be selectively imaged.

The above aspects of the present work deal with the control and measurement of light propagation in the regime of linear optics. The strongest field localization in metal nanostructures is, however, achieved at the high intensities, where nonlinear material properties come into play.

A second part of the work highlights the benefits of optical field enhancements for the selective spatially-confined generation of nonlinear signals. Specifically, field enhancement leads to the emission of ultrashort electron pulses from sharp metal nanotips, which function as novel bright nanometer-scale sources of single electrons with femtosecond timing. This observation carries significant potential for future time-resolved electron experiments.

Outline

This thesis is organized as follows:

Chapter 2 introduces some relevant concepts and experimental techniques, including the setup of the near-field optical microscope constructed for this work and a brief theoretical description of the near-field imaging mechanism.

Chapter 3 outlines the essential properties of surface plasmon polaritons, their excitation in periodic nanostructures and a method for solving the related scattering problem of Maxwell's equations.

Chapter 4 is devoted to the investigation of the far-field properties of effectively one-dimensional plasmonic crystals. Phase-resolved and angle-dependent experiments reveal the dynamics of light transmission through these structures. The coherent coupling between different SPP bands is shown to result in the formation of band gaps and drastic modifications of radiative SPP lifetimes, most strikingly yielding a very long-lived "subradiant" surface plasmon resonance. In a near-field spectroscopic experiment, the mode structures underlying different SPP resonances are imaged for the first time. The existence of surface plasmon modes of different symmetry is shown for bands on opposite sides of the plasmonic band gap, providing a direct experimental confirmation of this fundamental concept in the Bloch theory of periodic media. Furthermore, an immediate connection between the microscopic mode structure and the radiative SPP lifetime is experimentally established.

Chapter 5 focuses in more detail on the near-field imaging and spectroscopy of the plasmonic structures. A comparison with numerical simulations demonstrates that different electric and magnetic vector components of the optical near-field can be imaged with different probe types and imaging conditions. Changes in the near-field spectra very close to the sample surface are analyzed with respect to the influence of tip-sample couplings. The final section of chapter 5 introduces the concept and implementation of a new form of local light source, in which grating excitation is employed to launch SPPs towards the apex of sharp metallic tips. This work integrates both delocalized and localized aspects of the optics in metallic nanostructures in one optical element.

Chapter 6, in contrast, deals with the consequences of highly-localized field enhancements at such nanometer-sized tips. The emission of spatially-confined femtosecond electron pulses is shown to result from the enhancement of optical nonlinearities at the tip apex. Various aspects of this emission are characterized, and finally, it is utilized to implement a novel form of scanning-probe microscope. This tip-enhanced electron emission microscope (TEEM) monitors the electron generation while an illuminated metal tip is scanned in close proximity to the sample.

Chapter 7 concludes the thesis and gives a brief outlook on future prospects in the different fields of study.

2 Methods and Concepts

The following chapter summarizes experimental and theoretical methods used in this thesis, providing the reader with conceptual background for the original work in the following chapters. The first section briefly presents the light sources used in the experiments, and introduces the spectroscopic techniques and analysis. The second section focuses on the relevant aspects of near-field optical microscopy.

2.1 Light Sources, Characterization and Spectroscopy

2.1.1 Femtosecond Ti:Sapphire Oscillators

The experiments were performed with two commercial 80 MHz repetition rate broadband laser systems, "Scientific" and "Rainbow", both manufactured by Femtolasers Incin Vienna. The lasers are chirped mirror [16–18], Kerr-lens mode-locked titanium sapphire (Ti:Sapphire) oscillators [19–22] delivering optical pulses at a center wavelength of 800 nm and with pulse durations of 10 fs (Scientific) and 7 fs (Rainbow), respectively. These short pulses contain appreciable spectral intensity in a broad wavelength range. Typical spectra of the two lasers are shown in Figs. 2.1(a) and (c). The large spectral width of these lasers, in combination with their high brightness, makes them exceptionally useful for the spectroscopic experiments with high angular resolution presented in Sec. (4.1).

2.1.2 Pulse Characterization

The lasers mentioned above emit light pulses that are only few optical cycles in duration.[1] Their time-dependent electric field $E(t)$ can be characterized with the frequently employed interferometric autocorrelation (IAC) technique [23]. Two identical copies of the optical pulses are collinearly interfered with a variable delay τ in a nonlinear medium, typically a BBO-crystal, oriented for phase-matched second harmonic generation [24]. The intensity of a general nonlinear interferometric autocorrelation with an n-th order nonlinearity is given by

[1] At a wavelength of 800 nm: 1 optical cycle ~ 2.7 fs$= 2.7 \cdot 10^{-15}$ s.

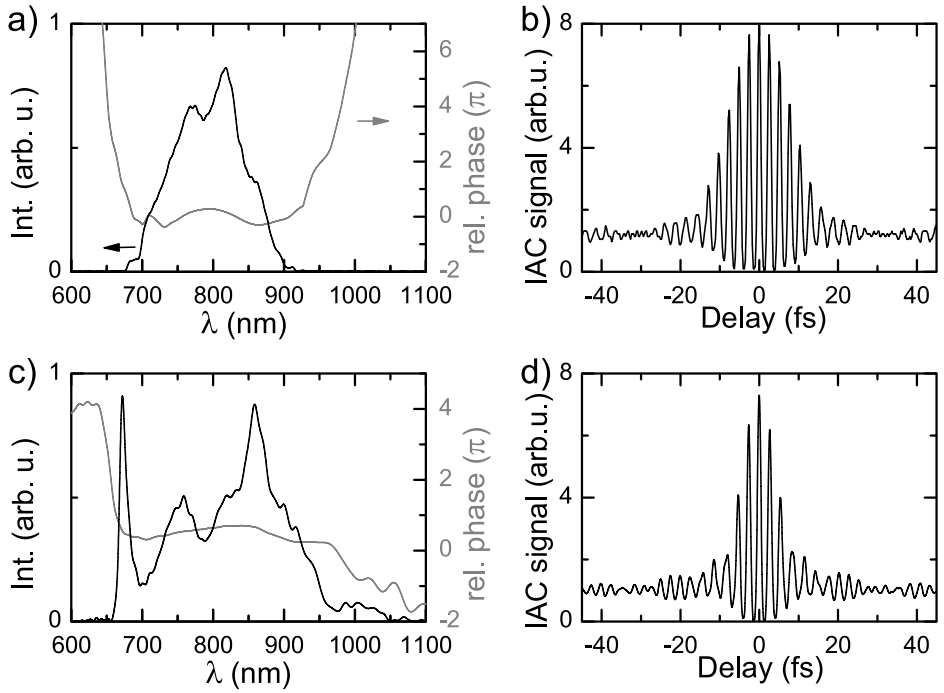

Figure 2.1: (a): Optical spectrum (black) and relative spectral phase (gray) of the 10-fs Ti:Sapphire laser oscillator. (b): Interferometric autocorrelation (IAC) measured for this laser. (c)-(d): The corresponding data for the 7-fs laser oscillator.

$I(\tau) = \int dt |E(t) + E(t-\tau)|^{2n}$. In the case of second harmonic generation, $n = 2$, and the ratio between the signal at zero delay and that at large delays should be 8. The IAC curves shown in Figs. 2.1(b) and (d) obtained in this way for the two femtosecond lasers described above fulfill this expectation acceptably well. The full-width-at-half-maximum (FWHM) of the IAC shown in Fig. 2.1(d) amounts to 10.0 fs, which yields a pulse duration of 6.5 fs assuming a hyperbolic secant pulse shape [25]. The data in Fig. 2.1(b) yield a longer pulse duration of approximately 11 fs.

Due to the lack of a one-to-one correspondence between a particular IAC trace and the underlying optical pulse, more sophisticated characterization techniques are required for a complete reconstruction of the optical field. The two main techniques currently available are "spectral phase interferometry for direct electric-field reconstruction" (SPIDER) and "frequency-resolved optical gating" (FROG). A detailed discussion of these techniques is beyond the scope of this thesis. Essentially, the necessary additional information is obtained by spectrally resolving the second harmonic signal generated via the nonlinear interaction of two (FROG) or three (SPIDER) laser pulses. These methods allow for a determination of the

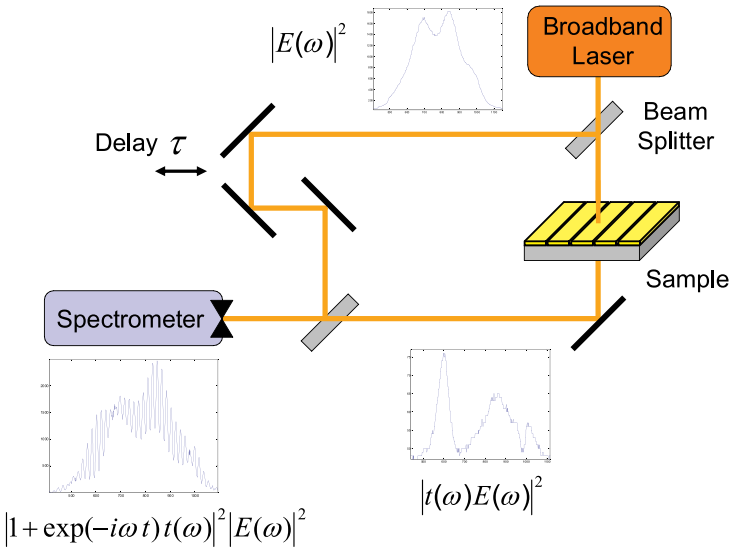

Figure 2.2: Spectral interferometry. The broadband laser pulses are split and sent through the two arms of a Mach-Zehnder interferometer. The spectral interferogram (bottom left) between the reference pulse (top) and the pulse transmitted through the investigated sample (bottom right) shows oscillations which can be adjusted by a delay τ.

(relative) spectral phase $\phi(\omega) = \arg(\tilde{E}(\omega))$ of a light pulse, where $\tilde{E}(\omega)$ is the Fourier transform (frequency representation) of $E(t)$. The phase curves are plotted in Figs. 2.1(a) and (c) as gray lines. From this measurement, the full time dependent electric field of a laser is obtained from the inverse Fourier transform. The only remaining information these methods cannot deliver is the absolute phase of the electric field, i.e., the temporal shift between the fast carrier frequency and the more slowly varying pulse envelope. This "carrier-envelope phase offset" [26, 27] is not directly relevant for the discussions in this thesis, so that it is not further considered.

For more in-depth coverage of the above methods, the reader is referred to Ref. [28] (FROG) or Ref. [29] (SPIDER). A comparison of different characterization techniques applied to the present 7-fs laser is published in Ref. [25].

2.1.3 Spectral Interferometry

The transmission of an optical pulse $E_{in}(t)$ through a passive, linear medium can be generally expressed in terms of the response function of the optical element, $a(t)$, so that the transmitted amplitude is expressed as [30]

$$E_{out}(t) = \int dt'\, a(t,t')E_{in}(t'). \tag{2.1}$$

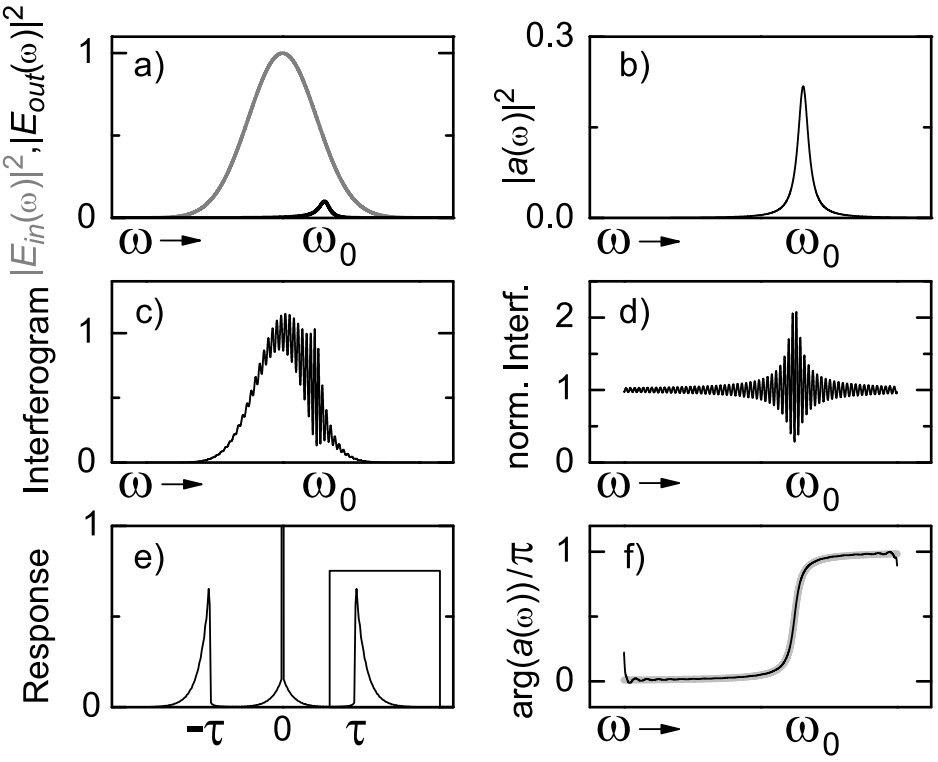

Figure 2.3: Intermediate steps in the phase retrieval algorithm. As an example, a Lorentzian transmission resonance at a frequency ω_0 is shown. (a): Spectrum of the incoming and the transmitted fields. (b): Normalized transmission spectrum. (c) Spectral interferogram. (d) Normalized spectral interferogram. (e) Magnitude of the Fourier transform of the normalized spectral interferogram. (f) Retrieved (black) and exact (gray) spectral phase of the Lorentzian resonance.

Causality leads to the constraint that $a(t,t') = 0$ for $t' > t$. If the system is also time-invariant, the explicit dependence on two time-variables can be replaced by the simplified dependence on time differences $a(t-t')$. In this case, Eq. (2.1) becomes a convolution in time, and it can be written as a product in frequency space of the incoming complex spectral amplitude[2] $E_{in}(\omega)$ with the complex transmissivity $a(\omega)$,

$$E_{out}(\omega) = a(\omega)E_{in}(\omega). \tag{2.2}$$

In chapter 4, we will discuss the transmissivity of resonant structures. While the magnitude $|a(\omega)|^2 = |E_{out}(\omega)|^2/|E_{in}(\omega)|^2$ can be easily determined by normal-

[2]Whenever the context permits, amplitudes in frequency space are denoted with the same letter as their temporal counterpart and without the tilde commonly used for the Fourier transform, i.e., $E(\omega)$ usually stands for $\tilde{E}(\omega)$.

ization of the transmitted spectrum, an interferometric technique is required for the retrieval of the phase information $\arg(a(\omega))$.

In spectral interferometry [31], a broadband optical pulse is sent through two arms of a dispersion-balanced Mach-Zehnder interferometer [see Fig. 2.2]. The light transmitted through the investigated medium is brought to interference with an undisturbed reference field from the same source. The superposition of both fields is spectrally resolved, and the intensity of the so-called spectral interferogram is given as

$$S(\omega) = |\exp(-i\omega\tau) + a(\omega)|^2 |E_{in}(\omega)|^2. \tag{2.3}$$

The rapid interference oscillations in the interferogram are due to the first term of this product, and the fringe spacing can be adjusted by the choice of the delay τ in the reference arm. A phase reconstruction for $a(\omega)$, illustrated by some intermediate steps shown in Fig. 2.3, proceeds as follows: i) The interferogram (c) is divided by the incoming spectrum $|E_{in}(\omega)|^2$ (gray curve in (a)), leaving a term, that, after expansion, reads (see (d))

$$\frac{S(\omega)}{|E_{in}(\omega)|^2} = 1 + |a(\omega)|^2 + 2\Re(a(\omega)\exp(-i\omega\tau)). \tag{2.4}$$

ii) A Fourier transform of this expression results in a component centered around zero, and two components that are shifted in the time domain by a positive and a negative value of the delay τ. The magnitude of this Fourier transform is shown in (e) and denoted with "response", because the temporal curve in the boxed region directly corresponds to the temporal response of the investigated structure to a pulsed excitation. In the case of this example, the Lorentzian lineshape corresponds to an exponentially decaying field envelope. iii) Selecting only the positive time component with a time-window filter [31] and back-transforming it into the frequency domain yields the complex $a(\omega)\exp(-i\omega\tau)$. Of this expression, the argument can be immediately evaluated numerically, compensating for the linearly increasing phase contribution $\omega\tau$. The result for our example is shown in Fig. 2.3(f) (black line). For comparison, the well-known π-phase change of a Lorentzian resonance is plotted as the thick gray line. Small deviations of the retrieved phase information from the ideal phase curve are only visible at the edges of the frequency domain, resulting from a limited bandwidth in the numerical calculations.

The procedure relies on the clear separation of the components in step iii), which can be achieved by choosing a delay that is large enough to make the oscillations in the interferogram more closely spaced than any significant variations in the transmitted intensity. In addition, in order to make the obtained phase information unambiguous, it needs to be checked whether the transmitted or the

reference light arrives at the detector first, i.e., whether the delay τ is negative or positive. Of course, a major prerequisite for the method is a good visibility of the fringes in the interferogram. Mechanical fluctuations often degrade the fringe visibility, because even small fluctuations in the relative path length shift the fringe pattern. On a timescale of seconds, fringes may be completely averaged out. One solution to this problem is an active stabilization of the interferometer with a frequency-stable cw-laser reference, e.g., a He-Ne-laser. In our case, we have solved the problem by using a fast line-scan charge-coupled-device camera after the monochromator. The camera is capable of integration times on the order of 1 ms, so that all mechanical vibrations up to 1 kHz do not influence the fringe visibility.

2.1.4 Short-Time Fourier Transform

After the determination of the complex transmissivity $a(\omega)$, the transmitted time transient $E_{out}(t)$ is obtained by back-transforming $E_{out}(\omega)$. An instructive visualization of a given time transient, containing both spectral and temporal information, can be obtained by a short-time Fourier transform. With a Gaussian-shaped window, for example, it takes the form:

$$W(f,t) = \left| \int dt' \, \exp\left(-\frac{(t'-t)^2}{2D^2} + ift' \right) E(t') \right|^2 \tag{2.5}$$

with D as the $(1/\sqrt{e})$-width of the window and $f = \omega/2\pi$. This two-variable function illustrates the temporal distribution of frequency components in the transient waveform. The temporal and spectral resolution of such a representation is given by the size of the selected window and the time-bandwidth-product of the windowing function, and should be chosen according to the characteristic spectral and temporal features of the pulse.

2.2 Aspects of Near-field Optical Microscopy

2.2.1 Optical Near-Fields

Near sources of electromagnetic radiation, oscillatory electric and magnetic near-fields are present that vary on length scales comparable to the size of those sources. Since electromagnetic sources may be much smaller than the wavelength they emit (e.g., single atoms, molecules, quantum dots, or small material clusters), characteristic length scales of the near-field can range from Ångstroms to typical values of few tens of nanometers.

We consider electromagnetic vector fields $\mathbf{E}(\mathbf{r},t)$ and $\mathbf{H}(\mathbf{r},t)$. The simplest example of a radiation source is the idealized point dipole. The electric field of an oscillating electric point dipole with frequency $\omega = ck$ and dipole moment $\mathbf{p} = \mathbf{p}_0 e^{-i\omega t}$ placed at the origin $r = 0$ can be written as the well-known sum of propagating and non-propagating contributions [30]:

$$\mathbf{E}_\mathbf{p}(\mathbf{r},t) = \frac{1}{4\pi\varepsilon_0}\left[k^2(\mathbf{n}\times\mathbf{p})\times\mathbf{n}\frac{e^{ikr}}{r} + (3\mathbf{n}(\mathbf{n}\cdot\mathbf{p}) - \mathbf{p})\left(\frac{1}{r^3} - \frac{ik}{r^2}\right)e^{ikr}\right],$$

$$\mathbf{H}_\mathbf{p}(\mathbf{r},t) = \frac{ck^2}{4\pi}(\mathbf{n}\times\mathbf{p})\left[\frac{e^{ikr}}{r} - \frac{e^{ikr}}{ikr^2}\right]. \tag{2.6}$$

Here, $\mathbf{n} = \mathbf{r}/r$ is the unit length vector along $\mathbf{r}$, and the first and second terms in each of the square brackets correspond to the propagating and non-propagating components of the fields, respectively. While the first (transverse) component prevails in the radiation zone (distances $r \gg \lambda$) with its r^{-1} dependence, the second dominates the field at distances $r < \lambda$, i.e., in the near-field. Very close to the dipole, the electric field dominates over the magnetic field due to the term proportional to r^{-3}. In this regime, the fields vary rapidly on the scale of the wavelength, i.e., possess derivatives for which $\left|\frac{\partial E_j}{\partial r}\right| / E_j > \frac{\omega}{c}$.

This last condition is not only satisfied near localized (point-like) sources, but also for delocalized surface waves of the form

$$\mathbf{E}(\mathbf{r},t) \propto \exp(i(k_x x - \omega t) - \kappa_z z), \tag{2.7}$$

with a real spatial exponential decay constant κ_z, so that in vacuum ($n = 1$), $\omega^2/c^2 = k_x^2 - \kappa_z^2$ and $k_x > \omega/c$. Such "evanescent", surface-bound fields appear, for example, in total internal reflection [32] and are part of all surface polariton excitations, such as the surface plasmon polaritons discussed in this thesis.

2.2.2 Limits to Far-Field Optical Microscopy

It is well known that the wave properties of light limit the spatial resolution of conventional optical microscopes. We will cover some essential reasons for this here, in order to highlight the difference between far-field and near-field microscopy. More detailed discussions are found in standard optics textbooks, such as Refs. [32–34].

In conventional optical microscopes, the light emitted (scattered, transmitted etc.) from a sample is collected by a lens or microscope objective and re-focused to produce an image. Since these microscopes are based on the collection of

electromagnetic fields in the radiation zone $r \gg \lambda$, neither the non-radiative part of a dipole field, nor a pure surface wave can be detected.

Generally, this kind of imaging can be described in terms of an optical transfer function f connecting the fields in the object plane with those in the image plane similar to the form of a linear response function discussed earlier, namely

$$f_{\omega,im}(x/a) = \int d\xi' \; g_\omega(x,\xi') f_{\omega,obj}(\xi'), \tag{2.8}$$

where x and ξ are spatial variables defined in the image and object planes, respectively, and a is an arbitrary magnification of the imaging system.[3] Neglecting certain off-axis aberrations [33], this integral can again be written as a product in Fourier space, this time with the wavevector component k_x as variable:

$$f_{\omega,im}(ak_x) = g_\omega(k_x) f_{\omega,obj}(k_x). \tag{2.9}$$

The limitations on the transfer function $g_\omega(k_x)$ are responsible for the finite resolution in all conventional optical microscopes. Specifically, the finite numerical aperture (acceptance angle) results in a cutoff at some value of k_x, so that $g_\omega(k_x) = 0$ for $k_x > k_{x,cut}$. Such a cut-off directly results in a resolution limit via the properties of the spatial Fourier transform, i.e., a restriction of the spatial frequencies to a width Δk_x limits the spatial resolution to roughly $\Delta x \sim 2\pi/\Delta k_x$. Modern methods offer numerous approaches to optimize the available resolution for a given numerical aperture (e.g., in confocal microscopy [36]), or to extend the numerical aperture to the absolute limit of a solid angle of 4π [37].

No matter which approach is taken, all conventional optical microscopes make use of only propagating waves to form an image. The wave equation for a field $f(r,t)$ in a medium of refractive index n,

$$\frac{n^2}{c^2}\frac{\partial^2}{\partial t^2} f(r,t) = \nabla^2 f(r,t), \tag{2.10}$$

leads with a wave ansatz $f(\mathbf{r},t) \propto \exp(i(\mathbf{k}\cdot\mathbf{r} - \omega t))$ to the dispersion of light,

$$\frac{n^2}{c^2}\,\omega^2 = k_x^2 + k_y^2 + k_z^2 = n^2 k^2 \text{ with } k = \frac{2\pi}{\lambda}. \tag{2.11}$$

Since waves propagating in transparent media have real wavevector components, $k_i \leq n\omega/c,\ i\ \varepsilon\ \{x,y,z\}$ for all waves propagating from the object to the image plane. Consequently, $g_\omega(k_i) = 0$ for $k_i > n\omega/c$, limiting the spatial resolution to the order of $\lambda = 2\pi/k$. The field components with $k_i > n\omega/c$ are non-propagating, evanescent fields, which can only be observed in the near-field of a source.

[3] For simplicity, the description is restricted to one scalar field. A detailed discussion of the point spread function for realistic and arbitrary vector fields can be found, e.g., in Ref. [35].

2.2.3 Development of Near-Field Microscopy

In 1928, Edward H. Synge made a proposal to overcome the limitations of conventional optical microscopes [38]. His idea was based on the illumination of a sample with a light spot much smaller than the wavelength, which could be scanned across the sample surface to obtain an image with a spatial resolution given by the spot size. Due to technical limitations, the concept could not be realized before 1984, when the fabrication of small apertures in metal films [39, 40] and techniques associated with the scanning tunneling microscope [41] made such local illumination and imaging possible. Shortly after the first near-field experiments had been performed under local illumination through an aperture, a reciprocal imaging technique was demonstrated, where the near-field light at an externally illuminated sample was collected through a metallic aperture [42].[4]

Another few years later, a third major development known as "apertureless" near-field microscopy was achieved by using sharp metallic tips as local scattering centers for near-fields [43–45]. A recent review on these methods can be found in Ref. [46]. Today, the relative importance of apertureless techniques has outgrown that of the traditional aperture methods, for reasons of higher spatial resolution or larger local field enhancements [see, e.g., Sec. (6.3)]. However, major improvements in aperture fabrication still and frequently lead to exceptional new results, such as the real-space observation of exciton wave functions [47]. Current key interests lie in specifically tailored near-field probes like individual nanoparticles [48, 49], molecules [50], or nano-fabricated optical antennae [51]. The study of probe-sample couplings with such probes is gaining significant attention.

2.2.4 Modes of Imaging and Probe Types

For the present work, collection and scattering type near-field microscopy of an externally illuminated structure are particularly important.[5] Fig. 2.4 shows schematics of the configurations employed in the near-field experiments reported here. In one class of experiments [(a) and (b)], the substrate side of a given sample is illuminated by weakly focused (opening angle about 1°) far-field radiation from one of the laser sources [Sec. (2.1)]. The electromagnetic field distributions on the opposite side of the metal nanostructures, e.g., resonant surface plasmon polaritons [Ch. 3], are detected in two alternative ways: (a) In the standard col-

[4] It should be mentioned that a strict separation between collection and illumination modes is not possible due to probe-sample interactions. For instance, in a collection experiment, scattering at the probe leads to local illumination of the sample.

[5] During the course of the experimental work for this thesis, two separate investigations [52–54] have made use of local illumination through an aperture, but lie outside the scope of metal nanostructures and are therefore not covered here.

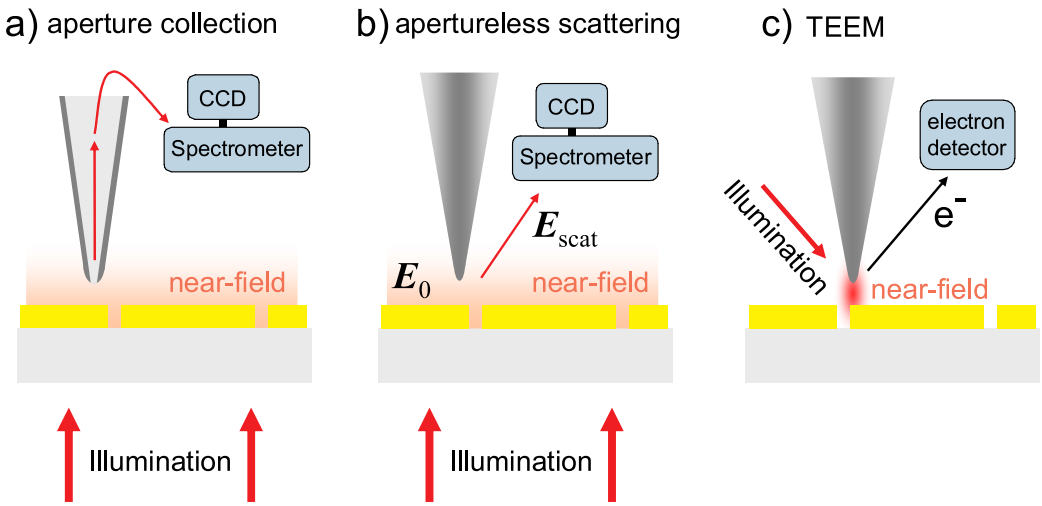

Figure 2.4: The different imaging methods used. The resonant electromagnetic modes of an externally illuminated metallic nanostructure are imaged and spectrally resolved either by collection through an aperture of a metallized fiber tip (a) or by apertureless scattering of the near-field (b). In a newly developed form of imaging performed under vacuum conditions (c), the probe-sample system is illuminated from the side, and the local generation of electrons is recorded. This imaging is termed TEEM for tip-enhanced electron emission microscope.

lection mode by coupling them through an aperture of a metal coated fiber tip; (b) in an apertureless mode by scattering the fields at a sharp probe. Different types of scattering probes, such as electrochemically etched metal tips or metal-coated fiber tips are used. In these cases, the collected or scattered light is dispersed in a grating monochromator and detected with a charge coupled device (CCD) camera. In order to detect weak signals in the aperture collection mode, a liquid nitrogen cooled CCD or an avalanche photodiode (APD) are employed. In all experiments, the tip position is fixed, and the sample is scanned.

In another type of experiment (c), both probe and sample are illuminated from the side. The local generation of electrons near the probe end leads to an alternative and novel kind of near-field imaging, the details of which are found in Ch. 6.

The various experimental configurations make use of different types of near-field probes. Highly resolved transmission electron microscope images of such tips are shown in Fig. 2.5. In the aperture collection experiments, commercial Aluminum-coated fiber tips were used (Veeco 1730-00, single-mode for $\lambda > 633$ nm, aperture diameter 50-80 nm). These aperture tips yield very reproducible results, and the overall tip geometry is often small enough to make them useful also in apertureless scattering experiments. Other apertureless scatter-

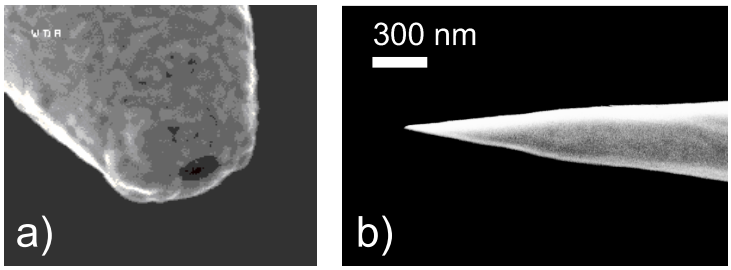

Figure 2.5: (a): Aluminum coated fiber probe with an aperture diameter of about 100 nm [cf. Ref. [55]]. (b): Electrochemically etched gold tip with a radius of curvature of few tens of nanometers.

ing experiments were performed with gold or tungsten tips, prepared by in-house electrochemical etching.

2.2.5 Implementation of the Near-Field Microscope

An ultra-stable near-field scanning optical microscope (NSOM) was constructed that produces images in the various configurations. A block diagram of this instrument is found in Appendix B. Photographs of the central part of the microscope are displayed in Fig. 2.6. The sample is mounted on a piezo scanner ("PicoCube" manufactured by PhysikInstrumente GmbH) with a three-dimensional travel range of $5 \times 5 \times 5$ μm and a capacitive position detection with a precision of better than 0.5 nm. A control signal to the scanner can be either directly amplified to set the voltage applied to the piezo ceramics, or, under active stabilization using capacitive position sensors, to set an absolute position in space. In the latter mode, otherwise unavoidable piezo drifts and hysteresis effects can be eliminated.

The distance between the tip and the sample is regulated by a shear-force feedback system [56] employing a tuning fork sensor [57, 58], which has been used in a number of high-resolution atomic force microscopes [59, 60]. The tips are glued on one tine of a quartz tuning fork, extending past the end of the fork by roughly 100 μm. The tuning fork is mechanically excited at its resonant frequency ($\sim$ 30 kHz) by applying a small AC voltage to a tube piezo, on which it is mounted (denoted as "dither-piezo"). The current induced between the two electrical tuning fork contacts by the mechanical oscillation is picked up and amplified by a transimpedance amplifier (gain up to 1 GV/A) placed close to the setup. A lock-in amplifier demodulates and further amplifies the signal, yielding an output voltage proportional to the momentary oscillation amplitude of the tuning-fork-tip system, with a demodulation bandwidth of usually 1 kHz. A current of about 4 nA cor-

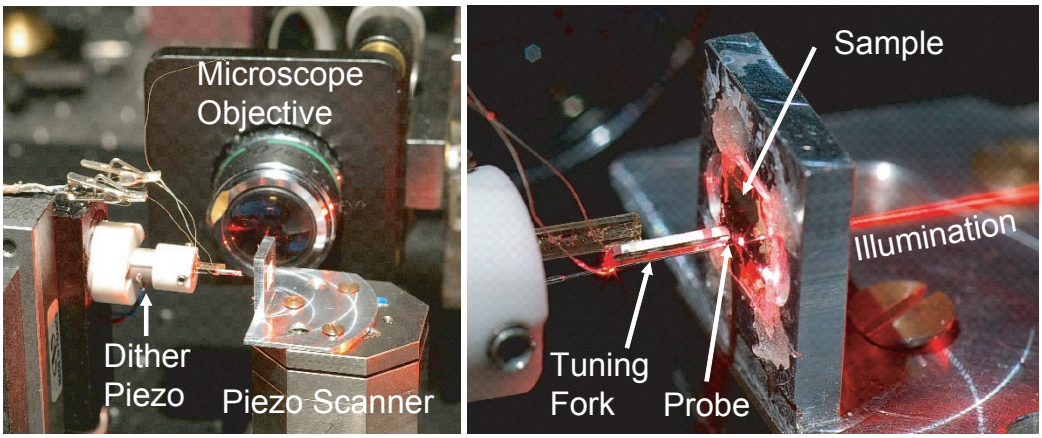

Figure 2.6: Photographs of the central part of the NSOM. Note that the tip orientation is horizontal, i.e., rotated by 90° with respect to the usual depiction.

responds to a mechanical oscillation amplitude of 1 nm.[6] The experiments were performed with oscillation amplitudes of this size to achieve high spatial resolution in the image while maintaining an amplitude detection noise ratio of less than $5 \cdot 10^{-3}$. If the tip is brought into nanometer proximity with the sample, mechanical shear-forces, which are still not fully understood microscopically [59, 61], lead to a shift of the resonance frequency and to increased damping of the oscillation. These changes result in a decrease of the oscillation amplitude for fixed dither-piezo excitation, allowing for a precise determination of the point of contact. Furthermore, via a PID-controlled[7] feedback of the amplitude signal into the positioning piezo, a stable tip-sample distance on the order of few nanometers can be maintained. This setup is capable of the measuring picoNewton interaction forces between the tip and the sample [58], so that in principle, even interactions as small as van der Waals forces are measurable [59]. It is important to note that the applied forces are smaller than those required to mechanically modify or deform the tips, which is essential for long-term and reproducible imaging. In order to minimize mechanical disturbances to the setup, the NSOM was placed on a passive vibration insulation table on top of the optical table, and a sound insulation housing was constructed.

In the so-called constant-distance imaging technique, a constant oscillation amplitude of the tuning fork below that of the out-of-contact amplitude is main-

[6] R. Pomraenke, private communication; based on an interferometric optical measurement of the tuning fork motion.

[7] A "**P**roportional-**I**ntegral-**D**ifferential"-controller is an element of a control loop that feeds the difference between the setpoint and the sensor signal, the "error signal", back to a control variable, and it does so with a controllable frequency-dependent gain. See Ref. [62] for details.

tained via the feedback loop by moving the sample towards or away from the tip. The sample is then scanned in the x-y plane perpendicular to the tip axis, and the sample motion in the z-direction directly reflects the surface topography. Most published NSOM measurements are obtained in constant-distance mode, because it provides the simplest way to record an image while limiting the interaction forces on the probe. Early in the development of near-field microscopy, it was recognized that the relative z-motion of the sample and the probe in this form of imaging may lead to "cross-talk" of the surface morphology onto an optical signal [63, 64], resulting in so-called topographic artifacts.[8] One way to identify such artifacts involves noting the variations in the optical signal and comparing them to the surface roughness [64]. If the optical signal varies significantly over distances that are comparable to the relative tip-sample motion, special care is needed in the interpretation of constant-distance imaging.

2.2.6 Theoretical Description of the Imaging Mechanism

Many theoretical approaches have been developed that describe contrast and image formation in near-field microscopy. Comprehensive overviews of early studies are found in Refs. [65, 66]; other reviews are given, for example, in Refs. [67–69]. The main difficulty of a theoretical description is the inherent complexity of this three-dimensional electrodynamics problem, comprising the tip and sample geometries and possibly multiple scattering between the two. Although general expressions are often found in the literature, analytical solutions of a particular problem are an exception, and numerical simulations are usually required to obtain a quantitative interpretation of images. A number of simplifications can, however, permit tractable analytical solutions that yield surprisingly good results in many circumstances.

We consider a scattering-type situation as the generic example. The geometrical arrangement and the respective incident and scattered fields are indicated in Fig. 2.4(b). The aperture collection setup can be treated in a similar way, with modifications discussed in Sec. (2.2.7). We begin by formulating the problem in terms of the vectorial Lippmann-Schwinger equation for the electric field, which is derived in Appendix C. Separating out a harmonic time dependence $\mathrm{e}^{-i\omega t}$, the expression for the sum of the incident and scattered fields is

$$\mathbf{E}(\mathbf{r}) = \mathbf{E}_0(\mathbf{r}) + k^2 \int d\mathbf{r}' \, [\varepsilon(\mathbf{r}') - \varepsilon_{ref}(\mathbf{r}')] \widehat{G}(\mathbf{r}, \mathbf{r}') \mathbf{E}(\mathbf{r}'). \tag{2.12}$$

Here, $\mathbf{E}(\mathbf{r})$ is the total electric field composed of the incident field $\mathbf{E}_0(\mathbf{r})$, which will usually be the optical near-fields in the absence of a probe, and the scattering

[8] See the following section for a description of NSOM image contrast.

contributions in the integral, which contains $\mathbf{E}(\mathbf{r})$ itself. $\varepsilon_{ref}(\mathbf{r})$ and $\varepsilon(\mathbf{r})$ are the dielectric functions of the geometry in the absence and presence of the probe, respectively. In the present context, it is sufficient to consider only linear, local and locally isotropic dielectric media. The Lippmann-Schwinger equation for the total field contains all multiple interactions between the probe and the sample. As in quantum mechanical scattering problems, it can in principle be solved iteratively by a Born series. In order to obtain an instructive expression for the electric field scattered to a detector placed in the far-field zone, an electric point-dipole approximation for the probe and the first Born-approximation for the scattered amplitude will be used.

The Green's tensor $\widehat{G}(\mathbf{r},\mathbf{r}')$ is of course the key to the solution of this problem. It describes the field at $\mathbf{r}$ for a point source at the position $\mathbf{r}'$. In general, $\widehat{G}(\mathbf{r},\mathbf{r}')$ contains the dipole contribution $\widehat{G}_0(\mathbf{r},\mathbf{r}')$ of the form of Eq. (2.6) emerging from $\mathbf{r}'$, plus the fields scattered from the sample surface, $\widehat{G}_s(\mathbf{r},\mathbf{r}')$, which can be incorporated by image dipole fields [70].

We are considering only situations in which the probe itself is embedded in air or vacuum, so that $\varepsilon_{ref}(\mathbf{r}) = 1$ over the integration region where it is different from $\varepsilon(\mathbf{r})$, and the terms multiplying the Green's tensor become the polarization $\mathbf{P}$. The presence of the probe can be treated in the simplest form by modeling it as a point dipole located at the probe position $\mathbf{r}_{pr}$ [70–73]. In this case, the integration in Eq. (2.12) reduces to

$$\mathbf{E}(\mathbf{r}) = \mathbf{E}_0(\mathbf{r}) + \frac{k^2}{\varepsilon_0}\widehat{G}(\mathbf{r},\mathbf{r}_{pr})\mathbf{p}, \tag{2.13}$$

where $\mathbf{p}$ is the induced dipole moment. It can be estimated via the polarizability of a small dielectric particle, for which $\mathbf{p} = \widehat{\alpha}_0\mathbf{E}$. The polarizability tensor of a sphere of radius R and of a material with dielectric function $\varepsilon(\omega)$, surrounded by vacuum, is given by

$$\widehat{\alpha}_0(\omega) = \alpha_0(\omega)\,\widehat{I} \doteq 4\pi\varepsilon_0 R^3 \frac{\varepsilon(\omega)-1}{\varepsilon(\omega)+2}\,\widehat{I}, \tag{2.14}$$

where $\widehat{I}$ is the unit tensor, i.e., the identity matrix. A general form for ellipsoidal particles much smaller than the light wavelength is found, e.g., in Ref. [74]. For very small probe-sample distances d, the presence of the surface can strongly modify the effective polarizability of the sphere parallel and perpendicular to the surface [75–77], which is sometimes called surface dressing [73, 78].[9] In the limit of a dielectric sample with small $\varepsilon_{ref}(\mathbf{r})$, the image dipole contribution becomes small, and the Green's tensor differs only slightly from a single dipolar

[9] Recently, this has been used in the development of a new type of optical microscopy [48].

form. In the other limit of a perfectly conducting surface opposing the tip, equal contributions of the dipole and its image have to be included in $\widehat{G}$. A general treatment for arbitrary surfaces is more complicated, involving Sommerfeld-type integrals [70, 79, 80]. Here, approximate expressions are derived, which contain the essential features of the surface dressing for dipoles parallel and perpendicular to the sample.

We consider a flat interface, which will be the highly reflective gold surface in the experiments. Part of the fields from the dipole are reflected from the surface and act back on the dipole, thus modifying its effective polarizability. The reflected fields can be described in terms of image dipoles with strengths $\pm\mathbf{p}\Delta$ for dipoles perpendicular $(+)$ and parallel $(-)$ to the surface, respectively, where $\Delta(\omega) = \frac{n(\omega)-1}{n(\omega)+1}$ is the reflectivity of the metal surface and $n(\omega)$ is the metal's refractive index.[10] The probe's dipole moment, which gives the field radiated away from the probe, is the total field, i.e., the incident plus reflected field, multiplied by the particle's polarizability. This is now rewritten as the product of the incident field with a new effective (surface-dressed) polarizability:

$$\mathbf{p} = \widehat{\alpha}_0\mathbf{E} = \widehat{\alpha}_{dr}\mathbf{E_0} \text{ and } \qquad \mathbf{E} = \mathbf{E}_0 + \mathbf{E}_{\pm\Delta\mathbf{p}}, \tag{2.15}$$

where $\mathbf{E}_{\pm\Delta\mathbf{p}}$ refers to the image dipole field Eq. (2.6) evaluated at the probe position, i.e., at a distance $2d$. At the flat surface considered here, the polarizability tensor remains diagonal, but splits into components parallel and perpendicular to the sample surface,

$$\widehat{\alpha}_{dr}(\omega) = \begin{pmatrix} \alpha_{\parallel}(\omega) & 0 & 0 \\ 0 & \alpha_{\parallel}(\omega) & 0 \\ 0 & 0 & \alpha_{\perp}(\omega) \end{pmatrix} \tag{2.16}$$

The components are calculated by solving for $\widehat{\alpha}_{dr}$ in Eq. (2.15), keeping in mind that image dipole field $\mathbf{E}_{\pm\Delta\mathbf{p}}$ is proportional to the total field, as well. Often, only the dominant contribution, i.e., the (quasi-static) dipole near-field of $\mathbf{E}_{\pm\Delta\mathbf{p}}$ is included, yielding [71, 75]

$$\alpha_{\parallel}(\omega) = \frac{8\alpha_0(\omega)d^3}{8d^3 - \alpha_0(\omega)\Delta(\omega)/4\pi\varepsilon_0}, \quad \alpha_{\perp}(\omega) = \frac{4\alpha_0(\omega)d^3}{4d^3 - \alpha_0(\omega)\Delta(\omega)/4\pi\varepsilon_0}. \tag{2.17}$$

The expressions including the retardation from the propagating components are not found so easily. In particular, the excitation of surface plasmon polaritons and

[10] It should be noted that the expression for the reflectivity given in many references, e.g. Refs. [71, 73, 77, 78], actually gives unphysical results for metals, namely an image dipole larger than the original dipole.

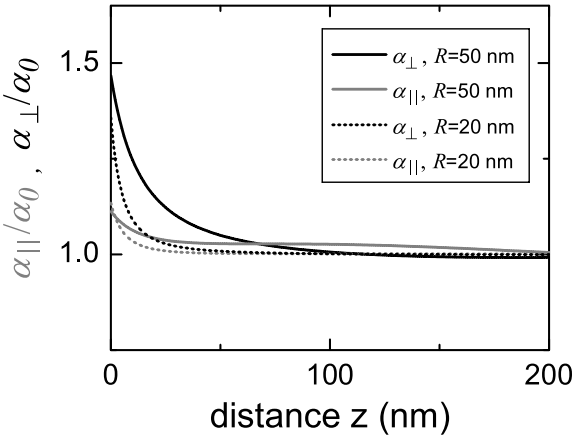

Figure 2.7: Increase of the effective polarizabilities perpendicular (black) and parallel (gray) to the surface for a perfectly conducting spheres of radii 50 nm (solid) and 20 nm (dotted) near a perfectly conducting surface.

the associated damping of the dipole complicate matters [70]. Since the reflectivity of gold is very large in the near-infrared wavelengths considered here ($\sim 98\%$ at 800 nm), the qualitative features are expected to be similar to those of a perfect conductor. Defining a phase factor $\phi = 2kd$, one obtains for a perfect conductor

$$\alpha_{\parallel}(\omega) = \frac{\alpha_0(\omega)}{1 - \alpha_0(\omega)\frac{k^3}{4\pi\varepsilon_0}\left(-\frac{1}{\phi} + \frac{1}{\phi^3} - \frac{i}{\phi^2}\right)e^{i\phi}},$$
$$\alpha_{\perp}(\omega) = \frac{\alpha_0(\omega)}{1 - \alpha_0(\omega)\frac{2k^3}{4\pi\varepsilon_0}\left(\frac{1}{\phi^3} - \frac{i}{\phi^2}\right)e^{i\phi}}. \tag{2.18}$$

Assuming a Lorentzian dipole resonance, similar expressions were derived in Ref. [69]. Note that by keeping only terms $O(\phi^{-3})$, expressions (2.17) are regained for $\Delta = 1$. The effective perpendicular (black) and parallel (gray) polarizabilities of Eq. (2.18) are plotted in Fig. 2.7 for perfectly conducting[11] small spheres with radii of 50 nm (solid) and 20 nm (dotted). They display a sharp increase very close to the surface, especially for the out-of-plane polarizability. For larger distances, propagation effects lead to a weak oscillatory behavior. The point $z = 0$ nm was defined as the position, where the perimeter of the sphere touches the surface, as in Ref. [77].

With the above definitions, the total field at the detector is related to the local field at the probe via a matrix multiplication. The detector is placed at a position in the far-field, where the incident field is zero. Assuming that those multiply scattered fields that differ from the surface dressing have a much smaller contribution to the signal than the incident field $\mathbf{E}_0(\mathbf{r}_{det})$, the total field can be replaced by this incident field (first Born approximation), yielding

$$\mathbf{E}(\mathbf{r}_{det}) \propto \widehat{G}(\mathbf{r}_{det}, \mathbf{r}_{pr})\widehat{\alpha}_{dr}(\omega)\mathbf{E}_0(\mathbf{r}_{pr}). \tag{2.19}$$

[11] See the next subsection for the meaning of "perfectly conducting".

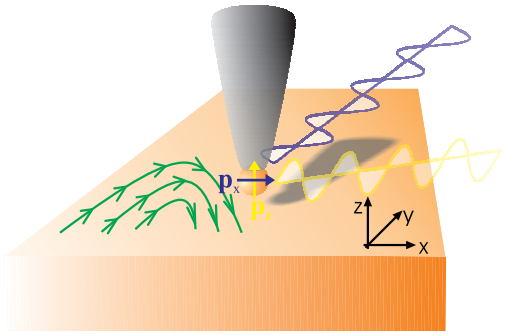

Figure 2.8: The optical near-field close to a sample surface (green) may generally have a complicated local polarization, inducing a dipole moment in the near-field probe with components parallel and perpendicular to the surface. Detecting the fields from different orientations and selecting different polarizations may allow for a reconstruction of the local near-field polarization.

Hence, within the above approximations, a relatively simple correspondence exists between the local near-field and the field at the detector. Scanning of the tip relative to the sample allows for a mapping of the near-field with a resolution no longer limited by the wavelength, but rather by the finite spatial extension of a real probe entering in the convolution of Eq. (2.12).

It is important to note that besides the near-field intensity, the local polarization of the optical near-field is also transferred to the far field via the Green's tensor. Figure 2.8 schematically depicts a vectorial near-field (green) containing electric field components parallel and perpendicular to the surface, which induce an electric dipole moment in the probe that can be decomposed into a sum of $\mathbf{p_x}$ and $\mathbf{p_z}$. These emit dipolar radiation with a polarization and angular distribution according to their orientation. For example, the fields stemming from $\mathbf{p_z}$ will be primarily radiated along the x-y-plane, polarized parallel to z. Therefore, by the choice of various detection angles and analyzing different polarizations, a reconstruction of the vectorial near-field polarization may be possible. Theoretically, such polarization effects in scattering NSOM are considered, e.g., in Refs. [80–82]. Experimental consequences and further discussion will be given in Ch. 5.

2.2.7 Magnetic Dipole Moments

The electric dipole approximation is a very common simplification of near-field scattering problems, although a brief consideration shows that even for rather small particles it is necessary to include other multipoles for a correct description of the image contrast. The electric dipole approximation for a particle is valid

as long as fields inside the particle are homogeneous, which implies that the particle is much smaller than the wavelengths of the electromagnetic fields both in the surrounding medium and also in the probe material itself. For metallic probes, this corresponds to particles smaller than the penetration depth ranging from a few nanometers up to few tens of nanometers. Aluminum, in particular, is often chosen as a coating material of aperture-type near-field probes for its small penetration depth. These probes are specifically designed to block the near-field light from penetrating the entire probe, so that for such tips, the electric dipole approximation cannot be expected to yield a valid description. Instead, Mie theory [83, 84] could be applied to the scattering problem to evaluate the different multipolar components of a specific probe geometry. Unfortunately, the extended tip geometry and the close-by sample surface make this a rather complicated task.

A first correction to the single electric point dipole is obtained by considering the probe, e.g., the aluminum coated fiber probe, as a highly conducting particle. In this case, the boundary conditions for the electromagnetic fields lead to additional magnetic dipole radiation, which becomes of almost equal importance for the particle's scattering cross-section [30]. For a perfectly conducting small[12] sphere of radius R, one can ascribe to the particle an effective magnetic dipole moment induced by $\mathbf{H}_{inc}$, in addition to the electric dipole moment induced by the electric field $\mathbf{E}_{inc}$. The dipole moments are expressed as [30]

$$\mathbf{p} = 4\pi\varepsilon_0 R^3 \mathbf{E}_{inc} \,, \qquad \mathbf{m} = -2\pi R^3 \mathbf{H}_{inc} \,. \tag{2.20}$$

To quantify the relative importance of these dipoles for the scattering, we look at the scattered fields of an incoming plane wave with an electric field amplitude E_{inc}. The amplitude of the corresponding magnetic field is $H_{inc} = E_{inc}\sqrt{\varepsilon_0/\mu_0}$. Now, the amplitudes of the electric fields in the far-zone of the induced magnetic and electric dipoles in Eq. (2.20) scale as $E_{s,el.} \propto \mathbf{p}$ and $E_{s,magn.} \propto \mathbf{m}\sqrt{\varepsilon_0\mu_0}$ [30], so that the scattered amplitudes differ by only a factor of two, $E_{s,el.} = 2E_{s,magn.}$. Therefore, the magnetic field sensitivity of a highly conducting probe should not be completely ignored.

Associating a magnetic dipole moment proportional to the external magnetic field to a particle made from a non-magnetic material may at first seem odd. The magnetic moment $\propto \int d\mathbf{r}(\mathbf{r} \times \mathbf{J})$ is, however, only a consequence of the circular currents induced in the sphere, which are proportional to the curl of the electric field. Since Maxwell's equations are coupled, the boundary conditions for the electric field near interfaces between non-magnetic dielectrics may be re-expressed as boundary conditions for the magnetic fields. In the case of a good

[12] "Perfectly conducting" implies that the electric field vanishes everywhere inside the particle. "Small" refers in this case only to much smaller than the wavelength of the incoming light, as the decay length in the particle is assumed to be zero.

conductor, the magnetic field is expelled from the material along with the electric field due to the shielding of the conduction electrons. This expulsion has an effect on the magnetic field as long as the frequency of the time-varying electromagnetic field is smaller than the metal's plasma frequency and larger than the inverse time constant of the magnetic field diffusion, which is very slow.

The induced magnetic dipole moment is not only important in the case of scattering from a highly conducting particle, but also for the transmission through a very small aperture, as Bethe has recognized in 1944 [85]. He considered the transmission through an aperture in a perfectly conducting sheet and found that the radiation in the far-zone can be decomposed as stemming from the superposition of an electric dipole oriented perpendicular and a magnetic dipole parallel to the sheet, both proportional to the respective electric and magnetic fields at the aperture. While his calculations of the near-field close to the aperture were later corrected by Bouwkamp [86], the decomposition was confirmed (except for a change in sign) [30]:

$$\mathbf{p} = -\frac{4}{3}\pi\varepsilon_0 R^3 \mathbf{E}_{inc,\perp} , \qquad \mathbf{m} = \frac{8}{3}\pi R^3 \mathbf{H}_{inc,\parallel} , \tag{2.21}$$

for a small aperture with radius R. This aperture can be viewed as a first approximation to the description of an NSOM aperture probe [Fig 2.5(a)]. The actual magnitude of the fields radiated away from these dipoles depends on the orientation of the incident field. For a p-polarized plane wave impinging close to tangentially on the aperture, the electric field amplitude generated in the far-field of the magnetic dipole is actually a factor of 2 larger than that generated from the electric dipole, as is found by comparison with Eq. (2.20). Thus, the maximum intensity at a given distance from the magnetic dipole is expected to be a factor of 4 larger than that of the electric dipole, a fact that is not prominently discussed in the literature. A theoretical study for an actual conical aperture tip has confirmed that also in that geometry, both electric and magnetic field components should contribute to the near-field signal [87].

In analogy to the electric dipole moments discussed in the previous subsection, the reflection from the sample causes a surface dressing of the magnetic dipoles. Here, the roles of the electric and magnetic fields are interchanged in the boundary conditions, i.e., for a perfect conductor, the normal component of the magnetic field vanishes at the surface. This results in the interchange of the labels $\perp$ and $\parallel$ in Eq. (2.18), which otherwise translate into the respective expressions for the magnetic polarizabilities.

2.2.8 Open Questions

The considerations in Sec. (2.2.7) indicate that the magnetic field should be an essential component in near-field microscopy with highly conducting probes. Experimental evidence for magnetic field imaging is, however, relatively slim. Only rarely has the possibility to image magnetic field components been suggested on the basis of measurements [88, 89]. For example, Ref. [88] reports an imaging of the magnetic field near metal nanoparticles, but states that unique probe conditions, specifically a well-defined metal film thickness on a dielectric tip, needed to be satisfied to observe such effects. On the other hand, it has been mentioned before [Sec. (2.2.1)] that the electric field is quantitatively dominant in the very near-field of an electric dipole, so that the near-fields of localized plasmon excitations, for example, may often not contain strong enough magnetic field components to be recognized in experiments.

It will be discussed in the next chapter that surface plasmon polaritons on the surface of a metal contain different field components, namely electric fields perpendicular to the surface and both electric and magnetic fields parallel to the surface. The question naturally arises which of these fields can be imaged in NSOM experiments with different probe types. This will be of particular importance for the imaging of the resonant modes of photonic nanostructures, as the different field components can have completely different spatial distributions.

Further open questions concern the influence of tip-sample couplings on the results of NSOM experiments. For simplicity, expressions in a first Born approximation including surface dressing were given, yet multiple scattering between the probe dipole and the sample can have effects on a sample's near-field modes beyond this approximation. Due to the near-field enhancement of the effective probe dipoles from the surface dressing, this will be of particular importance for small tip-sample distances.

These questions will be addressed in chapter 5 on the basis of results from NSOM experiments. The analysis of spectrally resolved data will be of key importance to the identification of imaged field components, near-field resonances and tip-sample couplings.

3 Surface Plasmon Polaritons in Metallic Photonic Crystals

In 1957, Ritchie derived the energy loss of electrons incident on thin metallic films due to collective excitations of the electron plasma [90]. Early experimental evidence of these surface plasma oscillations or "surface plasmons" [91] was presented in 1960 [92]. Since that time, considerable efforts have been devoted to the investigation of the various aspects of surface plasmons, for example their excitation on gratings [93]. Thorough experimental and theoretical reviews covering works up to the mid-1980s on the interaction of light with surface plasmons are found in Refs. [1, 94]. The electromagnetic fields associated with surface plasmons play a crucial role in the enhancement of a wealth of physical phenomena near surfaces, such as second-harmonic generation [95, 96], Brillouin-scattering [97], multi-photon electron emission [98] and, most prominently, the surface-enhanced Raman scattering effect (SERS) [2] discovered thirty years ago [99–102].

In recent years, the properties of surface plasmons, e.g., a strong surface localization, combined with large field enhancements, have increasingly motivated theoretical and experimental studies of surface plasmon excitations in metallic nanostructures [9]. Interesting model systems are periodic thin film gratings [11], the metallic counterparts of dielectric photonic crystals, that allow for a study of the resonant excitation of surface plasmons and their coupling to far-field radiation.

This chapter begins with an introduction to the basic concept and the properties of surface plasmon polaritons (SPPs). The following sections cover the excitation of SPPs in metallic photonic crystals and their role in the angle of incidence dependent light transmission. Finally, a theoretical method used to calculate the optical properties of the investigated structures is briefly described.

3.1 Essential Properties

Surface plasmon polaritons (SPPs) are surface-bound waves at an interface between two media, typically a metal and a dielectric. SPPs constitute a combined

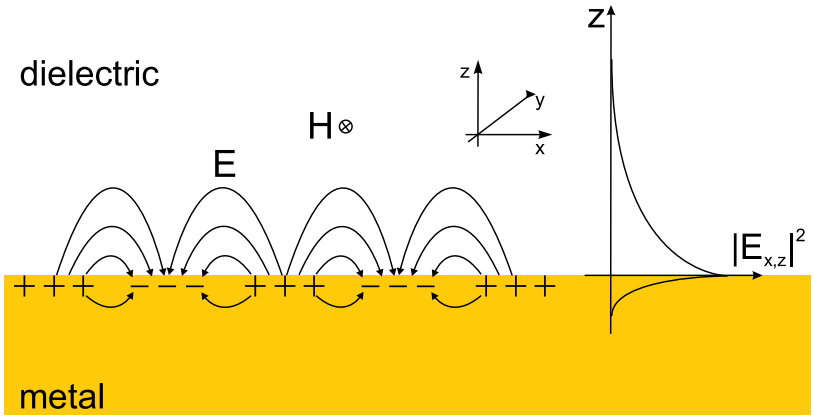

Figure 3.1: Schematic representation of the electromagnetic fields of a surface plasmon polariton. Surface charge oscillations are associated with an electromagnetic field decaying exponentially from the surface into both media.

mode between the collective oscillation of conduction electrons (plasmon) at the surface of the metal and the electromagnetic mode near the interface [see Fig. 3.1]. The existence of SPPs follows directly from Maxwell's equations [1, 30] under the condition that the real part of the metal's dielectric function $\varepsilon_m(\omega)$ is negative and larger in magnitude than that of the dielectric, i.e., $-\Re(\varepsilon_m) > \Re(\varepsilon_d)$. Most aspects of surface plasmons can be described in terms of Maxwell's equations with a complex frequency-dependent dielectric function of the metal. In the following, some basic properties are summarized.

3.1.1 Fields, Energy Densities

The fields of an SPP propagating along the x-direction can be fully described by the magnetic field component in the y-direction parallel to the surface and the electric field components in the x- and the z-directions parallel and perpendicular to the surface (defined as $z = 0$ nm), respectively. The electromagnetic mode is therefore of the transverse-magnetic (TM) type, with a spatial dependence in the two media of the form

$$\begin{aligned} &\mathbf{H}_j = \hat{\mathbf{y}} H_{y,j} f_j(x,z) \ , \ \mathbf{E}_j = (\hat{\mathbf{x}} E_{x,j} + \hat{\mathbf{z}} E_{z,j}) f_j(x,z) \ , \\ &f_j(x,z) = \exp(ik_x x - \kappa_{z,j}|z|) \ , \end{aligned} \tag{3.1}$$

where $\hat{\mathbf{x}}$ is the unit vector along the x-direction, and the index j stands for the dielectric ($j = d$) or the metal ($j = m$).

The relative field strengths are easily computed from Maxwell's equations and the boundary conditions for the electric and magnetic fields (continuity of E_x and

H_y, and $\varepsilon_m E_{z,m} = \varepsilon_d E_{z,d}$). For our purposes, the fields of a metal-air (or vacuum) SPP are of primary interest, so that we set $\varepsilon_d = 1$ for the moment. Expressed in terms of the relative dielectric function of the metal, ε_m, one obtains the following relations for the complex field amplitudes in vacuum:

$$E_{z,vac} = -\sqrt{\varepsilon_m} E_{x,vac} \quad , \quad H_{y,vac} = -\sqrt{\varepsilon_m + 1}\sqrt{\frac{\varepsilon_0}{\mu_0}} E_{x,vac}. \tag{3.2}$$

The relatively large negative real part of the dielectric function of gold ($\varepsilon = -24 + 1.6i$ at 800 nm [103]) permits only weak electric fields along the x-direction. The ratio between E_z and H_y is very close to that of a plane wave (propagating along x), i.e., the impedance of free space $Z_0 = \sqrt{\mu_0/\varepsilon_0}$.

In general, surface plasmon polaritons are of a mixed plasmonic and photonic nature. The SPPs studied in this thesis are predominantly of photonic character, i.e., for the present experimental conditions, most of their electromagnetic energy is contained in the fields outside of the metal. This is quantified by considering the electromagnetic energy in both media. The time-averaged energy density in a non-magnetic, electrically dispersive medium is given by [104]:

$$\overline{u} = \frac{1}{4}\left(\frac{d(\omega\varepsilon(\omega))}{d\omega}\varepsilon_0|E|^2 + \mu_0|H|^2\right). \tag{3.3}$$

In order to reach an analytic expression for the energy density of an SPP in the metal, a Drude type dielectric function is used [105](see below), taking into account only the dominant real part. In this case, the dispersive term multiplying the electric component reduces to $(2 - \varepsilon_m)$. After expressing the energy densities in the dielectric and the metal in terms of the magnetic field and integrating over the metal and dielectric half-spaces, the ratio between the electromagnetic energies in the metal and the dielectric results as:

$$\frac{W_d}{W_m} = \frac{\varepsilon_m^2}{(1-\varepsilon_m)\varepsilon_d} \approx \frac{-\varepsilon_m}{\varepsilon_d}. \tag{3.4}$$

For a light frequency corresponding to a wavelength of 800 nm, about 96% of the electromagnetic energy of an air-metal SPP is contained outside the metal, which is in part responsible for the long SPP propagation lengths, even on absorptive metals.

3.1.2 Decay Constants, Dispersion Relation, Damping

The electromagnetic fields associated with an SPP exponentially decay away from the interface into both the dielectric and the metal [Eq. (3.1)]. The respective

decay constants are

$$\kappa_m = \frac{\omega}{c}\left(\frac{-\varepsilon_m^2}{\varepsilon_m+\varepsilon_d}\right)^{1/2}, \quad \kappa_d = \frac{\omega}{c}\left(\frac{-\varepsilon_d^2}{\varepsilon_m+\varepsilon_d}\right)^{1/2}, \tag{3.5}$$

so that the fields decay by a factor $|\varepsilon_m/\varepsilon_d|$ more rapidly in the metal than in the dielectric. For the air-gold SPP and a light wavelength of 800 nm, the decay constants correspond to decay lengths for the field intensities $1/(2\kappa_j)$ of 306 nm and 13 nm in air and gold, respectively.

Surface plasmon polaritons travel along the interface with phase velocities close to the vacuum speed of light. The SPP dispersion for the in-plane wave vector component $k_{x,SPP}$ is given by [1]:

$$k_{x,SPP} = \frac{\omega}{c}\left(\frac{\varepsilon_m\varepsilon_d}{\varepsilon_m+\varepsilon_d}\right)^{1/2}. \tag{3.6}$$

This dispersion relation has far-reaching consequences for the physics of SPPs. The propagation of SPPs on metal films is damped by optical absorption in the metal. The decay length is obtained from the imaginary part of the complex propagation constant in Eq. (3.6). The distance L, after which the intensity of a propagation SPP is reduced due to absorption by a factor of $1/e$, is

$$L = \frac{1}{2\Im[k_{x,SPP}(\omega)]}, \tag{3.7}$$

which amounts to $L \approx 43\ \mu$m at 800 nm.

In a situation, where a spatially homogeneous SPP excitation is provided, the absorption decay may be preferably described in terms of temporal damping. The damping time (or lifetime), after which the SPP intensity has decreased by a factor of $1/e$, is expressed as

$$T = \frac{1}{2\Im[\omega(\Re[k_{x,SPP}])]}, \tag{3.8}$$

where in practice, one can first obtain $k_{x,SPP}$ for a particular real frequency by the use of Eq. (3.6) and then re-enter this value to find the imaginary part of ω.[1] At a wavelength 800 nm, a lifetime $T \approx 145$ fs follows.

For practical and instructive purposes, we consider a free electron gas with a complex Drude response [105]

$$\varepsilon_m(\omega) = 1 - \frac{\omega_{pl}^2}{\omega(\omega+i\gamma)}, \tag{3.9}$$

[1] An alternative expression is found in Ref. [1].

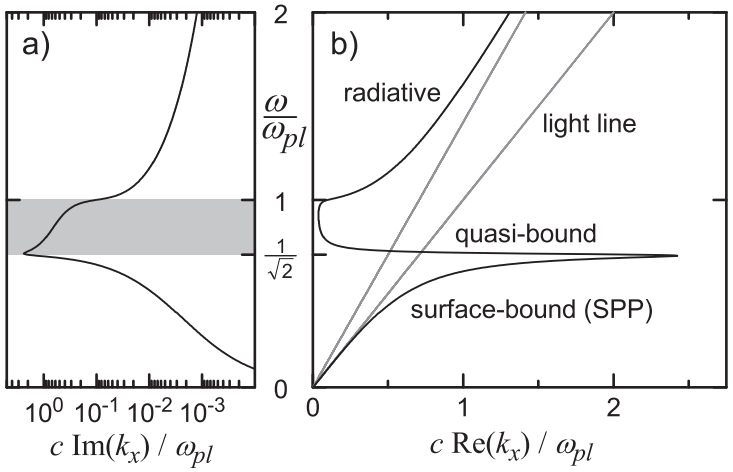

Figure 3.2: Surface plasmon dispersion curve for a Drude metal with $\gamma = 0.02\ \omega_{pl}$ (and at a vacuum interface). Frequency versus imaginary (a) and real (b) parts of the in-plane wave vector component k_x. The branch below $\omega_{pl}/\sqrt{2}$ corresponds to surface-bound plasmon polaritons (SPP).

where ω_{pl} is the plasma frequency and γ is the dephasing rate. Many of the optical properties of metals are already captured within this simple model. The dispersion relation $\omega(k_x)$ is plotted in Fig. 3.2, separately for the real and imaginary parts of k_x and with the axes normalized to the plasma frequency. One observes a typical polariton splitting dispersion [106] that is induced by a coupling between the electromagnetic field dispersion (given by the light line) and a wave-vector independent mode, given by the bulk plasma oscillation at ω_{pl}. This coupling leads to an avoided crossing and to a splitting into a lower and an upper polariton branch, separated by a gap between ω_{pl} and $\omega_{pl}/\sqrt{2}$, in which only very lossy modes exist [shaded area in Fig. 3.2(a)]. The upper polariton branch represents radiative and unbound plasmon polariton modes (following the notation of Ref. [107]), while the lower branch up to the plasmon polariton gap corresponds to the surface-bound plasmon polaritons with which this thesis is concerned. The gray curves show the asymptotic behavior of the plasmon polariton dispersion for small and high frequencies. At low frequencies, the dispersion approaches the "light line" $\omega = ck_x$, whereas at high frequencies, the asymptote is given by $\omega = \sqrt{2}ck_x$.

In this thesis, most of the experimental work is dealing with SPPs in metallic nanostructures made from gold. The dielectric function of gold deviates significantly from a Drude behavior[2], so that hereafter, experimentally determined val-

[2]The interband absorption edge (about 2 eV at room temperature [108]), which is due to transitions between the filled d-band and empty conduction band states, leads to the yellowish appear-

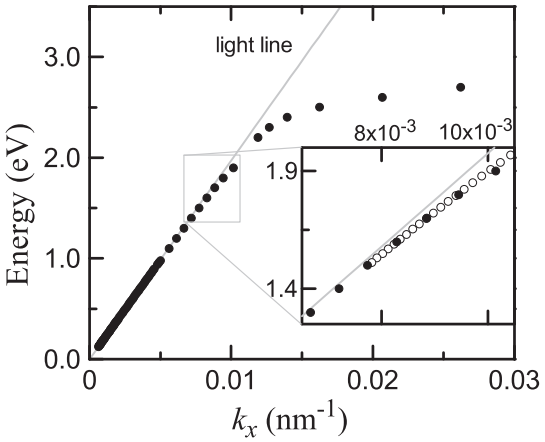

Figure 3.3: Surface plasmon polariton dispersion for gold, calculated from experimentally determined values for the dielectric function (open circles Ref. [109], full circles Ref. [103]). The inset demonstrates that the SPP dispersion is very close to the light line in the photon energy range of the broadband Ti:Sapphire lasers.

ues of the dielectric function of gold are used, published in Johnson and Christie's seminal paper [109] and in the "Handbook of Optical Constants of Solids", edited by E. D. Palik [103].

Figure 3.3 shows the SPP dispersion for the dielectric function of gold, magnifying the photon energy range relevant to this thesis, namely the range between 1.3 eV ($\sim$950 nm) and 1.9 eV ($\sim$650 nm) spanned by the broadband Ti:Sapphire lasers described in Ch. 2. As in the previous case of the Drude dispersion, the in-plane surface plasmon polariton momentum $k_{x,SPP}$ of Eq.(3.6) is always larger than that of a plane wave of light impinging on a metal surface at any angle θ, given by $k_{x,light} = \frac{\omega}{c}\sin(\theta)$. In light of this fact, it is often stated that the SPP dispersion relation $\omega(k_{x,SPP})$ "lies outside the light cone". In other words, on a smooth metal surface, simultaneous momentum and frequency (or energy) conservation forbids SPP excitation by incoming far-field radiation.

3.2 SPP Excitation on Metal Films

The momentum mismatch between far-field radiation and SPPs can be overcome in a number of alternative ways. One option is the excitation of SPPs by evanescent fields, for which $k_{x,ev.}$ may be larger than $\frac{\omega}{c}$. A prominent and widely used implementation of evanescent SPP excitation is the Kretschmann-Raether, Kretschmann [110, 111] or Otto geometry [112], in which the evanescent fields created by total internal reflection at a dielectric prism excite SPPs on a thin metal film evaporated onto the prism. Another natural possibility utilizes scattering by

ance of gold and results in drastic deviations from a simple Drude behavior in the visible part of the spectrum [105]. At near-infrared and longer wavelengths, a Drude model serves as a better approximation.

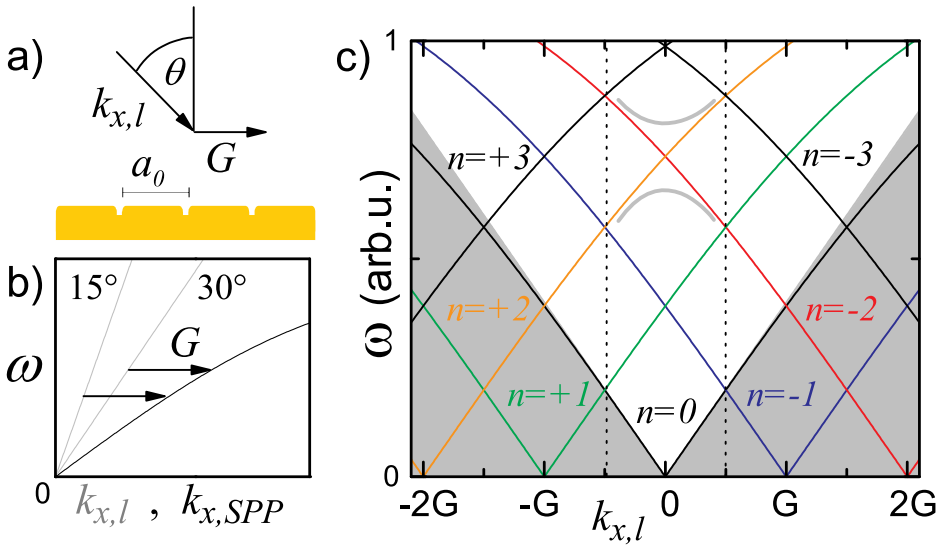

Figure 3.4: Excitation of surface plasmon polaritons by grating coupling. (a): Scattering at a periodic surface corrugation can supply additional momentum G. (b): At different angles of incidence, scattering to different parts of the SPP dispersion is possible. (c): SPP zone scheme displaying different SPP "bands" as a function of the incoming light momentum $k_{x,l}$. The shaded areas lie outside the light cone and are therefore not directly accessible by far-field radiation. At the intersection of different bands, couplings result in the appearance of band gaps [117, 118], as indicated by the two gray curves near the zone center.

surface defects [70] or roughness, which are present in all real metallic films. This breaking of the translational invariance relieves the momentum conservation constraints, and the far-field excitation of surface plasmon polaritons is induced by scattering. The efficiency and angular dependence of this coupling strongly depend on the specific surface conditions and were studied early on [113–116].

Gratings with well-defined periodicity comprise a particular and artificially producible type of "roughness" [93]. In the case of a grating on an otherwise smooth surface [Fig. 3.4(a)], the spatial invariance is broken, except for translations of integer multiples of the lattice period a_0. Accordingly, momentum conservation in k-space is required only modulo the grating vector $G = 2\pi/a_0$. Hence, far-field excitation of SPPs on a grating can be achieved if [119]

$$k_{x,l} \doteq \frac{\omega}{c}\sin(\theta) = k_{x,SPP}(\omega) \pm n \cdot G. \tag{3.10}$$

In this way, the momentum mismatch between the far-field radiation and the SPP dispersion relation is overcome, and different SPP frequencies can be excited for different angles of incidence [Fig. 3.4(b)]. These excitations appear as resonances,

e.g., in the reflection spectra of gratings [1]. Solutions to Eq. (3.10) are possible at every angle for various values of n. Gratings often have lattice constants on the order of the wavelength of the excitation light. The solutions to Eq. (3.10) can be viewed as the SPP dispersion being folded into the first Brillouin zone of the structured surface, in complete analogy to other periodically modulated media. The result of this procedure is a SPP band structure shown in Fig. 3.4(c), where curves corresponding to different integer values of n are indicated. Near the intersection points of the different bands in the zone center and at the zone boundaries, couplings between the different modes will lead to a splitting of these bands (gray lines in the zone center as an example) [117, 118]. This aspect will be covered in Sec. (4.3).

For thin-film metallic gratings on dielectric substrates, SPPs on both sides of the grating can be excited. These SPPs possess different dispersions and consequently appear at different wavelengths in angle-dependent reflection or transmission spectra. The different SPP bands are labeled according to their diffracted order and the excited interface, namely AM[$\pm n$] and SM[$\pm n$] for air-metal and substrate-metal SPPs of order $\pm n$ [cf. Eq. (3.10)], respectively. For metal films thinner than the decay lengths in the metal, strong coupling through the metal film may occur, leading to a different SPP dispersion [1, 94]. In this work, however, only films thicker than the penetration depth are studied, so that only couplings due to protrusions in the films need to be considered.

3.3 Light Transmission through Plasmonic Crystals

The advantages of grating excitation have been utilized early on in the study of surface plasmon polaritons [1]. In recent years, the subject has garnered immense interest due the remarkable properties associated with SPPs in modern nano-fabricated thin metallic film transmission gratings. Ebbesen and coworkers [11, 119] discovered an extraordinarily large optical transmission efficiency through a square periodic arrangement of holes in a thin metallic film [see Fig. 3.5]. The holes were much smaller than the wavelengths of the transmitted light; yet, at certain wavelengths, the transmission could even exceed unity when normalized to the geometrical fraction on the surface occupied by the holes. This was orders of magnitude larger than expected from classical diffraction theory for an individual subwavelength hole in a metal film [85, 86], which drops rapidly for wavelengths above the hole cutoff. These observations were explained with the resonant excitation and subsequent transit of surface plasmon polaritons on and through the structure [11, 119–121], respectively. Although there has been great debate and controversy about this assignment [122–125], it is now widely accepted and supported by a wide variety of experimental observations, including

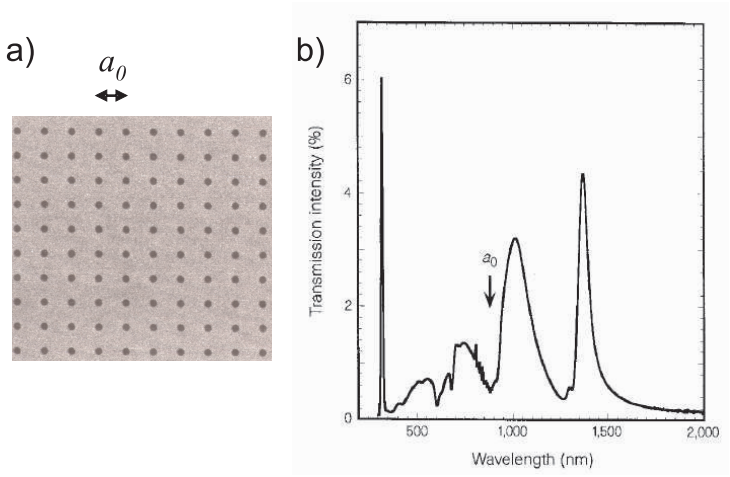

Figure 3.5: (a): Scanning electron microscope image of a square nanohole array similar to those used in the experiments of Ebbesen *et al.* (b): Transmission spectrum for normal incidence for an array with lattice period 900 nm, hole diameter 150 nm and silver film thickness 200 nm (from Ref. [11]).

near-field optical microscopy [13, 126, 127]. The latest review on properties of light transmission through individual holes and arrays is found in Ref. [128].

The realization that SPPs may be employed to localize and geometrically squeeze light into extremely small volumes has sparked great efforts to understand in detail the underlying effects, and to eventually control light propagation and localization on a subwavelength scale [9]. In this context, the periodically modulated or perforated thin metal films mentioned above, sometimes called "plasmonic crystals" in analogy to photonic crystals, play an important role as well-defined model systems.

This work will focus particularly on the dynamical aspects of light transmission through such structures and how they are influenced by the coherent couplings among different SPP modes. Further, the optical near-fields associated with SPP resonances will be of interest, as the SPP modes of a given structure directly translate into its far-field properties. In this pursuit, the metallic photonic crystals will be the primary subject of investigation; however, the characteristic field distributions at SPP resonances will also reveal information about both the relevant methods of near-field imaging (particularly polarization-selective imaging) and effects related to tip-sample couplings.

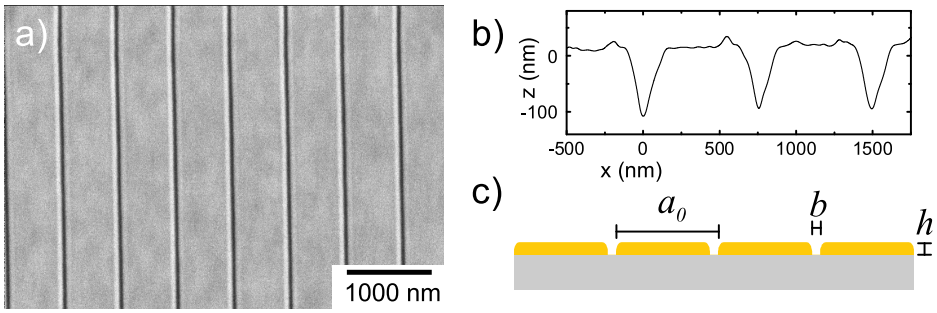

Figure 3.6: The investigated periodically patterned thin-film gratings. (a): Scanning electron micrograph of a one-dimensional slit array in a gold film. (b): Cross-section as measured with the shear-force topography detection. (c): Definitions of the structural parameters lattice period a_0, slit width b and film thickness h.

3.4 Investigated Structures

In this thesis, experimental results and theoretical models are presented for one-dimensional plasmonic crystals consisting of optically thick ($\sim$ 100 nm) gold films evaporated on sapphire substrates. The films are perforated with periodic arrays of slits with widths around 50 nm and lattice periods between 600 nm and 900 nm. The samples are fabricated by gold evaporation followed by electron beam lithography and Argon ion lift-off in the group of Prof. D.-S. Kim at Seoul National University. Structures with a highly precise periodicity were obtained. Their outstanding surface quality produces exceedingly long SPP propagation lengths. A top-view scanning electron micrograph of one of the structures is shown in Fig. 3.6(a). The cross-section, measured with the shear-force atomic force microscope described in Sec. (2.2.5), is plotted in Fig. 3.6(b), and the definitions of the geometrical variables used hereafter are shown in Fig. 3.6(c).

3.5 Solution of the Scattering Problem

It was mentioned earlier that most aspects of surface plasmon polaritons can be described in terms of Maxwell's equations with local and frequency-dependent dielectric functions of the respective materials. This work focuses on one-dimensional metallic photonic crystals, for which numerical solutions of Maxwell's equations can be obtained with available methods. We are interested in solving the scattering problem displayed in Fig. 3.7. An incoming plane wave is scattered by the structures into transmitted and reflected diffraction orders. The propagating diffraction orders are detectable in the far-field, while the SPP exci-

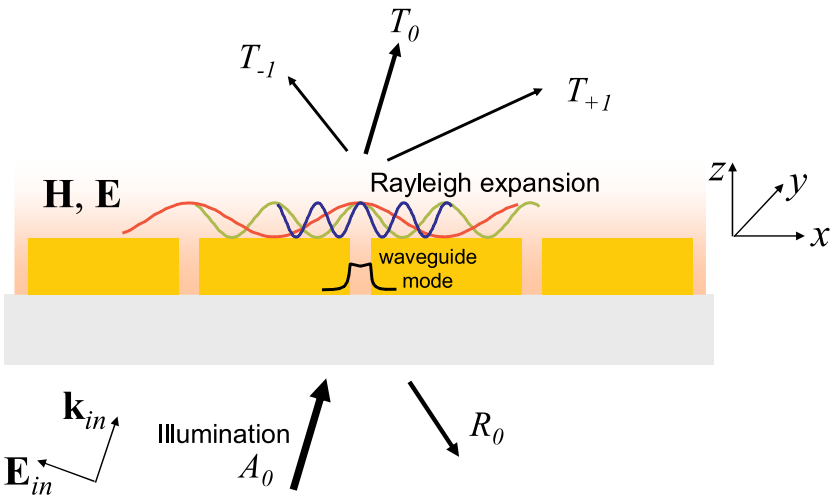

Figure 3.7: Schematic depiction of the scattering problem. A p-polarized wave with amplitude A_0 is incident on the periodic structure, generally at inclined incidence with a wave vector $\mathbf{k}_{in}$. We are interested in the transmitted and reflected amplitudes of the diffraction orders T_n and R_n, $n \in \{0, \pm 1, \pm 2, ..\}$, which can be either propagating or evanescent.

tations correspond to evanescent surface waves.

The proper choice of method is essential for a quantitative agreement between theoretical computations and the experimental results, such as transmission spectra or near-field optical images. Although we deal with a rather clear and simple geometry, i.e., a periodic arrangement of rectangular metallic slabs on a dielectric substrate, many methods suffer from difficulties in solving the scattering problem for these structures. For example, in finite-difference time domain (FDTD) calculations [129], a satisfactory implementation of varying angles of incidence is rather involved. Other methods designed for scattering at periodic dielectric structures, such as many transfer matrix formalisms, often exhibit very slow or even a lack of convergence when confronted with metallic structures.

We found a scattering matrix method introduced by Lochbihler and Depine for gratings made from highly conductive materials to deliver good results and fast convergence. The numerical method was implemented in the programming environment of MATLAB.[3] Several comprehensive articles describe the approach in detail [130–135], and a complete reproduction of all expressions would go beyond the scope of this thesis. For that reason, only the principle steps are sketched, and the reader is referred to the cited literature for a more explicit treatment.

The Lochbihler method is based on an approximation employing the so-called surface impedance boundary conditions (SIBC) for the electromagnetic fields at

[3] Version 6.5 (R 13), manufactured by TheMathworks, Inc.

the surface of good, but finite conductors. These relate the tangential components of the electric and magnetic fields at a metal surface [30],

$$\mathbf{E}_{\parallel} = Z\hat{\mathbf{n}} \times \mathbf{H}_{\parallel}, \tag{3.11}$$

where Z is the surface impedance of the metal, which can be approximated as [136, 137]

$$Z = \sqrt{\frac{\mu_0}{\varepsilon_0 \varepsilon(\omega)}} = \frac{Z_0}{n(\omega)}, \tag{3.12}$$

with the free-space impedance Z_0. The SIBCs are an excellent approximation, as long as the radii of curvature at the metallic surfaces, where they are applied, are not smaller than the penetration depth of the fields.

In the present variant, the SIBC method solves for the magnetic field in the y-direction (perpendicular to the figure plane in Fig. 3.7). Using the SIBCs, the magnetic field inside the nanoslit waveguide is expanded in a sum of waveguide eigenmodes (modal expansion) with lateral spatial profiles [133]

$$u_m(x) \propto \frac{\eta}{\beta_m} \sin(\beta_m x) + cos(\beta_m x). \tag{3.13}$$

Here, $\eta = -i\frac{\omega}{c}Z$, and β_m is related to the mode propagation constant along the z-direction, μ_m, via

$$\mu_m^2 + \beta_m^2 = \frac{\omega^2}{c^2}. \tag{3.14}$$

The eigenvalues β_m are the solutions to the complex transcendental equation

$$\tan(\beta_m b) = \frac{2\eta\beta_m}{\beta_m^2 - \eta^2} \tag{3.15}$$

for a waveguide of width b. The waveguide modes can be viewed as surface plasmon modes traveling along the vertical walls of the structure with their peak amplitudes located at the boundaries. For any film thickness, at least the zeroth mode (sketched in Fig. 3.7) propagates, and its propagation constant μ has a large real part. For the very thin slits considered here, the higher order modes are strongly damped in the waveguide and accordingly do not contribute to a coupling of both interfaces. For very narrow slits, an approximate expression for the lowest order β_0 is found by replacing the tangent with its argument, resulting in

$$\beta_m = \sqrt{2\eta/b + \eta^2}. \tag{3.16}$$

Above and below the metal structure, the field is decomposed as a Rayleigh expansion into sinusoidal diffraction orders (sketched above the structure as colored waves in Fig. 3.7) with propagation constants

$$\chi_n = \sqrt{\frac{\omega^2}{c^2} - \alpha_n^2} \quad , \quad \alpha_n = \frac{\omega}{c}\sin(\theta) + n \cdot G, \tag{3.17}$$

where θ and G are again the angle of incidence and the lattice vector, respectively. In this expansion, the field above the structure is, for example, expressed as

$$H_y = \sum_{n=-\infty}^{\infty} T_n \exp\left[i(\alpha_n x + \chi_n z)\right]. \tag{3.18}$$

Here, $z = 0$ nm is again defined as the height of the upper structure surface. Depending on the order n, these waves are either propagating waves ($\frac{\omega}{c} > |\alpha_n|$) or evanescent surface waves ($\frac{\omega}{c} < |\alpha_n|$), such as the fields of an SPP. The coefficients in the two expansions (Rayleigh and modal expansion) are used to set up a matrix equation from the respective boundary conditions at $z = 0$ nm and $z = -h$ (h is the thickness of the metal film). At the lateral positions of the slits, the boundary conditions are the continuity of the magnetic field and its vertical derivative, i.e., the derivative along the z-direction, which is proportional to E_x. At the boundary between the metal and the free spaces, the SIBCs are used again.

The resulting matrix equation is solved numerically, yielding the amplitudes of the transmitted and reflected diffraction orders. The magnetic field H_y is obtained by propagating these amplitudes to any given point above the structure with Eq. (3.18), and the electric vector field $\mathbf{E}$ is found from the respective spatial derivatives of H_y.

This method yields transmission and reflection spectra, as well as the electromagnetic fields near the surfaces of the structure. Whenever it is necessary or instructive, the experimental data will be compared with the results of this method. The focus will, however, stay on the experimental side. First, one has to keep in mind that the numerical method makes use of an approximation, whose entire range of validity still has to be investigated for the present structures. Second, the calculations are performed for an idealized rectangular structure, which in reality cannot be manufactured. Rounded edges of the cross-sections, very small imperfections in the grating periodicity, or a finite surface roughness are not easily incorporated in a numerical calculation, but impossible to avoid for a realistic structure. The physical consequences of these deviations from an ideal structure necessitate experimental investigation. The method could be extended to structures of arbitrary cross-section with additional effort [132], but finite surface roughness or disordered structures are quite hard to model. In essence, we are interested in the properties and limitations of real structures, searching for basic and general principles.

In combination with the far-field experiments, these full numerical computations will serve as complementary information to more simple or intuitive phenomenological models. With respect to the near-field optical experiments, the simulations yield the spatial distribution of all components of the vectorial electromagnetic near-field. This will promote a direct identification of different near-field imaging contrasts, and will clarify which field components are actually imaged.

4 Femtosecond Surface Plasmon Dynamics and Far-Field Transmission

In this chapter, the results of far-field light transmission experiments through one-dimensional plasmonic crystals are presented and discussed on the basis of theoretical modelings. Different SPP excitations in angle-dependent transmission spectra are identified. The dynamics of SPP excitations are revealed by employing interferometric autocorrelation and phase-resolved spectral interferometry, which allows for the evaluation of femtosecond electric field transients transmitted through these structures. A complete mapping of the complex SPP band structure is demonstrated. Coherent couplings between SPPs lead to a splitting of SPP bands, associated with drastic variations in the SPP lifetime. A first near-field spectroscopic experiment yields the SPP Bloch modes of the crystal.

The chapter is structured as follows: The first three sections focus on results of various far-field transmission experiments, covering angle-dependent transmission (4.1), transmission dynamics (4.2) and coupling phenomena (4.3), such as band gap formation. In these sections, besides the presentation of experimental data, simple, phenomenological models are employed to discuss the essential physics behind the observed effects.

A further description resolving particular aspects not contained in these simple models is found in the remaining sections of the chapter. Section (4.4) introduces a radiative coupling model, offering more insight into the resonant nature of the SPP-assisted transmission and related effects, such as Fabry-Pérot resonances. Since this model is still of a phenomenological type, the results of the full solution of the scattering problem and the discussion of remaining questions are presented in Sec. (4.5).

This structure of increasing completeness in the theoretical description has been chosen to illustrate which components of the theoretical modeling are essential to explain certain observations, aiming at a deeper and more useful understanding than a mere and immediate comparison of the experimental results with a full scattering solution.

4.1 Angle-Dependent Transmission

A first characterization of the structures is performed by far-field, angle of incidence dependent light transmission [Fig. 4.1(a)]. The samples are illuminated with weakly focused 10-fs light pulses from a broadband Ti:Sapphire laser oscillator centered at a wavelength of 800 nm [see Sec. (2.1)], linearly polarized perpendicular to the slits, i.e., *p*-polarized.[1] For a grating with a period of $a_0 = 650$ nm, transmission spectra are displayed in Fig. 4.1(b) at angles of incidence from normal ($\theta = 0^\circ$) to $\theta = 60^\circ$ in steps of 2°. The spectra are normalized to the incident laser spectrum. Different transmission peaks that shift with varying angles of incidence are discernible. Three exemplary transmission spectra are magnified in Figs. 4.1(c)-(e). The absolute transmission is up to roughly 10 per cent, which is comparable to results from other studies [138]. One observes the asymmetric or dispersive lineshapes that are also typical for two-dimensional thin film transmission gratings [11, 119, 130, 139]. This aspect will be covered in more detail in Sec. (4.2.2). It should be noted that the transmission spectra differ only marginally for illumination from the air or the substrate side, which is well-known in the case of nanohole gratings [11]. Certain differences in reflection spectra have been reported in Ref. [140].

Surface plasmon polaritons can be excited on either side of the metallic film, i.e., on the air-metal or the substrate metal interface [119]. In order to identify the different types of SPP excitations leading to the features in the transmission spectra, we compare the wavelength and angle dependence of the transmission peaks with the solutions of the grating coupling equation [Eq. (3.10)]. In Fig. 4.2, the transmission spectra for the above grating are displayed on a linear color scale, together with solutions to the SPP grating coupling equation, for air-metal (AM) or sapphire metal (SM) SPP excitations. The respective integer diffraction orders n are indicated in the brackets. It appears that the grating coupling equation for the SM interface yields wavelengths near the peaks, where the transmission is actually close to zero. A theoretical work has predicted this behavior, interpreting it as the "negative role" SPPs play in the transmission through such nanoslit gratings [122]. It will be shown later that such a transmission dip is actually part of the same SPP resonance as the peak itself.

The qualitative agreement between the expected SPP resonances and the experimentally found transmission peaks is similar to that found for nanohole arrays [119], and shows that both AM and SM SPP resonances can be studied in this sample.

[1] In an alternative nomenclature, this polarization is also called "transverse magnetic" or "TM" polarization, because the magnetic field is perpendicular to the plane of incidence.

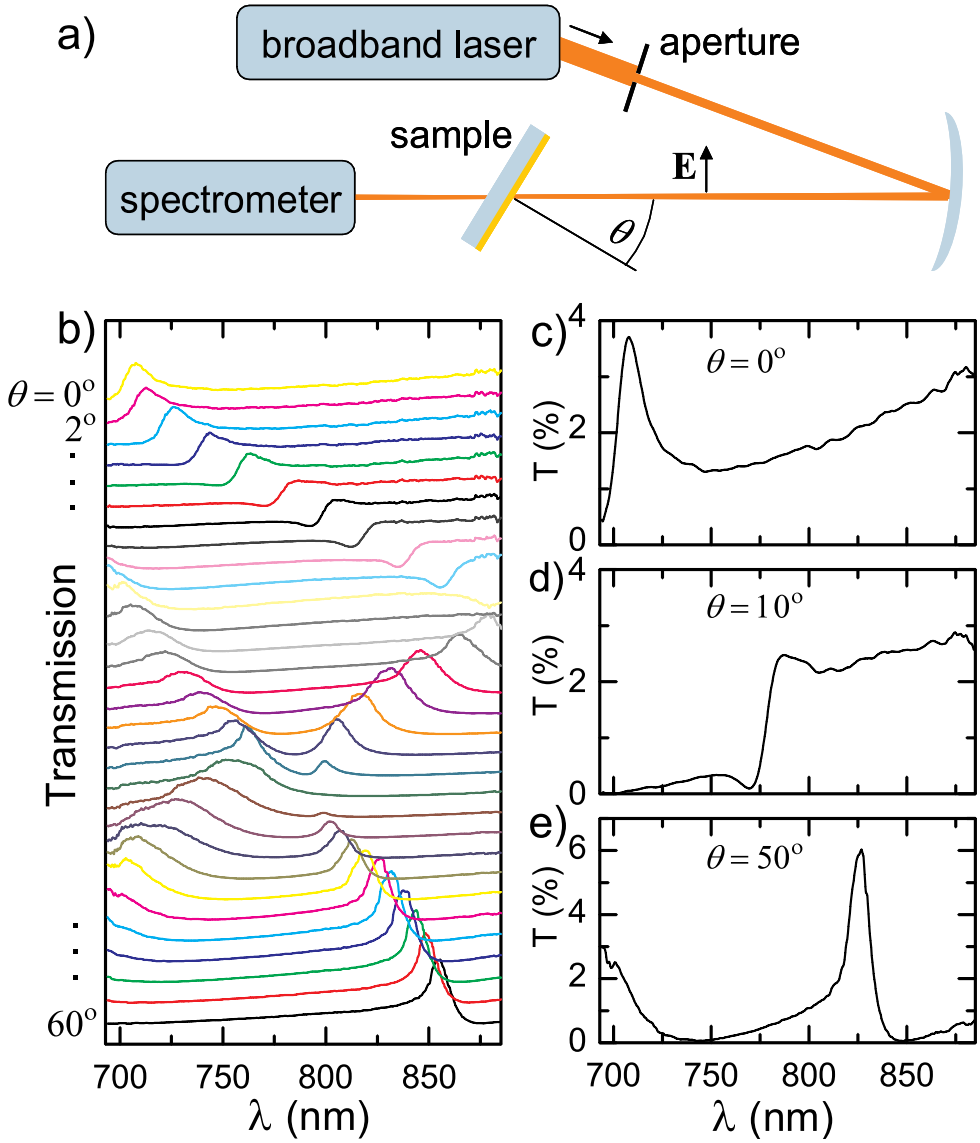

Figure 4.1: Angle-dependent transmission spectra of a grating with $a_0 = 650$ nm, $d = 150$ nm and $b = 50$ nm on a sapphire substrate. (a): Experimental setup. The incident p-polarized laser light is narrowed with an aperture and weakly focused onto the sample with a spherical mirror ($f = 30$ cm). (b): Transmission spectra in steps of 2°. (c)-(e): Three examples of transmission for the indicated angles.

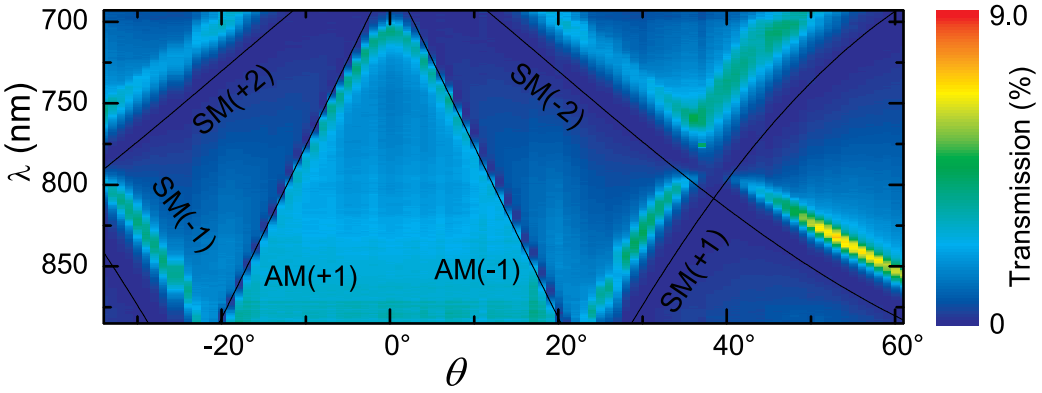

Figure 4.2: (a): Angle- and wavelength dependent transmission through the $a_0 = 650$ nm grating and solutions to the grating coupling equation, Eq. (3.10), for sapphire-metal (SM) and air-metal (AM) SPPs corresponding to different evanescent diffraction orders $n = \pm 1, 2$.

4.2 Transmission Dynamics

The investigation of time-resolved transmission through metallic photonic crystals is of fundamental interest, as these structures are considered key elements in future photonic devices, aiming at unprecedented levels of microscopic light control [8, 9]. It is by now well-accepted that SPP excitations with lifetimes in the range of few tens of femtoseconds govern the transmission properties. However, the actual dynamics of these excitations have not been fully understood. Several investigations cover different aspects of the dynamics of light transmission through plasmonic crystals, including a number of theoretical works [129, 141]. Experimentally, a time delay in the transmission of 100-fs light pulses through an array of nano-holes has been found to be on the order of 10 fs [13–15]. The interpretation of this delay, attributed to either a finite transit time through the apertures [14] or to the SPP lifetime [13] remains controversial, partly because the pulse durations used previously were longer than the radiative SPP lifetimes in such plasmonic crystals.

4.2.1 Interferometric Autocorrelation

Here, the first pulse transmission experiments through plasmonic crystals are reported, which make use of optical pulse durations significantly shorter than the lifetimes of the relevant SPP excitations. We begin by directly studying the pulse shapes of the 10-fs light pulses as they are transmitted through the slit grating [Fig. 4.3(a)].

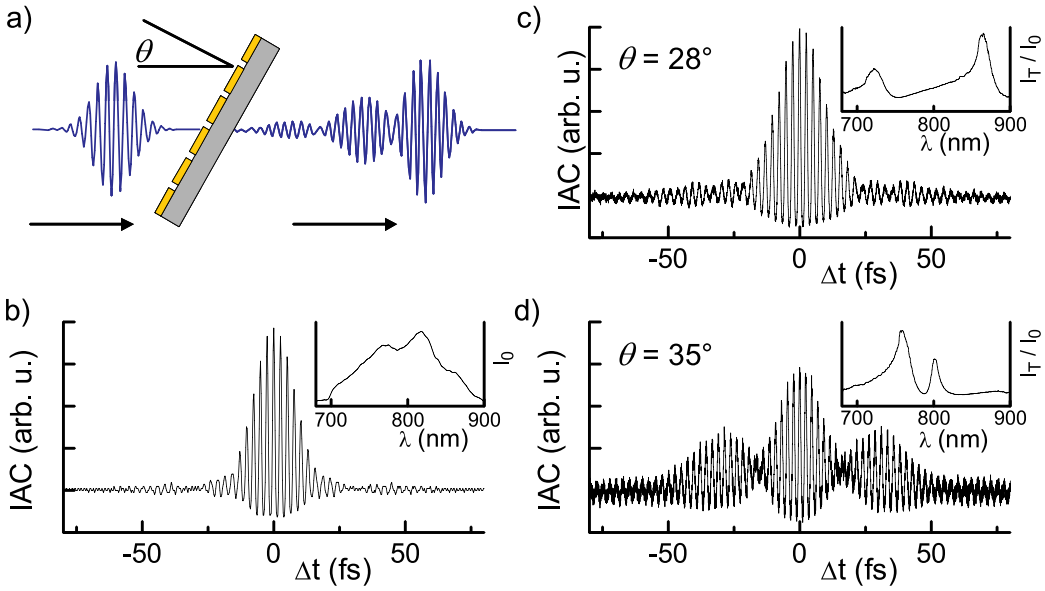

Figure 4.3: (a): Schematic of the experimental setup. (b): Interferometric autocorrelation (IAC) of the incident 10-fs light pulses. (c)-(d): IAC of the light transmitted through the plasmonic crystal at $\theta = 28°$ (c) and $35°$ (d). The laser and spectrum (b) and linear transmission spectra [(c),(d)] are shown in the insets.

Interferometric autocorrelations (IACs) [see Sec. (2.1.2)] are measured for the incident laser pulses [Fig. 4.3(b)] and the pulses transmitted through the structure at different angles of incidence [Figs. 4.3(c) and (d)]. The corresponding laser spectrum and the normalized transmission spectra are shown in the insets. Two angles of incidence with markedly different IACs for the transmitted pulses have been selected. At an angle of $\theta = 28°$, the laser spectrum overlaps only weakly with the sapphire-metal (SM) SPP resonances [cf. Figs. 4.2 and 4.1]. The transmitted light consists of a strong initial peak of duration comparable to the incident pulses, and a second long-lived but weak component from the transmission peaks at the edges of the spectral range. When the overlap between SPP resonances and laser spectrum is optimized by angle tuning [Fig. 4.3(d)], the resonant contribution is strongly enhanced, and the time profile of the transmitted light is dominated by the pronounced polarization beating between the two SM SPP resonances persisting for more than 50 fs.

4.2.2 Phase-Resolved Measurements

The interferometric autocorrelation measurements already give a first impression of the dynamics of light transmission. A quantitative extraction of the relevant

parameters is, however, not straightforward, because there is no simple one-to-one correspondence between a given IAC trace and the underlying electric field transient. One possibility to infer upon a field transient is to set up a specific mathematical model, followed by a fitting of its parameters to the experimental IAC trace and the measured transmission spectra [142].

In our work, we use a different approach and measure the electric field transients transmitted through the structure directly by the use of spectral interferometry, as introduced in Sec. (2.1.3). Precise knowledge of the incident pulses leaves the determination of the transmitted pulses to a linear interferometric measurement, in which the spectral variation of the transmission-induced phase change is obtained along with the transmitted amplitude. If we define $E_{in}(\omega)$ and $E_{out}(\omega)$ as the incident and transmitted complex field amplitudes in the frequency domain, the transmissivity $t(\omega)$ relating the two via Eq. (2.2) is determined as

$$E_{out}(\omega) = t(\omega)E_{in}(\omega). \tag{4.1}$$

The electric field transients are then calculated by a Fourier transform. In Fig. 4.4(a), the incident laser pulses $E_{in}(t)$ are plotted (left) with the laser spectrum and the spectral phase (right).[2] Figures 4.4(b)-(d) contain a set of representative electric field time transients of the transmitted pulses $E_{out}(t)$ for different angles of incidence, together with the respective normalized transmission $T = |t(\omega)|^2$ and the spectral phase of the transmissivity, $\varphi = \arg(t(\omega))$. [3]

In these three transients, characteristic features of the light transmission through the plasmonic crystals can be identified. At an angle of incidence of 8° (b), the transmitted pulse consists of a strong initial burst, followed by a long-lived, weaker tail. The normalized transmission spectrum shows a broad continuum and a resonance around 750 nm, which corresponds to an AM[-1] SPP resonance that is evident in a 2π phase change of the complex transmissivity.[4] The relative amplitudes of the burst and the tail can be altered by angle-tuning the overlap of the laser spectrum with the continuum and the resonance [143]. Increasing the angle of incidence to a value of 49°, where mostly a single SM SPP resonance is observed (c), results in a time trace dominated by the long-lived component. At angles, where several SM SPP resonances (± 1 and ∓ 2) are covered by the laser spectrum, such as $\theta = 33^\circ$ shown in (d), a strong temporal beating of the emission is found in the electric field transients.

[2] Note that the carrier-envelope phase offset in these measurements is not known [see Sec. (2.1.2)].

[3] For easier comparison with the preceding and following graphs, the quantities are plotted as a function of wavelength rather than frequency.

[4] Note that this differs from the π phase change of a single Lorentzian. This is due to the interference with the continuum discussed below.

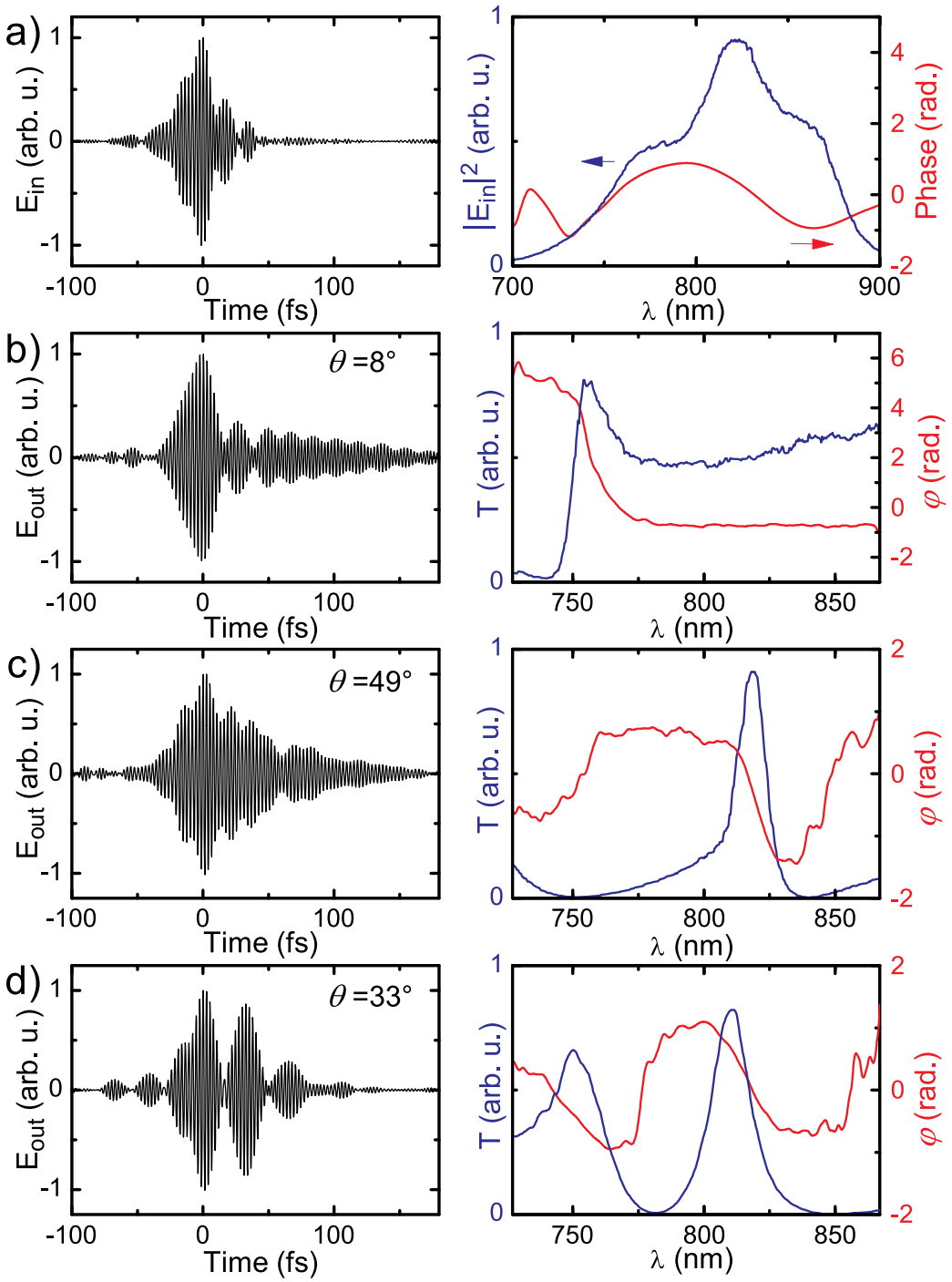

Figure 4.4: Incident and transmitted pulses through a 650 nm slit array. (a): Electric field transient (left graph), spectral intensity (blue) and spectral phase (red) of the incident pulses. (b)-(d): Transmitted pulse structures (left column), normalized transmission T (blue) and spectral phase φ (red) of the transmissivity for angles of incidence $\theta = 8°$(b) (AM resonance), 49°(c) and 33°(d) (SM resonances).

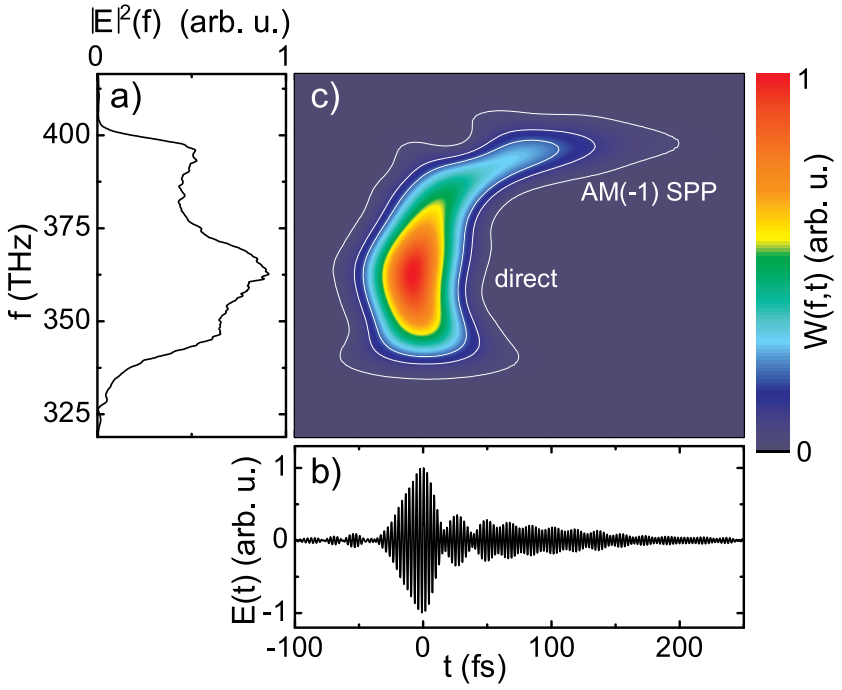

Figure 4.5: (a): Optical spectrum of the pulses transmitted through a 650 nm slit array at an angle of $\theta = 8°$. (b): Pulse structure in the time domain. (c): Short-time Fourier transform showing that the transmitted pulse consists of an initial burst and a delayed long-lived SPP contribution.

The measurements show directly that the time structure of the transmitted light pulses is given as a superposition between two components of different temporal characteristics: (i) the impulsive burst due to nonresonant transmission through the nano-slits E_{nr}, which is similar in duration to the incident pulse, and (ii) the damped emission from different SPP excitations at resonance frequencies ω_j and with damping constants Γ_j, namely

$$E_{out} \propto E_{nr} + \sum_j E_j \exp(-i\omega_j t - \Gamma_j t). \tag{4.2}$$

The dynamical aspect of this transmission can be further visualized by performing a short-time Fourier transform [see Sec. (2.1.4)]. For the transmission at 8°, Fig. 4.5 shows besides the time transient (b) the (unnormalized) spectral intensity of the transmitted pulses (a), and in color scale the windowed Fourier transform (c) function $W(f,t)$ with a Gaussian time window of 20 fs width. This image immediately reveals the delayed resonant AM SPP emission following the nonresonant direct transmission.

In the spectral domain, the interference between the resonant and the nonresonant transmission channels gives rise to asymmetric so-called "Fano" lineshapes, as predicted theoretically [144] and found on the basis of far-field transmission spectra [145]. Originally derived by U. Fano [146], such lineshapes appear, whenever a continuum is coupled to a resonance, for instance in the autoionization process in atomic physics [147]. This particular lineshape, although expressed in a somewhat different form in the original work,[5] can be written for the complex transmission amplitude as

$$t(\omega) = a_{nr} + \sum_j \frac{a_j e^{i\phi_j} \Gamma_{rad,j}}{\omega - \omega_j + i(\Gamma_{rad,j} + \gamma_j)}. \tag{4.3}$$

Here, a_{nr} is the spectrally flat or slowly varying nonresonant transmission amplitude, and a_j and ϕ_j are the (real) oscillator strengths and phases, respectively. The real frequencies ω_j correspond to SPP resonances at either the AM or SM interface [119]. The resonance width Γ_j contains two terms: a nonradiative damping γ_j due to absorption in the metal, and the radiative damping $\Gamma_{rad,j}$ of the SPP modes, which is in most cases dominant [13]. In the numerator, only the radiative damping constant appears, as only this contribution leads to emission. Figure 4.6 illustrates the composition of the Fano lineshape as a sum of a nonresonant and a resonant contribution through the structure. The well-known π-phase change across the Lorentzian resonance leads to constructive interference on one side of the resonance and destructive interference on the other, resulting in the typical dispersive shape and a shift of the peak transmission amplitude with respect to the resonance wavelength [145]. Thus, the resonant excitation of surface plasmons is responsible for a transmission enhancement [11] at certain wavelengths and a reduction [122] at others, as indicated with the gray-shaded ares near the green curve.

A simultaneous fit of the Fano lineshape function [Eq. (4.3)] to the transmission and spectral phase of an individual SM SPP resonance is shown in Figs. 4.6(c) and (d), demonstrating excellent agreement for the resonance energy and linewidth as given in Fig. 4.6(c). This supports in particular that for a single SPP resonance, the total linewidth $\hbar\Gamma = \hbar(\gamma + \Gamma_{rad}) = 10.3$ meV is significantly larger than the expected intrinsic Ohmic losses on a planar gold/sapphire interface of about $\hbar\gamma = 4$ meV, evaluated from Eq. (3.8) for the wavelength around 800 nm and the dielectric function from Ref. [103]. Thus, the resonance is predominantly radiatively broadened, and the SPP lifetime, i.e., the time, after which the SPP mode intensity has decreased by a factor of $1/e$, is found to be $T_1 = 1/(2\Gamma) = 1/(2(\gamma + \Gamma_{rad}))$, which is 32 fs - much shorter than the intrinsic

[5] The equivalence of the often used form of the Fano lineshape with the following expression is shown in Appendix D.

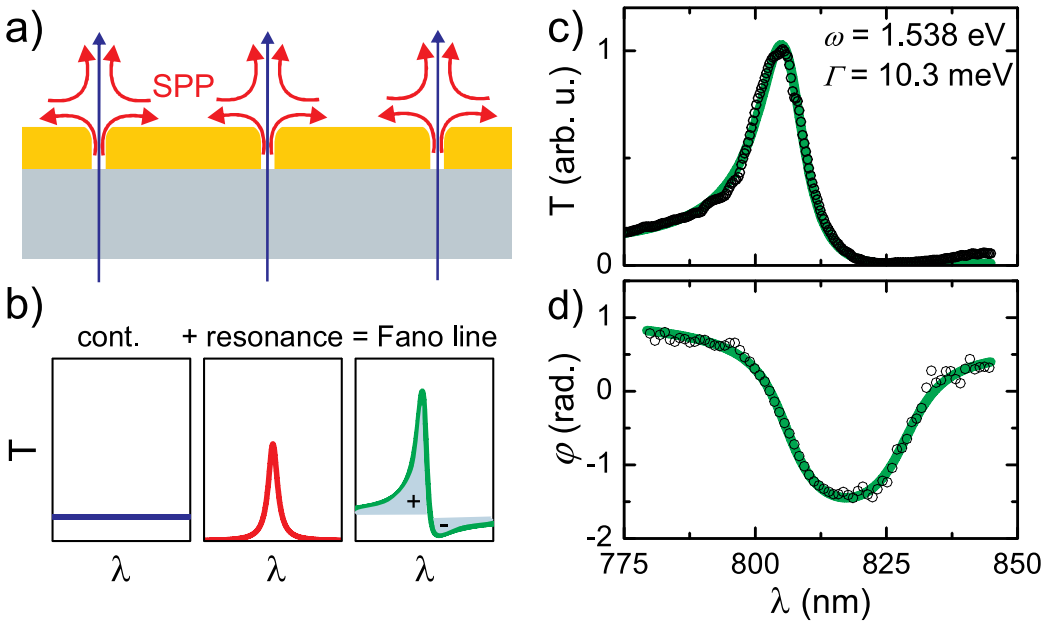

Figure 4.6: (a): Schematic representation of the resonant (red) and direct (blue) transmission components. (b): Illustration of a Fano-type resonance as the interference between a continuum and a resonant contribution, resulting in constructive (+) and destructive (-) interference of both components in the far-field. (c)-(d): Simultaneous fit of a Fano resonance (green lines) to the squared magnitude (c) and the spectral phase (d) of the measured complex transmissivity (open circles) at $\theta = 44°$.

absorptive damping time of about 80 fs. These small lifetimes are limited by a Rayleigh-like scattering of surface plasmon polaritons at the nano-slit scattering centers [13].

4.2.3 Complex Far-Field Transmission Map

Performing spectral interferometry as a function of the angle of incidence allows for a detailed mapping of the complex SPP band structure. Figure 4.7 shows transmission spectra (a) and the spectral phase (b) between 700 and 900 nm. Strong phase variations occur at the resonance wavelengths connected to the AM and SM excitations. Different phase behavior is found for the two kinds of resonances, namely a 2π phase change for the air-metal-SPP and a phase dip for the substrate-metal SPP. At all angles, the spectra and the phase curves are consistently modeled by Eq. (4.3), taking the relevant SPP resonances into account. It should be noted that a quantitative extraction of all parameters, in particular of the resonance phases and the oscillator strengths, requires such phase-resolved measurements,

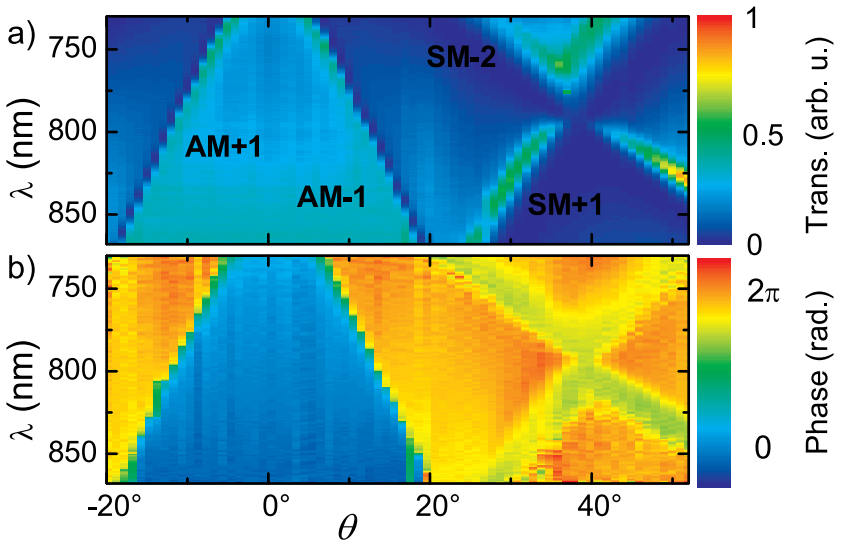

Figure 4.7: Angle-resolved transmission $T(\omega,\theta)$ (a) and phase $\varphi(\omega,\theta)$ (b) for a nanoslit array with $a_0 = 650$ nm.

since from a transmission spectrum alone, these parameters cannot be uniquely determined.[6]

In previous work on nano-hole arrays, e.g., in Ref. [145], only asymmetric profiles with a tail on the longer wavelength side have been observed. It is obvious from the above figures that the AM resonances show this behavior, as well, while the SM transmission peaks possess asymmetric tails towards the short-wavelength side. This question is intimately related to the differences between nano-slit arrays, which support a propagating waveguide mode for all wavelengths, and nano-hole arrays, which do not. More details on this issue will be given in Sec. (4.4).

The phase-resolved transmission experiments indicate an interpretation of the transmission as an interference between a nonresonant and a resonant transmission contribution of different temporal structures, allowing for a precise determination of the relevant resonance parameters, such as the complex oscillator amplitudes, resonance frequencies and damping rates. Further investigation is warranted to find out what determines these parameters, and how they can be systematically influenced. In the following section, the coherent coupling between different SPP modes and its consequences for the emission are studied. On the basis of near-field optical microscopy, a direct connection between far-field transmission characteristics and the SPP field distributions is established.

[6] In Appendix D, it is shown that identical Fano lineshapes can be obtained for different oscillator strengths and phases.

4.3 Coherent Couplings

The present time-resolved experiments and previous studies [13, 14] have demonstrated a strong SPP-coupling to far-field radiation, limiting SPP lifetimes to few tens of femtoseconds. This poses a constraint on using these structures in novel photonic elements, such as plasmonic resonators or nano-waveguides. The question arises how to control radiative SPP damping in order to overcome these constraints.

In general, radiative decay phenomena can be strongly modified by coherent couplings between the relevant optical excitations. For two resonant systems, e.g., two atoms separated by less than one wavelength, the radiative coupling leads to the formation of collective states and cooperative effects in their radiative decay, namely super- and subradiance [148]. Specifically, subradiance reflects the suppression of radiative damping for the collective state with an antisymmetric character of the wave function. These phenomena are currently of great interest as they play a dominant role in the optical properties of a variety of dense, microscopic systems, e.g., trapped ions [149], Bose-Einstein condensates [150], molecular aggregates [151, 152], or coupled semiconductor quantum dots [153] and wells [154].

In plasmonic crystals, both the coherent coupling between polaritonic excitations and their coupling to the radiation field is induced by periodic variations of the dielectric function [12]. Whereas the resulting band gap formation has received much attention [117, 118], there are only few studies of coupling-induced phenomena in the radiative damping of polariton modes [142, 155].

In the plasmonic crystals studied here, the quantitative understanding of the lineshape function is the key to the analysis of coherent SPP couplings, such as band gap formation and radiative decay phenomena. A fitting to the Fano lineshape yields the SPP band structure $\omega_j(\theta)$ and the damping constants $\Gamma(\theta)$.[7]

In this section, band gap formation and the effects of coherent couplings on the radiative lifetimes of SPP modes are investigated. We begin by studying the linewidth variations at the SM[+1,-2] anti-crossing in far-field transmission measurements. In order to gain a more detailed microscopic understanding of the observed radiative decay phenomena, the zone center band gap of the AM[+1,-1] modes is further studied. In addition to far-field transmission measurements, near-field optical spectroscopy is employed to give a direct picture of the microscopic mode structure near the SPP band gap.

[7] Note that a high angular resolution is necessary to correctly measure the linewidths, because the strong angle-dependent line shifts lead to smearing and broadening of lines for reduced angle resolution. Using a laser with high directionality simplifies those measurements significantly.

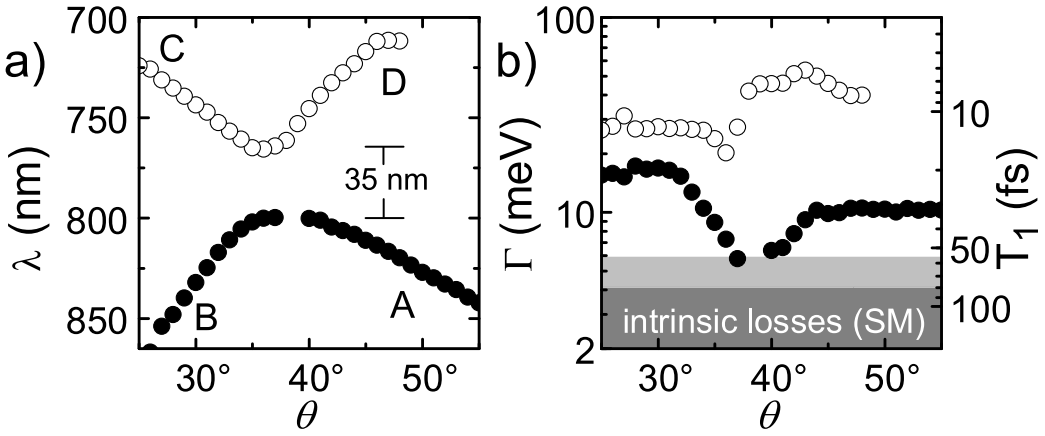

Figure 4.8: Formation of a plasmonic band gap for substrate-metal SPPs, evaluated from a fit to the Fano lineshape. (a): Resonance wavelengths of the two branches. Two values are missing for the lower branch near $\theta = 38^\circ$ due to a disappearance of the peaks at these angles. (b): Linewidths and corresponding lifetimes of both branches (logarithmic scale). The upper borders of the light gray and gray shaded areas correspond to the expected intrinsic (absorptive) SPP damping for the dielectric function tabulated in Refs. [103] and [109], respectively.

4.3.1 Substrate-Metal Zone Boundary Band Gap

The 650 nm array has been chosen for optimum overlap of the SM[+1,-2] resonances with the laser spectrum. The resulting resonance wavelengths of the approaching bands near the Brillouin zone boundary around 38° are plotted as circles in Fig. 4.8(a). One observes a clear anti-crossing of the SPP bands of about 35 nm, corresponding to a band gap energy E_G of 72 meV.

Along with the splitting of the resonance frequencies, drastic intensity and linewidth variations are found. The linewidths of the upper and lower branches are plotted in Fig. 4.8(b) as the open and black circles, respectively. On the right, the ordinate is labeled with the corresponding SPP lifetimes. It was mentioned before that the dominant line broadening mechanism for these SPP resonances is radiative damping [13], caused by the coupling of SPP modes to the far-field continuum consisting of one or more diffraction orders. The linewidth variations therefore immediately reflect the modifications of radiative damping associated with the coupling to the far-field, which can be altered by the coupling among different SPP modes.

Far from the anticrossing, the four modes, denoted by A,B,C and D in Fig. 4.8(a), possess damping constants ordered as $\Gamma_A < \Gamma_B < \Gamma_C < \Gamma_D$. Qualitatively, this sequence can be understood in terms of the different types and num-

bers of damping channels, i.e., diffraction orders, these modes can couple to.[8] A quantitative comparison with theoretical calculations is found in Sec. (4.5).

Beyond these initial differences in radiative decay far from the anti-crossing, the damping rates are further modified by the coupling between the SPP modes near the anti-crossing. In particular, the lower energy branch displays a narrowing near the anti-crossing with a minimum linewidth of $\Gamma \approx 5.5$ meV (full-width at half-maximum (FWHM) is 2Γ). This corresponds to a lifetime of about 60 fs, which is much closer to the intrinsic damping time than the lifetimes of the SPP resonances far from the anti-crossing, which have lifetimes down to a couple of femtoseconds, such as the upper SM branch (open circles in Fig. 4.8). The upper borders of the areas shaded in light gray and gray indicate the intrinsic SPP lifetimes expected for the dielectric function ($\lambda = 800$ nm) from Refs. [103](56 fs) and [109](80 fs), respectively.

Moreover, the peak intensity decreases upon approaching the anti-crossing angle, and eventually, the line disappears at $\theta = 38^\circ$. This line-narrowing is direct evidence for a coupling-induced suppression of radiative damping, i.e., for an example of subradiance [148]. Near the anti-crossing, the type of SPP damping changes from predominantly radiative ($\Gamma_{rad} > \gamma$) to absorption-limited ($\gamma > \Gamma_{rad}$).

In this SM zone boundary case, the effects of the coupling on the radiative lifetimes are somewhat masked by the differences of the decay rates of the uncoupled modes, as discussed above. Especially the asymmetry of the band structure at the zone boundary significantly complicates the interpretation. A full scattering solution in Sec. (4.5) will be shown to yield such variations in the angle-dependent linewidths.

Both subradiant SPP decay and band gap formation are expected to be intimately connected with the formation of new coupled SPP eigenmodes of different spatial symmetry [118, 148, 156, 157], which cannot be directly explored for the substrate-metal SPP excitations. Thus, the next subsection examines a band gap formed by air-metal SPPs in the zone center.

4.3.2 Air-Metal Zone Center Band Gap

For the purpose of studying the air-metal SPP band gap near the zone center, a sample with a larger lattice period of $a_0 = 750$ nm is chosen. We have recently demonstrated that this larger lattice constant mainly brings about a red-shift of all resonances by about 100 nm [143], thus providing better overlap of the laser spectrum with the spectral range of the AM[+1,-1] anti-crossing. An overview angle-dependent transmission spectrum for this sample, labeling the different SPP

[8] Furthermore, the shorter wavelength of the upper branch also contributes to enhanced radiative damping compared with the lower branch [13].

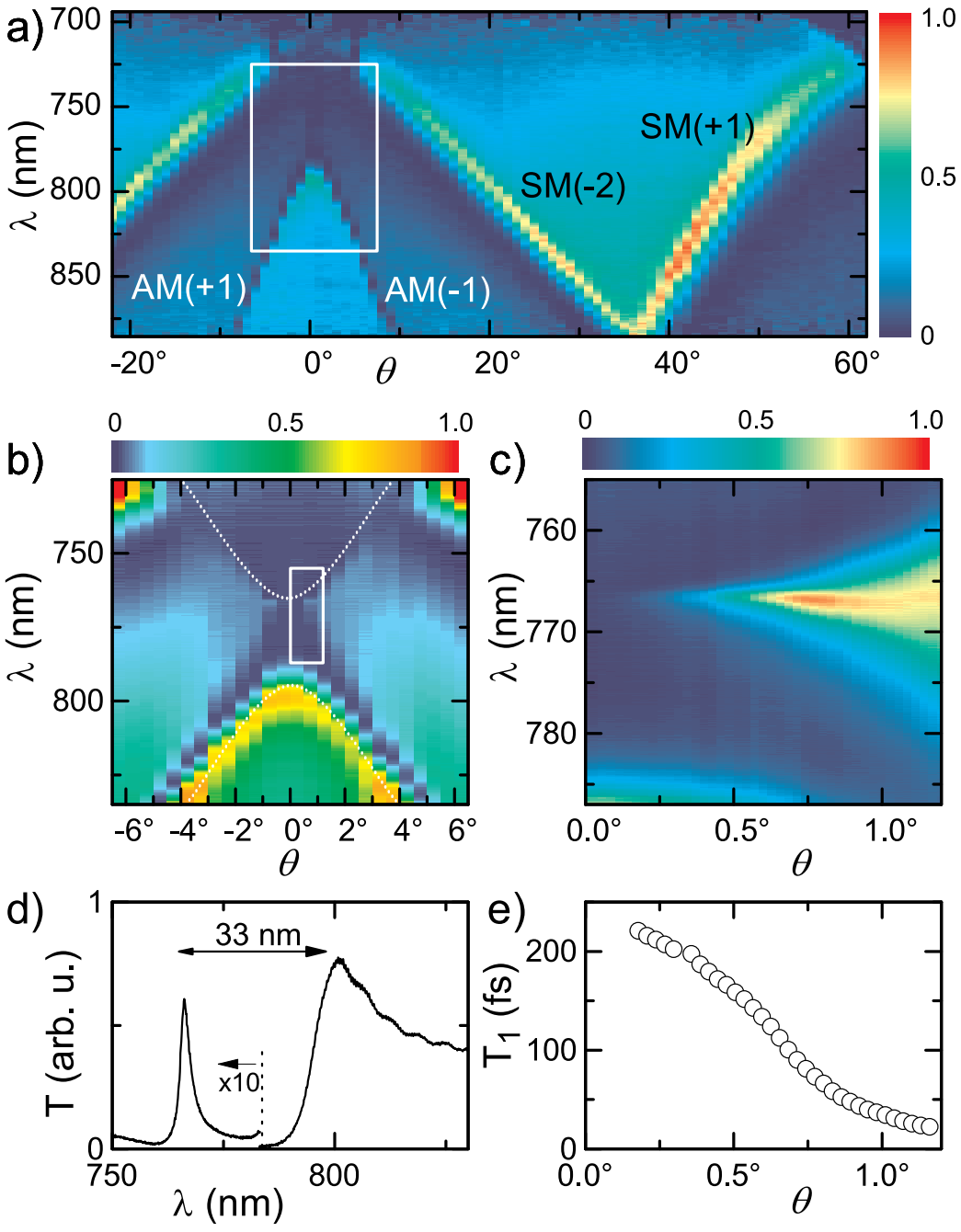

Figure 4.9: Angle-resolved transmission for a nanoslit array with $a_0 = 750$ nm. (a): Overview transmission image. (b): Magnified view of the region near the AM[+1,-1] anti-crossing, corresponding to the white rectangle in (a). The dotted lines indicate the anti-crossing. (c): Further fine close-up into the short-wavelength narrow line near normal incidence [see rectangle in (b)]. (d): Transmission spectrum around 0.6 degrees, displaying a narrow and a broad asymmetric resonance, separated by a band gap of about 30 nm. (e): Lifetime of the narrow resonance as a function of the angle of incidence, assessed from fits to the Fano lineshape function.

bands, is shown in Fig. 4.9(a). Two consecutive magnifications (indicated by the white rectangles) of the regions of interest are displayed in Figs. 4.9(b) and (c), resulting from two separate experiments. In Fig. 4.9(b), one observes the range of the AM[+1,-1] anti-crossing (white dotted lines as a guide to the eye). This image is dominated by the interference between contributions from the lower SPP branch and the continuum transmission, so that the upper branch is more difficult to discern. Figure 4.9(c) shows a scaled up image of the weak signal from this upper branch [see white rectangle in (b)]. In these experiments, optimal angle-resolution (better than 0.2°) was achieved by closing the aperture on the illuminating beam.

The SPP resonances are most easily identified in a transmission spectrum near normal incidence ($\theta = 0.6°$), which is plotted in Fig. 4.9(d). It exhibits two Fano-type transmission peaks, a spectrally broad and intense long wavelength resonance around 800 nm and a much narrower and weaker short wavelength peak at 766 nm (note the magnification factor of 10 for the transmission from the dashed line to the left). The band gap energy of about 70 meV is similar to that found for the SM zone boundary in the previous subsection.[9] The angle-dependent far-field spectra displayed in Fig. 4.9(c) reveal a strong change in linewidth of the narrow resonance for small angles of incidence. This linewidth decrease, evaluated by fitting Fano-lineshapes to the data, corresponds to a drastic increase in SPP lifetime T_1 to more than 200 fs when θ is reduced from 1.2 to 0.2 degrees, as shown in Fig. 4.9(e). Such extremely long lifetimes, more than an order of magnitude larger than previously reported [13], are again strong evidence of an efficient radiative damping suppression for this coupled SPP mode.

The maximum observed lifetime greater than 200 fs for the subradiant AM resonance is larger than in the case of the SM anti-crossing. This is a result of the smaller intensity in the metal for an AM SPP compared with an SM SPP [cf. Eq. (3.4)]. However, the lifetimes found for the AM resonance are even larger than what is expected, if the tabulated dielectric functions are used in Eq. (3.8). The intrinsic lifetimes at a light wavelength of 770 nm are 140 fs and 90 fs from Refs. [109] and [103], respectively. Different factors may contribute to this small but noticeable discrepancy, which will be discussed in Sec. (4.5.3).

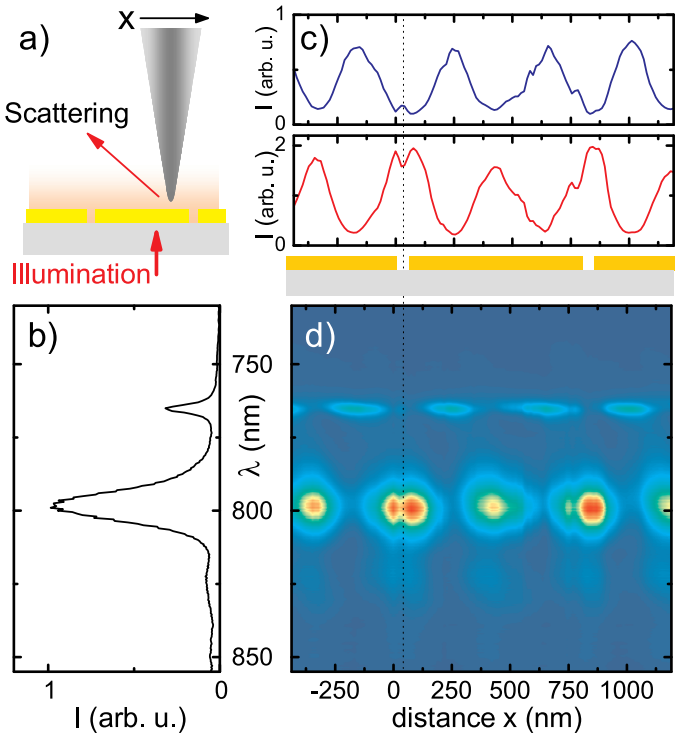

Figure 4.10: Near-field optical spectroscopic line scan of the AM band gap ($a_0 =$ 750 nm), providing direct evidence for SPP Bloch modes. (a): Experimental configuration. An aluminum coated fiber tip is used to scatter the near-fields Near-field intensity as a function of position and wavelength. (b) Spatially averaged near-field spectrum. (c): Spatial dependence of the near-field intensity at 766 nm (narrow resonance). (d): Spatial dependence of the near-field intensity at 800 nm (broad resonance). (Detection conditions: unpolarized, $\varphi = 90°$, $\beta \approx 50°$; see Sec. (5.2.2) for details and definitions.)

4.3.3 Super- and Subradiant Surface Plasmon Bloch Modes

Near-field optical spectroscopy immediately reveals the microscopic origin of the damping suppression. Measurements were performed on the same structure in the scattering configuration with an aluminum coated fiber tip, as sketched in Fig. 4.10(a). Weakly focused broadband illumination near normal incidence is again provided with the broadband Ti:Sapphire laser, and the scattered signal in tip-sample contact is spectrally dispersed and detected with a CCD spectrometer

[9]The two cases differ in that the narrow AM resonance is on the shorter wavelength side of the band gap, whereas the narrow resonance of the SM anticrossing is at the longer wavelength side. Since this aspect is related to the asymmetries of the individual peaks, it will be discussed in a later section [Sec. (4.4)].

[see Sec. (2.2.5)].

Figure 4.10(b) shows the spatially averaged near-field spectrum, normalized to the incident spectrum. The broad and the narrow resonances found in the far-field transmission forming the air-metal SPP band gap are evident. Several differences between this near-field spectrum and the far-field spectrum Fig. 4.9(d) can be pointed out. First, the strong Fano-shaped asymmetry of the resonances has largely disappeared. Second, the broad background on the long wavelength side of the broad resonance is much weaker than the SPP resonance itself. And finally, the relative magnitude between the two SPP resonances has changed dramatically, so that in the near-field, the intensity ratio between the strong and the weak resonance are about 3:1, while in the far-field, this ratio is roughly 13:1.

Figure 4.10(c) contains the spatial near-field intensity distributions $I(x)$ along the surface at the wavelengths of the narrow (blue, top, termed *dark mode* from now on) and the broad (red, bottom, termed *bright mode*) resonances. The spectrally and spatially resolved near-field scan is shown in Fig. 4.10(d). In the wavelength range of the broad resonance, $I(x)$ shows maxima at the slits and slightly weaker maxima in the center between slits. In contrast, at the wavelength of the narrow resonance, $I(x)$ shows almost negligible intensity at the slits and two strong maxima in-between the slits.

Let us first account for the differences between the near- and the far-field spectra. They can all be understood by considering the resonant nature of these excitations. The spectrally very broad direct transmission through the nano-slit waveguide, the bright SPP resonance and the dark SPP resonance constitute a sequence of excitations with increasing quality factor. As in other types of resonators, e.g., a Fabry-Pérot cavity, the ratio between then intensities inside and outside of the cavity scales with the quality factor [33]. Here, the far-field transmission detects the intensity outside, whereas the near-field experiment directly probes the intensity inside the resonator. Thus, in the near-field, the amplitude of the dark SPP mode is increased relative to that of the bright SPP mode. The spectrally very broad nonresonant transmission does not correspond to a surface bound near-field mode, so that its spectral amplitude at the surface is reduced relative to both SPP resonances. Consequently, the near-field spectra display a reduced Fano asymmetry compared with the far-field spectra.

The mode profiles in Fig. 4.10(c) directly represent the microscopic counterpart of the band gap splitting in the far-field transmission spectra. The periodic structuring of the surface induces a coupling of the SPP modes traveling to the left and the right on the surface, resulting in new coupled normal modes. These are the first order Bloch modes of this structure, in analogy to other periodically perturbed systems, e.g., in solid state physics [106]. At normal incidence, the lateral inversion symmetry of the surface has as a consequence SPP states of definite parity, i.e., the field distributions of the coupled modes are symmetric and

antisymmetric, yielding the intensity distributions shown in Fig. 4.10(c). From those intensity maps, it is apparent that the dark mode is coupled weaker to the far-field than the bright mode. The nanoslits serve as the scattering centers, promoting the damping of the SPP modes into the far-field continuum. As the dark mode has a very small amplitude at these scattering centers, its radiative damping is effectively reduced and strictly zero at normal incidence.[10]

These arguments can be framed into a simple coupled-mode model, for now only considering the two AM modes propagating to the left and to the right on the surface, namely the evanescent eigenmodes of Maxwell's equations for a perfectly smooth surface. They are denoted as $|j\rangle$ with $j = l, r$, have mode frequencies ω_j and a spatial dependence of the field amplitude along the surface of $|l, r\rangle \propto \exp(\mp i k_{x,SPP} x)$. The relation between $k_{x,SPP}$ an ω_j is the SPP dispersion [1][cf. Sec. (3.1.2)]. The spatially periodic change in the dielectric function induced by the nanoslits locally alters the electromagnetic energy density and thus gives rise to frequency shifts V_{ll} and V_{rr} and, most importantly, to a coupling V_{lr} of the two modes. This coupling results in the band gap splitting of the real parts of the normal mode SPP frequencies [118]. A number of different expressions have been used in the literature on perturbative treatments of metallic or dielectric photonic structures [158, 159]. At this point, the specific expression for the coupling is not paramount, because quantitative results will be obtained in a non-perturbative calculation in a later section, anyway [Sec. (4.5)]. Here, we are mostly interested in a description qualitatively containing the physical phenomena. Thus, for example, the strength of these interactions can be approximated to first order as the spatial overlap integral of the modes, including a perturbation given by the change in the dielectric function [159]

$$V_{ij} \simeq -\frac{1}{2}\langle i|\varepsilon^2 \Delta(\varepsilon(\mathbf{r})^{-1})|j\rangle, \tag{4.4}$$

where $\Delta\varepsilon(\mathbf{r})$ denotes the local perturbation of the dielectric function,[11] and the states are normalized, so that $\langle j||\varepsilon||j\rangle = \omega_j$.[12] Moreover, the nanoslits couple the evanescent SPP modes of the ideal interfaces to the continuum of propagating far-field modes $|m\rangle$ [145], i.e., induce radiative damping

$$\Gamma_{ij} \simeq 2\pi \sum_m \langle i|\varepsilon^2 \Delta(\varepsilon(\mathbf{r})^{-1})|m\rangle\langle m|\varepsilon^2 \Delta(\varepsilon(\mathbf{r})^{-1})|j\rangle. \tag{4.5}$$

[10] Even for larger slits and finite mode overlap with the slits, the coupling to the zeroth diffraction order would still be forbidden from symmetry reasons. In other words, the fields scattered from both edges of the slits would destructively interfere in the zeroth order of the far-field.

[11] This perturbation is given by the replacement of ε_m by ε_d at the slit positions.

[12] Because of the field discontinuities at the slits, some care is warranted when using perturbation expressions [159].

It is essential that the presence of the slits not only leads to a damping of the individual resonances (Γ_{ll}, Γ_{rr}), which has been discussed before [145], but also causes a radiative coupling (Γ_{lr}, Γ_{rl}) among the SPP modes via interference in the far-field continuum. The above terms are cast into a coupled mode matrix with eigenvalues describing the resonances of the coupled system and their radiative decay:

$$\begin{pmatrix} \omega_l - i\gamma_l & 0 \\ 0 & \omega_r - i\gamma_r \end{pmatrix} + \begin{pmatrix} V_{ll} - i\Gamma_{ll} & V_{lr} - i\Gamma_{lr} \\ V_{rl} - i\Gamma_{rl} & V_{rr} - i\Gamma_{rr} \end{pmatrix}. \tag{4.6}$$

Here, γ_j is again the non-radiative damping constant due to absorption in the metal. We are mainly interested in the coupling to the zeroth diffraction order. From simple symmetry considerations, it is evident that at small angles, the diagonal terms for the coupling to the zeroth order are the same for both modes, $\gamma \doteq \gamma_l = \gamma_r$, $V \doteq V_{ll} = V_{rr}$ and $\Gamma \doteq \Gamma_{ll} = \Gamma_{rr}$. The geometrical dimensions of the perturbation are much smaller than the SPP wavelength, so that only small amplitude changes of the uncoupled modes across the width of the slit are present. Hence, the off-diagonal terms are very similar to the diagonal ones, $\Gamma \simeq \Gamma_{lr} = \Gamma_{rl}$.

The detuning $\Delta(k_{x,SPP}) = \omega_r(k_{x,SPP}) - \omega_l(k_{x,SPP})$ between the two unperturbed resonances depends on the angle of incidence via $k_{x,SPP} = \omega/c\sin(\theta) \pm G$. It can be continuously varied by angle tuning and is zero at normal incidence. With the above definitions, a further simplified matrix results:

$$\begin{pmatrix} \omega_l - i\gamma & 0 \\ 0 & \omega_l - i\gamma + \Delta \end{pmatrix} + (V - i\Gamma) \begin{pmatrix} 1 & 1 \\ 1 & 1 \end{pmatrix}. \tag{4.7}$$

The new complex frequencies of the coupled modes are found by diagonalization, resulting in

$$\begin{aligned} \omega_{+,-} = &\ \omega_1 - i\gamma + \Delta/2 + V - i\Gamma \pm A/2, \\ A = &\ \sqrt{\Delta^2 + 4(V - i\Gamma)^2}. \end{aligned} \tag{4.8}$$

The corresponding coupled eigenmodes are $|+,-\rangle = \pm c_1|1\rangle + c_2|2\rangle$, with coefficients $c_{1,2} = \sqrt{(A \mp \Delta)/2A}$. Using this model, optical transmission spectra can be simulated by using Eq. (4.3). Further, the predictions for the real and imaginary parts of the coupled mode frequencies can be compared to the experimental data with Fano line fits. The fitting results for the resonance wavelengths and the linewidths of the upper (open circles) and lower (solid circles) bands are plotted in Figs. 4.11(a) and (b), respectively. Similarly to the SM zone boundary [Sec. (4.3.1)], the coupling between these two resonances results in the opening of an SPP band gap of frequency spacing $2V$, when the SPP modes are angle-tuned into resonance. The results of the model calculation are shown as the solid lines for $\hbar V = -35$ meV.

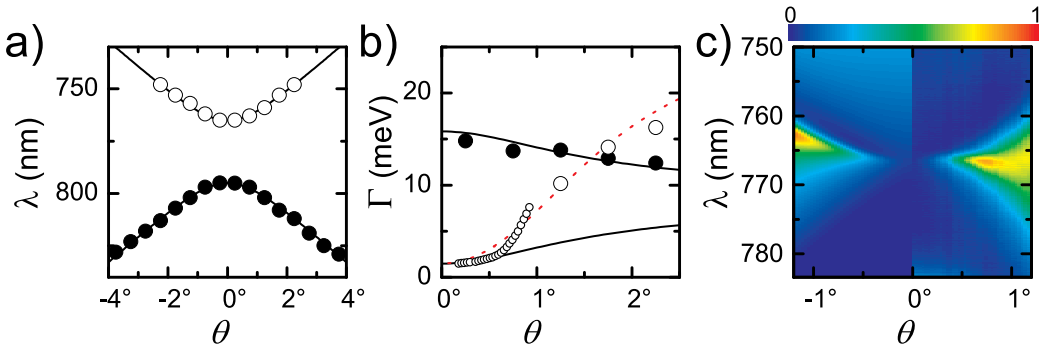

Figure 4.11: Complex band gap formation following from the coupling matrix from Eq. (4.6). (a): Splitting of the real parts of the mode frequencies in the experiment (circles) and the model (lines). (b): Splitting of the imaginary parts of the coupled mode frequencies in the experiment (circles) and the model for $\hbar\Gamma = 7$ meV (solid lines) and 30 meV (dotted red line). (c): Model calculation (left) and experiment (right) for the angle-dependent transmission close to normal incidence.

In addition to this band gap formation, the coupling induces a redistribution of the radiative damping rates [Figs. 4.11(b)] into the modified linewidths $\Gamma_{+,-} \doteq \gamma + \Gamma \mp \Im(A/2)$. The broad mode exhibits only small variations in linewidth upon approaching the degeneracy point (solid circles), whereas the dark mode $|-\rangle$ narrows significantly close to zero degrees, as mentioned before. Its radiative coupling to the far-field continuum $\Gamma_{rad,-} \doteq \Gamma + \Im(A/2)$ decreases continuously with decreasing detuning, and radiative damping is fully suppressed at $\Delta = 0$. Here, the linewidth of the resonance is no longer limited by radiative damping but by the intrinsic losses γ. While the linewidth of the bright mode and the asymptotic behavior of the dark mode at $\theta = 0°$ are well-described for $\hbar\Gamma = 7$ meV, a much larger value close to $\hbar\Gamma = 30$ meV has to be assumed if one wants to describe the dark mode linewidth variation for larger angles (dotted red line). This is very likely due to the fact that additional diffraction and therefore damping is possible for the upper (narrow) mode at finite angles. Although a fully quantitative modeling is therefore not possible with only a single and constant damping parameter, the qualitative behavior of the narrow mode in the angle-dependent spectra is reproduced: In Fig. 4.11(c), the model calculation (left), using Eqs. (4.3) and (4.8), is juxtaposed with the experimental results (right). One observes the narrowing of the asymmetric resonance with decreasing θ until $\Gamma_{rad,-} < \gamma$, followed by a decrease of the dark mode intensity, vanishing at the degeneracy point.

Coming back to the plasmonic crystal's unit cell, this pronounced suppression of radiative damping is manifested in the spatial near-field mode profiles

in Figs. 4.10(c) and (d). The mode overlap of the symmetric $|+\rangle$ mode (red curve in (c)) with the nanoslit scattering centers is larger than that of the uncoupled modes $|l,r\rangle \propto \exp(\pm iGx)$, thus increasing the radiation damping $\Gamma_{rad,+}$. For the antisymmetric $|-\rangle$ mode (blue curve), however, both maxima of $I(x) \simeq |\exp(iGx) - \exp(-iGx)|^2$ are now between the nanoslits. The field intensity at the slits is strongly reduced and the radiative damping rate $\Gamma_{rad,-}$ becomes vanishingly small. Essentially, the coupling of the SPP modes via the nanoslits introduces a well-defined relative phase between the radiation fields emitted from the uncoupled modes. For the antisymmetric mode this interference is destructive and radiation damping is suppressed.

This phenomenon is in close analogy to previously observed interference phenomena in the radiative damping of other, e.g., atomic or molecular, multi-level systems [149, 160]. In such systems, however, the finite radiative damping of the uncoupled systems is often larger than their radiative coupling, and the suppression of radiative damping is much less pronounced [149]. In the system considered here, the intrinsic damping is sufficiently weak to reach the strong radiative coupling limit ($\Gamma > \gamma$).

While the introduced phenomenological model captured the physical mechanisms underlying the coupling among SPP modes, the actual angle-dependent linewidth variations of the SM and AM SPP band gaps were somewhat more complicated than those predicted from the simple model, when only the zeroth diffraction order was considered. This calls for a full, scattering-matrix-based solution of Maxwell's equations [130, 157]. In addition, a more detailed description is necessary to address the coupling between SPP modes and the waveguide mode in the nanoslit. These issues will be addressed in Secs. (4.4) and (4.5).

4.4 Radiative Coupling Model

The terms "super-" and "subradiance" were used for the observations in the previous section to stress the cooperative nature of the radiative decay induced by the coupling. The elements exhibiting the cooperative decay were the delocalized SPP modes $|l\rangle$ and $|r\rangle$ connected with the initially undisturbed, spatially extended flat surface polarizability. In that sense, this two-mode system represents a momentum space analog of the cooperative decay of two "point" polarizabilities, for example two atoms [149].

Alternatively, and to a certain extent equivalently, one may think of the very same problem in terms of the complementary real space situation. In that representation, the slits serve as elementary polarizable units, which are radiatively coupled via the propagating surface plasmons.

This section will introduce this slightly different point of view, which will be

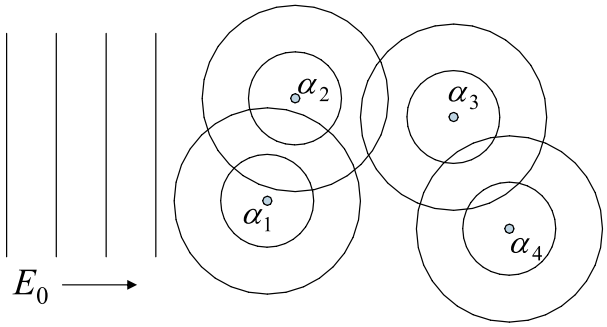

Figure 4.12: A set of polarizable particles illuminated with a plane wave E_0. The reradiated fields interfere with each other and E_0 at the particles, which constitutes radiative coupling.

useful in a number of ways. First, the surface plasmon resonances appear directly in the calculation of scattering amplitudes and do not have to be introduced a priori. Second, the reason for the absolute transmissivity enhancement of a system of slits or nanoholes with respect to its individual components becomes clear immediately. Third, Fabry-Pérot effects are easily discussed. Finally, the presence of a probe near the plasmonic crystal can be incorporated in the description in a natural way, which will be useful in a following chapter.

The first subsection briefly introduces the theoretical framework, before our specific periodic system is modeled, and computed angle-dependent far-field transmission spectra are compared with the experimental ones.

4.4.1 Theoretical Framework

The calculations are restricted to a single scalar field, and it will become clear that many of the observed effects already appear within this approximation.[13] We consider a set of N particles with index l and polarizabilities α_l, which are illuminated by a source having a field amplitude at the particles of $E_0(\mathbf{r}_l)$ [see Fig. 4.12]. The fields reradiated from the particles are proportional to α_l and act on each other, so that the total field amplitude at $\mathbf{r}_l$ is given as a sum of the incident plus all the scattered fields [71, 162, 163]:

$$E(\mathbf{r}_l) = E_0(\mathbf{r}_l) + \sum_{m=1,m\neq l}^{N} \alpha_m E(\mathbf{r}_m) G(\mathbf{r}_l, \mathbf{r}_m). \tag{4.9}$$

Here, $G(\mathbf{r}_l, \mathbf{r}_m)$ is the Green's function relating the amplitude at $\mathbf{r}_l$ to those from the points $\mathbf{r}_n$. In the case of a scalar field as depicted in Fig. 4.12, G takes the form of a spherical wave. Due to the interference of all reradiated fields with each other and with the incident field E_0, the effective polarizability of the set of particles may be drastically influenced by cooperative radiation effects. This

[13] Furthermore, only the linear responses are considered. A recent study investigating nonlinear radiative couplings is found in Ref. [161].

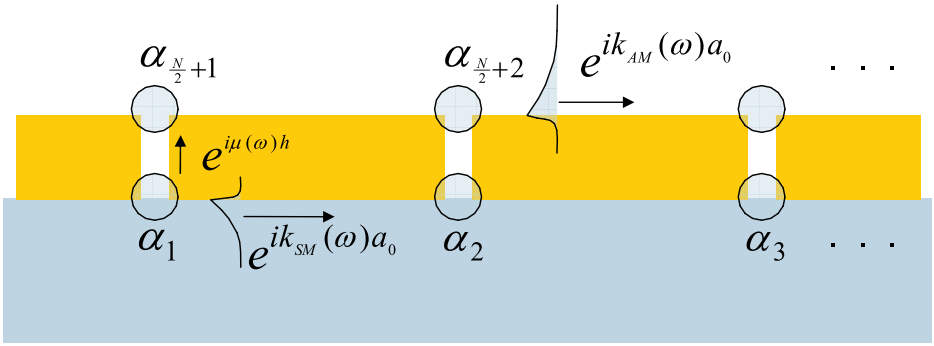

Figure 4.13: The slit array modeled as a set of N polarizabilities located at the top and bottom of the slits. The polarizabilities are coupled via SPPs on both sides of the interfaces and via the slit waveguide.

modified reaction of the particle set to the incident field E_0 is called radiative coupling. In a related context, the radiative coupling of an electric dipole with its image has been discussed in Sec. (2.2.6). Equation 4.9 is a set of coupled linear equations for the actual fields $E(\mathbf{r}_l)$, which can be rewritten as a matrix equation relating the incident and total fields,

$$(\widehat{I}-\widehat{\alpha}\widehat{G})\mathbf{E}=\mathbf{E}_0 \quad \text{or} \quad (\widehat{I}-\widehat{\alpha}\widehat{G})^{-1}\mathbf{E}_0=\mathbf{E} \tag{4.10}$$

Here, $\widehat{I}$ and $\widehat{\alpha}$ are diagonal identity and polarizability tensors of size $N\times N$, respectively, $\widehat{G}$ is the Green's tensor evaluated for all combinations of particle positions, and $\mathbf{E}_0$ and $\mathbf{E}$ are $N\times 1$ row vectors of the incident and total amplitudes with components $E_0(\mathbf{r}_l)$ and $E(\mathbf{r}_l)$, respectively.[14] The inversion in Eq. (4.10) represents the self-consistent field solution of the radiatively coupled system [73].

4.4.2 Model System

Now, we consider a specific simple system of polarizable particles mimicking the periodically structured metal films studied here. In Fig. 4.13, the actual geometry and the idealized dipole array are superimposed.[15] Polarizabilities α_l are placed at the top and bottom of the slits, as they serve as the scattering centers coupling far-field light to surface excitations. The excitation of SPPs from such surface defects has been studied experimentally and theoretically [70, 164–166]. A mutual coupling between the α_l is possible via surface plasmon polariton excitations

[14] $\widehat{\alpha}$ and $\widehat{G}$ should not be confused with the three-dimensional tensors they represented earlier in Sec. (2.2.6).

[15] Both the fields and the structure are translationally invariant in the y-direction, so that this extruded dimension is separated out and not further considered.

and through the slit waveguide. For such localized surface protrusion in a metal film, the Green's function of SPP propagation is a Hankel function [163], being a two-dimensional analog of a spherical wave. We are looking at a system which is translationally invariant in the y-direction, so that the SPP propagator in this effectively one-dimensional system is a simple plane wave. The phase factor in the propagation of SPP waves between the point dipoles l and m is given by the frequency-dependent wavenumbers of the respective substrate-metal (SM) or air-metal (AM) SPPs. In general, the Green's tensor should be composed of three components corresponding to the coupling via SPPs on either side of the metal film and through the waveguide [see Fig. 4.13],

$$\begin{aligned}\widehat{G} &= \widehat{G}_{AM} + \widehat{G}_{SM} + \widehat{G}_{WG} \\ G_{lm} &= f\exp(ik_{AM}(\omega)a_0|l-m|)\Theta(l-N/2)\Theta(m-N/2)(1-\delta_{l,m}) \\ &\quad + g\exp(ik_{SM}(\omega)a_0|l-m|)\Theta(N/2+1-l)\Theta(N/2+1-m)(1-\delta_{l,m}) \\ &\quad + q\exp(i\mu(\omega)h)(\delta_{\frac{N}{2}+l,l} + \delta_{l,\frac{N}{2}+l}).\end{aligned} \tag{4.11}$$

Here, δ is the Kronecker symbol, a_0 and h are again the lattice period of the array and the film thickness, respectively, and the Heaviside function $\Theta(x)$ is 1 if $x > 0$ and zero otherwise. The waveguide propagation constant μ is calculated from Eqs. (3.14) and (3.15). For a 50 nm wide gold waveguide at a wavelength of 700 nm (900 nm), the effective refractive index of the waveguide mode, i.e., $\mu c/\omega$, is $1.44 + 0.012i$ ($1.41 + 0.010i$). The waveguide mode is thus propagating and only weakly damped, with a phase shift $\phi = \mu d \simeq 1.7$ rad (1.3 rad) and a damping of about 2% in intensity between both interfaces.

Depending on the specific geometry, the SPP excitation efficiencies at the polarizabilities may be different at the two interfaces, and the complex coefficients f and g have been introduced to account for this, along with the cross-interface coupling constant q. These parameters could generally also depend on frequency, which is not taken into account in our circumstances, both because resonances of individual slit edges are very broad with respect to our frequency window of interest, and because the current set of constant parameters is sufficient to satisfactorily describe the experimental data.

Finally, the polarizabilities α_l need to be defined. They are determined by the shape and size of the nano-slits. Considering that in Eq. (4.9) only products of the Green's tensor with the polarizability appear, the α_l are set to 1 without loss of generality.

4.4.3 Far-field Transmission

We first compare experimental angle-dependent far-field transmission spectra of the 650 nm period slit array with the results of the dipole array. The illuminating

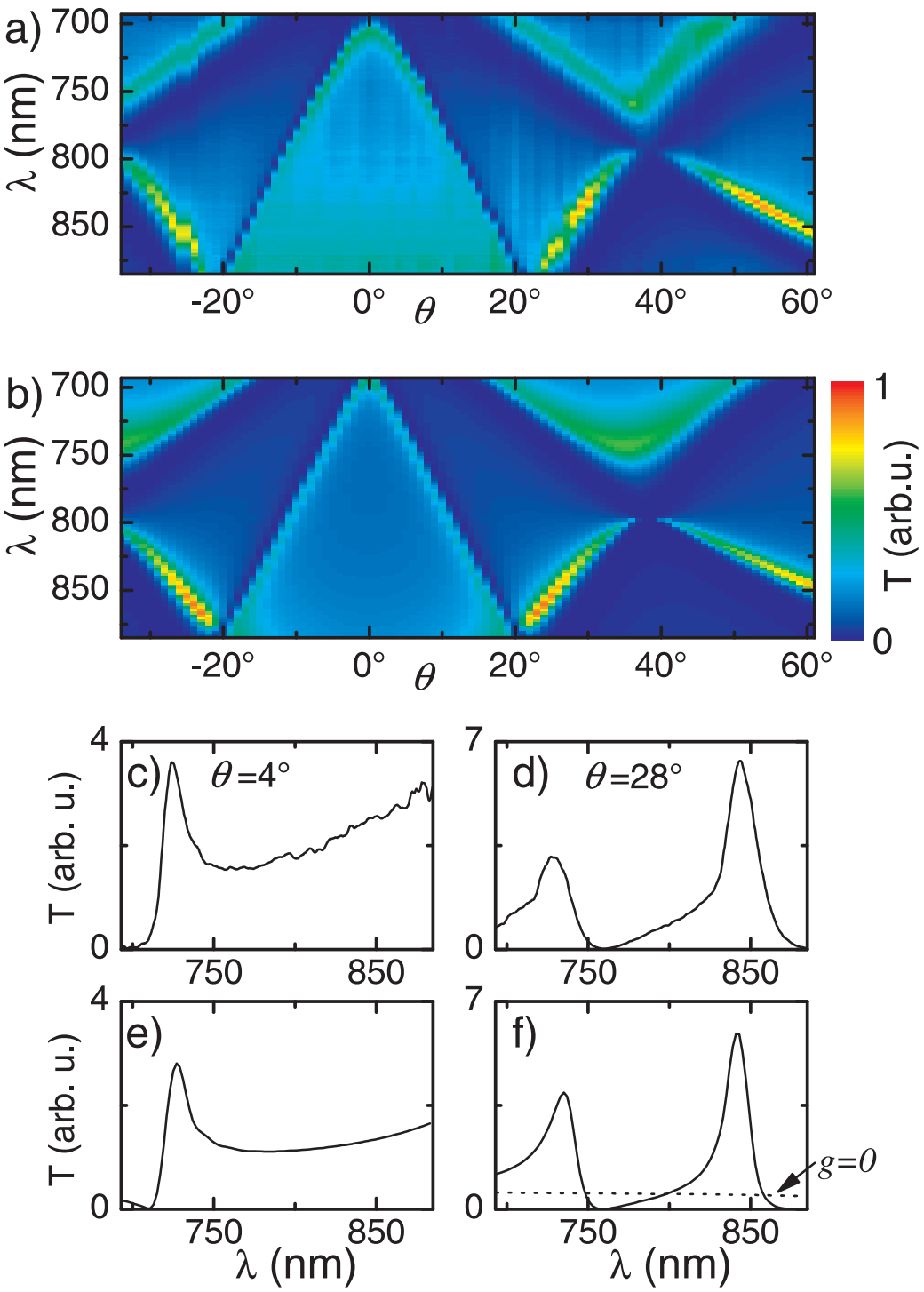

Figure 4.14: Angle-dependent experimental transmission spectrum (a) and calculated zeroth order transmission of a periodic system of point dipoles (b), radiatively coupled via air-metal and sapphire metal SPP modes. (c)-(d): Experimental transmission spectra at two different angles of incidence displaying air-metal (c) and sapphire-metal (d) SPP resonances. The corresponding simulated spectra are shown in (e) and (f).

field for an angle of incidence θ and unit amplitude, incident from the substrate side, is given as $E_0(\mathbf{r}_l) = \exp(i\sin(\theta)a_0 l\omega/c)$ for $l \leq N/2$ and zero otherwise. As no light is directly transmitted through the film, the transmitted fields are given as the superposition of the fields radiated away from the dipoles alone. If the number N of polarizabilities becomes large enough, the radiation can be characterized with respect to different diffraction orders. We are interested in the zeroth order transmitted wave, the amplitude of which is expressed in terms of the total fields $E(\mathbf{r}_l)$ at the upper interface

$$E_{tr} \propto \sum_{l=N/2+1}^{N} \exp(-i\sin(\theta)a_0 l\omega/c)E(\mathbf{r}_l) = \sum_{l=N/2+1}^{N} E_0^*(\mathbf{r}_{l-N/2})E(\mathbf{r}_l). \quad (4.12)$$

The total fields were calculated by numerically solving Eq. (4.10) for a given set of coupling parameters and a number of slits of 100-200, in accordance with the actual structures in the experiments. In Fig. 4.14, the experimental angle-dependent transmission spectrum of the 650 nm period slit array is shown (a), together with the calculated transmitted intensity of the periodic array of point dipoles (b), coupled in the way discussed above. Below, experimental spectra at angles of incidence of $\theta = 4^\circ$ (c) and 28° (e) and the respective results of the calculation [(d) and (f)] are plotted. Using a dimensionless form of the Green's function, the parameters for this calculation were $f = -0.09 + 0.14i$, $g = -0.33 - 0.35i$, and $q = 0.65$. These values have been chosen for good correspondence with the experimental spectra, and they are of similar magnitude as recent theoretical predictions of the SPP excitation efficiency at single nanoslits [167]. Specifically, for very narrow slits, that work predicted an SPP excitation efficiency increasing with the dielectric function of the substrate, which is confirmed by the present experiments, namely $|g| > |f|$.

In the simulated spectra, the SPP transmission resonances are apparent, following the flat surface SPP dispersion relation entering the model. Also, the Fano-shaped asymmetries of the transmission resonances, the band gap splitting and the subradiant mode narrowing can clearly be reproduced. Certain deviations are observed with regard to the increasing spectrum for longer wavelengths at small angles of incidence. With the parameters given, the model slightly underestimates this increase. Also, the exact magnitudes of the band gaps have not been perfectly modeled. Given the simplicity of the model containing only three frequency-independent parameters, it is interesting, how well this system can consistently account for many aspects of the experimental data.

The SPP resonances obviously originate from constructive interference of the SPP waves excited at the individual polarizabilities, which is inherent in this radiative coupling description. As a result, the amplitude of the waves coupling into and through a particular nanoslit waveguide is strongly enhanced by the in-

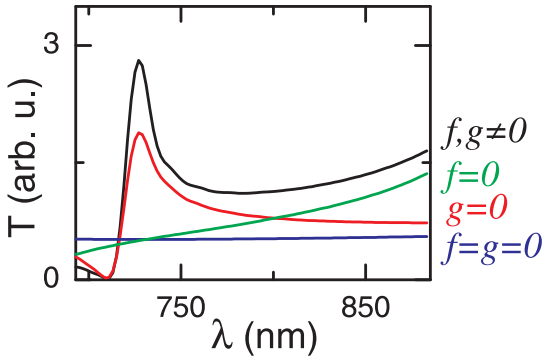

Figure 4.15: Simulated transmission spectrum of the dipole model with the parameters given in the text (black) and for systems with switched-off SPP coupling on the air-metal (green), the sapphire-metal (red) or both (blue) interfaces.

terference of the incident plane wave and the SPP waves generated at all the other nanoslits. This causes the integral transmissivity of the array at the resonances to exceed far that of N independent polarizabilities, and immediately explains the large transmission efficiency frequently found for such periodic systems, which has been termed "extraordinary" [11] or "astonishingly high" [168] when compared with the transmission of the individual array constituents.

In light of this abstraction, the harshly fought dispute of whether SPPs are responsible for such unusual transmissions, or if other explanations need to be deployed, is resolved in our observation that any form of radiative coupling, promoted either by surface plasmons, other surface modes or diffracted waves, will result in similar effects.[16]

The resonant transmission enhancement due to SPP-mediated radiative coupling on either interface is illustrated by switching off the respective coupling constants in the simulation. The dotted line in Fig. 4.14(f) represents the calculated transmission, if g, i.e., the SM SPP coefficient in the Green's tensor in Eq. (4.11), is set to zero, keeping the other coefficients the same as before. A further visualization of the interference among different transmission components is found in Fig. 4.15, where the simulated transmission spectrum at an angle of incidence of $\theta = 4^\circ$ is compared with a simulation, in which the different SPP coupling coefficients f, g, or both, are set to zero. For example, this analysis allows us to identify the increasing transmission for longer wavelengths as a spectrally broad SM SPP resonance near the SM[$\pm$1] anti-crossing, which is outside the available wavelength range. Figure 4.15 further exemplifies the transmission enhancement if SM and AM SPP resonances spectrally overlap, comparing the red ($g = 0$) and black ($f, g \neq 0$) curves. This is expected to be even more prominent if the modes on both interfaces are brought into exact resonance [171, 172].

[16] Consider, for example, the prediction [169] and subsequent observation [170] of tailored evanescent bound modes on structured, nearly lossless metals (in the microwave frequency range).

4.4.4 Band Gap and Fabry-Pérot effects

The introduced model is quite practical, because the parameters matching the experimental data can be used to evaluate and discuss some properties of the plasmonic crystal. Concerning the band gaps and the splitting into a narrow and a broad mode, which are both predicted by the model, the coefficients of the Green's tensor directly translate into the real and imaginary parts of the SPP band gaps via the complex transmission and reflection coefficients they represent for SPPs traveling on the surface. For example, the parameters needed to describe the experimental data can be used to infer upon the properties of a single nanoslit. The relation between the parameters in the radiative coupling model and the complex transmission and reflection coefficients of a single slit (depicted in Fig. 4.16) are easily derived. For an incoming AM SPP, the coefficients of SPP transmission t_{AM} and reflection r_{AM} across a single slit are expressed as the coherent sum of the directly transmitted or reflected amplitudes [$(1+f)$ for transmission, f for reflection], plus a contribution of multiply scattered waves in the waveguide,

$$t_{AM} = 1 + f + f\sum_{n=1}^{\infty} q^{2n}\exp(i2\mu(\omega)h) = 1 + \frac{f}{1-q^2\exp(i2\mu(\omega)h)} \qquad (4.13)$$

and $r_{AM} = t_{AM} - 1$. For the parameters given above, the transmissions $|t_{AM}|^2$ and $|t_{SM}|^2$ are about 0.9 and 0.7, respectively, and reflections range from a few up to ten per cent. These numbers are in quite good agreement with recent theoretical calculations using the method of multiple multipoles [166]. The larger reflectivity of the SM SPP at the sapphire-metal interface likely originates from the fact that the SM mode is more confined to the metal than the AM mode [cf. Eq. (3.3)]. Moreover, the radius of curvature of the slit edges is smaller at the SM than at the AM interface, which has consequences for the reflectivity and the SPP coupling into the waveguide mode [166]. An experimental study of the SPP coupling constants of single slits in a silver film can be found in a recent Ph.D. thesis [164].

The Fabry-Pérot (FP) form of the transmission and reflection coefficients in Eq. (4.13) leads to an oscillatory dependence of the band gap parameters on the film thickness. In particular, the magnitude of the frequency splitting is predicted to be resonantly enhanced, when the slit reflectivity is increased due to a nanoslit FP resonance. Furthermore, the thickness dependent phase change induced upon transmission and reflection of SPPs from the slits can alter, which branch of the band gap (the upper or the lower one) becomes subradiant and which one becomes superradiant at the anti-crossing. These effects are expected to be most prominent for somewhat larger film thicknesses on the order of or larger than the inverse propagation constant μ.

Somewhat surprisingly, our collaboration has found Fabry-Pérot-type reso-

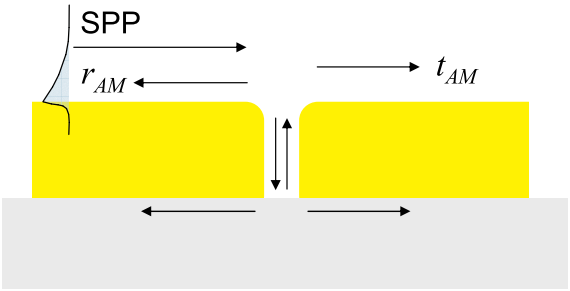

Figure 4.16: Transmission and reflection of an SPP incident on a single slit. Both the reflected and the transmitted amplitudes are given as the sum over direct and multiply reflected components in the waveguide.

nances[17] even for relatively thin films ($h \sim 100$ nm) in experiments performed in Prof. Dai-Sik Kim's laboratory at Seoul National University. The findings, including a more explicit theoretical coverage, have recently been published in Ref. [138]. Here, only one experimental result from that study is presented that directly evidences a controlled modification of SPP band gaps. In the experiment, the SM[$\pm$1] anti-crossing of a slit array with a lattice period $a_0 = 540$ nm, film thickness $h = 75$ nm and slit width $b \approx 100$ nm is observed in angle-dependent transmission spectra [Figs. 4.17(a) and (c)]. A band gap of about 25 nm is formed, and the typical narrowing and disappearance of one of the bands is found for $\theta = 0°$, in this case for the shorter wavelength band at a wavelength $\lambda_0 \approx 978$ nm. When the nanoslit waveguides are filled with an immersion oil of a refractive index $n = 1.512$, the propagation constant in the waveguide changes accordingly. The experimentally found FP resonance nearest to the anti-crossing changes from $\lambda_{FP,n=1} = 725$ nm to $\lambda_{FP,n=1.5} = 1150$ nm [138], thus shifting from wavelengths shorter than the anti-crossing range to longer wavelengths. This has a dramatic effect on the appearance of the SM[$\pm$1] SPP band gap, as shown in Figs. 4.17(b) and (d). Now, the longer wavelength band has become the subradiant one, displaying narrowing and vanishing intensity at $\theta = 0°$. Motivated by these results, the term "band gap polarity" was introduced in Ref. [138] and defined to describe the types of band gaps found, i.e., a band gap of *negative* polarity is one of the form in Fig. 4.17(c), one of *positive* polarity is of the form in Fig. 4.17(d).

Interestingly, an exceedingly small slit width of only about 10 nm had to be assumed to make the theoretical simulations predict FP waveguide resonances at the observed wavelengths. A decrease of the slit width leads to larger effective propagation constants of the waveguide modes [see Refs. [173, 174] or directly Eqs. (3.14)-(3.15)], thus resulting in FP resonances even for such thin samples. It is still an open question why such very narrow slit widths had to be assumed to obtain a quantitative description of the resonances attributed to the waveguide, and perhaps, a better understanding of the resonances in these very narrow and

[17] The signature of an FP resonance is a very weak angle dependence in the transmission spectrum.

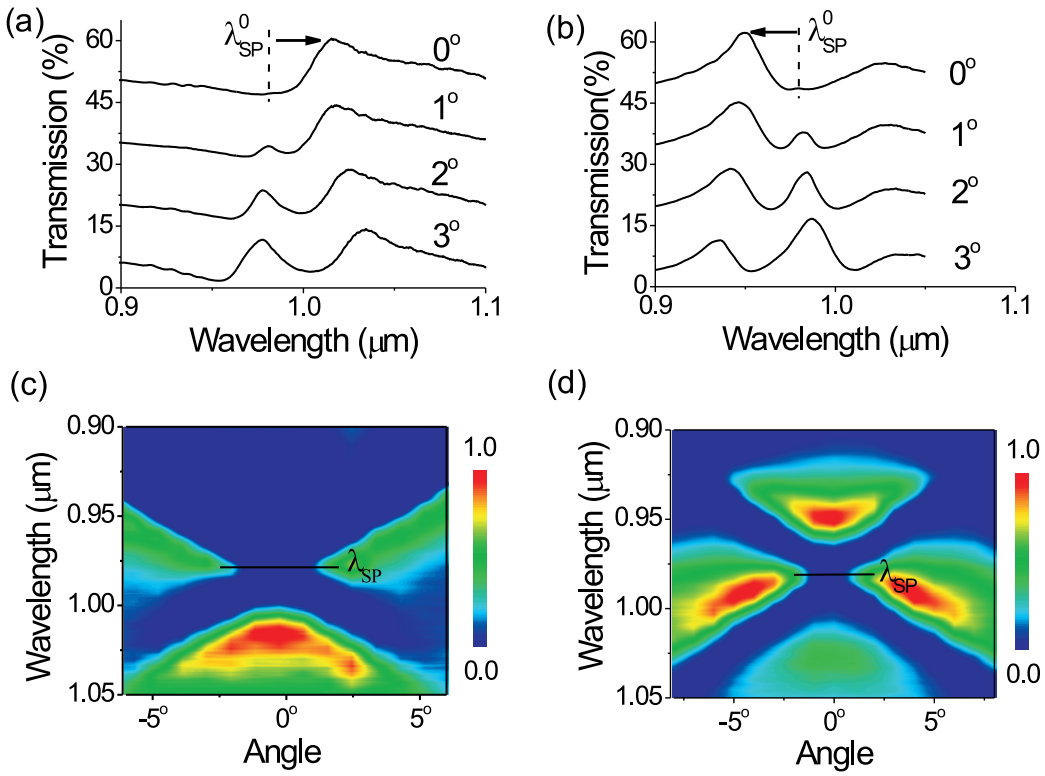

Figure 4.17: Fabry-Pérot induced change of the band gap polarity of an SM[$\pm$1] anti-crossing for a nanoslit array with $a_0 = 540$ nm. Angle-dependent light transmission for the structure in air [(a) and(c)], and immersed in an oil of refractive index $n = 1.512$ [(b) and (d)]. Note that different angle-dependent spectra in (a) and (b) are vertically offset by 15% for clarity. (from Ref. [138]).

thin waveguides will be necessary to resolve this issue. For example, the contribution of higher-order waveguide modes could differ for such thin samples from the predictions of the SIBC approximation [see Sec. (3.5)].

In any case, these experiments demonstrate the ability to tailor the properties of SPP band gaps due to other resonances, e.g., in the waveguide connecting both interfaces, even if such resonances are not immediately apparent in all transmission spectra, because they may be relatively broad or may peak outside of the experimentally accessible wavelength window.

Besides the role they play in the coupling constants and the polarity of SPP band gaps, the waveguides also determine the relative phase between the transmission continuum and the SPP resonances far from anti-crossings, and are therefore responsible for the type of asymmetry, i.e., red-shifted, blue-shifted or even symmetric, found for the Fano-lineshapes from Sec. (4.2.2). Up to now, only

red-shifted Fano resonances and SPP band gaps of negative polarity have been reported in the literature from experiments on two-dimensional nanohole arrays [see, e.g., Refs. [11, 119, 145]]. Evidently, the SM resonances found for the $a_0 = 650$ and 750 nm samples are blue-shifted, and display a positive polarity at the S$[\pm 1, \mp 2]$ band gap. Both the propagation and the coupling of SPPs into the waveguide connecting the upper and lower interface will be different due to the dimensionality of the waveguide. The small holes of the two-dimensional arrays, viewed as tube waveguides, are excited at frequencies lower than their cutoff, so that no propagating waveguide modes exist. In the case of the nanoslits, no such cutoff is present and the lowest (TEM-)waveguide mode is always propagating, which is in part responsible for the blue-shifted SPP resonances and the positive polarity of some band gaps. A detailed theoretical treatment covering the differences between propagation constants through one- and two-dimensional apertures in metal films with finite conductivity is found in Ref. [120].

4.4.5 Near-field modes

The above model also allows for a calculation of the corresponding near-field distributions. The SPP mode profiles are obtained from the field amplitudes at the dipoles on the upper interface, propagated to the points of observation $\mathbf{r}_{pr} = (x_{pr}, y_{pr}, z_{pr})$,

$$E(\mathbf{r}_{pr}) = \sum_{m=N/2+1}^{N} \alpha_m E(\mathbf{r}_m) f \exp(ik_{AM}(\omega)|x_{pr} - x_m|) \exp(-\kappa_{AM}(\omega) z_{pr}). \quad (4.14)$$

Here, the incident fields ($m \leq N/2$) do not appear due to the illumination from the substrate side, and a further modeling of the (non-SPP) radiated fields from the polarizabilities was not performed, as a more complete description is available with the modal expansion method in the next chapter.

An accurate description of the experimental data has already been reached for the far-field transmission spectra, and the agreement for the near-field modes shown in Fig. 4.18 is equally convincing. Here, the calculation was performed for the $a_0 = 750$ nm sample and an angle of incidence of 0.7°. One observes the same splitting of the spatial modes into a symmetric and antisymmetric mode as in the experiment [Fig. 4.10]. Again, the mode displaying small overlap with the polarizabilities is spectrally narrow, i.e., weakly coupled to the far-field.

The question arises, how this result is now to be interpreted, as we have only studied a previously unspecified scalar field, and the more complicated near-field polarization of an SPP wave should enter in the NSOM measurement. In principle, this single field could stand for the magnetic field along the y-direction, which

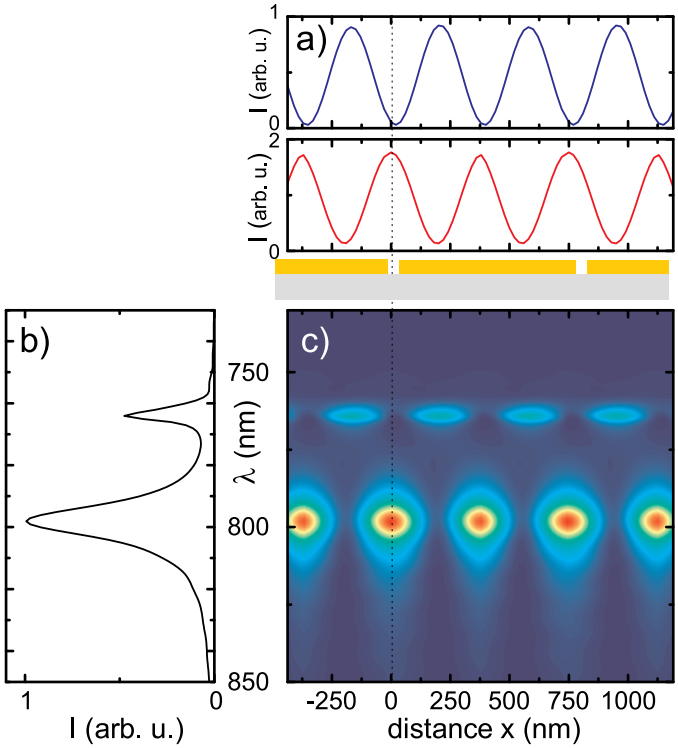

Figure 4.18: Near-field optical spectroscopic line scan ($z_{pr} = 0$ nm) simulated with the array of point dipoles ($a_0 = 750$ nm). The Figure is presented in the same way as Fig. 4.10 to promote an easier comparison.

completely characterizes the scattering problem in this TM-polarized case. However, no motivation for such an interpretation has been given so far, and a more detailed theoretical analysis and further experiments are required to get a complete picture of the electromagnetic vector fields in these structures. Chapter 5 is be devoted to further near-field studies. The remaining section of the present chapter will deal with the numerical computations using the scattering matrix model introduced in Sec. (3.5).

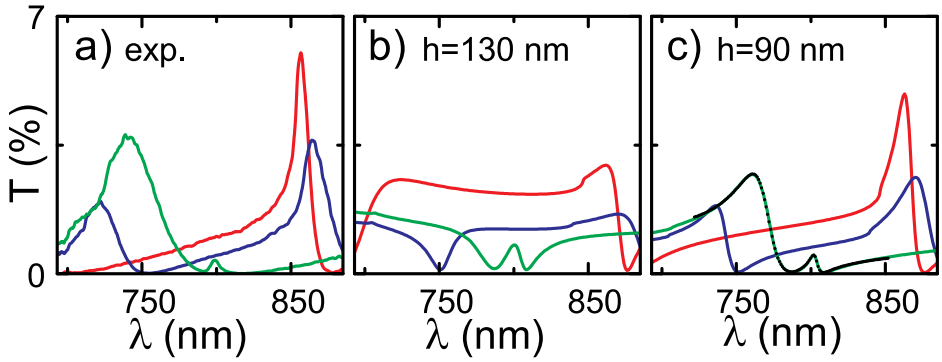

Figure 4.19: (a): Experimental transmission spectra of the 650 nm array for angles of incidence θ of 26°(blue), 40°(green) and 61°(red). (b): Simulated transmission spectra for a slit width of $b = 50$ nm and a film thickness of $h = 130$ nm. Although resonances at similar wavelengths as in (a) are observed, the lineshapes differ drastically. (c): The simulation for a film thickness of 90 nm. As in the experiments, the resonance parameters for the simulation can be obtained from fitting of the Fano lineshape function. An exemplary two-resonance fit is shown in (c) as the small black circles.

4.5 Scattering Matrix Method

In the preceding section, a radiative coupling model with coupling parameters obtained from the experiment was used. While this allowed for a discussion of some of the observations, an *ab initio* simulation is valuable to find out, to what extent the real structures possess the properties of idealized systems, where they deviate etc. Furthermore, such simulations yield the complete field distributions in the structure, which will be important for the subsequent chapter. In this section, the scattering matrix method introduced in Sec. (3.5) is used to compute angle-dependent far-field transmission spectra of the investigated structures, and the results are compared with the experimental findings.

4.5.1 Substrate-Metal Zone Boundary Band Gap

We first return to the sample with a 650 nm lattice period, which displayed the SM SPP band gap at the zone boundary [see Sec. (4.3.1)]. The nominal parameters for this sample are a slit width $b = 50$ nm and a film thickness $h = 120(\pm 20)$ nm. Whereas the lattice period is very precisely known from calibrated scanning electron micrographs, a limited uncertainty on the exact film thickness and the slit width exist, in the latter case in particular because of the non-rectangular cross-section of the structure.

With the SIBC method, angle-dependent transmission spectra can be calcu-

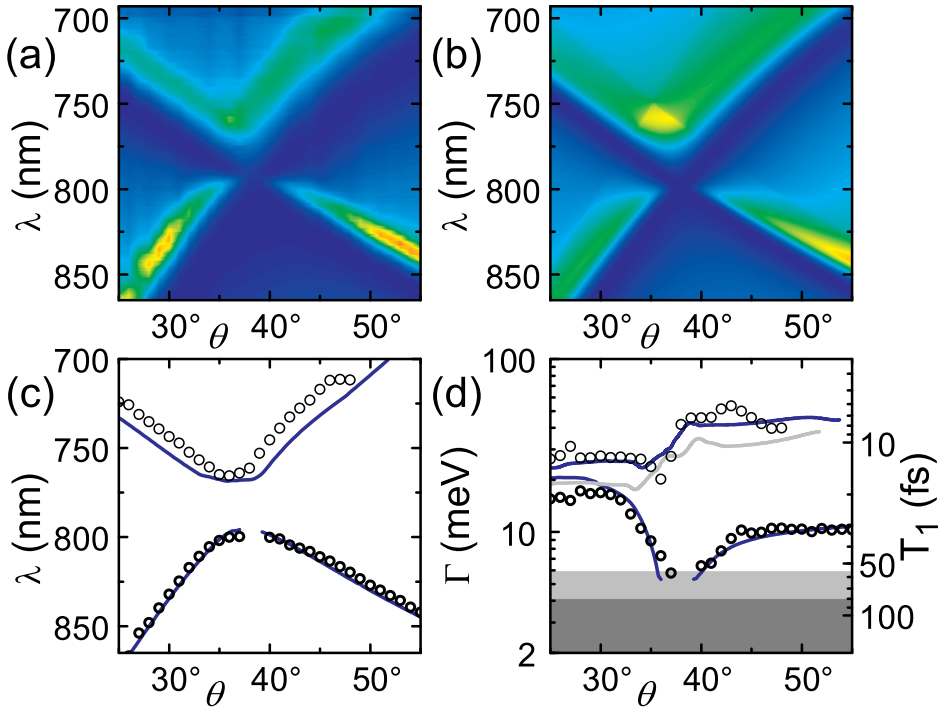

Figure 4.20: Color-scale images of the experimental (a) and simulated (b) angle-dependent transmission spectra near the SM[+1,-2] anti-crossing for the 650 nm slit array. (Structure parameters in the simulation: $b = 80$ nm, $h = 90$ nm.) The resonance wavelengths (c) and linewidths (d) were obtained by Fano-lineshape fits to the experimental and simulated spectra, and are shown as circles and blue lines, respectively. For comparison, the gray line shows the angle-dependent linewidth of the upper branch for a narrower slit width of 50 nm. The gray-shaded areas correspond, as in Fig. 4.8, for the expected intrinsic limits to the linewidths due to absorption in the metal.

lated, which are usually in qualitative, often in quantitative agreement with the experimental data. Figure 4.19 shows measured transmission spectra containing SM SPP resonances and corresponding simulated spectra. The linewidths and lineshapes resulting from these simulations depend sensitively on the slit width and film thickness, so that significant spectral modifications are found when the geometrical parameters are changed within their experimental uncertainty intervals. Thus, the slit width and the film thickness are adjusted within reasonable bounds to conform to the experimental results. For example, the sensitivity of the simulated spectra to the film thickness is demonstrated in Fig. 4.19. Here, experimental transmission spectra for different angles of incidence (a) are contrasted with the results of simulations using a slit width of 50 nm and film thicknesses of 130 nm (b) and 90 nm (c). It was mentioned earlier [Sec. (4.4.4)] that the exact

film thickness in the case of nanoslit arrays plays a crucial role for the asymmetry of the Fano lineshapes of these SM transmission resonances, which is evident in Figs. 4.19(b) and (c). In contrast to the experiment, the lineshapes for the 130 nm thickness calculation no longer appear as peaked blue-shifted resonances, but rather as dispersive lineshapes (red line around 860 nm) or even as transmission dips (blue line around 750 nm). Upon a reduction of the film thickness to 90 nm (c), the experimental lineshapes are approximately obtained, including a rather accurate quantitative prediction of the transmission on the order of a few per cent.

Some deviations from the experiment can be spotted for the linewidths in the calculation. Since the SIBC method is a numerical procedure, which generates the transmission and reflection spectra and not directly the poles or resonances of the scattering matrix, further analysis is necessary to quantify the linewidths and the resonance positions from the simulation. A fitting using Fano lineshapes is again employed, yielding excellent results, as can be seen in Fig. 4.19(c), where the small black circles represent a two-resonance fit to the green transmission spectrum. Further away from the resonances, the simulation very slightly deviates from the Fano fit due to the influence of other, e.g. AM, transmission resonances.

The Fano lineshape model allows us to quantitatively compare the experimentally observed complex band gap, i.e., the splitting of the real and imaginary parts of the transmission poles, $\omega - i\Gamma$, with those obtained from the calculation. In Figs. 4.20(a) and (b), the experimental and simulated transmission spectra are shown in color scale for the entire range of angles of incidence displaying the SM SPP anti-crossing. Quite good agreement is obtained by this calculation for the general shape and a number specific details, such as the narrowing and disappearance of the longer wavelength mode or the broadening of the upper branch for larger angles of incidence. Figures 4.20(c) and (d) contain a comparison of the resonance wavelengths and the linewidths, respectively, of the experiment (circles) with those from the simulation (blue lines). The band gap formation (c) is clearly reproduced, and the simulation also accounts for the more complicated variations of the linewidths (d). The narrowing of the lower branch, resulting in SPP lifetimes close to the limit posed by the intrinsic damping is reproduced, as well as the step-shaped lifetime decrease of the upper branch. In these calculations, a slightly larger slit width of 80 nm has turned out to yield more accurate results, which is evident by inspection of the linewidth of the upper branch for a calculation with a 50 nm slit width (gray line in Fig. 4.20), predicting smaller linewidths than those found in the experiment.

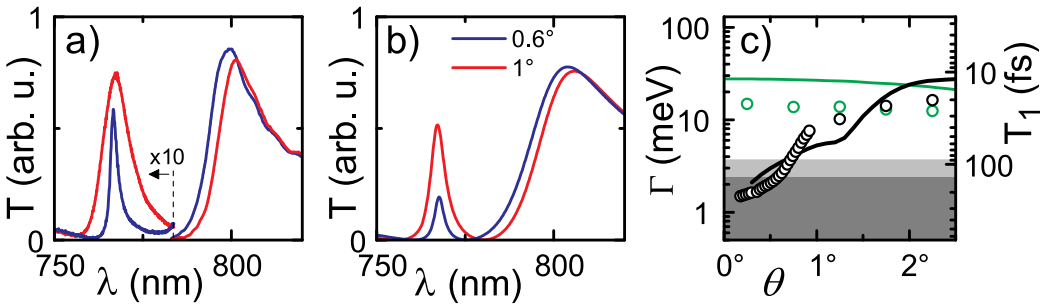

Figure 4.21: (a): Transmission spectra near normal incidence for the $a_0 = 750$ nm array at angles $\theta = 0.6°$(blue) and $\theta = 1°$(red), displaying the bright and dark AM SPP resonances. (b): Simulated transmission spectra (SIBC method). (c): Angle-dependent linewidths for the bright (green) and dark (black) resonances in the experiment (circles) and the simulation (lines).

4.5.2 Air-Metal Zone Center Band Gap

A similar analysis can be performed for the air-metal zone boundary of the $a_0 = 750$ nm array from Sec. (4.3.2). In Figure 4.21, experimental transmission spectra for two small angles of incidence ($\theta = 0.6°$(blue) and $\theta = 1°$(red)) are plotted in (a), the corresponding simulated transmission spectra in (b) for $h = 130$ nm, $b = 50$ nm. Qualitative agreement is found, i.e., the splitting into a narrow long-wavelength and a broad shorter-wavelength mode is reproduced, and the narrow SPP resonance wavelength of 766 nm is very accurately predicted. Clearly, the relative peak heights do not match up, as the dark resonance appears much weaker in the experimental spectrum (note the factor 10 magnification from the dotted line to the left in (a)). Furthermore, the bright resonance appears broader in the simulation than in the experiment.

The earlier analysis of this band gap in terms of simple coupled mode model failed to explain the rapid broadening of the dark resonance with an increase of the angle of incidence. Applying the Fano-lineshape fitting for the simulation, the predicted angle-dependent linewidths are determined for this band gap, and the results are plotted in Fig. 4.21(c) for the broad (green line) and narrow (black line) resonances, again contrasted with the experiment (circles). Although the agreement for neither resonance is quantitative, the strong variations in linewidth for the narrow mode and the weaker dependence for the broad mode are found. The overestimate of the broad resonance linewidth is systematic, and one can check if this varies as a function of the structural parameters.

In the case of the SM SPP resonance, a slit width and film thickness were found that satisfactorily accounted for the experimentally found linewidths and

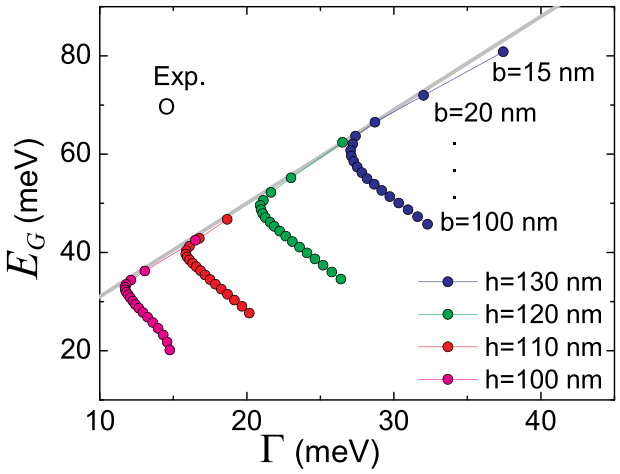

Figure 4.22: Dependence of the magnitude of the band gap E_G and the width of the bright AM SPP resonance on the slit width b and film thickness h. For very narrow slits, a linear relationship is approached (gray line), which yields a narrower resonance for a given band gap size than in the experiment (large black circle).

band gap parameters. At the air-metal interface, is has not been possible to find such geometrical parameters. Figure 4.22 shows the resulting energy splitting E_G and the width of the broad resonance Γ in the simulation for a sequence of film thicknesses and slit widths. A series of calculations has been performed, in which the slit width was varied in steps of 5 nm, starting at 15 nm and ending at 100 nm, i.e., definitely covering the actual structural slit width, and for four different film thicknesses from 100 nm to 130 nm. The experimentally found linewidth and the band gap splitting are shown as the black circle. It is evident that the simulation does not yield a band gap, which agrees with the experiment. Interestingly, for the somewhat larger slit widths, an increasing slit width not only results in stronger radiative damping, but also in smaller band gaps (portions of the lines going to the lower right). For very narrow slits ($b < 50$ nm), the gap increases along with the damping, and a linear relation is approached, which is approximated with the gray line as

$$E_G = 1.9\,\Gamma + 12\ \text{meV}. \tag{4.15}$$

The importance of the waveguide for the SPP band gap is apparent from the thickness dependence of both the linewidth and the band gap size.[18] Evidently, the experimentally found band gap is beyond the range predicted by the simulation. Specifically, the ratio between the separation of both resonances and the bright mode's damping is larger in the experiment, which leads to the fact that the apparent band gap is in a sense "wider" or "deeper" than in the simulation, and the finite spectral overlap between both resonances (or their interference) is reduced.[19] This may in fact be useful for nano-optic devices, and the reason for this observation

[18] It has been pointed out earlier that this dependence will be oscillatory for larger film thicknesses due to FP effects.

[19] The finite spectral overlap will be even more obvious in the near-field, where the Fano-type asymmetry is reduced [cf. Sec. (4.3.3)].

is very likely found in the rounded cross-section of the real structures, resulting in reduced scattering into the far-field compared with sharper edges [166]. Intuitively explained, the SPP excitations on the surface can bend into and out of the nanoslit waveguide more efficiently for rounded than for perfectly rectangular cross-sections. It appears that the influence of this modified SPP scattering on the imaginary part of the resonance frequencies (damping) is larger than on the real part of the band gap (mode splitting).

4.5.3 Concluding Remarks

In this chapter, the coherent couplings of surface plasmon polaritons in plasmonic nanostructures were studied using space- and time-resolved optical spectroscopy. Starting from the dynamical aspect of the light transmission, the radiative decay was found to be drastically modified near SPP band gaps. The formation of antisymmetric SPP modes gives rise to a pronounced suppression of radiative damping and leads to surprisingly long SPP lifetimes of more than 200 fs. Such a control of radiative damping by tailoring SPP mode profiles is an essential prerequisite for designing and implementing efficient nanoplasmonic devices such as wave guides or resonators.

The simple interpretation in terms of the Fano lineshape model has proven very useful to quantify band gap characteristics, allowing for a comparison between the experiments and theoretical simulations for idealized structures. Perhaps, more detailed simulations accounting for the non-rectangular cross-sections will help to answer remaining questions, for example concerning the large magnitude of the observed AM band gap, when compared with the linewidth of the bright mode.

On the other hand, the subradiant modes with lifetimes in the range of the intrinsic limits are indicative of the high quality of the investigated samples. Even small short- or long-range disorder would significantly deteriorate the values found [175]. A question which should be addressed is why the subradiant SPP lifetimes found appear to slightly exceed those expected for an unstructured metal surface, given the complex dielectric function of gold from standard tables. A recent experimental study on similar structures has confirmed the findings with lifetimes larger than 200 fs [176], and the authors of that work suggested a reduced mode-overlap of the dark SPP resonance with the metal to be responsible for the decreased absorptive damping. While this may be part of the answer, the very thin slits of the present structures do not indicate such large deviations of the antisymmetric mode from a standing SPP wave on a smooth film, and neither did the SIBC computations yield lifetimes much longer than those of an unstructured film.

In addition, it should be noted that the two most frequently used tables from

Refs. [109] and [103] differ among themselves by more than 30% concerning the imaginary part of the dielectric function, which directly translates into the scatter of predicted lifetimes. Both studies inferred upon the dielectric function from measurements of the transmission and reflection from thin gold films. Without going into the details of the particular evaluation procedures, it is obvious that multiple factors influence the results of such measurements of a metal's dielectric function.

The specific properties of a particular metal film, such as its exact thickness, surface quality, crystalline orientation or the grain size of a polycrystalline film will influence the result of a measurement of the dielectric function. Unavoidable surface roughness and a resulting excitation of surface plasmons will cause a modification (, typically but necessarily a reduction,) of both the transmission and the reflection of such a film. Scanning electron microscope and atomic force microscope images of the films used in the present study have displayed an extraordinarily small intrinsic surface roughness, pointing towards one explanation for the unexpectedly long SPP lifetimes found.

Furthermore, one has to keep in mind that using a wavevector-independent dielectric function is an approximation, which fails for very large fields gradients in the metal. While for SPPs on metal films, isotropic, k-independent dielectric functions are widely used, certain deviations from this approximation may already be present for the decay lengths on the order of 10 nm. Such questions are still largely unexplored in metal nanostructures, and would provide for a very interesting field of study.

The results presented here cover exclusively one-dimensional periodic slit structures, partly because of the noticeable lack of data from high-quality lamellar structures in the literature. We have, however, also performed experiments for square arrays of subwavelength holes [11], yielding quite similar results, in the sense that the Fano-picture, the associated SPP dynamics and the complex band gap formation displayed the same characteristics. The differences concerning the waveguides connecting both interfaces have already been mentioned.

The microscopic mode structure in the unit cell of the plasmonic crystal has been imaged by near-field spectroscopy, supplying a straightforward explanation for the observed subradiant damping suppression. It will be necessary to investigate, what is actually imaged in such experiments, i.e., which components of the electromagnetic field contribute to the near-field signal generated in a particular experimental setup. Chapter 5 is devoted to further experiments and analysis in view of these questions.

5 Near-Field Microscopy and Spectroscopy of Plasmonic Nanostructures

In the preceding chapter, the optical properties of the plasmonic crystals were studied in great detail by the use of phase-resolved far-field experiments and a broadband near-field microscope measurement. Transmission resonances were identified as surface plasmon polariton excitations on either side of the metallic film, and a direct physical connection between the far-field properties and the underlying near-field SPP mode structure was established.

Now, we can utilize our understanding of these structures to go on and learn more about the imaging of microscopic SPP field distributions. In near-field optical experiments, unresolved challenges concern the image formation process, in particular with respect to the contribution of different components of the vectorial near-field. In this chapter, these questions are addressed on the basis of measurements with several kinds of near-field probes. It is shown that the probe type and the detection conditions critically influence the resulting spatial and spectral image contrast.

The first two sections further motivate and describe the present experimental approach, and characteristic data for different near-field tips are summarized. The distance-dependent near-field spectroscopy developed here is shown to be a useful tool for the visualization of SPP surface modes and the fields propagating away from the surface.

Subsequent sections discuss and further analyze the experimental data, contrasting it with numerical simulations based on the SIBC method presented earlier. This allows for a discussion of the different field components contributing to the near-field contrast [Sec. (5.3)]. Specifically, it is shown that aperture collection imaging is sensitive to the in-plane magnetic field, while the apertureless scattering methods image several electric and magnetic field components. In the case of very sharp metal tips, the out-of-plane electric field can represent the dominant contribution.

The distance-dependent collection of local spectra in the half-space above the sample gives unique access to the study of the subtle effects stemming from tip-

sample interaction. The related observations and a discussion are contained in Sec. (5.4).

The final section of the chapter [Sec. (5.5)] introduces a novel form of near-field light source that makes use of the resonant SPP excitation on the shaft of a metallic tip.

5.1 Motivation

The inherent surface-bound nature of SPP excitations requires the methods of near-field optics for their immediate observation. Measurements of the electromagnetic fields associated with surface plasmon polaritons have been the subject of numerous near-field optical studies. In early experiments, the distance-dependent SPP decay [177] and lateral spatial distributions have been imaged on unpatterned metallic films [162, 178] excited in the Kretschmann geometry. Later, NSOM allowed for the imaging of SPPs excited in nanostructures [179], such as metal stripes [180] or other waveguide structures [181]. More recently, the spatial distributions of SPP resonances in periodic structures were imaged [13, 126, 127, 182].

Such a mapping of resonant modes in a plasmonic crystal yields important insights into the physics of these structures and supplies complementary information to far-field characterizations. For example, the imaging of spatial SPP damping in a periodic nanohole array has helped to identify radiative damping as the prime cause for line broadening in plasmonic crystals [13], and the imaging of Bloch modes in the previous chapter explained the suppression of radiative damping for the antisymmetric mode [127].

We have not yet discussed what the detected intensity in these experiments exactly represents. Obviously, the interpretation of the image contrast in NSOM experiments is as old as the technique itself [65, 66]. Of particular interest are the contributions of different electromagnetic field components to the image, i.e., problems related to near-field polarization. In the optical far-field, the polarization of transverse, propagating electromagnetic fields is easily determined by standard polarizer components. In the optical near-field, however, light scattering at nanoscopic objects introduces a strong mixing of both transverse and longitudinal fields, resulting in complex and spatially rapidly varying *local* electromagnetic field vectors. Consequently, in near-field optical experiments, the question which of the polarization components is actually measured has been the subject of a controversial and ongoing debate [89].

Theoretical studies suggest that different types of near-field probes should result in different image contrasts [87]. For example, collection mode images with uncoated dielectric probes are predicted to represent the intensity of the total elec-

tric field at the probe position [87, 183], and experimental measurements are usually interpreted in this way [162].

In the case of metal-coated probes, however, the situation is much more complicated. Specifically, we have mentioned in Sec. (2.2.7) that small apertures in metals are expected to detect both electric and magnetic fields [85–87]. However, even for metal-coated probes, the majority of near-field measurements, e.g., of SPP fields [126, 179, 182], are discussed in terms of the electric field alone, and the magnetic field is largely neglected.

Most near-field optical experiments do not allow for a straightforward determination of the field components entering the signal, which is particularly complicated in three-dimensional geometries. In comparison, for a number of reasons, the present nanostructures serve as well-defined model systems for the study of near-field contrasts under different imaging conditions. First of all, the reduced number of only three nonzero electromagnetic field components promises a significantly simplified interpretation. Secondly, the mode structure of these different field components is drastically distinct, e.g., the spatial intensity maxima and minima of the electric and magnetic fields are clearly shifted with respect to each other. Finally, also the local spectral content, measured in our broadband experiments, serves as a signature of different field components.

In the recent aperture collection experiments performed by Linden *et al.* [89], one-dimensional structures somewhat similar to ours have been investigated, in which also only two components of the electric and one component of the magnetic field were present. The authors state that theoretically, a contribution of the out-of-plane electric and in-plane magnetic fields is expected, following the Bethe argument [Sec. (2.2.7)]. They show numerical simulations for the in-plane electric and magnetic fields, stating better agreement of the measurements with the magnetic than the electric fields. However, no calculations are shown for the out-of-plane electric field, and no argument is given, why this strong component does not prominently appear in their experiments. As this in stark contrast to the Bethe-Bouwkamp prediction [85, 86] and other established theoretical works [87], these issues require further investigation.

5.2 Polarization Sensitive Near-Field Spectroscopy

For the purpose of studying SPP surface modes and the emergence of the NSOM contrast, a broadband scanning near-field microscope was developed that allows for near-field imaging at the surface or in close vicinity to the nanostructures [Sec. (2.2.5)]. A first result obtained with this instrument was shown in Sec. (4.3.3). In this chapter, we present spectrally resolved near-field measurements made either in tip-sample contact or in a distance-dependent imaging as

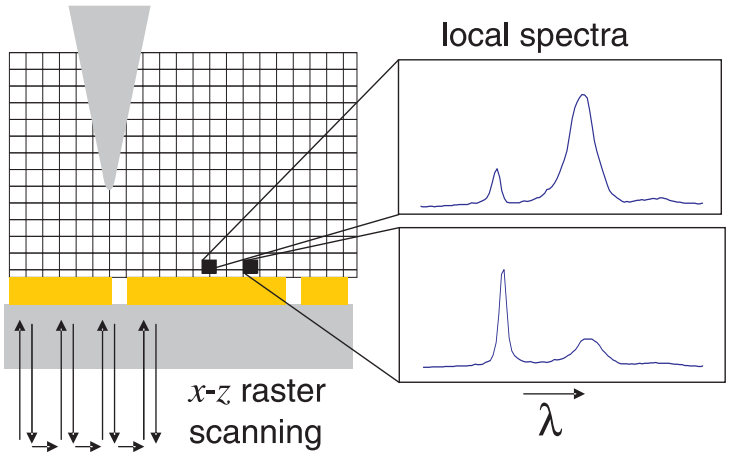

Figure 5.1: In the distance-dependent near-field spectroscopy, an optical spectrum is detected at every point on a grid in the x-z-plane perpendicular to the sample surface. The sample approaches the surface up to the point of tip-sample contact, then retracts and shifts laterally, before the next approach is made.

displayed in Fig. 5.1. In this mode, near-field spectra are measured in a two-dimensional plane perpendicular to the sample surface. Such experiments were performed with metal-coated fiber probes in aperture collection and in apertureless scattering mode, and with sharp electrochemically etched metal probes in apertureless scattering mode. We begin with the aperture collection imaging.

5.2.1 Aperture Collection Imaging

In Sec. (4.3.3), resonant surface modes in the periodic structures were observed. A simple near-field experiment illustrates the SPP character of these resonances. Collection of the near-field light through an aperture tip yields near-field images such as those shown in Fig. 5.2(a). Here, the near-field intensity in tip-sample contact is shown for an illumination from the substrate side with $\lambda = 810$ nm, and for an incident polarization with the electric field parallel (top) and perpendicular (bottom) to the slits, detected with an avalanche photodiode. In s-polarization (top), a stripe-like intensity distribution is found, with maxima at the slit positions. Switching to p-polarization results in the additional maxima in the center between the slits, which evidences the excitation of a standing surface wave, as also found in the apertureless scattering experiment discussed earlier [see Sec. (4.3.3)]. The upper half of this image was scaled up by a factor of about ten, as the absolute intensity in the s-polarized case is much weaker, just as for the far-field transmission. The spatially (in the y-direction) averaged sections are shown below the

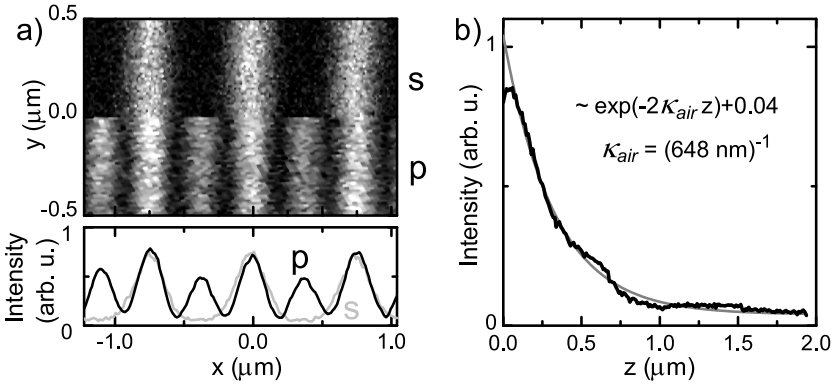

Figure 5.2: (a): Collection-mode near-field microscope images for illumination parallel (p) and perpendicular (s) to the slits. The absolute intensity of the upper half is scaled up by a factor of about ten. (b): Near-field intensity approach curve (black line) and expected decay for the SPP intensity on a smooth gold film ($\lambda = 810$ nm in both figures).

image as gray (s-pol.) and black (p-pol.) lines.[1]

An obvious question is if these spatial oscillations represent the intensity of the local electric field or of one of its components, and how they depend on the distance from the surface.

The former question will require a comparison with theoretical calculations, which will be performed in Sec. (5.3). The latter is answered by an experiment, where the distance-dependent intensity is collected through the fiber aperture, the result of which is plotted in Fig. 5.2(b). Here, the intensity at a lateral position between the slits is measured for distances from around 2 μm down to tip-sample contact ($z = 0$ nm). One finds a strongly increasing intensity, with a decay constant in very good agreement with the expected decay constant κ_{air} of an air-metal SPP at this optical frequency (gray curve). Thus, both the dependence on the incident polarization and the spatial decay are direct evidence for the SPP character of this surface wave. An only small offset is added to the exponential decay to account for the transmitted far-field light, further illustrating the strong enhancement of the fields at the surface. Weak oscillations in the experimental curve are mostly due to the interference between the evanescent SPP fields and the propagating components radiated away from the slits, and the slight saturation and drop right near $z = 0$ nm is likely due to a modification of the collection efficiency very close to the surface [see Sec. (5.4)].

[1] In order to detect the weak signals for s-polarization, a relatively large aperture had to be used, limiting the spatial resolution in this measurement to about 150 nm. For the collection mode data shown hereafter, apertures with diameters smaller than 100 nm and a liquid nitrogen cooled charge coupled device detector with lower noise level were used.

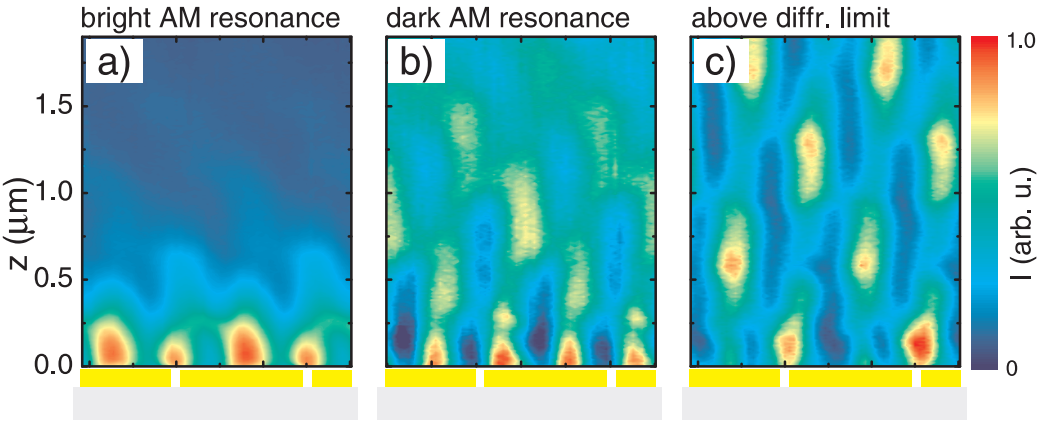

Figure 5.3: x-z-imaging of the nanoslit array for various wavelengths. (a): The bright SPP mode ($\lambda = 800$ nm, see Sec. (4.3.3) for terminology) appears as a standing wave localized to the surface, the maxima at the surface again appearing at the slit positions (indicated below the image) and in the center between the slits. (b): The dark mode ($\lambda = 766$ nm) shows some interferences in the far-field and has its maximum intensity between the slits at the sample surface. (c): At wavelengths shorter than the diffraction limit (here ~ 700 nm), strong interference pattern propagating into the half-space above the sample is observed.

It is clear that the structure and the near-field images are translationally invariant in the extruded (y-)dimension. Therefore, the electromagnetic field distributions are completely characterized by their variations in the cross-sectional x-z-plane perpendicular to the sample, measured in the scanning mode depicted in Fig. 5.1.

The essential spatial features of the resulting three-dimensional data set (intensity $I(x,z,\lambda)$) are illustrated by drawing sections at the characteristic resonance wavelengths of the structure. In Fig. 5.3, such images are shown for the wavelengths of the bright and dark SPP resonances, as well as for a wavelength of 700 nm, where three propagating far-field modes exist above the sample (700 nm $< a_0 = 750$ nm). The x-z-image for the bright SPP resonance (around $\lambda = 800$ nm) shown in Fig. 5.3(a) directly visualizes the surface-localized standing wave SPP mode with maxima at and in the center between the slits. For the dark mode wavelength [Fig. 5.3(b)], the intensity maxima at the surface are again found in-between the slits. Finally, for a wavelength around 700 nm [Fig. 5.3(c)], where a substrate-metal SPP resonance is expected from the far-field transmission experiments [cf. Fig. 4.9], the maxima are at the slits, with weak antinodes in-between the slits. While some interference oscillations are also found in the intermediate zone at somewhat larger distances in (a) and (b), this last image is

dominated by a strong interference pattern reaching into the far-zone above the sample. The slight tilt of this pattern, along with the small asymmetry in all images, is mostly due to the small but finite angle of incidence on the structure required for the excitation of the dark mode.[2]

By the use of symmetry arguments, the phase of the standing wave pattern for the bright SPP mode can already give a first hint towards the obtained image contrast. At exactly normal incidence,[3] the incoming plane wave, polarized along x, displays a sign change in the electric field upon inversion of this lateral coordinate, which must convert into the symmetry of the near-field modes as well. The inversion centers of the structure are the center of the slits and in the middle between the slits. Thus, any *out-of-plane* field components must have nodes and change sign at these inversion centers. The *in-plane* field components, however, do not have to be zero at the inversion centers, but should generally display a local extremum. In other words, the in-plane fields draw their sign change from the inversion of the in-plane direction of the local field vectors, while the out-of-plane component changes sign due its antisymmetric spatial mode. The symmetric shape of the measured pattern at the surface thus indicates that the out-of plane electric field does not strongly enter the near-field signal.

In Sec. (5.3), it will become clear that the above image contrast mainly stems from the in-plane magnetic field component. In the search for alternative image contrasts, we consider in the following the apertureless scattering mode.

5.2.2 Apertureless Scattering

The traditional collection mode aperture-based near-field imaging has a number of assets, making it a useful tool to study the near-field distributions at our plasmonic crystals. It offers a virtual absence of background light and a very reliable, reproducible imaging. However, the apertureless techniques often allow for higher spatial resolution, larger signal levels and easier access to a polarized detection of the near-field signal.

Al-Coated Fiber Tip

Although the intended use for the Al-coated fiber probes is collection mode imaging, these tips have turned out to also yield good apertureless scattering near-field images. Several factors are beneficial, for example, the high smoothness of the coating, resulting in low levels of background light scattered from the tip shaft.

[2] Some small additional tilt can be caused by an imperfect rectangular mounting of the sample on the scanner.

[3] Note that the dark mode vanishes at normal incidence. This is understood by the use of the similar symmetry arguments.

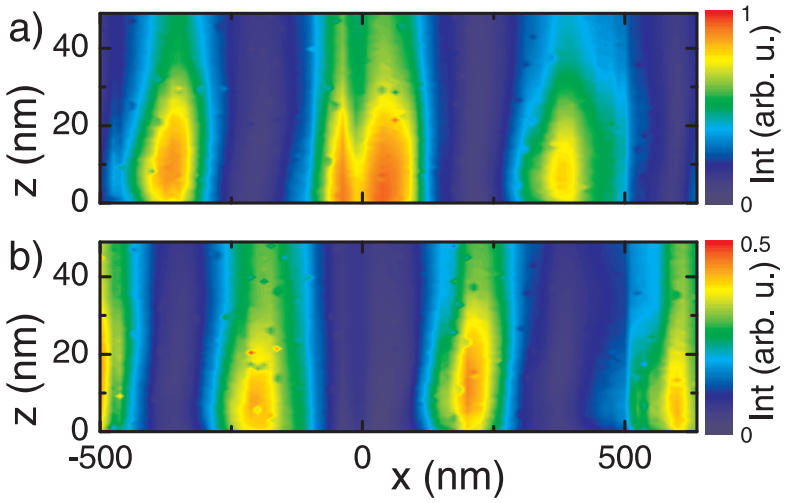

Figure 5.4: x-z-imaging for the bright (a) and dark (b) SPP resonances in close proximity to the sample, measured in the apertureless scattering mode. The smaller features at the lateral position of the slit ($x \approx 0$) extend somewhat into the space above the sample, demonstrating that they are not topographic artifacts. Note that the images are stretched in the vertical direction, and that the color codes are different, i.e., the absolute maximum intensity for the dark mode is about half that of the bright mode.

Moreover, their geometric size on the order of 50-200 nm in width yields a sizeable scattering cross-section. Furthermore, these tips are mechanically somewhat more robust than exceedingly sharp metal tips made from a more ductile metal, such as gold. Finally, the tips can also be used in apertureless mode, if, due to imperfect fabrication procedures, no aperture is present, i.e., when the tip is fully coated. In those cases, the tip end and its coating may be small enough to resolve finer details than the aperture collection, such as mode substructure with dimensions comparable to the slit width.

Specifically, the apertureless scattering experiment from Fig. 4.10 in Sec. (4.3.3) showed some finer structure at the slits, namely a very small dip for the bright mode around $\lambda = 800$ nm and a small peak at the dark mode ($\lambda = 766$ nm). The technique of scanning in the direction perpendicular to the sample can clarify, if such smaller details are due to a topographic artifact [64], or if they are true features of the optical fields. The images in Fig. 5.4 are close-up x-z-scans near the surface for the bright (a) and dark (b) modes. One clearly sees that the smaller features near the slit ($x \approx 0$) also appear in this representation, reaching into some distance from the sample. Thus, topographic artifacts can be ruled out for these images, which display a lateral spatial resolution of about 50 nm. Apparently, the spatial patterns measured in this scattering setup are

quite similar to those found in the aperture collection, namely a roughly $\cos^2(x)$ oscillation for the bright mode and a $\sin^2(x)$ oscillation for the dark mode.

In the experiments, we have found that these patterns acquired in apertureless scattering not only depend sensitively on the specifics of the sample illumination (angle of incidence, beam divergence, etc.), but also on the detection conditions. Specifically, by changing the azimuthal or polar angle of the collecting microscope objective with respect to the tip end, or by analyzing the polarization of the scattered light, different aspects of the near-field appear more prominently.[4]

The following experiment demonstrates that different spatial and spectral structures are obtained with polarized detection and for detection from a different observation angle. The near-field data shown in Fig. 5.5 were taken very close to normal incidence and with a collecting microscope objective at an azimuthal angle $\varphi = 90^\circ$ [same as the previous measurements in Figs. 4.10 and 5.4], i.e., placed along the slit direction, as drawn in Fig. 5.5(a). The polar angle β was, however, reduced from 50° [Figs. 4.10 and 5.4] to about 15°, with a numerical aperture of the collecting microscope of 0.4. The spatially averaged near-field spectra obtained for orientations of the polarization analyzer along the z- and x-directions[5] are plotted in Fig. 5.5(b) as the red and blue lines, respectively.

Both spectra contain the bright mode around 800 nm. The normal incidence results in the absence of the dark mode, except for a hardly discernible feature at 750 nm.[6] More importantly, a stark difference in the spectra is found on the long-wavelength side of the resonance, where the x-polarized spectrum displays a stronger tail. The spatially resolved spectral line scan [Fig. 5.5(c)] reveals that this tail is originating from the slit positions alone, and not from the regions between the slits. Furthermore, the oscillatory standing wave patterns in both images are shifted with respect to each other. For example, the measurement with z-polarized detection displays local minima at the slit positions ($x = 0$ nm), which is in stark contrast to all our previous measurements and suggests that a different field component may have been imaged here. These observations will be further analyzed in Sec. (5.3).

[4] Also, the numerical aperture of the microscope objective, i.e., the solid angle of the collected light, plays a role.

[5] Note the somewhat inclined positioning of the microscope objective, which is necessary to efficiently collect the scattered intensity. Therefore, the polarization analyzer is not exactly oriented along z.

[6] This data was taken from a sample with a slightly shorter lattice period ($a_0 \approx 735$ nm) and larger slit width ($b \approx 100$ nm), the optical properties of which were, however, similar to the 750 nm array, apart from a corresponding shift of the dark mode resonance wavelength and a larger broadening of the bright mode.

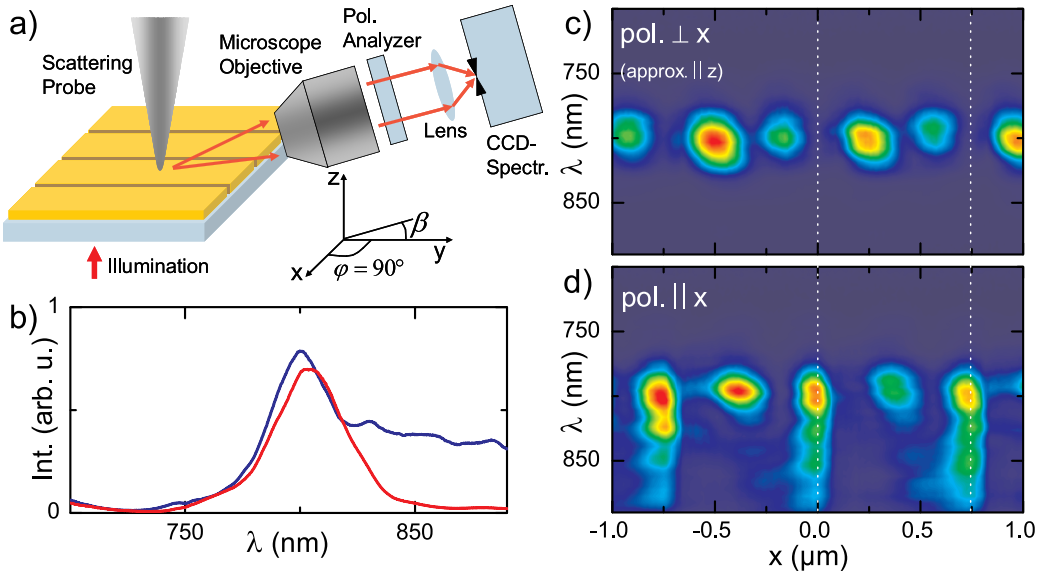

Figure 5.5: (a): Apertureless scattering spectroscopy experiment with polarization-resolved detection. The sample is oriented such that the light scattered roughly into the y-direction is collected by the microscope objective (azimuthal angle $\varphi = 90°$; polar angle β). (b): Spatially averaged near-field spectra for analyzer positions perpendicular (red) and parallel (blue) to the x-axis. The perpendicular polarization is close to parallel to the z-axis. (c)-(d): Corresponding spatially resolved line spectra for perpendicular (c) and parallel (d) polarization. The dotted white lines indicate slit positions.

Sharp Au Tip

The preceding paragraph demonstrated that the near-field scattered by a probe contains different polarization components. In general, the signal detected in the far-field will be a result of a transformation of the different field components present at the tip location into far-field patterns, which may be composed of different multipole contributions, depending on the probe geometry and the corresponding multipolar scattering efficiencies.

Very sharp metallic tips have been shown to allow for a selective imaging of longitudinal fields, for example by second harmonic generation in the focus of a laser beam [184, 185]. Due to the large on-axis polarizability of such nanotips, they effectively act as a nanoscopic polarizer, whose "extinction ratio" is determined by the local z-directional field enhancement. Gold tips are particularly suited for such purposes, as they have been shown to display plasmon resonances in their scattering cross-section [186].

We have performed several apertureless near-field scattering experiments with such sharp gold tips, investigating if the out-of-plane component of the electric

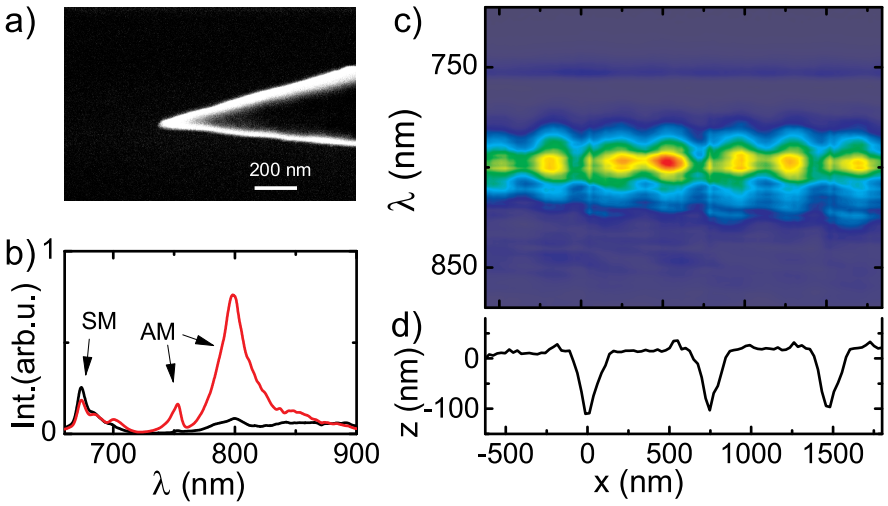

Figure 5.6: (a): Scanning electron microscope image of an electrochemically etched gold tip used for apertureless scattering near-field spectroscopy. (b): Spatially averaged near-field spectra obtained in contact (red) and at a distance of 1 micrometer (black), displaying a clear surface enhancement of those modes resonant on the air-metal interface. (c): Spatially resolved near-field spectral line scan on the surface. The intensity maxima of the bright mode are located between the slits, as can be seen by comparison with the surface topography in (d).

field in the plasmonic crystals can be imaged in this way. Such linear scattering experiments are complicated by background scattering from an often somewhat rough shaft of the electrochemically etched tips [187]. The selection of tips with smooth surfaces after scanning electron microscope characterization has proven to be necessary to reduce such effects.

Figure 5.6 presents an experimental result obtained with a gold tip with an apex diameter of about 30 nm [see Fig. 5.6(a)], measured in the same geometry as shown in Fig. 5.5. A spatially (along x) averaged near-field spectrum (red) is plotted in Fig. 5.6(b), together with a spatially averaged scattering spectrum taken at a tip-sample distance of about 1 μm (black). The spectrum measured in contact displays the bright and dark resonances much stronger than the $z = 1$ μm spectrum, thus proving the near-field sensitivity of the scattering of these AM SPP resonances. In contrast, the peak around 680 nm, corresponding to an SM SPP resonance of the SM[$\pm$1] anti-crossing, appears equally strong in both spectra.

A spatially resolved near-field spectrum in the wavelength range of the AM SPP resonances is displayed in Fig. 5.6(c). In contrast to some of the previous measurements, the antinodes of the bright resonance here both appear between the nanoslits, as can be seen by comparison with the topography shown in Fig. 5.6(d).

The observed modulation depth for both modes is, however, not as large as previously found, i.e., the intensity at the local minima is still about half of the intensity at the maxima. Nevertheless, it will be shown in Sec. (5.3) that the observed spatial structure evidences a significant contribution of $|E_z|^2$ in the scattered signal.

5.3 Discussion

The experimental data presented in the preceding section provided strong evidence that several components of the optical near-field can be imaged in the apertureless and aperture-based modes. Depending on the detection conditions and the probe used, different spatial and spectral structures were observed for essentially identical illumination conditions. In this section, the experiments are compared with theoretical computations using the SIBC method.

It will be shown that the aperture collection experiments are well-described with the intensity of the in-plane magnetic field alone. In contrast, a more complicated interference between different field components is found for apertureless scattering with these rounded tips. Finally, the enhanced axial polarizability of very sharp metal tips results in an imaging dominated by the out-of-plane electric field component.

5.3.1 Aperture Collection

We begin again with the aperture collection mode imaging. In Fig. 5.7, experimental distance-dependent measurements [(a)-(b)] are shown together with computations for the spatial distributions of the squared magnitudes of H_y[(c)-(d)], E_x[(e)-(f)] and E_z[(g)-(h)]. The three other components of the electromagnetic field are zero for the TM polarized case. Images are shown for two "signature" wavelengths, namely the bright AM SPP resonance wavelength with large mode intensity at the surface [(a),(c),(e),(g)], and an SM SPP resonance wavelength shorter than the diffraction limit [(b),(d),(f),(h)].

First, consider the AM SPP resonant mode. Almost equal intensity is experimentally found at the slit positions and in the center between the slits. This has been reproduced for a number of aperture tips, always yielding very similar results. The distance-dependent measurements show how the intensity pattern evolves away from the surface, namely laterally slightly asymmetric and axially oscillatory. Such behavior is also found for the magnetic field and for the in-plane electric field images [(c) and (e)], highlighted by the contour lines drawn for a value corresponding to the mean intensity at a distance of about 500 nm. However, while in the case of the magnetic field intensity, the amplitude at the surface is only slightly larger at than in-between the slits, the in-plane electric field inten-

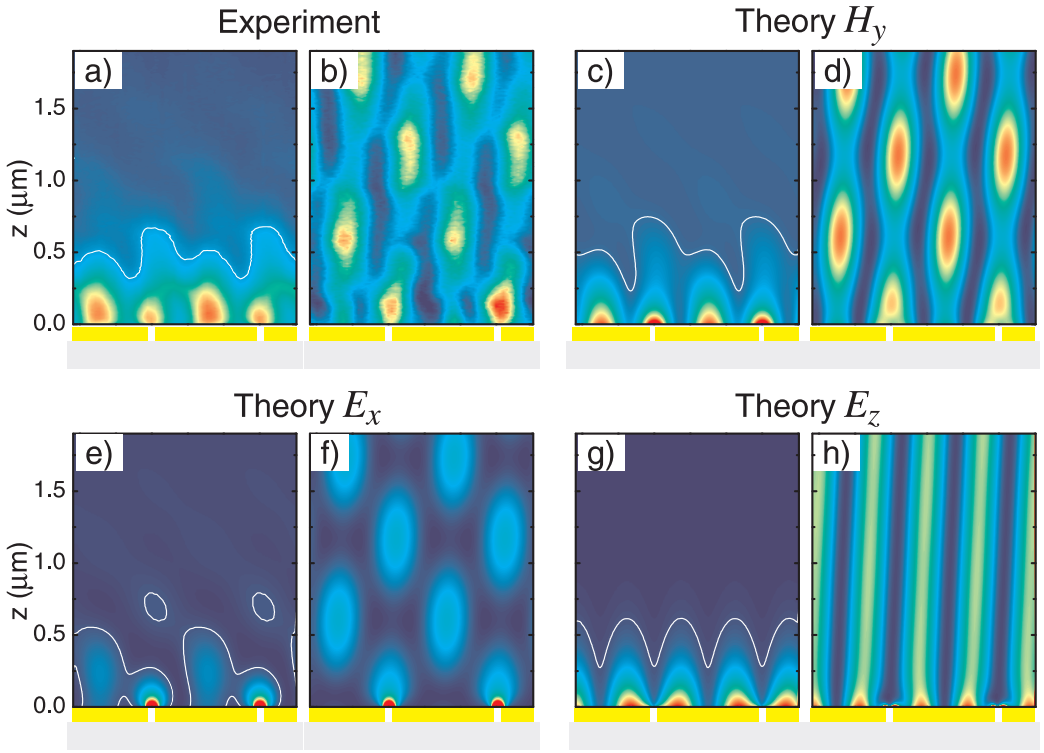

Figure 5.7: Comparison of the experimental x-z image for the bright SPP mode (a) and a wavelength shorter than the diffraction limit (b) with the corresponding results of the intensity distributions (magnitude squares) calculated from the modal expansion method for the magnetic field along the y-direction [(c) and (d)], and the electric field parallel [(e) and (f)] and perpendicular to the surface [(g) and (h)].

sity is actually about a factor of 10 stronger at the slits than in the center between the slits, so that the depicted color scale had to be saturated in order for the image not to be completely dominated by the intensity at the slits. It is clear that the low intensity between the slits results from the small in-plane fields of SPPs [see Sec. (3.1.1)].

In contrast, the out of plane electric field intensity $|E_z|^2$ in Fig. 5.7(g) is quite symmetric, and it neither displays maxima at the slits, nor does the image above the surface show an asymmetry or a similar z-dependent oscillatory behavior as the other two components. This is due to the only very weak out-of-plane component of the zeroth diffraction order at such a small angle of incidence.

Therefore, drastic deviations from the experiment are found in the spatial intensity distributions for both the in- and out-of-plane components of the electric fields. Perhaps surprisingly, a much better correspondence with the squared mag-

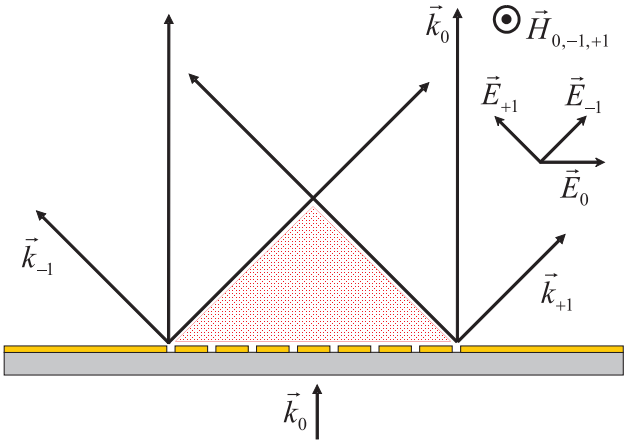

Figure 5.8: Interference of diffracted orders in the shaded area above the grating and for a wavelength, at which the zeroth and first diffraction orders are present. The out-of plane electric field is only significant for the $n = \pm 1$ diffraction orders, while contributions from all three orders are relevant for both the magnetic field and the in-plane electric field.

netic field is found. Some noticeable discrepancy of the experiment from the magnetic field calculation lies in the stronger increase of the theoretical image close to the surface. This is a result of a distance-dependent collection efficiency, which we have found also for SPPs traveling on an unstructured metal film, and which will be addressed in Sec. (5.4).

The shorter wavelength images [(b),(d),(f),(h)] represent further evidence for the interpretation in terms of a magnetic field imaging. Close to the surface, the experimental image displays maxima at the slits and weaker maxima in-between the slits, just as the magnetic field image. The in-plane electric field image is again dominated by the intensity close to the slits. Away from the surface, an oscillatory interference pattern in the x- and z-directions is found for both the magnetic as well as the in-plane electric field images. However, the difference between the $|H_y|^2$ and $|E_x|^2$ images lies in the fact that the former [(d)] has a more stripe-like form than the latter [(f)], which is almost fully modulated along the z-direction. Again, the $|E_z|^2$ image is very different from the experiment, characterized by two equal maxima between the slits at the surface and a homogeneous stripe-shaped pattern away from the surface.

These three patterns are easily explained in terms of the relevant diffraction orders and their field components, as sketched in Fig. 5.8. For near-normal illumination, the zeroth transmitted order has only a very weak E_z component, so that the $|E_z|^2$ pattern imaged in the shaded area corresponds to a *two-wave* interference, resulting in a stripe-shaped pattern. On the other hand, the in-plane fields

H_y and E_x have are present in all three diffraction orders, leading to a *three-wave* interference above the grating, characterized by an oscillatory behavior in both the x- and z-directions.

The additional difference between the $|H_y|^2$ and $|E_x|^2$ images in the modulation depth along z stems from the different magnitudes of the $n = \pm 1$ and $n = 0$ for both fields, i.e., the fact that H_y is equally large for all three orders, while E_x is weaker in $n = \pm 1$ than in $n = 0$. The absence of a second local maximum at the surface for the E_x field becomes also clear by considering the diffraction from a single slit.

It has been stated before [Sec. (2.2.7)] that an effective magnetic dipole moment can be associated with an aperture in a metallic sheet, thus explaining why the near-field collection mode images contain a $|H_y|$ contribution. However, the question arises why the dominant electric field component, i.e. the out-of-plane field E_z, appears not to be efficiently imaged in collection mode, although it is quite significant for SPPs. One reason is that the electric field emitted from the aperture in a plane sheet is indeed expected to be stronger from the magnetic than the electric dipole [Sec. (2.2.7)]. For conical geometries, theoretical works have calculated the near-field [188] and far-field [189] distributions of the transmission, and the collection of both electric and magnetic field components has been proposed [87]. An experimental study has verified that the fields radiated from an aperture tip can be decomposed to a good approximation into magnetic and electric dipole contributions [190], although the electric dipole was found to be oriented *in the plane* of the aperture, contrary to Bethe's prediction for the plane sheet aperture, and indicating a reduced importance of the out-of-plane electric field.

Another explanation for the absence of E_z lies in the axial symmetry of the tip and the properties of the collecting fiber. The present experiments have been carried out with a single-mode fiber [see Sec. (2.2.4)]. The single-mode property of this fiber can lead to an efficient suppression of the collection of axial fields, an argument previously made in a theoretical work by Bozhevolnyi [191]. Figure 5.9 gives a schematic depiction of the excitation of the transverse fiber waveguide mode from out-of-plane dipoles $\mathbf{p}_1, \mathbf{p}_2$ induced symmetrically around the aperture by the sample field E_z. In the waveguide, the fields necessarily destructively interfere in the symmetric TEM00 fiber mode, thus suppressing the collection of E_z. For non-perfect symmetry of the experiment, E_z collection may no longer be forbidden [191], but rather reduced.

The situation certainly changes, if a lateral gradient is present for the field across the distance dx. In this case, a signal proportional to $\mathbf{p}_2 - \mathbf{p}_1$, or $dx(\partial_x E_z)$ for a small dx, is expected. It is notable that this derivative is part of the expression for H_y, highlighting how an effective magnetic dipole can arise from a geometrical

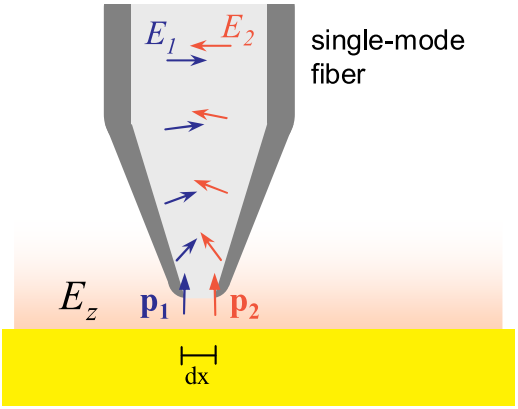

Figure 5.9: Schematic depiction of the fields coupled into a single mode fiber at a probe aperture. For perfect cylindrical symmetry of the fiber and the aperture, excitation of the fiber mode is forbidden for an out-of-plane local excitation field E_z. This is exemplified from the destructive interference of the mode amplitudes E_1 and E_2 generated from the two dipoles $\mathbf{p}_1$ and $\mathbf{p}_2$, respectively.

arrangement of non-magnetic, electric dipoles.[7]

In summary, the present experiments inevitably point to an imaging dominated by the in-plane magnetic field in aperture collection mode in these structures, supported by theoretical considerations. Nevertheless, this conclusion may come as a surprise, given the scarce discussion of the optical magnetic component in the experimental literature on near-field microscopy. With few exceptions, e.g., Refs. [88, 89], near-field experiments are mostly discussed in terms of the electric fields alone, perhaps due to their quantitative dominance over the magnetic field in many near-fields, e.g., for localized plasmon resonances [192]. In the case of delocalized polariton modes, however, this is not necessarily the case [see Sec. (3.1.1)]. Some readers may still feel uncomfortable with a term such as optical "magnetic field imaging". Equivalently, we could call it imaging the curl of the electric field [cf. Sec. (2.2.7)], which would stress the fact that it is based on the permittivity rather than the permeability of the probe material. One should keep in mind that non-magnetic materials are frequently associated with effective magnetic properties, quite prominently in the rapidly emerging field of optical metamaterials [193].

[7] A complete magnetic dipole along y would be equivalent to an infinitesimally small square arrangement of four electric dipoles oriented in a way forming a small loop. This also becomes clear when considering that the optical magnetic dipole can be visualized as a small alternating loop current, while the electric dipoles represent oscillating linear currents.

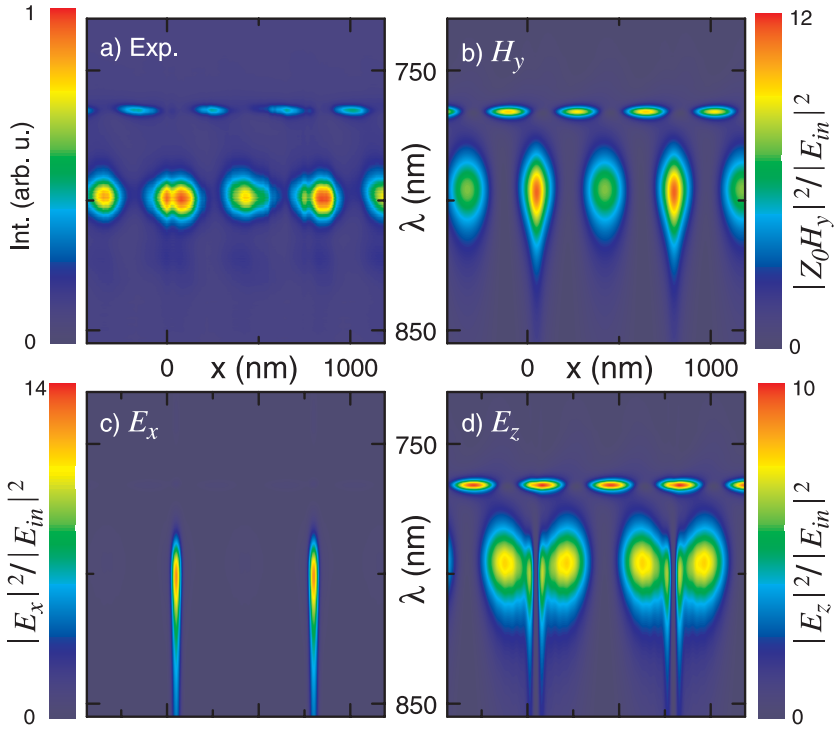

Figure 5.10: Spatially resolved near-field spectra in the experiment (a) and simulated images for the squared magnitudes of the H_y (b), E_x (c) and E_z (d). The color scales are normalized to the square of the electric field amplitude E_{in} incident on the substrate side. ($a_0 = 750$ nm, $b = 50$ nm, $h = 130$ nm, intensities evaluated at a distance of $z = 10$ nm.)

5.3.2 Apertureless Scattering

The apertureless scattering experiments are shown to yield several near-field components. The different contributions are discussed on the basis of the numerical calculations, beginning with the coated fiber tips.

Al-Coated Fiber Tip

A spatially resolved scattering spectrum [see Sec. (4.3.3)], measured in tip-sample contact, is shown in Fig. 5.10(a), together with the squared magnitudes of the three non-zero field components H_y (b), E_x (c) and E_z (d), calculated for a distance of 10 nm from the surface and an angle of incidence $\theta = 0.5°$. As expected, the SPP Bloch modes appear most prominently in the fields H_y and E_z, while the in-plane electric field is strongly confined to the slit regions. The actual linewidth of the simulated broad resonance is larger than in the experiment, very likely originating from the non-rectangular cross-section of the real structure [cf. Sec. (4.5.2)]. The

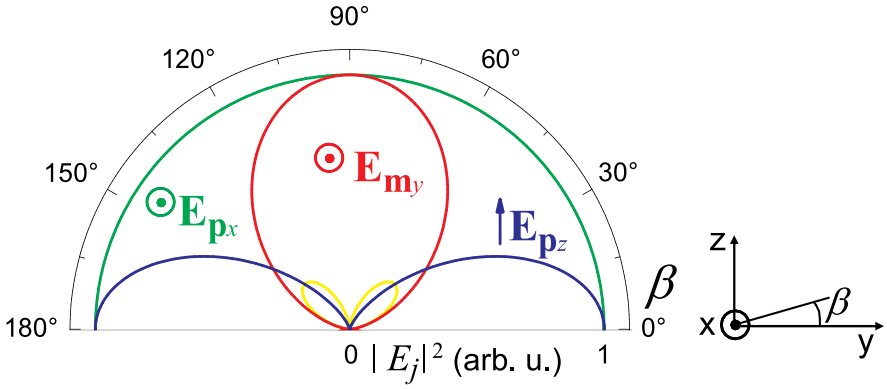

Figure 5.11: Polar plot of the radiated intensity from the magnetic and electric dipoles and corresponding polarizations of the electric far-field.

phase of the experimental standing wave pattern matches the H_y intensity well, although the dips at the slit positions for the bright mode are not contained in this field. The E_z mode does show a dip at the slits, but is almost zero in the center between the slits, in obvious disagreement with the experiment.[8]

Apparently, this apertureless scattering experiment reflects more than one vector component of the optical near-field. The dominant component is given by H_y, but limited contributions of the other fields need to be considered to account for the data. Most generally, a composition of the signal detected in the far-field will contain both interfering and non-interfering terms, depending on the polarization and angular dependence of the scattered fields.

In the point dipole approximation, electric and magnetic dipole moments $\mathbf{p}_x$, $\mathbf{p}_z$ and $\mathbf{m}_y$ are induced in the probe, which radiate into the far-field corresponding to the angular and polarization characteristics of their respective orientations [see Sec. (2.2.1)]. For the detection with $\varphi = 90°$, the electric field vectors in the far-field of these dipoles scale as

$$\mathbf{E}_{\mathbf{p}_x} \propto \hat{\mathbf{x}}\,, \quad \mathbf{E}_{\mathbf{p}_z} \propto -\hat{\mathbf{y}}\sin\beta\cos\beta + \hat{\mathbf{z}}\cos^2\beta\,, \quad \mathbf{E}_{\mathbf{m}_y} \propto -\hat{\mathbf{x}}\sin\beta. \tag{5.1}$$

The magnitude squares of these dependencies are indicated in the polar plot of Fig. 5.11, together with the polarizations of the electric fields far from the dipoles. Whereas the fields from both the magnetic dipole (red) and the in-plane electric dipole (green) are completely oriented in the x-direction, the field from the out-of plane dipole (blue) is mostly oriented along z, the small y-polarized component shown as the yellow line. Furthermore, the $\cos^4\beta$ dependence of the intensity from the out-of-plane dipole results in a stronger directionality of its radiation (into the y-direction) than the z-directed radiation from $\mathbf{m}_y$.

[8] Also remember that these dips are not a topographic artifact [see Fig. 5.4].

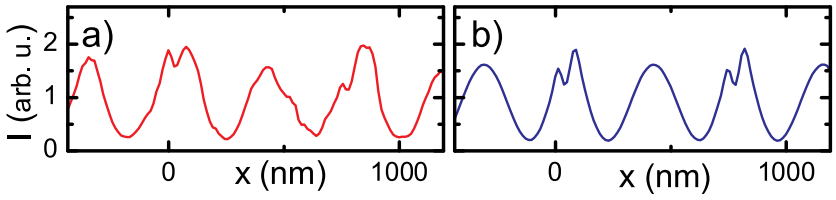

Figure 5.12: (a): Scattered near-field intensity of the bright mode. (b): Composition of different simulated field components (see text).

These considerations show that the fields from $\mathbf{p}_x$ and $\mathbf{m}_y$ interfere with each other in the far zone, i.e., on the detector, while that from $\mathbf{p}_z$ does not interfere with the other two fields. It should be noted that the 0.4 numerical aperture corresponds to an acceptance halfangle of the microscope objective of 24°, so that a significant range of (both polar and azimuthal) emission angles contributes to the signal. Nevertheless, at the polar angle of $\beta = 50°$, the contribution from $\mathbf{p}_z$ is expected to be smaller than at $\beta = 15°$, and the polarization properties of the fields vary only slowly over the collection solid angles.

The contributions from the three different dipoles are estimated by comparison of the experimental intensity profiles with a combination of the three simulated field components. Figure 5.12 shows the experimental intensity trace of the bright mode $\lambda = 800$ nm (a) and a composition of the simulated fields (b) at this wavelength of the form

$$I(x) = |Z_0 H_y + aE_x + bE_z|^2 + |fE_z|^2 \tag{5.2}$$

with $a = f = 0.3$ and $b = -0.05$. Since the different field components have such characteristic spatial dependencies, an almost one-to-one correspondence exists between the more subtle features of the near-field trace and the coefficients of the summation, allowing us to break it apart as follows: H_y appears as the major contribution. The addition of $0.3E_x$ results in the small dip at the slits due to destructive interference. The very small coherent addition of $-0.05E_z$, likely due to some polarization rotation in the scattering, is responsible for the small (shifted) asymmetry of the standing wave pattern to the right, which can only be reproduced via a coherent mixing of the antisymmetric E_z with the other two inversion symmetric fields.[9] The incoherent contribution of $|0.3E_z|^2$ leads to the small deviation from full modulation in the standing wave. This last term could in principle also be a result of the finite spatial extension of the probe. However, the high spatial resolution near the slits renders this unlikely. Taking into account the polar

[9]Even for these small non-zero angles of incidence, two in-plane field patterns are quite symmetric.

detection angle, the probe's electric (α_j) and magnetic (μ_y)[10] polarizabilities can be expressed relative to α_x in a dimensionless form:

$$\alpha_z/\alpha_x \simeq \frac{f}{a\cos^2\beta} \approx 2.4, \tag{5.3}$$

$$\mu_y\varepsilon_0/\alpha_x = \frac{1}{a\sin\beta} \approx 4.4. \tag{5.4}$$

Here, α_x has been chosen as the reference, as it theoretically does not depend on the polar angle. The small b value (neglected in the above evaluation) is a cross-term corresponding to some polarization mixing. These values should be viewed more as estimates rather than precisely determined values, both because we have not integrated over the solid angle accepted by the objective, which could certainly be done, but more importantly, because a more exact extraction of a, b and f would require a more exact periodicity of the measured intensity trace. In any case, the analysis suggests that the magnetic field sensitivity in this imaging mode is still significant.

The reduction of the polar detection angle enhances the contribution of E_z and decreases that of H_y in the scattered intensity, as visualized in Fig. 5.11. Furthermore, polarization selection in the far-field pronounces different field components. Such behavior was observed in the measurements at a small polar angle $\beta = 15°$,[11] as is evident from a consultation of both the spectral and spatial features shown in Fig. 5.13.

First, consider the tail on the long wavelength side in the spatially averaged near-field spectrum for polarized detection, Fig. 5.13(a). This tail is only present for an analyzer orientation parallel to the x-direction (blue curve), which is expected to select the emission from the in-plane electric dipole $\mathbf{p}_x$ [cf. Fig. 5.11]. Figure 5.13(b) shows the spatially averaged near-field spectra for the different squared field components $|E_x|^2$(blue), $|H_y|^2$(green) and $|E_z|^2$(red). Indeed, the in-plane electric field displays a much stronger long wavelength tail to the resonance compared with the other two field components, and it is localized at the nanoslit waveguides [cf. Figs. 5.10 and 5.5].[12]

Besides the E_x component, H_y significantly contributes to the measured spatial intensity. In the curve plotted in Fig. 5.13(c), E_x is responsible for the strong intensity at the slit positions, and H_y results in the standing wave pattern with antinodes in the center between the slits (indicated by the shaded stripes). The relative

[10]The magnetic polarizability is defined as the constant of proportionality between the magnetic dipole moment and the magnetic field, $\mathbf{m}_y = \hat{\mathbf{y}}\mu_y H_y$.

[11]These measurements were performed with a different tip from the same batch, within which usually quite similar results were obtained.

[12]It has been discussed before that the actual linewidth and resonance wavelength cannot both be matched with a single set of structure parameters [Sec. (4.5.2)].

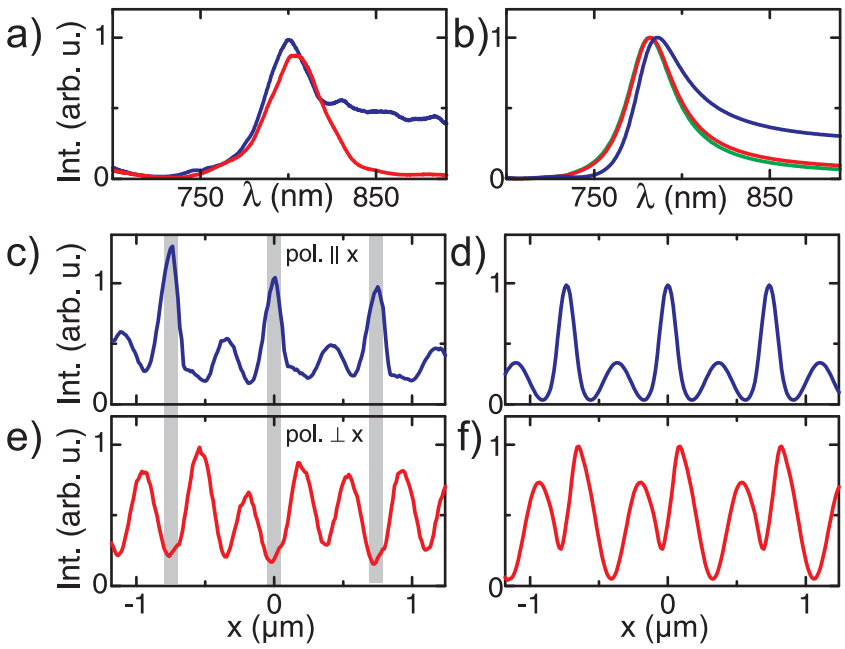

Figure 5.13: Spectral and spatial behavior in apertureless scattering from an aluminum coated fiber tip under polarized detection. (a): Spatially averaged near-field spectra for analyzer orientations parallel (blue) and perpendicular (red) to the x-axis. (b): Simulated spatially averaged spectra for $|E_x|^2$(blue), $|H_y|^2$(green) and $|E_z|^2$(red). (c): Spatial intensity trace for parallel polarization ($\lambda = 815$ nm). (d): Squared linear combination of E_x and H_y (see text). (e): Spatial intensity trace for perpendicular polarization ($\lambda = 795$ nm), i.e., the polarization close to parallel to z. (f): Squared linear combination of E_z and H_y (see text).

contributions are quantified from the superposition shown in Fig. 5.13(d), namely $|Z_0 H_y - E_x|^2$.[13] The theoretical traces were spatially averaged over a 50 nm width to account for the finite resolution in the experiment.

In the case of out-of-plane orientation of the polarization analyzer [Fig. 5.13(e)], the standing wave pattern is spatially shifted, with two antinodes between the slits and local minima in the center between the slits, being an important signature of E_z for the bright SPP mode. The superposition approximately describing this trace is $|Z_0 H_y - 3E_z|^2$ [Fig. 5.13(f)], where E_z is dominant, and H_y is responsible for the small asymmetry of the curve. This interference with H_y,

[13] It is yet unresolved, why this measurement shows an enhancement of the signal at the apertures from the interference of both components, while a reduction was found before [see Fig. 5.10]. Very likely, the particular tip geometry and its spectral response influence the relative phase of the different waves scattered at the probe.

pointing to noticeable polarization rotation, is not contained in the simple dipole model [Fig. 5.11].

Hence, further studies will have to resolve in more detail how the probe geometry influences the specific scattering efficiencies, and how important higher probe multipoles are for the image formation due to scattering at coated fiber tips. In addition, the local polarization mixing is not unambiguously quantified from the present experiments. Nevertheless, let us recall the encouraging qualitative features found for this measurement at a smaller polar angle, namely an increased signature of E_x relative to H_y in the expected horizontal polarization, and an increased signature of E_z in the vertical polarization.

Sharp Au Tip

For a sharp gold tip, a local out-of plane electrical polarization selection is expected to be "built into" the transfer matrix relating the near-field with intensity in the far-field. These experiments were not covered in such great detail, in part because such measurements have more often been impaired by background scattering from the tip shaft. Nonetheless, near-field sensitivity was demonstrated also for the scattering of SPP modes with these probes [see Fig. 5.6(b)], and the phase of the standing wave pattern obtained for the bright mode (two antinodes between slits in Fig. 5.6(b)) is indicative of $|E_z|^2$, as in the z-polarized detection with the coated fibers. Unfortunately, the quite weak modulation depth suggests some incoherent contribution (up to about 30 per cent) from the other field components, as well. Polarization-analyzed measurements are expected to suppress these contributions, but such experiments have not yet been performed.

A further indication for an imaging of the out-of-plane electric field with such tips is obtained from a distance-dependent imaging experiment. Figure 5.14(a) displays a color-coded image of the intensity recorded in an x-z-image above the surface for a wavelength around 700 nm, exciting an SM transmission resonance [cf. Fig 5.6(b)]. In contrast to the respective aperture collection image, Fig. 5.7(b), this stripe-like image reflects a two-wave interfere pattern. Such a two-wave interference is predicted only for the out of-plane electric field, due to the first ($n = \pm 1$) diffraction orders interfering in the far-field [see Fig. 5.8]. One should, however, be careful not to over-interpret this particular result, as also other effects, such as a wavevector-dependent scattering efficiency, could in principle result in such a two-wave interference. At this stage, it appears that a selective E_z imaging is possible also in a linear elastic, i.e., frequency-preserving, scattering experiment from sharp gold tips. Nonetheless, nonlinear experiments involving, for example, frequency conversion at the tip-apex may be better suited to suppress background light and obtain a higher localization of the signal to the tip apex [184, 185, 194–196].

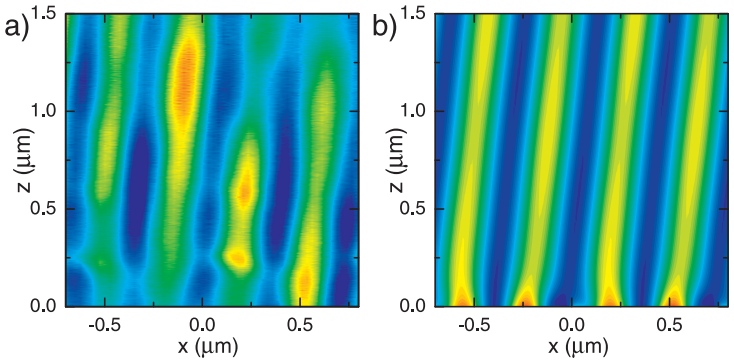

Figure 5.14: (a): Distance-dependent scattered intensity from a sharp gold tip, measured at a wavelength of 700 nm, shorter than the diffraction limit for the first diffraction orders. (b): Simulated intensity of the out-of-plane electric field, $|E_z|^2$ [cf. Figs. 5.7(d) and (f) for $|H_y|^2$ and $|E_x|^2$, respectively].

5.3.3 Concluding Remarks

In this section, we have identified different electromagnetic field components close to the plasmonic crystals in measurements using different types of near-field optical probes and detection conditions. A tabulated summary of the most important field components found in the different experiments is given in Fig. 5.15. In particular, the aperture collection measurements constitute an imaging clearly dominated by the component of the magnetic field in the y-direction, justified by the Bethe-Bouwkamp argument and symmetry considerations. In the scattering from very sharp gold tips, mostly the out-of-plane electric field was observed, stemming from the large linear susceptibility along the tip axis.

A contrast resulting from a mixed contribution of both magnetic and electric fields was found in the scattering from the aperture tips. Here, the contrast depends sensitively on the detection conditions, i.e., the choice of polarization and the polar detection angle. In particular, the experiments indicate that E_z detection is mostly possible for observation orientations close to the sample plane, while for larger polar angles, emission from H_y appears more pronounced. Significant polarization rotation from these tips has also been found, and contrary to the aperture collection imaging, these results were somewhat more specific to a particular probe geometry. Postprocessing of the tips, e.g., by focused ion beam milling, could improve the selectivity of particular field components.

So far, we have not conducted a systematic near-field spectroscopic study of the dependence on the azimuthal detection angle, which should be equally important. These first results disclose both possibilities and complications in the interpretation in terms of interfering local electromagnetic field components.

probe type→ ↓configuration	sharp Au tip	Al-coated fiber tip
apertureless scattering	$\sim \|E_z\|^2$ significant background	$\sim \|aH_y + bE_x\|^2$ for $pol.\|x$ $\sim \|cH_y + dE_z\|^2$ for $pol.\|z$ $a,b,c,d = f(\beta,\varphi)$
aperture collection	N.A.	$\sim \|H_y\|^2$ low background

Figure 5.15: Tabular summary of the field components observed for sharp gold tips and Al-coated fiber tips under different detection conditions.

The reduced dimensionality of the sample system has greatly simplified the interpretation, downsizing the problem to three independent field components with characteristic spatial and spectral dependencies. In a fully three-dimensional system, the greater overlap (or similarity) of the spatial variations from different field components, together with the polarization mixing already encountered here, presents a quite complicated task for the future.

Within similar geometries, a recent study carried out at Seoul National University has further pursued the possibility of local polarization-selective imaging for monochromatic fields, leading to a joint publication with Prof. Dai-Sik Kim's group [49]. In those experiments, standing wave patterns on flat dielectric and metallic surfaces are imaged by the same means of apertureless scattering. Moreover, the scattered intensity is detected for a large sequence of polarization analyzer orientations, thus resulting in polar plots of the scattered intensity. In this way, a more precise determination of the polarization rotation induced by the probe becomes possible, and the scattered signal can be normalized with respect to a previous far-field tip characterization [74]. This work allows for a reconstruction of the essential components of a generally elliptical local optical polarization state, namely its degree of ellipticity and the orientation of its major axes.[14]

Further developments, potentially making use of several detectors oriented in different directions, may some day result in a full three-dimensional and quantitative determination of the local vectorial electromagnetic field near nanostructures. In order to achieve this, more has yet to be learned on tip-sample interactions and the effects they have on the imaging of a given near-field. The near-field spectroscopic techniques developed here represent a unique handle on the study of such interactions, which appear prominently in the spatial variations of near-field spectra, as discussed in the following section.

[14] A more in-depth coverage of this study is beyond the scope of this thesis, and the reader is referred to Ref. [49] for further details.

5.4 Resonance Shifts and Tip-Sample Couplings

Electromagnetic coupling phenomena on the nanometer scale are of considerable interest, both from a fundamental physics point of view, and in light of the intended functionality of future nano-photonic devices. Currently, diligent studies increasingly focus on a tailored modification of the radiation properties of individual emitters or microscopic resonators. For instance, reports have shown that by changing the dielectric environment of single molecules and metal nanoparticles [197–199], or semiconductor quantum dots [51], their radiative lifetimes and quantum efficiencies can be strongly altered in a controlled way. A new form of near-field microscopy has been demonstrated, which is based on spectral modifications of a nanoparticle resonance [48].

Concerning the nanoscale electromagnetic coupling to resonators, theoretical works suggest the possibility of substantial control of microcavity resonances with near-field probes [200]. Experimental studies have achieved a probe-controlled modification of the quality factor of whispering gallery modes in a dielectric microsphere [201]. Very recently, tip-induced perturbations to the lasing properties of such resonators were discovered [202].

In the case of metallic systems, some experimental works investigated near-field spectroscopy of single metal nanoparticles [203–205] or resonant periodic structures [89, 127]. However, no systematic studies of tip-sample coupling effects in such systems exist that could shed light on the interaction of a local probe with delocalized surface plasmon polariton modes. Recently, a significant spectral red-shift of a near-field resonance was reported upon the approach of a metal-coated fiber tip [89]. In that experiment, the probe ended in a relatively large flat area of a size larger the unit cell of the periodic structure. The authors have simulated the presence of the probe by adding in their calculations a plane metallic sheet close to the sample surface, reproducing some spectral shift.

Up to this point, the influence of the scanning probe on the states or resonances of our sample system has not been discussed, and it is clear that the supposition of a non-invasive imaging is only an approximation, which can, however, be a very good one. This section focuses in more detail on spectral variations in the near-field microscopic experiments, and it is analyzed which effects are related to tip-sample interactions and which are not.

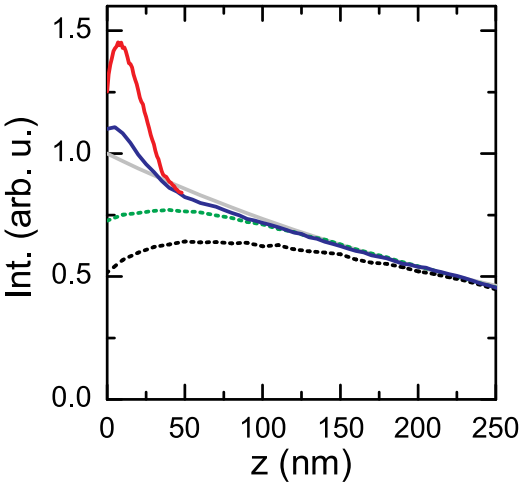

Figure 5.16: Distance-dependent near-field signal for different tips and imaging modes at a lateral position between slits and a wavelength of 800 nm. Solid: Apertureless scattering with Al-coated fiber tips. Dotted lines: Aperture collection. For comparison, the exponential SPP decay for this wavelength is plotted as the gray line.

5.4.1 Observations

Intensity Changes

One of the most apparent alterations of the measured data from the theoretically computed fields in the absence of a probe has been briefly mentioned before, namely the non-exponential distance-dependent intensity very close to the sample. Specifically, while the theoretical calculations predict an exponential rise of the SPP intensity all the way down to $z = 0$ nm, the measured near-field intensity in some cases increases stronger, or saturates and eventually drops close to the sample. The particular distance-dependent near-field signal varies among probes and with the employed imaging conditions. Figure 5.16 shows some approach curves at a wavelength of 800 nm (AM SPP resonance) and for four different Al-coated fiber tips, used either for apertureless scattering (solid) or by collecting the near-field intensity through the aperture (dotted). Deviations from a single SPP exponential (gray) are found to a varying degree for all tips. In the scattering, additional enhancement, followed by a drop very close to the sample is found, while the aperture collection traces always stay below the exponential. The downward deviation of the collected SPP intensity from the theoretical curve was reported already in one of the early near-field studies of surface plasmons [178], where it was identified as significant frustration of the near-field, if the tip is very close to the sample.

Spectral Modifications

Such a monochromatic measurement cannot distinguish, if a given intensity change is a result of resonance shifts, line broadenings or a uniform amplitude modification of the entire spectrum. Thus, distance-dependent near-field spec-

troscopy yields substantially more information. In close proximity to the sample, all such spectral changes have been observed in the experiments. Qualitatively similar modifications to the local near-field spectra are observed for different probes, the magnitudes of which, however, are specific to a particular tip. Generally, it should be noted that the spectral shifts we observe for the fiber tips are smaller than both the linewidth and the splitting of the resonances, indicating that the present imaging technique is a relatively non-invasive one.

Exemplary data for such subtle spectral changes are shown in Fig. 5.17 for the apertureless scattering experiments made with the tip corresponding to the red line in Fig. 5.16. The intensity in the x-z-plane perpendicular to the sample at a wavelength of the bright SPP mode is shown in Fig. 5.17(a). The roman numbers (I) to (IV) indicate lateral positions, for which the local spectra at the surface and at a distance of 50 nm are compared. In Fig. 5.17(b), spectra are shown at the position (I) and for $z = 50$ nm (blue) and $z = 0$ nm (red). Here, the amplitude of the narrow resonance increases upon an approach of the surface, while that of the broad resonance decreases. The opposite is occurring at the lateral position (II) shown in Fig. 5.17(c). These spectral changes can be further visualized by plotting the difference of the spectra measured at the two distances, as shown in Fig. 5.17(d). This depiction also allows for more subtle effects such as linewidth changes or resonance shifts to be identified. For example, small shifts of the narrow resonance are found from the dispersive shapes of the differential spectra plotted in Figs. 5.17(e) and (f), corresponding to lateral positions (III) and (IV), respectively. A dip surrounded by two maxima for the broad resonance in Fig. 5.17(f) indicates a line broadening during the approach.

The measurement of a spectrum at every point in the x-z-plane allows for a determination of the locally varying resonance parameters given by the amplitudes, linewidths and resonance frequencies $a_j(x,z)$, $\Gamma_j(x,z)$ and $\omega_j(x,z)$. They are obtained by fitting a double resonance Lorentzian function to the data [cf. Eq. (4.3)]. The lineshape model fits the local spectra quite well, although small deviations are typically found on the long wavelength tail of the broad resonance, potentially due to the finite structure size of the experimental grating.[15] It is necessary for a satisfactory modeling of the experimental data to consider a coherent sum of the two resonances, i.e., spectral interference between both modes is included.

[15] We have found similar spectral features in calculations based on the radiative coupling model introduced in Sec. (4.4) for a reduced number of polarizabilities.

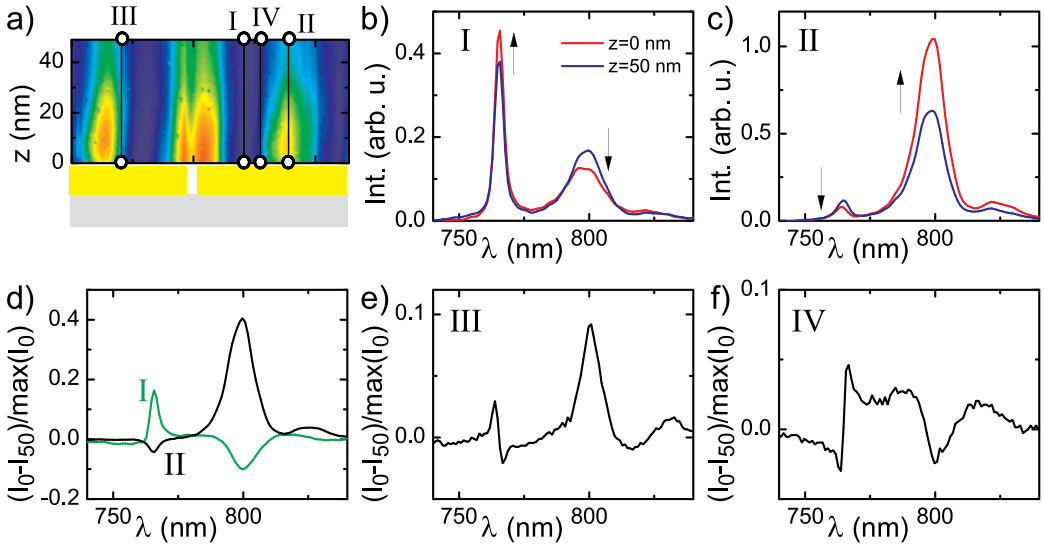

Figure 5.17: (a): *x*-*z*-scan at 800 nm (bright SPP mode) indicating the positions (circles) at which local spectra are plotted. (b): Spectra at the lateral position (I) for a distance of 50 nm (blue) and in tip-sample contact (red). (c): The equivalent at the lateral position (II). Differential spectra for the approach at (I) (green) and (II) (black), highlighting different changes in the relative peak heights. (d): Differential spectrum at (III), revealing a small blue shift of the narrow resonance. (e): Differential spectrum at (IV), revealing a small red shift of the narrow resonance.

5.4.2 Discussion

These observations are a result of several effects, in which the tip-sample coupling plays an increasing role. They can be categorized as spectral changes that

- are also present in the fields in the absence of the probe [0th order, “uncoupled”].
- can be attributed to a sample-induced modification of the spectral scattering efficiency of the probe (surface dressing) [1st order, “renormalizable”].
- further result from a modification of the resonant sample modes due to the presence of the probe [2nd order, “invasive”].

The different orders are not introduced in a strict mathematical sense, but rather indicate the different complexities of the respective couplings. The zeroth order is trivial, i.e., no coupling is involved. The subsequent paragraph will give an example of such spectral changes. The first order coupling describes changes that are mainly due to modifications of the response of the tip alone. Specifically, the

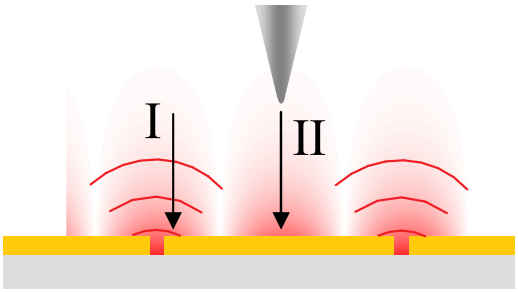

Figure 5.18: The interference between propagating and evanescent components of the optical near-field can be probed by comparing spectra for the approach at lateral positions near the slits (I) and between the slits (II).

image dipole contribution to the probe polarizability [see Sec. (2.2.6)] alters the scattering cross-section and thus the signal detected in the far-field. Such effects are expected even for arbitrarily small probe dipoles and could in principle be removed from the measured data by a spectral normalization, if the surface dressing were sufficiently well-characterized for a particular tip.[16] In contrast, the second order effects will come in, when a significant fraction of the surface waves reaching the probe is backscattered to interact again with the surface polarizabilities. The resulting multiple scattering will have to be solved in a self-consistent theoretical approach taking into account the probe and the specific sample geometry. Although these two couplings can be physically distinguished in some situations, they will never appear completely independently of each other.

Peak Shifts from Interference

Not all observed peak shifts in near-field spectroscopy need to be related to tip-sample coupling effects. In some cases, a plain interference between the relevant near-field modes is inherent to the sample and can result in spectral variations, which may be hard to distinguish from tip-sample couplings.

For example, the interference between the SPP modes and the directly transmitted light through the nanoslits leads to a distant-dependent peak shift in the near-field for approach curves taken at lateral positions close to the slits. Figure 5.18 schematically depicts the measurement of two approach curves for lateral positions at which the bright mode is strong in the scattered signal from the coated fiber tips, i.e., near the slits (I) and in the center between the slits (II) [see Sec. (5.2.2)].

The theoretically expected distance-dependent near-field spectra at positions (I) and (II) are displayed in Figs. 5.19(a) and (c), respectively. At each distance, the color-coded images are normalized to the mean spectral intensity for better visibility. Individual near-field spectra are plotted in Figs. 5.19(b) and (d) for distances of $z = 200$ nm (blue) and $z = 0$ nm (red). For the first approach ((b), I),

[16] In our case, the surface dressing would be quite similar to that of a plane gold surface.

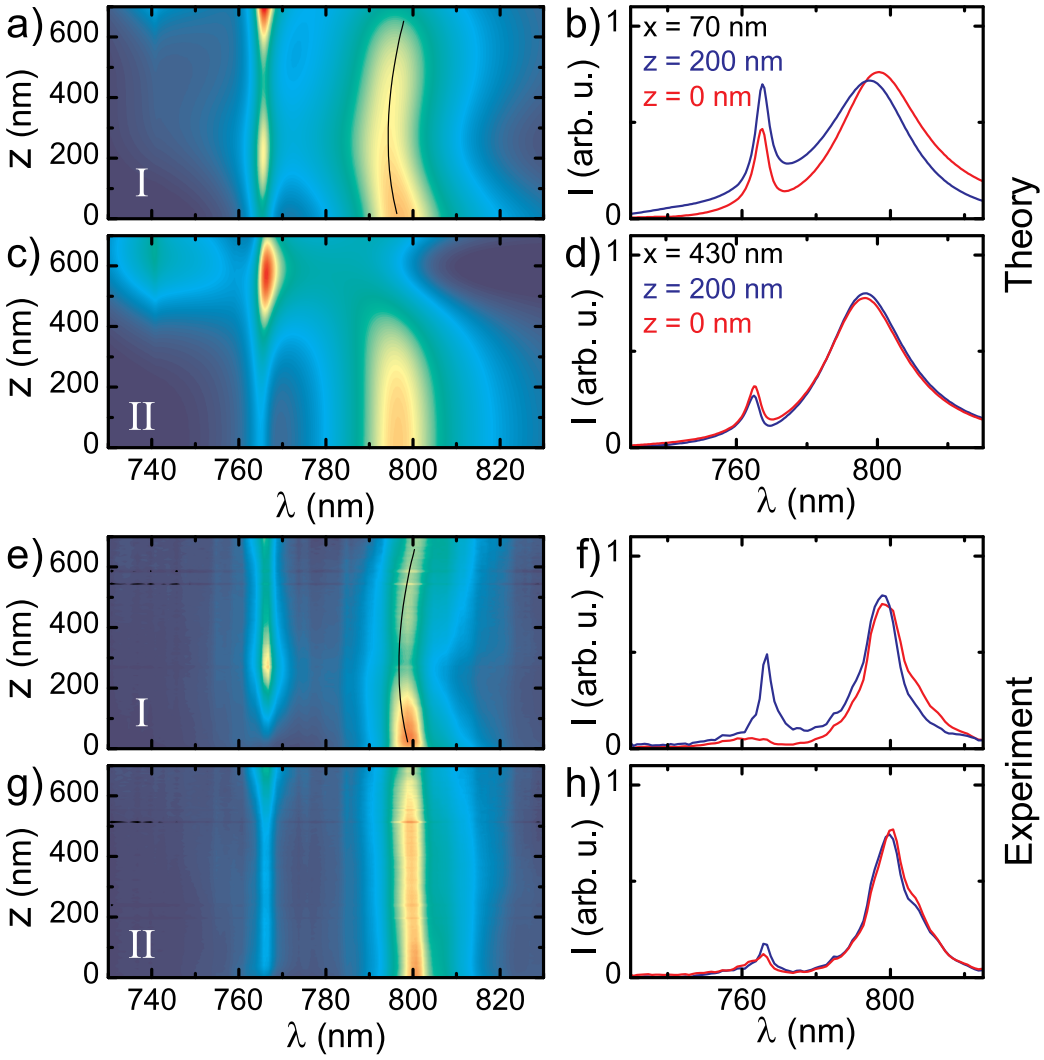

Figure 5.19: Computed distance-dependent near-field spectra ($|H_y|^2$ from the modal expansion method) showing shifts in the observed bright SPP peak. At each distance, the spectra are normalized to the mean value in the wavelength window shown. The color-coded images contain the normalized distant-dependent spectra at the lateral position of the slit ($x = 0$ nm in (a)) and in the center between the slits ($x = 375$ nm in (c)). The individual spectra correspond to distances of $z = 200$ nm (blue) and $z = 0$ nm (red). A significant peak shift is only observed for $x = 0$ nm in (b).

taken near a slit, the simulation yields a clear spectral variation of the broad SPP peak with a pronounced red-shift in the last 200 nm from the surface (solid line as a guide to the eye). In contrast, very small spectral variations are predicted close to the surface for the approach between the slits (II), see Fig. 5.19(d).

The corresponding experimental data are shown in Figs. 5.19(e)-(h), displaying very similar behavior.[17] A spectral red-shift of the broad SPP peak is observed close to the surface when the approach is performed near the slit [Figs. 5.19(e) and (f)], while only very minor spectral shifts are found upon approaching the surface between the slits [Figs. 5.19(g) and (h)].[18]

The above peak shifts on length scales of $z > 100$ nm originate from interfering components of the optical near-field. The spatial phase slip, proportional to $e^{i\frac{\omega}{c}z}$, of the fields radiated away from the slits leads to a z-dependent relative phase between this component and the SPP mode with a phase that is (very close to) constant with respect to z. Also for the far-field transmission spectra, the relative phase between the continuum and the resonance is the essential parameter for the asymmetry of the Fano lineshape [Sec. (4.2.2), Eq. (4.3)], so that the variation of the relative phase along z directly results in the observed peak shifts.

Tip-Sample Couplings

Other spectral modifications upon the approach of resonant modes by a near-field tip are a result of tip-sample couplings. A proper three-dimensional and vectorial theoretical modeling of our system, including the tip geometry, is a quite complicated task and certainly beyond the scope of the present thesis.

Instead, we consider again the simplified scalar radiative coupling model introduced earlier in Sec. (4.4), where the slits were treated as point polarizabilities coupled via SPP excitations and through the nanoslits. Within this model, the probe can be incorporated as an additional polarizability, in an attempt to simulate an actual near-field experiment. This is sketched in Fig. 5.20. Along with the probe, its image polarizability needs to be included, which leads to surface dressing, as discussed in Sec. (2.2.6). The scattering of the surface plasmon modes at the probe introduces additional radiative coupling with the slit polarizabilities. In this sense, the first order effect above is mostly related to the interaction of the probe with its own image. On the other hand, the second order effect is a result from single and multiple scattering between the probe and the sample polarizabilities. This scattering will be strongly enhanced *via* the surface dressing, thus the term second order.

[17] Recall the fact that larger linewidths were obtained in the simulations also for the far-field spectra [Sec. (4.5.2)].

[18] The amplitude decrease of the narrow mode in tip-sample contact [Fig. 5.19(f)] is, however, not predicted by the calculation.

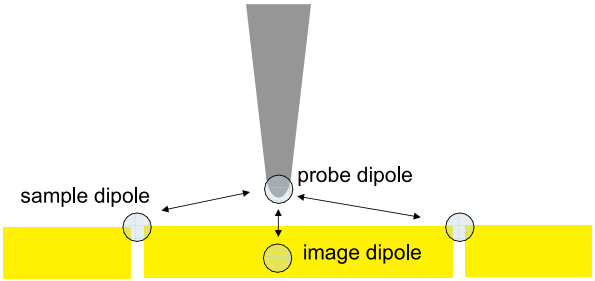

Figure 5.20: Addition of a probe dipole to the array of point dipoles introduced in Sec. (4.4). The arrows indicate the radiative coupling of the probe dipole with its image and the sample dipoles.

As mentioned above, the near-field measurement can be modeled by inclusion of the probe polarizability α_{pr}. The recorded signal is then proportional to the squared dipole moment of the probe $|\alpha_{pr}E(\mathbf{r}_{pr})|^2$. The expression for the fields at the probe position is given in Eq. (4.14). Now, also fields scattered at the probe have to be included in the self-consistent treatment. The scattering of SPP waves at the probe are included as an additional term in the Green's tensor, Eq. (4.11), as

$$\frac{i}{4}H(k_{AM}|x_l - x_{pr}|)\Theta(l - N/2), \tag{5.5}$$

where H is a Hankel function [163]. Surface plasmon waves are emerging from the probe with an amplitude proportional to α_{pr}, propagating to the polarizabilities α_l on the upper surface of the structure. The planar geometry of the problem in principle requires an extension of the previous model to also the extruded y-dimension. In this first, crude approximation to the full dipolar Green's function [79], the radial decay of the circular SPP wave generated by the probe is accounted for by the Hankel function, and in essence, SPP waves scattered by the probe with a finite in-plane momentum in the y-direction are assumed to be never backscattered to the probe, intuitively justified by the translational invariance of the sample.

The image dipole of the probe leads to a surface dressing, effectively making the probe polarizability a function of the distance from the nearly plane metal surface, $\alpha_{pr}(z)$. For an out-of-plane electric or in-plane magnetic dipole, induced in the probe by the two dominant components of SPP fields at the surface, the scattering efficiency will be increased close to a metallic surface [cf. Sec. (2.2.6)]. Thus, a scattering signal that increases stronger than the undisturbed fields is expected for such dressed dipoles.

Self-consistent model calculations were performed including dressed probe dipoles scaling as described in Sec. (2.2.6). Figure 5.21(a) shows the result of calculations of the scattered intensity $|\alpha_{pr}(z)E(z_{pr})|^2$ including only the surface dressing (dotted), or calculating self-consistently the multiple scattering of the probe with the sample (solid) for a 30 nm and a 70 nm perfectly conducting parti-

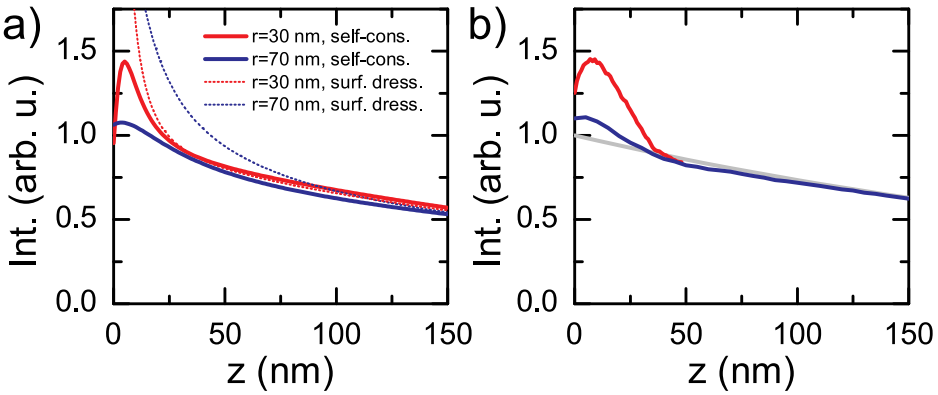

Figure 5.21: (a): Simulated intensity scattered from two probe polarizabilities with radii of 30 nm and 70 nm, including only the probe's surface dressing in unperturbed sample modes (dotted) or including self-consistently the fields scattered at the probe. (b): Experimental SPP scattering approach curves for two different Al-coated fiber probes.

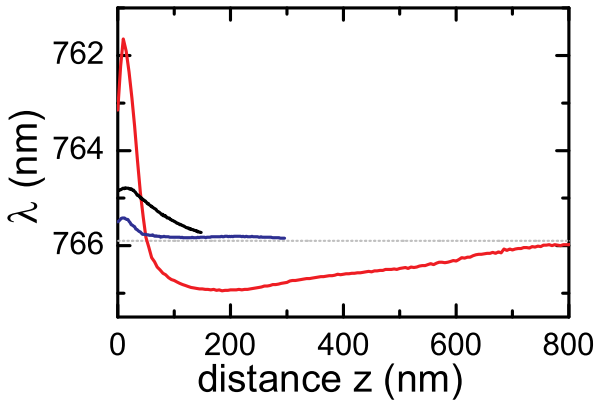

Figure 5.22: Resonance shifts of the dark mode observed with three near-field probes corresponding to different degrees of invasiveness. The largest shifts (red line) are found for an intentionally damaged tip. (Gray line: resonance wavelength in the far-field).

cle.[19] The curves are calculated for a lateral position close to the center between the slits, at a wavelength of the bright mode, and were normalized to the intensity at a distance of 200 nm. One clearly sees the drastically increasing scattering efficiency from the surface dressing [77] for the dotted lines. This increase in the scattering efficiency, however, also leads to enhanced SPP-to-SPP scattering at the probe, which eventually results in a decrease of the total scattered signal in the self-consistent calculation. This enhanced scattering near the surface is expected to also contribute to the reduction of the collection mode intensity [cf. Fig. 5.16] in what one might call "near-field shadowing".

These coupling-induced amplitude changes are accompanied by resonance shifts. Because of varying SPP-to-SPP scattering efficiencies among different

[19]For simplicity, the surface dressing equation for a perfectly conducting surface is used.

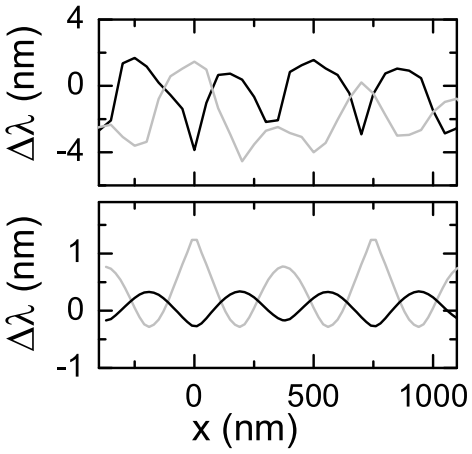

Figure 5.23: Top: Lateral dependence of the dark mode resonance shift from a distance of $z = 1000$ nm down to tip-sample contact ($z = 0$ nm). Bottom: Computation for a 100 nm diameter particle, displaying a similar oscillatory behavior with weaker resonance shifts.

probes, the magnitude of resonance shifts was found to depend on the size of the scatterer, which is illustrated in Fig. 5.22. The resonance shift of the dark mode is plotted as observed for three different scattering tips[20] at about the same lateral position in the unit cell ($x \approx 50$ nm). The curves display similar shapes, but differ in amplitude. The largest shift (red curve) is observed for a tip which had been mechanically enlarged by exerting pressure from the front, i.e., by a controlled "crashing" of the tip on a glass substrate. This method can be quite reproducible if performed carefully, and it is also used to create apertures in coated fibers used for collection mode NSOM [47]. Increasing the probe size and with it its scattering dipole moments not only increases the intensity scattered into the far-field, but also leads to increased in-plane SPP scattering and thus to larger spectral shifts.

The magnitude and sign of the resonance shifts depend on the lateral position in the unit cell of the plasmonic crystal, resulting in an oscillatory dependence of the resonance parameters on the in-plane coordinate x. For the most invasive probe, the change of the two resonance wavelengths are plotted in Fig. 5.23. Here, the resonance shift is displayed as the difference between the wavelengths in tip-sample contact and at a distance of 1000 nm, i.e., $\Delta\lambda = \lambda(x, z = 0 \text{ nm}) - \lambda(x, z = 1000 \text{ nm}))$, for the bright mode (gray) and the dark mode (black). The oscillatory curves demonstrate that this probe locally modifies the observed band gap. Specifically, compared with the far-field experiments, the band gap is reduced at $x = 500$ nm (blue-shift of the bright mode, red-shift of the dark mode) and expanded at $x = 0$ nm.

Qualitatively similar dependencies are found in the self-consistent model calculations, as depicted in the lower graph of Fig. 5.23, namely a distance-dependent resonance shift and the resulting periodic variations of the splitting between the two resonances. Essentially, the scattering probe acts as a moveable defect in

[20] All three tips are Al-coated fiber tips.

the unit cell that introduces additional coupling among the SPP Bloch modes [cf. Sec. (4.3.3)]. Thus, it leads to a local modification of the observed SPP band gap, resulting, e.g., in modifications the mode spacing. Along with these changes, linewidth and amplitude variations were observed, both experimentally and theoretically, with magnitudes also scaling with the scattering dipole moments. A more detailed discussion of these observations and further theoretical computations would go beyond the scope of this thesis.

These calculations, performed for a 100 nm radius particle, do not yet quantitatively describe the experimental data, something that could likely be improved by optimizing the size or shape of the modeled scatterer or by adopting a specific spectral response for the probe. Up to now, we have only developed a simple scalar model, which was solved numerically, accounting self-consistently for the tip-sample interferences. A full three-dimensional treatment is expected to yield a significantly better understanding of these coupling phenomena, which will be necessary for a tailoring of the local plasmonic band gap by controlled insertion of point defects.

Measurements with a moveable scattering center, such as the ones presented here, could provide a direct means for quantifying the relevant nanoscopic electromagnetic coupling constants. We will attempt this in the near future with the experimental results at hand. At this point, we leave the discussion with two main assertions. Firstly, small probe dipoles result in only marginal alterations of the spectral and spatial structures. This demonstrates that a quite non-invasive imaging and spectroscopy of these systems is possible. Secondly, multiple scattering between larger probe dipoles and the sample polarizabilities results in proximity-enhanced and laterally periodic modifications of the local SPP resonance parameters, specifically the band gap properties.

5.5 Launching Surface Plasmons Onto Nanotips

This section presents a separate investigation dealing with the concept and implementation of a new form of local light source, which is, however, based on some of the principles encountered previously. In this study, the delocalized properties of SPP excitations on flat metallic surfaces are merged with the light localization at highly curved geometries. Specifically, a traveling SPP wave will be converted into a localized excitation of a sharp metallic tip.

It has been mentioned before [Sec. (5.2.2)] that the linear and elastic scattering from sharp metallic probes is complicated by background light scattering, for example from the tip shaft. Problems of this kind also arise in experiments where an external far-field illumination is focused onto a tip in order to provide a local excitation. Such a scattering background may not pose great difficulties

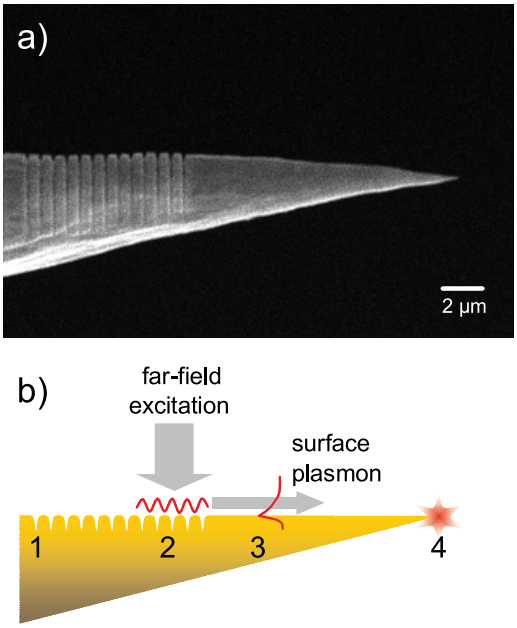

Figure 5.24: (a): Scanning electron microscope image of a metallic tip prepared with a grating coupler on the shaft. (b): Principle of the nonlocal excitation of the tip apex. Far-field radiation excites surface plasmon polaritons on the grating, which propagate to the tip end and reradiate.

in experiments where the signal depends nonlinearly on the intensity or where the signal is spectrally shifted with respect to the excitation [206]. Other experiments, e.g., local broadband absorption spectroscopy [53], heavily rely on low background levels. Experiments with aperture illumination can provide this, but suffer from low throughput efficiencies.[21] It would therefore be highly desirable get the low background levels of an aperture probe with the high field intensities of an apertureless probe, ideally in the absence of dispersion.

Surface plasmon polaritons may offer a route to such an efficient local illumination via the tailored excitation and propagation of SPPs on metal waveguides [180, 207]. We intend to implement a new form of nano-focusing that is based on the geometrical focusing of SPPs traveling on the shaft of a near-field tip acting as a tapered SPP waveguide. In such a geometry, large field enhancements have been theoretically proposed [208], although a very efficient optical excitation of SPPs on a metallic conical tip has not yet been achieved. Here, we realize a local femtosecond light source based on the focusing of SPPs on nano-fabricated metallic tips with radii down to 10 nm. By the use of focused ion beam milling,

[21] In addition, dispersion limits temporal resolution with fiber probes to the range of several hundred femtoseconds.

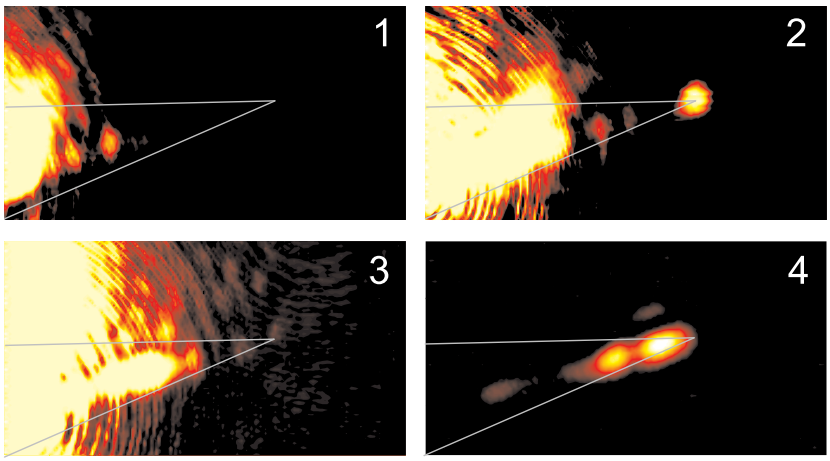

Figure 5.25: Series of microscope images recorded for illumination of the tip at the four positions indicated in Fig. 5.24(b). Image (2) demonstrates the nonlocal excitation of the tip end by illuminating the grating. The absolute intensity scattered from the very end of the tip in image (2) reaches about half of that under direct tip illumination.

one-dimensional gratings are written onto the tip shaft, several micrometers away from the apex. Illumination of the grating with a broadband laser leads to resonant excitation of SPPs, which travel to the tip apex and are reradiated.

A scanning electron microscope image of one of the nanofabricated metallic tips is shown in Fig. 5.24(a). It is an electrochemically etched gold tip [186] with a radius of curvature at the tip apex of roughly 20 nm and an opening angle of about 15°. Periodic structures on metallic surfaces allow for the resonant excitation of SPPs via grating coupling [1]. We intend to make use of this effect by writing a linear grating with a periodicity of approximately 750 nm onto the tip shaft by focused Ga ion beam milling. Such gratings have been prepared on a number of tips with different tip shapes and distances from the tip end.

The tip is illuminated with light from the 7-fs Ti:Sapphire laser oscillator [see Sec. (2.1)]. The light pulses are focused onto the tip shaft, roughly perpendicular to the grating [see Fig. 5.24(b)] with a microscope objective (numerical aperture 0.4, working distance 16 mm) to a spot size of roughly 5 μm. The light scattered from the tip out of the figure plane is collected with a second objective and imaged either onto a video camera or the entrance slit of a monochromator. The illuminating microscope objective is placed on a piezo scanner, allowing for a precise positioning of the optical focus on the tip.

Images of the light scattered from the tip are recorded for various positions of the illumination on the tip. In Fig. 5.24(b), different characteristic illumination positions are labeled by the numbers (1) to (4), referring to illumination on the

grating far from the tip end (1), on the grating closer to the tip end (2), between the grating and the tip end (3), and directly on the tip end (4). The corresponding scattered light images are shown in the image series of Fig. 5.25. For illumination on the left end of the grating, strong scattered light is observed from the grating itself (1). Moving the focus to the right on the grating, one observes a strong signal from the tip end (2). This directly reflects the reradiation of SPPs excited on the grating, which traveled towards and converged in the tip apex, as illustrated in Fig. 5.24(b). Such an image is obtained only for polarization perpendicular to the grooves, i.e., for the polarization in which SPP excitation is possible [1]. We have observed this strong nonlocal tip excitation for several of such nano-fabricated tips, and the best results were found for tips with minimal surface roughness between the grating and the tip apex.

Further movement of the illumination towards the tip apex and off the grating results in a disappearance of this light spot (3) due to a lack of efficient SPP excitation on the tip shaft. In image (4), the tip apex is directly illuminated, and scattered light is found from a region close to the tip end.

It is important to note that the maximum intensity of the scattered light in (4) is not at the very end of the tip, in stark contrast with (2). For illumination with far-field light, the scattering cross-section depends on the illuminated metallic area. Towards the apex, the tip is much thinner than the optical focus, so that the intensity scattered from the apex becomes small compared with the somewhat thicker region close to the tip end. Moving the focus further to the right and eventually away from the tip does not shift the scattering pattern, but only results in a decrease of the scattered intensity.

This observation has two main consequences. First, it clarifies that the emission in (2) is indeed stemming from an area much smaller than the optical focus and the light wavelength. Second, it demonstrates the physical difference in the excitation conditions underlying the images (2) and (4). Whereas image (4) is a result of far-field excitation and scattering, evanescent surface waves are responsible for the excitation of the tip apex in image (2). The SPPs excited in the grating likely travel all the way to the tip end before they are reradiated, which will have to be proven by future near-field experiments. Due to this fundamentally different form of tip excitation, light localization at the apex is achieved in the linear optical regime, i.e., with arbitrarily small excitation power. Often, the enhancement of optical nonlinearities at the tip apex has to be employed to obtain strong light localization [184, 194–196].

In the following, the resonant nature of this nonlocal excitation of the tip apex is discussed. In the experiments, the optimum condition for the tip excitation was found for slightly de-focused illumination on the grating, which resonantly enhances the coupling efficiency to SPPs [165]. Depending on the angle of incidence, different SPP frequencies can be excited. This behavior is measured by

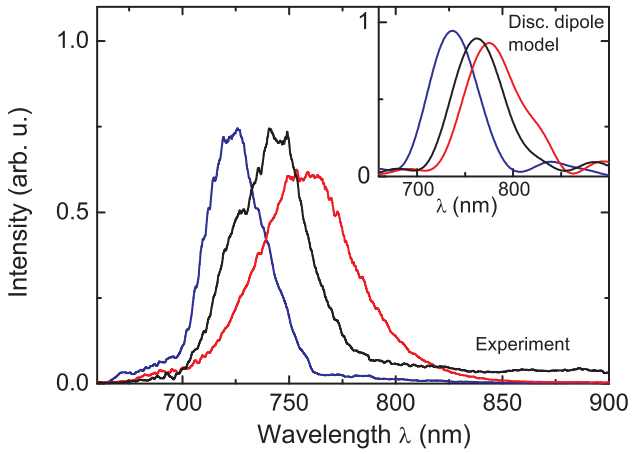

Figure 5.26: Recorded spectra from the tip end for different excitation conditions (angles of incidence) on the grating. A shifting and broadening of the spectra is observed for varying the angle of incidence by only few degrees. Similar behavior is found within a simple discrete dipole model (inset).

spectrally resolving the light scattered from the tip apex under illumination of the grating. In Fig. 5.26, three scattering spectra are displayed for different angles of incidence. The spectra are normalized to the laser spectrum. One observes clear resonant features at wavelengths of 720, 740 and 760 nm, close to the grating period, which is expected for an SPP resonance on a grating. The three angles of incidence are near the normal, with a difference of about 2° between them. The absolute angle of incidence could not be exactly determined in the experiment, due to a lack of a well-defined specular reflex from the tip shaft. The strong dependence on the excitation conditions evidences that this tunable resonant behavior is indeed an effect of the collective excitation of the grooves and not a pure resonance of the tip itself [186].

Model calculations were performed for a scalar discrete dipole model with SPP scattering [181], in which the grooves at the grating and the tip apex are simulated as point dipoles, using the same method as in previous computations within the radiative coupling model introduced in Sec. (4.4). The incident fields are impinging on the grating alone, and the resulting field at the apex is self-consistently calculated as a function of wavelength and angle of incidence. The inset in Fig. 5.26 shows the results of these calculations for angles of incidence of 3.5° (red), 4.5° (black) and 6.5° (blue), leaving the polarizability of the grooves as a free parameter. The qualitative agreement between these model calculations and the experimental results supports the interpretation of the grating resonance effect.

Interesting questions concerning the dynamics of this new local light source arise. The SPP resonances on such gratings are radiatively broadened [13], with SPP lifetimes ranging from few tens to few hundreds of femtoseconds [127] [see Ch. 4]. In this case, the resonance width is mainly determined by radiative coupling and by the number of grooves present and illuminated on the tip. Furthermore, the particular shape of the grooves, which can act as resonant cavities, may influence the resonant excitation. The experimentally found linewidths suggest the possibility of launching SPP wavepackets of a duration on the order of 10 fs onto the tip shaft. Theoretical results indicate that significant chirp may be acquired by an SPP wavepacket upon propagation on a tapered conical waveguide [208]. In that case, previous dispersion compensation will have to be applied to achieve the shortest possible pulses at the tip end. Further experimental work will be necessary to resolve this issue, e.g., by investigating the frequency-converted light generated at the tip apex [184, 185, 194, 196]. This will also help to quantify the absolute local intensities at the tip apex and the achievable field enhancements in this tapered waveguide [208].

In conclusion, the possibility of an effective nonlocal excitation of the apex of a sharp metallic tip by virtue of grating coupling has been demonstrated. Tunable resonances are found in the spectrally resolved light scattered from the tip apex. Such nano-fabricated tips will serve as a useful nano-scale light source in illumination apertureless microscopy and spectroscopy, in particular because of the spatial separation of the grating excitation from the tip apex.

6 Femtosecond Electron Emission from Metal Tips

This chapter covers experimental results on a novel source of femtosecond electron pulses. Localized free electron emission is observed from sharp metallic tips as the ones used in the previous experiments. The emission, confined to the tip apex due to field enhancement, is found to originate from fourth-order multiphoton processes. The effective nonlinear order can be reduced by the application of a negative bias voltage, increasing tunneling from lower excited electronic states. Bias voltage dependent experiments show that the electron emission stems from a highly excited non-equilibrium carrier distribution, which in turn demonstrates that the emission occurs on a time scale of few femtoseconds, shorter than the electron thermalization time. Finally, the high sensitivity of the electron emission on the local dielectric environment is used to introduce a new form of scanning probe microscopy, realized as the tip-enhanced electron emission microscope (TEEM).

Before the experimental results are shown, the following two sections further motivate this work [Sec. (6.1)] and recall relevant mechanisms of electron emission [Sec. (6.2)] that will be important for the subsequent discussions.

6.1 Motivation

Ultrafast electron diffraction [209–211] and microscopy [212, 213] are fascinating approaches to the study of microscopic structural changes with picosecond or even sub-picosecond temporal resolution. Together with femtosecond x-ray diffraction [89, 214], these emerging techniques promise unparalleled insights into the physics and chemistry of ultrafast processes.

In all ultrafast electron experiments, similar physical difficulties are encountered that complicate the achievement of very short electron pulse durations. These problems originate in the propagation of the electrons from the source to the sample [215]. Specifically, temporal smearing of the electron pulses generated in a femtosecond photocathode occurs due to an initial kinetic energy spread among different electrons, and due to the mutual repulsion of electrons, if low repetition

rates in an experiment require large particle numbers in the individual pulses.

Such difficulties are currently overcome by the development of sophisticated and small (few cm) femtosecond electron guns capable of delivering keV electron pulses of durations down to 400 fs,[1] recently measured with a novel optical-electronic cross-correlation technique [216, 217].

Despite such substantial progress, the development of alternative sources for femtosecond electron pulses will be essential in order to reach the regime below 100 fs [218]. Furthermore, a higher spatial coherence of new sources is very desirable, being currently limited by the optical spot size in a photocathode of larger than 1 μm. Here, such an alternative approach pursued, in which ultrashort electron emission of single electrons is induced from individual metallic nanotips at the high repetition rates of a laser oscillator.

A number of previous works have dealt with light induced free electron emission from sharp metallic tips similar to those also employed for DC emission in scanning tunneling [41] or field emission electron microscopes [219]. For example, nanosecond and picosecond optical pulses were used to induce electron emission from a tungsten tip [220], and material ablation was found with ns optical pulses from tips with 1 μm tip radii and for tip bias voltages up to 50 keV [221, 222]. More recently, 100 fs pulses from an amplified kHz laser were used to emit electrons from a tungsten tip, which were then funneled through a micro-capillary for spatial localization [223].

The work most closely related to ours is that of Peter Hommelhoff *et al.*,[2] who studied electron emission from tungsten tips by the use of 65 fs laser pulses in the presence of tip bias voltages in the kV range [224]. At moderate peak powers and for sharp tips, the authors attributed an electron emission that linearly depended on the incident laser power to tunneling emission followed by single-photon absorption ("photofield emission"). At higher peak powers and for a broken tip displaying some surface roughness, a nonlinear dependence on the laser power was found, interpreted as optical field tunneling emission from states close to the Fermi energy (see below).

Hommelhoff *et al.* argue that both of these processes should be prompt with respect to the incident laser pulses [224]. In the case of photofield emission, however, this assertion does not take into account the carrier dynamics in the tip after the optical absorption, which results in significant charge densities above the Fermi energy even after the light pulse. Optical field emission is by definition only possible during the laser pulse, but it has yet to be demonstrated that this is in fact occurring under given experimental conditions, since a number of other processes exist that also scale nonlinearly with the incident power but need not

[1] Group of Prof. R. J. Dwayne Miller at University of Toronto.

[2] Group of Prof. Mark A. Kasevich at Stanford University.

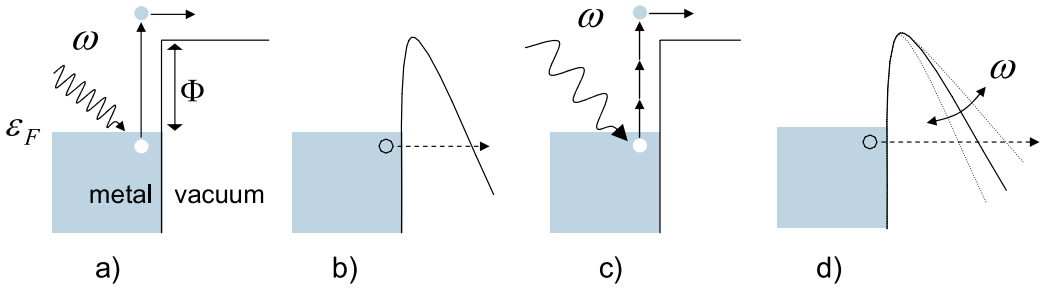

Figure 6.1: Electron emission processes from metals. (a): Standard photoelectric effect. (b) Fowler-Nordheim tunneling. (c) Multiphoton photoelectric effect. (d) Optical field emission.

lead to prompt electron emission.

Thus, more needs to be found out about the underlying emission processes and the time scales on which they are occurring. Furthermore, the question remains, if such localized electron emission can also be achieved in the absence of high bias voltages. This would be one prerequisite for using the localized electron emission in imaging applications, where a sample is in nanometer proximity of the tip. This chapter contains experimental results and discussion with regard to these questions. We proceed with a brief summary of different electron emission processes involving static and optical fields.

6.2 Electron Emission from Metals

Metals are characterized by a finite density of electronic states at the Fermi energy, which is the energy up to which the electronic levels are filled. The Fermi energy in metals is typically several electronvolts below the vacuum level (about 5 eV in the case of gold), which means that the electrons are bound to the material with at least this binding energy. Electrons can be emitted from metals in various ways involving electric or electromagnetic fields. Figure 6.1 depicts some of the associated processes, ordered roughly with respect to their experimental appearance and theoretical understanding.

Photoelectric Effect

In the well-known photoelectric effect (a), first observed in the late 19th century and first explained by Einstein [225], an electron escapes a metal after absorption of a photon of energy $\hbar\omega$ larger than the work function Φ. The photoelectric effect can be defined as a three-step process [226, 227], in which the absorp-

tion event is followed by propagation to the surface and eventually transmission into the vacuum. Upon propagation to the surface, the electron experiences elastic and inelastic collisions (electron-phonon, electron-electron, electron-defect), corresponding to energy and momentum redistributions. Alternatively, photoemission is described in terms of a direct optical transition between an electronic state confined to the solid (bulk or surface state) and a vacuum state leaking into the solid. For more details, the reader is referred to Ref. [227].[3]

Field Emission

The so-called Fowler-Nordheim tunneling (b) [229] involves the application of a high negative static bias voltage to a metal. If the resulting surface electric field is large enough to correspond to a potential drop of several Volts over a distance of a nanometer or less, quantum mechanical tunneling of electrons from filled states at and below the Fermi energy becomes possible.

Within the WKB approximation [230], the transmission coefficient of an electron of energy E through the triangular barrier of height $\Phi - E$ created by a surface electric field F is [229]

$$T(E) = \exp\left(-\frac{4\sqrt{2m}(\Phi - E)^{3/2}}{3\hbar eF}\right). \tag{6.1}$$

Here, we have set the original Fermi energy to zero, so that the we can use the work function Φ as a parameter. This function can be integrated over the filled density of states of the metal, yielding the tunnel current density j. If image charge effects of the tunneling electrons are taken into account [229], j is expressed as

$$j = \frac{e^3F^2}{16\pi^2\hbar\Phi t^2(y)}\exp\left(\frac{-4\sqrt{2m}\Phi^{3/2}v(y)}{3\hbar eF}\right). \tag{6.2}$$

Here, v and t are elliptical dimensionless Nordheim functions of the variable $y = e^{3/2}\sqrt{F/4\pi\varepsilon_0}/\Phi$ (see Ref. [229] and corrected expressions in Ref. [231]). $t^2(y)$ is a slowly varying function often set to a value of 1.1, and $v(y)$ is frequently approximated as $v(y) = 0.95 - y^2$ [232, 233]. The overall tunneling current J is the surface integral over the current density j.

Multiphoton Photoelectric Effect

With the emergence of short-pulse lasers of high peak intensities, the nonlinear regime of photoemission became accessible [234, 235]. In multiphoton photoe-

[3] Due their initial appearance in the theoretical description of low-energy electron diffraction (LEED), such states are also called "time-reversed LEED-states" [228].

mission (c), a number of photons of an energy, which may be smaller than the work function, are absorbed by the same electron. If the sum of the photon energies $\hbar\omega$ of N photons is larger than the metal work function Φ, an N-photon emission process can be observed, ideally possessing a laser power dependence of the electron current of $J \propto P^N$ [234, 235]. A number of effects can alter this power dependence, for instance space charge effects [236] or a recently suggested photoelectric anomaly in layered structures [237]. Multiphoton processes can occur in a stepwise or a coherent form [238, 239]. Due to the rapid dephasing (or momentum relaxation) of excited electrons in metals [240], stepwise processes within the optical pulse duration tend to dominate for pulse lengths longer than a few femtoseconds [239]. In this work, 7-fs pulses are used for multiphoton electron emission, so that both coherent and stepwise processes must be considered.

Optical Field Emission

In the case of multiphoton emission, the lowest nonlinear order giving rise to electron emission is the dominant one, so that in this perturbative regime, the power series of nonlinear polarizations can be truncated at the respective order [241]. For larger optical intensities, higher-order nonlinearities significantly contribute to the electron emission. An early observation of this so-called above-threshold ionization (ATI) from Xenon atoms is reported in [242], which could still be treated in a perturbative way. At even larger peak powers, the optical electric field can become large enough to allow for tunneling of electrons within one optical half-cycle (d) [243, 244]. The transition between the multiphoton-regime and this optical field emission is quantified in terms of the Keldysh parameter [243]

$$\gamma = \sqrt{\frac{\Phi}{2U_p}}, \tag{6.3}$$

where U_p is the ponderomotive potential, calculated from the trajectory of a free electron in a time-varying electric field:

$$U_p = \frac{e^2 I}{2mc\varepsilon_0\omega^2}. \tag{6.4}$$

Here, I is the light intensity, m is the electron mass and ω is the optical frequency. For $\gamma \gg 1$, multiphoton processes dominate, while the tunneling regime is defined by $\gamma \ll 1$. This strong-field regime is now reached by modern mode-locked lasers, which have opened the door for the field of attosecond physics [245–250]. Usually, these works deal with atomic or molecular systems in the gas phase. In solid state systems, clear signatures of ATI are still the exception. The typical increased kinetic energy of the emitted electrons in ATI has recently been reported from a silver (100) surface [251].

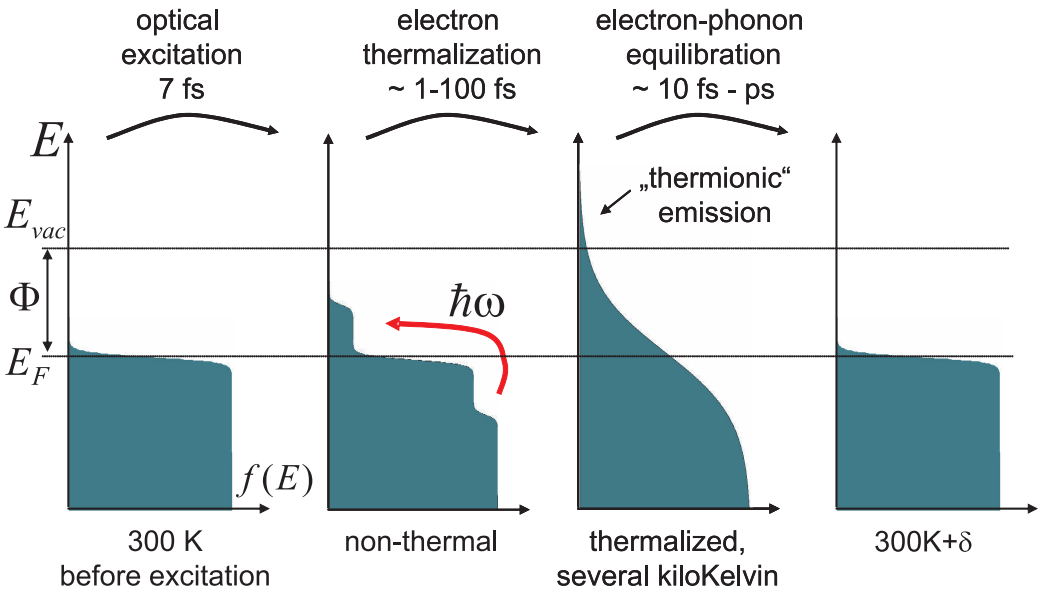

Figure 6.2: Typical dynamics of the electron distribution in metals under ultrafast optical excitation. The features of the distribution functions are somewhat exaggerated to illustrate the effect of thermionic emission.

Thermionic Emission

In addition to the above effects, electron emission can be induced by purely thermal effects following laser irradiation, even at pulse energies which are not sufficient to heat the entire solid to temperatures, at which thermal emission is found. In order to explain this, we qualitatively discuss the dynamics of the electronic system in metals following femtosecond laser excitation.

Before the excitation, the distribution function corresponds to a Fermi-Dirac distribution at room temperature (300 K). The intense optical pulse transfers carriers above the initial Fermi energy, leaving the system in a non-equilibrium state. Electron-electron-scattering results in a rapid thermalization on a time-scale of few to few tens of femtoseconds, which occurs partly already within the pulse duration. Due to the comparatively small heat capacity of the electronic system, temperatures of several thousand Kelvins can be reached in this transient state. During this time, a fraction of the carriers will have energies above the vacuum level and can be emitted from the metal. This is called thermionic emission. On the picosecond time scales of the electron-phonon equilibration, the electronic system looses a major portion of its energy content to the lattice and cools down. Two-temperature models for the electron and phonon subsystems [252] are used to account for such carrier-lattice dynamics. It should, however, be noted that such

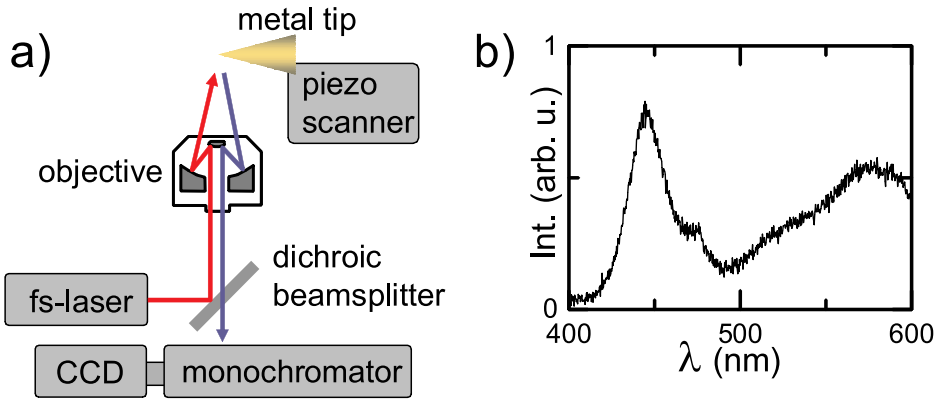

Figure 6.3: (a): Experimental setup for the detection of nonlinear frequency conversion from a metallic tip. Optical pulses from a fs-laser are focused with a Cassegrain mirror objective onto the tip. An image is obtained by scanning the tip through the laser focus and by detecting the spectrally dispersed backscattered light. (b): Spectrum of the frequency-converted light for one of the tips, consisting of a second-harmonic contribution and a broad continuum.

a description in terms of thermalized distributions does by definition not account for effects occurring on time scales shorter than the electron thermalization time.

6.3 Enhancement of Optical Nonlinearities at the Tip

In the previous chapters, we have encountered the polarizability of a sharp metallic tip a number of times. For instance, it has been shown in Ch. 5 that the scattering of surface plasmon polaritons from a sharp gold tip is sensitive to the SPP's out-of-plane component of the electric field. One disadvantage in such linear scattering scenarios are the small scattering cross-sections of small objects, so that the field enhancement of a sharp tip is sometimes at the cost of a reduced linear scattering cross-section. This deteriorates the signal-to-background ratio and therefore complicates the respective experiments. One possibility to overcome these limitations has been demonstrated in Sec. (5.5), where a specifically designed probe based on a novel form of near-field SPP focusing was introduced.

In this section, it is shown that, by going to the regime of nonlinear optics, the above problems in linear experiments can disappear entirely, and that the properties of such metallic tips may be completely dominated by the very end of the tip.

We begin by looking at the scattering of light from a sharp gold tip, which was

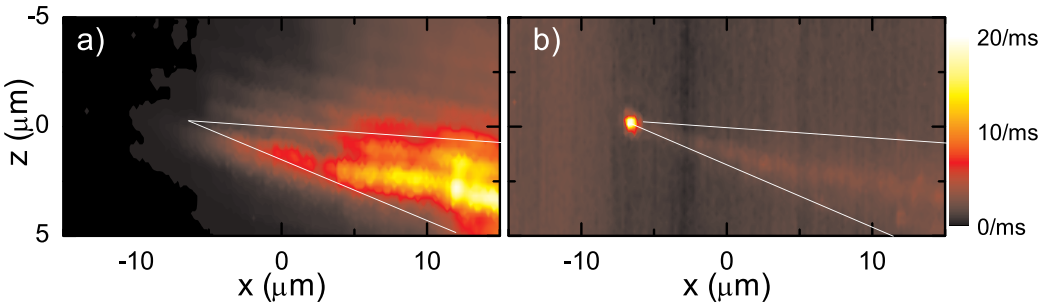

Figure 6.4: Strong localization of optical frequency conversion at the apex of a gold tip (indicated by the white lines). (a): Back-scattered fundamental laser light. (b): Frequency-converted light confined to the tip apex.

electrochemically etched to a radius of curvature of about 20 nm. Illumination of such a sharp tip with femtosecond light pulses results in nonlinear frequency conversion [184, 185, 194, 195]. We measure this optical frequency conversion in the experimental configuration shown in Fig. 6.3(a). A given tip is illuminated with femtosecond light pulses from a Ti:Sapphire oscillator, linearly polarized along the tip axis, focused down to a spot size of 1.5 μm by a reflective Cassegrain microscope objective (numerical aperture 0.4, working distance 10 mm). Compared with conventional refractive objectives, such a mirror objective has the great advantage of very little spectral dispersion, which is essential for the efficient generation of nonlinear optical signals. The tip is mounted on a piezo scanner which allows it to be raster scanned through the laser focus in the plane perpendicular to the optical axis. The backscattered light is separated from the incoming laser by a dichroic beam splitter, dispersed in a monochromator and detected with a liquid nitrogen cooled charge coupled device camera (CCD), yielding a spectrum at every point in the scanning routine.

An exemplary spectrum of the frequency-converted light for one of the tips is shown in Fig. 6.3(b). The generated light is typically composed of the second harmonic of the laser pulses (at wavelengths around 450 nm) and a broad continuum in the range between 450 and 700 nm, which is likely due to two-photon induced luminescence [194]. The relative amplitudes of the second harmonic and the continuum contribution vary for different tips, which likely originates in different microscopic tip structures and/or crystalline orientations at the tip apex.

Some amount of the fundamental laser light scattered back from the tip and transmitted through the dichroic beam splitter serves as a reference. The image in Fig. 6.4(a) shows this backscattered laser light as a function of the focus position on the tip over an area of 10×30 μm^2. The image clearly resembles the tip shape, which is indicated by the white lines. Close to the tip end, where the tip

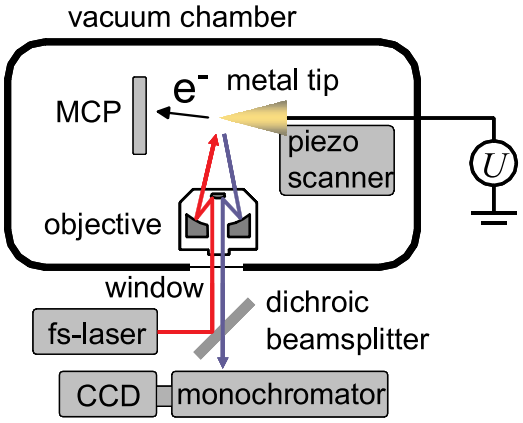

Figure 6.5: Experimental setup of the simultaneous detection of electron emission and nonlinear light generation. The setup shown in Fig. 6.3 has been placed in a vacuum chamber, and the optical pulses are coupled into the chamber through a thin quartz window. The emitted electrons are detected with a micro-channel-plate (MCP). An arbitrary bias voltage U can be applied to the tip.

becomes thinner than the laser focus, the scattered intensity decreases due to the limited linear scattering cross-section. The image in Fig. 6.4(b), displaying the photon rate detected in the wavelength range outside of the laser spectrum, looks remarkably different. One observes an intense concentration of this nonlinear light generation at the very end of the tip. This localization of the frequency-converted light is a direct consequence of the enhanced field present at the tip apex.

6.4 Electron Emission from the Tip Apex

Recently, it has been demonstrated by Kubo *et al.* that two-photon electron emission microscopy (2PPEEM) is sensitive to local optical field enhancements and can be used to image hot spots on corrugated metal surfaces [253]. The previous section examined the optical nonlinearities leading to optical frequency conversion, and we found that the tip geometry allows for the controlled excitation of the tip apex as an individual hot spot, which suggests that also nonlinear polarizations of higher orders, leading to electron emission, will be localized at the tip apex.

6.4.1 Localized Electron Emission

In order to study the possibility of inducing electron emission from such sharp metal tips, the earlier experimental setup [Fig. 6.3] is modified and placed in a high vacuum chamber with a base pressure of about 10^{-7} mbar [see Fig. 6.5]. The femtosecond light pulses are coupled into the vacuum chamber through a 150 μm thin quartz window. An electron detector consisting of two micro-channel-plates (MCP) is placed opposite to the tip, and voltage pulses from the MCP detector due to single electron events are counted with an electronic discriminator (not shown).

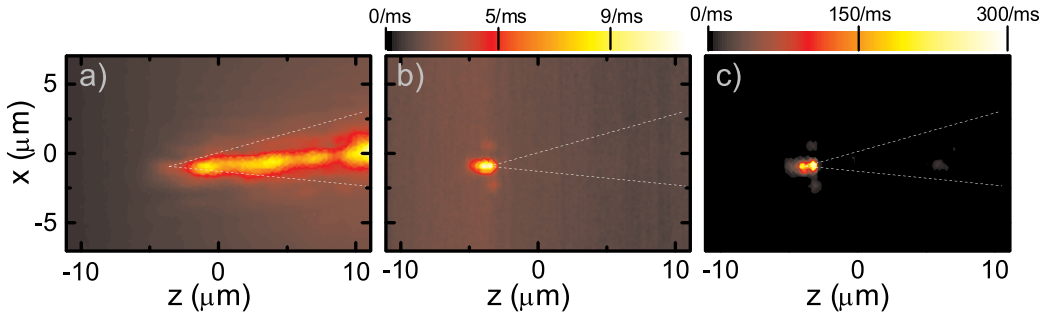

Figure 6.6: (a): Spatial scan of the fundamental 7-fs laser light backscattered from a sharp gold tip (dotted lines). (b): Nonlinear light generation localized at the very end of the tip. (c): Simultaneous electron emission. (Images at $U = 0$ V.)

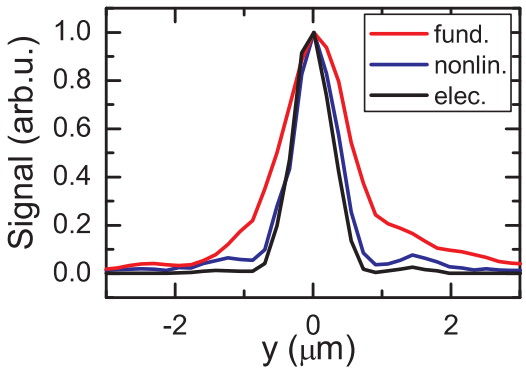

Figure 6.7: Fundamental, nonlinear light and electron signal averaged along the x-axis near the tip apex and normalized to 1. The peak is narrowest for the electron emission. The respective (Gaussian) peak widths are 1.0, 0.65 and 0.54 μm.

A variable bias voltage U can be applied to the tip, but is left at $U = 0$ V for the initial experiments.

Rather than only detecting the frequency-resolved backscattering, we now simultaneously detect the electron emission as a function of the focus position on the tip. Figure 6.6 shows, as before, the fundamental laser frequencies backscattered from the tip (a) and the frequency-converted backscattering (b), but now also the detected electron current emitted from the tip in Fig. 6.6(c). The signal is peaked at exactly the same position as the optical nonlinear light generation, namely at the tip apex, providing evidence that the same optical field enhancement is responsible for both kinds of emissions.

As mentioned earlier, the 1.5 eV photon energy is well below the gold work function (5 eV), so that a linear photoemission is not possible with the laser spectrum used. Further indication that the electron emission is of a relatively high nonlinear nature is obtained by analyzing the images in Fig. 6.6. The illuminating spot size, assessed from (a), is roughly 1 μm $\cdot$ 2 μm. In the image of the frequency-converted light (b), the nonlinearity reduces the spot size over which emission occurs, and the spot size is even further reduced in the electron emission

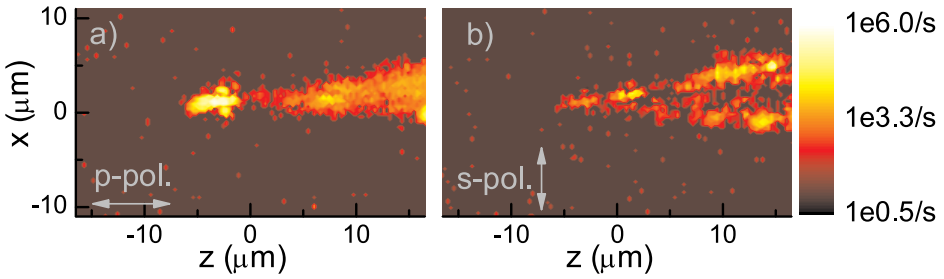

Figure 6.8: Electron generation rate (logarithmic color scale) for an incident polarization parallel (a) and perpendicular (b) to the tip axis. For perpendicular polarization, the electron emission from the tip apex is suppressed by more than two orders of magnitude.

image, as displayed in Fig. 6.7. This reduction in spot-size, being a direct consequence of the nonlinear nature of the emission, is completely equivalent to the improvement in spatial resolution one obtains in other types of scanning focus microscopes depending on nonlinear excitation, such as the two-photon fluorescence microscope [254]. It should be noted that the emission area is still substantially smaller than these micrometer dimensions. As will be shown Sec. (6.5.2), the emission is actually confined to an area determined by the curvature of the tip.

6.4.2 Polarization Dependence

Before the nonlinearity of the electron generation is studied in further detail, we first demonstrate that emission depends on the high directionality of the optical susceptibility along the tip axis. In Fig. 6.8, the electron emission is shown for polarizations of the incident light parallel (a) and perpendicular (b) to the tip axis. In order to resolve finer details and to make the emission for perpendicular polarization even visible, the images are shown on a logarithmic color scale covering six orders of magnitude. In Fig. 6.8(a), the strong emission from the tip apex is seen, in combination with the weak background from the tip shaft. (The imperfect focus shape seen on a logarithmic scale is not relevant for the further studies.) For perpendicular polarization, the emission from the apex is reduced by more than two orders of magnitude, illustrating the polarization selectivity of the local field enhancement. In addition, the qualitative nature of the background of the image changes. While for parallel polarization, the background stems from the front face of the tip shaft, the emission in perpendicular polarization resembles the border of the tip shape. This is understood when considering that this emission is preferentially occurring at sites of smaller field enhancement that are efficiently excited when the electric field is pointing away from the surface.

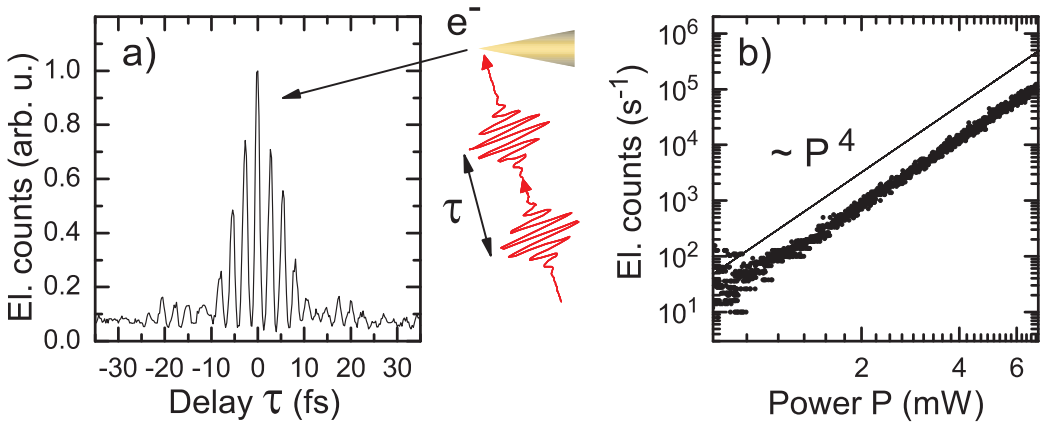

Figure 6.9: (a): Electron signal as a function of relative delay between a pair of phase-locked laser pulses (interferometric autocorrelation). (b): Fourth-order power dependence of the electron emission.

6.4.3 Multiphoton Photoemission

Physical insight into the origin of the emission is obtained by interferometric autocorrelation [cf. Sec. (2.1.2)] and the power dependence of the emission. The focus reduction mentioned in Sec. (6.4.1) already gives a first hint towards the high nonlinearity of the electron emission. Further evidence of this is obtained in the IAC shown in Fig. 6.9(a), where the electron signal is plotted as a function of the relative delay τ between a pair of phase-locked pulses from the 7-fs laser oscillator. A strong enhancement (>25) of the electron signal is found for zero delay compared with the delay for times much longer than the incident pulses. For a second order nonlinearity, this peak-to-baseline ratio should be 8, so that the larger value found here is indicates higher nonlinear order. A quantitative extraction of the nonlinear order of the emission from this peak-to-baseline ratio would require a very accurately determined power ratio and almost perfect spatial overlap of the two pulses on the tip. Very recently, the peak-to-baseline ration has been used as a measure of the nonlinearity, although no assessment of the actual order has been given [255].

We decided to perform a direct quantitative measurement by placing a continuously variable neutral density filter, consisting of a thin glass slide and a metallization with various thicknesses, into the laser path and measuring both the transmitted light and the generated electron current. In Fig. 6.9(b), the electron emission current J is plotted as a function of the incident power P on a double-logarithmic scale. The graph shows a straight line with a slope of 4, i.e., the curve can be expressed as $\log(J) = a + 4\log(P)$. This is equivalent to $J = 10^a P^4$, so

that the electron emission scales with the fourth power of the incident laser power. This shows that the emission involves the absorption of four laser photons, either in a step-wise or in a coherent four-photon process. The 5 eV work function of gold is consistent with the absorption of four laser photons in the photon energy range of 1.5 eV. It should be pointed out that a contribution of thermionic emission based solely on single-photon absorption processes can depend on the incident power also in a highly nonlinear way. We have, however, observed an extremely high sensitivity of the electron emission on the dispersion of the incident pulses, showing that the emission process scales nonlinearly with the peak power and not only with the pulse energy, as would be the case for thermionic emission following single-photon absorption. Furthermore, the bias voltage dependent emission characteristics are inconsistent with a thermal carrier distribution, as will be shown later. Thus, an important contribution of thermionic emission can be ruled out for the experiments without exceedingly large bias voltages.

The knowledge of the underlying nonlinear order of the emission process allows us to estimate the absolute field enhancement at the tip apex. Comparing the emission rates from the tip apex with those from the tip shaft in Fig. 6.6, taking into account the relevant areas, from which emission occurs, yields the local electric field enhancement with respect to the incoming laser field: $\alpha = |E_{loc}/E_{inc}|$. The field enhancement factors from nonlinear light generation (P^2 dependence) and electron emission are about $\alpha = 15$ and 10, respectively. These values can be seen as lower limits to the actual field enhancement, since the reference region on the shaft also contains some nanometer-scale roughness with a distribution of electric field hot-spots with increased optical nonlinearities. Still, these numbers are in rather good agreement with theoretically predicted values ($\alpha \approx 12$) for gold tips of similar sharpness [184]. It is expected that for these gold tips, a localized surface plasmon resonance significantly contributes to the field enhancement [186].

Let us briefly come back to this IAC trace [Fig. 6.9(a)]. For a completely coherent process depending in eighth order on the incident fields, a peak-to baseline ratio of 125:1 is expected. The reduced value found in our case is likely due to several factors. In order to obtain a mechanically very stable and dispersion-free interferometer for the IAC, purely reflective optics including a split mirror to separate the two beams have been used. This poses a certain limit on the spatial overlap on the tip, somewhat reducing the peak-to baseline ratio. Furthermore, the presence of ultrafast and incoherent stepwise four-photon processes [239] will also reduce the obtained ratio.

It should be noted that the experimental IAC trace for the 7-fs pulses is a factor of 1.5 longer than what is expected for an instantaneous fourth-order nonlinearity. In addition to the stepwise processes mentioned above, this may be due to either a small pulse stretching introduced by the focusing objective, or due to the finite bandwidth of the field enhancement from a localized surface plasmon resonance

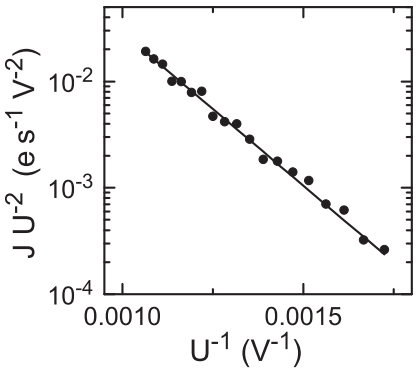

Figure 6.10: Fowler-Nordheim plot of the tunnel emission of a gold tip (circles) and a fit to a FN dependence (line).

at the tip [186].

A more detailed analysis of femtosecond IAC traces under different excitation conditions could yield valuable information on the energy and momentum relaxation of the excited carriers [240],[4] but is outside the scope of the present work. In the following, a variable negative bias voltage is applied to the tip, which also yields more in-depth information on the femtosecond excitation of the tip.

6.4.4 Addition of a Bias Voltage

In the absence of laser radiation, the application of a negative bias voltage results in Fowler-Nordheim (FN) tunneling [cf. Sec. (6.2)], and the current-voltage characteristic can be used to calibrate the properties of the tip, i.e., to determine the proportionality constant between a macroscopically applied bias voltage U and the resulting surface electric field F. This depends mostly on the radius of curvature of the tip, but can also vary with the distance of the tip from the anode. Figure 6.10 shows the tunneling current of one of the tips used in the experiments. The data is shown as a so-called FN plot, in which J/U^2 is plotted on a logarithmic scale against $1/U$, resulting in a straight line [see Eq. (6.2)].[5] From the slope of the data, a surface electric field of $F \approx 10^{-2}$ nm^{-1} U is deduced.

After such initial characterizations, the electron flux J is studied systematically as a function of incident laser power P and tip bias voltage U. Figure 6.11 shows a data matrix $J(U,P)$ (a), together with curves at constant incident power (b) and constant Voltage (c). First, the power dependence for different voltages [Fig. 6.11(c)] is discussed. At low bias voltages, we find, as before, a fourth order power dependence. Raising the bias voltage results in a background

[4] It has been pointed out in Ref. [240] that such few femtosecond autocorrelation traces carry a lot more information than the frequently used term "coherent artifact" from the superposition of the incident fields suggests.

[5] Noticeable deviations from the straight line due to the function $v(y)$ come into play only for larger fields.

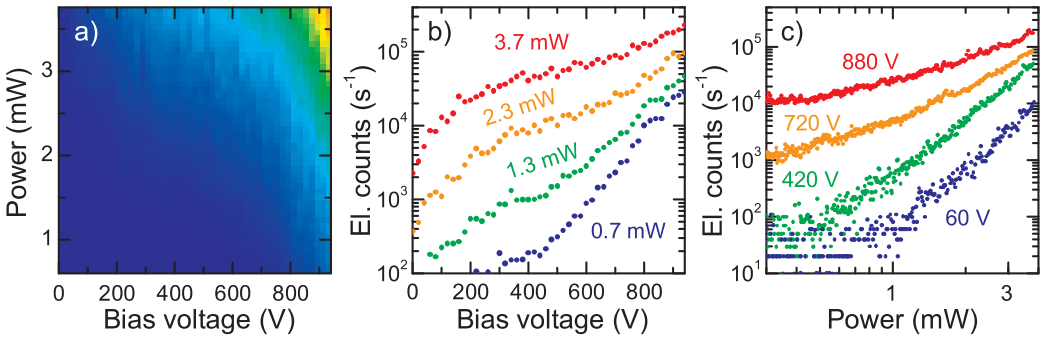

Figure 6.11: (a): Power and voltage dependent electron emission. (b): Voltage dependent curves. (c): Power dependent curves.

due to the FN tunneling mentioned above, and, most importantly, in a decrease of the power dependence of the emission. At 880 V, the electron flux is only slightly nonlinear with a power dependence $\propto P^{1.5\pm0.1}$ around $P = 3$ mW. The gradual decrease of the power dependence, evaluated for the slope of the curves around 3 mW, is plotted in Fig. 6.12(a). The curve starts at the value of 4 with convex curvature, has an inflection point near 500 V and approaches 1 for larger bias voltages.[6] In Fig. 6.12(b), an explanatory tunneling scheme is depicted, together with the WKB tunneling probability T as a function of the state energy for moderate (blue) and large (red) magnitudes of the bias voltage. For zero bias, only electrons excited to states above the vacuum level can escape the metal. At the high bias voltages, the multiphoton electron emission is complemented by tunneling from lower-lying electron states populated by, e.g., linear absorption. From the simultaneous frequency-conversion [Sec. (6.4)], we also have evidence for significant two-photon absorption. Since both of these processes are of lower order and the resulting populations are considerably larger than the four-photon-absorption [239], the emission will be increasingly dominated by them with increasing bias.

Generally, it is not trivial to make a direct assignment between a given non-integer power dependence and the relative contributions of the different underlying absorption processes. Also, a determination of specific initial states would require further investigation, e.g., by photoelectron emission spectroscopy [256]. The redistribution of carriers due to the optical pulse itself and due to scattering processes complicate a quantitative determination of linear and different multi-photon absorption cross-sections. Rather than attempting such an analysis, we intend to learn something about the carrier distributions resulting from different

[6]The DC field emission at $P = 0$ mW is subtracted from the curves for the determination of the power dependence.

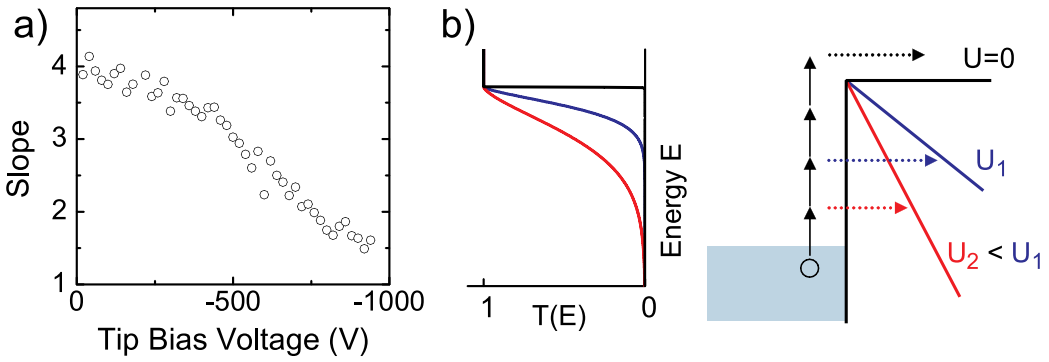

Figure 6.12: (a): Slope of the double-logarithmic power dependence as a function of bias voltage. (b): Illustration of the bias-voltage-induced reduction of the effective nonlinear order. Applying a bias voltage from zero (black) over moderate (blue) to high (red) magnitudes, lower excited states increasingly contribute to the emission.

incident intensities. For this purpose, we consider the voltage dependent electron emission. In Fig. 6.11(b), $J(U)$ is displayed for four different incident powers (circles). The gradual decrease of the power dependence from a fourth-order nonlinearity at low bias voltages towards linear emission at high voltages is evident in the decreasing separation between the curves (logarithmic scale) with increasing voltage.

We have mentioned earlier that the femtosecond excitation of the gold tip generates a transient carrier distribution with a pronounced population well above the Fermi energy [236, 257]. For a given tip, the voltage-dependent electron flux $J(U,P)$ at a particular optical power P carries information on the underlying energy distribution of excited carriers. In an extension of the conventional Fowler-Nordheim approach, $J(U,P)$ is given by an integral over the energy- and voltage-dependent transmission coefficients $T(E,U)$ times a distribution function of the optically excited carriers $f(E,P)$:[7]

$$J(U,P) \propto \int_0^\infty dE\, T(E,U)\, f(E,P). \tag{6.5}$$

Here, the emission probability $T(E,U)$ of a state at energy E for a bias voltage U is calibrated by the field emission tip characterization [Fig. 6.10]. Knowledge of $T(E,U)$ permits a reconstruction of the carrier distribution $f(E,P)$ from the measured functional dependence $J(U,P)$. The function $f(E,P)$ is a time average over the transient nonequilibrium electron distribution during the course of the emission process. No assumptions about the density of states are made, so that

[7] A similar expression for thermal carrier distributions is used in Ref. [258].

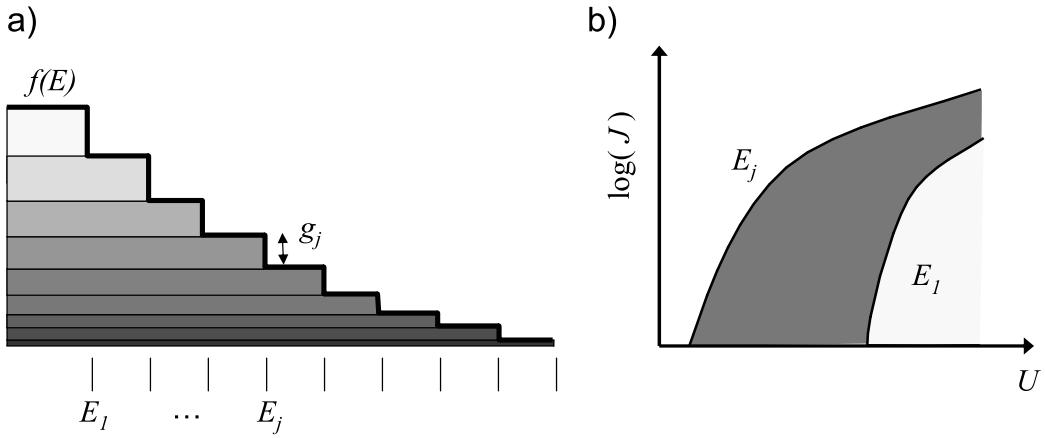

Figure 6.13: (a): Composition of the carrier distribution $f(E)$ as a sum of steps of height g reaching up to energies E. (b): Schematic depiction of the different current-voltage characteristics of a step reaching up to high energies (dark) and low energies (light gray).

$f(E,P)$ describes absolute carrier densities.[8]

Mathematically, Eq. (6.5) is a contraction, which means that some information is lost by the integration, and we cannot directly invert this equation to solve for $f(E,P)$. As a consequence, certain assumptions on $f(E,P)$ have to be made, and a reduced number of parameters should be employed to describe the distribution function. It will, however, become clear that certain characteristic properties of the carrier distribution can indeed be reconstructed.

Equation (6.5) is discretized and rewritten as a matrix equation in an attempt to obtain an approximate solution for $f(E,P)$. The variable U is naturally written as a discrete vector with its components U_i, $i \in \{0,1,..,50\}$ denoting the voltages $U_i = i \cdot 20$ V from 0 to 1000 V, at which the electron emission is measured. For the discretization in energy, the distribution functions are approximated as a sum of step-shaped components reaching up to different energies, as depicted in Fig. 6.13(a). In Fig. 6.13(b), the electron currents are schematically shown for two components of different maximum energy, illustrating how an experimentally measured current may be constructed from a weighted sum of a number of such curves.

In the particular ansatz, somewhat rounded steps in the form of Fermi-type functions with offset energies E_j, widths ΔE and weights g_j are used. The com-

[8] Under the assumption of constant density of states, this carrier density is proportional to the population function.

position of the distribution function then reads

$$f(E,P) = \sum_j \frac{g(E_j,P)}{e^{-\frac{E-E_j}{\Delta E}}+1}, \tag{6.6}$$

where $g(E_j,P)$ is the coefficient of the carrier density in the box reaching up to the energy E_j [see Fig. 6.13(a)]. This transformation yields a matrix for the resulting tunneling current at the voltage U_i for each of these j components via

$$S(E_j,U_i) = \int_0^\infty dE \frac{1}{e^{-\frac{E-E_j}{\Delta E}}+1} T(E,U_j). \tag{6.7}$$

With these definitions, the desired matrix equation can be expressed as

$$J(U_i,P) = \sum_j S(E_j,U_i) g(E_j,P). \tag{6.8}$$

Least squares solutions for $g(E,P)$ are calculated numerically by minimizing the error functional

$$\varepsilon = \sum_i |J(U_i,P) - \sum_j S(E_j,U_i) g(E_j,P)|^2 \tag{6.9}$$

for every incident power. The minimization is performed under the further constraint of non-negativity of the components of g.[9] As a result of this constraint, only non-inverted, i.e., monotonically decreasing distribution functions are captured, which excludes a strong resonant behavior at specific energies. The experimental data can be entirely described within this class of distribution functions. From the optimized coefficients g, the corresponding distribution functions are calculated via Eq. (6.6). Figure 6.14(a) shows again the voltage-dependent emission curves at four incident powers (circles). The reconstructed distribution functions are shown in Fig. 6.14(b) for these four incident powers. As a cross-check, the solid lines in Fig. 6.14(a) represent the electron currents [Eq. (6.8)] resulting from these four distribution functions, which are in excellent agreement with the experimental results. The choice of the energy resolution, i.e., the difference between two adjacent values of E (1 eV in Fig. 6.14) and the width of the Fermi functions ΔE (0.3 eV in Fig. 6.14) has proven to be of minor importance, and very similar results are obtained for a finer energy resolution.

The distribution functions possess a markedly non-thermal character and are mainly composed of two components: (i) A strong low-energy component close

[9] For the optimization, the function "lsqnonneg" from the MATLAB programming environment (manufactured by TheMathworks Inc.) was used.

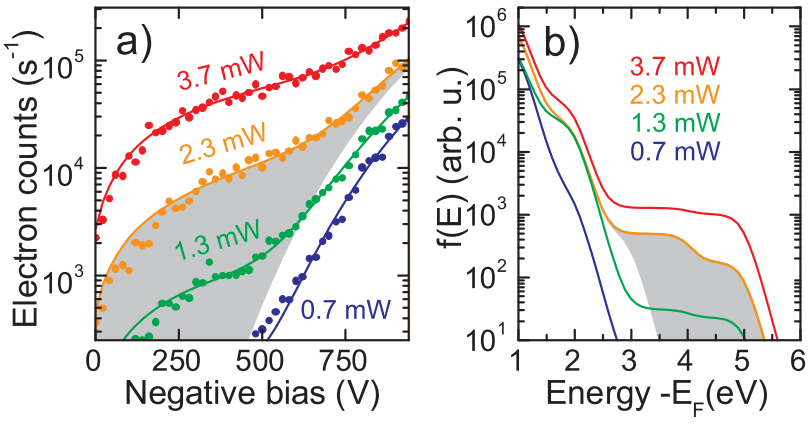

Figure 6.14: (a): Voltage dependent emission curves (dots) and the currents (lines) predicted from the reconstructed carrier densities shown in (b).

to the Fermi energy which originates from single-photon absorption; its energy content scales approximately linearly with the incident optical power. (ii) A non-thermal high energy shoulder which emerges between 3 eV and 6 eV [indicated by the gray-shaded area in Fig. 6.14(d) for $P = 2.3$ mW] with a strong nonlinear power dependence, resulting from multiphoton absorption from states below and up to the Fermi energy. It is this second component in the distribution functions which is responsible for the emission at low bias voltages, as is illustrated by the large gray-shaded area in Fig. 6.14(c) that corresponds to emission from the shaded area in the distribution function in Fig. 6.14(d). Although a substantial electron emission is already present at zero bias voltage, there is a sharp rise in electron flux upon increasing the bias from zero to 100 V. This fact suggests that the major fraction of the non-thermal component populates states somewhat below the vacuum level.

The strong non-thermal character of the electron distributions has direct consequences for the time structure of the emitted electrons. For low voltages, the rapid thermalization [see Sec. (6.2)] of electrons limit the population lifetime of the relevant high-energy states [240, 259] and, thus, the duration of the emitted electron pulses. For very large negative bias, lower-lying states of longer lifetime [260] contribute significantly to the emission, possibly resulting in longer electron pulses.

A comment should be made on Keldysh-type [224, 243] optical field emission from the Fermi energy potentially occurring because of the high electric fields of the excitation pulses. In our experiments, despite the short laser pulses and the substantial field enhancement at the metal tip, we estimate a Keldysh parameter of about 4 at $P = 3$ mW. We thus expect that the present experiments are well in the

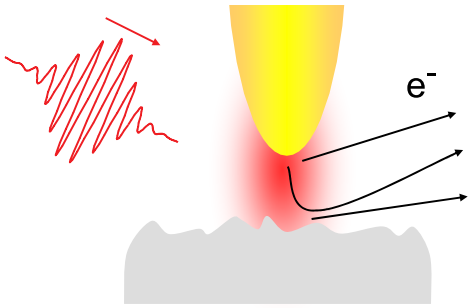

Figure 6.15: Concept of the tip-enhanced electron emission microscope, indicating possible contrast mechanisms due to (i) a modification of the electron yield from the tip, (ii) local electron emission from the sample induced by the enhanced fields near the tip end, (iii) single or multiple scattering of electrons at the tip and/or the sample.

multiphoton regime [261], although at this stage, a limited contribution of optical field emission cannot be definitely excluded at the very bias voltages. At lower bias voltages, the situation is clear, as we find the same fourth order power dependence for various tips at zero bias, whereas optical field emission should strongly depend on the local field enhancement and thus vary from tip to tip. Furthermore, for optical field emission, a saturation of the power dependence to a finite value (4 in our case, cf. Fig. 6.12) is not expected at zero bias. Instead, optical field emission predicts a steeply increasing power dependence for a reduction of the bias [255].

6.5 Tip-enhanced Electron Emission Microscope

In the previous section, it has been shown that the local field enhancement at the apex of metallic tips leads to a localized emission of electrons. The strong confinement of this emission, together with the high nonlinearity of the generation process, makes this emission highly sensitive to the local dielectric environment of the tip. Therefore, this nanometer-sized electron emitter can serve as an ideal probe to image optical fields on nanometer length and femtosecond time scales near surfaces. Here, a first application is developed in the form of a device, which monitors the locally varying generation rate of electrons as the probe is raster-scanned near a sample surface. This new type of microscope is termed tip-enhanced electron emission microscope (TEEM).

6.5.1 Concept

An important asset of the observed localized multiphoton-emission in the absence of large bias voltages is the fact that it allows this femtosecond electron source to be brought in nanometer proximity of a sample to perform high resolution imaging with it. The high optical nonlinearity of the emission, combined with the optical field enhancement, makes this electron source exceptionally sensitive to the local

dielectric environment of the tip.

Figure 6.15 depicts a number of different mechanisms that could lead to an image contrast when a such a tip is scanned across a surface. First, the probe's effective polarizability and with it the optical field enhancement [Sec. (6.4.3)] are strongly modified, when the probe is approached by a dielectric or metallic surface [Sec. (2.2.6)], effecting a modification of the electron yield from the tip. Second, if a metallic sample is investigated, also the possibility electron emission from the sample could be relevant. Finally, the scattering of electrons from the sample could be employed to obtain a spatial contrast. The femtosecond duration of the electron pulses emitted from the tip can permit low energy electron scattering experiments to be performed with down to ten femtosecond temporal resolution. Today, hardly any ultrafast time-resolved low energy electron methods are available.

6.5.2 Implementation and Results

In order to demonstrate the ability to use this field-sensitivity for high resolution imaging, a tip-enhanced electron emission microscopy (TEEM) setup is developed. It is based on the near-field scanning optical microscope described in Sec. (2.2.5). Slight modifications were carried out for the microscope to operate under vacuum conditions, such as the inclusion of a motorized coarse tip-sample approach or the addition of an electrical contact to the probe to avoid charging effects under electron emission. The compact TEEM setup has proven to be very stable mechanically (below 1 nm relative tip-sample vibration), even in the presence of an operating rotary vane and a turbomolecular pump maintaining the vacuum.

With this setup, a first experiment has been carried out, in which an illuminated tungsten tip displaying localized electron emission similar (though somewhat weaker) to the gold tips discussed above is approached by a nanostructure consisting of a $\sim$100 nm wide groove in a gold surface [see Sec. (3.4)].[10] The experimental configuration is shown in Fig. 6.16(a). While the tip position is kept fixed, the local electron generation rate is monitored as the sample position is scanned relative to the tip in the x-z-plane perpendicular to the sample plane. Specifically, approach curves in the z-direction are recorded for every position along the x-direction. The height of tip-sample contact is found by shear-force detection in a standard atomic force microscopy fashion, and the absolute sample position is read out from the capacitive sensors of the piezo scanner [cf. Sec. (2.2.5)]. In this way, a cross-section of the groove structure is simultane-

[10] For this experiment, a sharp tungsten tip was chosen because of its better mechanical durability compared with the gold tips.

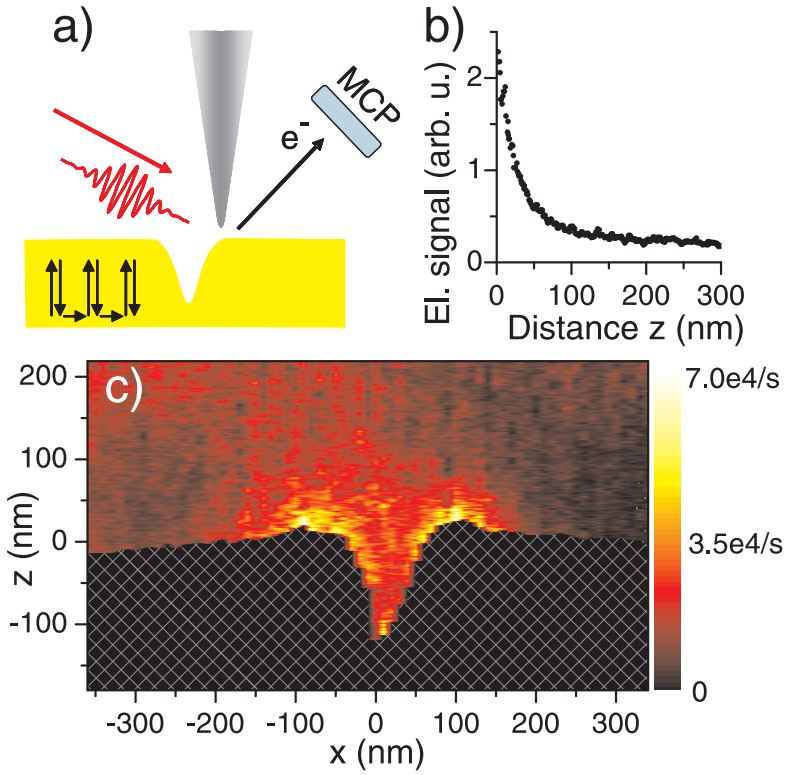

Figure 6.16: Results of the TEEM measurement at a V-shaped nanometric groove in a gold film. (a): Experimental setup, indicating the sample scanning in the plane parallel (x-direction) and perpendicular (z-direction) to the sample surface. (b): Electron current approach curve near a groove edge. (c): Two-dimensional distance-dependent TEEM image. The cross-section of the groove is indicated by the area containing the crossed lines. The surface topography, corresponding to the upper border of this area, was simultaneously measured by shear-force detection.

ously obtained, shown as the black area filled with crossed lines in the bottom of Fig. 6.16(c). The region above this area corresponds to the half-space above the sample. The color-coded image of Fig. 6.16(c) represents the local electron generation rate as a function of relative tip-sample position with a spatial resolution of few tens of nanometers, limited only by the sharpness of the nanostructure features and the tip. This TEEM image demonstrates both surface sensitivity and lateral resolution. It is clearly visible that the electron detection rate is strongest when the tip is close to one of the groove edges. A typical electron signal approach curve near one of the groove edges is shown in Fig. 6.16(b), where the electron signal increases by a factor of about 5 in the last 50 nm away from the surface.

These results show directly that the electron signal is predominantly generated in the gap between tip and sample and that the spatial resolution of this microscope is thus given by the size of the metal tip and not by the wavelength of the illuminating light. In more detail, the image is understood when considering the near-field distribution at such an illuminated nanometer-scale slit. In diffraction from an ideal rectangular slit it is known [86] that the electric field component polarized along the z-direction, i.e, along the tip axis, diverges near the slit edges, giving rise to strong field localization. Although the slit in the present sample has a rounded cross section, this field localization is still pronounced, leading to the strong increase in local electron yield near the groove edges. This demonstrates that the tip-enhanced electron emission indeed images, in a nonlinear way, the z-component of the local electric field.

6.5.3 Concluding Remarks

In the preceding sections, it was shown that localized electron emission and imaging are possible from such sharp metallic tips, even in the absence of large bias voltages, permitting us to make a close approach to the sample. In the first imaging experiment, the locally varying generation rate is the contrast mechanism in proximity of this metal nanostructure. Only one light field is incident on the structure, and the signal represents the reaction of the position dependent tip-sample geometry to this field.

It is understood that a time-resolved experiment would even more clearly demonstrate the potential of the present approach. The first extension of this TEEM microscope is the illumination with a pair of pulses of variable time delay in a pump-probe type setup. A number scenarios is possible, in which the pump pulse could excite an electromagnetic surface wave spatially overlapping with the tip, such as a surface polariton wave. This would allow for a study of wave-packet dynamics [253] with nanometer and femtosecond precision, perhaps also for non-conducting samples.

Alternatively, one could probe a local electronic or structural change induced in the sample, though the latter may be hard to achieve with the current oscillator's peak amplitudes. Also, cumulative effects at the 80 MHz repetition rate need to be avoided.

It should be noted that it is not an obvious finding that the electrons in the present experiments are able to efficiently escape the tip-sample gap at very small distances. Much is yet to be learned about elastic and inelastic surface scattering in such nanoscale geometries. This will also be necessary to interpret the results of future experiments, in which the interaction of the generated electrons with the sample via scattering or diffraction will be responsible for the image contrast.

7 Conclusions

The conclusions give a short summary of the main results of this thesis, followed by an outlook on further developments of selected aspects.

Summary

The experimental approach of the present work is based on the combination of near-field optical microscopy and coherent broadband spectroscopy. Accessing the physics of metallic nanostructures, in particular metallic photonic crystals, both from far-field characterization and a near-field optics perspective offers unique insights into these systems. Essential findings are:

- The dynamics of femtosecond light transmission through metallic photonic crystals is governed by a superposition of a nonresonant, fast component and the excitation and re-emission of both radiatively and nonradiatively broadened surface plasmon polariton (SPP) resonances. [Sec. (4.2)]

- The enhanced resonant transmission through these perforated thin film gratings is a result of radiative coupling between the grating constituents, which is mediated by SPPs traveling on either interface of the metal film. [Sec. (4.4)]

- Such coherent couplings result in SPP band gaps and drastic redistributions of radiative damping rates, leading, e.g., to subradiant SPP lifetimes on the order of 200 fs. Near-field microscopic spectroscopy reveals the symmetric and antisymmetric spatial character of SPP Bloch modes at the band gap. [Sec. (4.3)]

These observations are combined with further near-field spectroscopic experiments and numerical computations in a study of the imaging contrast in near-field optical microscopy of SPP modes. The main results of this part of the thesis are:

- Aperture collection images of SPP modes represent predominantly the in-plane magnetic field component. Out-of-plane (axial) electric fields are suppressed due to symmetry reasons. [Sec. (5.3.1)]

- Apertureless scattering images usually contain several electromagnetic field components, the relative contribution of which can be controlled via the far-field detection conditions. Sharp metallic tips can image the axial electric field component of SPPs. [Sec. (5.3.2)]

In a further investigation, the findings on grating coupling and localization of surface plasmons are employed in the development of a new form of local light source:

- Surface plasmon polaritons can be launched towards the apex of metal nanotips via a resonance in a linear grating on the tip shaft. [Sec. (5.5)]

The final part of the thesis demonstrates femtosecond electron generation from metal nanostructures excited by 7-fs light pulses, establishing:

- Optical field enhancement at ultrasharp metallic tips results in localized multiphoton emission of single electrons at high repetition rates and with femtosecond timing. [Sec. (6.4)]

- A novel scanning probe microscopy technique (TEEM) gives rise to an image contrast with such localized emission by raster scanning a sample in nanometer proximity of an illuminated tip. [Sec. (6.5)]

Future Prospects

A number of the results obtained in the present study can serve as the starting point for further investigation. For example, the subradiant SPP modes have some quite interesting properties, which could indeed make them technologically relevant. The exceedingly long SPP lifetimes of about 200 fs are only limited by absorptive losses in the metal, which is gold in our case, and not by radiative damping from scattering into the far-field at the slits.[1] Yet, this does not mean that the subradiant SPPs don't "see" the slits in the sense that there is no scattering involved, and that for this mode, the surface acts essentially as a smooth gold film. On the contrary, the multiple in-plane scattering at the slits is the essential ingredient for this high finesse surface resonator. This property makes the dark mode resonance a promising candidate for a very compact in-plane distributed feedback laser, if a gain medium is placed close to the surface.[2] This promising scenario has not yet been pursued. Currently, we investigate hybrid semiconductor-metal nanostructures regarding exciton-plasmon couplings and possible amplification of SPP propagation.

[1] These losses would be further reduced in silver, for example.

[2] Compare the work of Ref. [262] for SPP-assisted lasing at a wavelength of 17 μm.

Specific further studies are also directed at a better understanding of the nonlocal tip excitation by SPP propagation on metallic nanotips [Sec. (5.5)]. In upcoming experiments, the nonlinear signals generated at the tip apex can be detected, and a dispersion control should allow for an optimization of the output, perhaps including procedures known from coherent control experiments [263]. This will also resolve the open question of SPP dispersion on these tapered waveguides.

In the area of polarization selective near-field imaging and spectroscopy [Ch. 5], numerous further developments lie ahead. In particular, the isolation of the magnetic field components will be of considerable interest also in the near-field characterization of other structures, for example those exhibiting optical magnetic resonances [264]. In these systems, especially tip-sample couplings will have to be considered in greater detail, because the localized character of such resonances will make them more vulnerable to the disturbance from a near-field probe than the delocalized resonances observed in this work [cf. Sec. (5.4)]. It was mentioned before that the spectroscopic near-field techniques employed here will serve as an excellent gauge for the quantitative determination of coupling constants. Eventually, attempts will be made to approach the ultimate near-field characterization, that is, a full three-dimensional and vectorial description of the electromagnetic fields close to an arbitrary surface.

The observation of localized emission of femtosecond electrons presented in Chapter 6 constitutes the most recent result of the present work, but perhaps also that of the largest potential for future developments. Some possibilities for upcoming experiments in a geometry similar to the TEEM setup have been discussed in Sec. (6.5.3). However, even in the absence of a sample, much can still be learned about the electron emission process. Specifically, a sensitivity of the electron current to the carrier envelope phase of the ultrashort illuminating pulses has not been demonstrated. Theoretical simulations suggest that for the currently available pulse durations, this may be difficult to achieve [255], although experiments are still inconclusive.

The different topics this thesis alluded to could be intriguingly combined by studying the ponderomotive acceleration of electrons in intense, ultrashort surface plasmon polariton fields [265, 266]. A first application would be the femtosecond gating of electrons in such fields, for which numerical calculations have recently been carried out [267]. The local electron source and plasmonic nanostructures represent ideal components for a realization of an electron-optical pulse cross-correlation device [216].

A further interesting question is, if the present electron source will be able to compete with already developed ones or novel, RF-acceleration based ultrafast sources very recently proposed theoretically [218]. Critical points in a comparison would be properties such as total electron flux, brightness, temporal resolution and a source's long term stability. It should be noted that the localized source

can overcome the pulse duration constraints of extended femtosecond photocathodes discussed in Ref. [218], even though it is based solely on DC acceleration. Even for moderate bias voltages, the electric field resulting at the tip apex will be much larger than the average field in an extended photocathode at voltages, for which such a device would suffer electrical break-down. The giant potential drop near the tip apex leads to an exceedingly rapid electron acceleration, which reduces temporal smearing from propagation effects by orders of magnitude. Finally, comparing the spatial coherence of different photocathodes, such a single emitter will not be outperformed by any other source.

Bibliography

[1] Heinz Raether. *Surface Plasmons on Smooth and Rough Surfaces and on Gratings*. Springer, 1988.

[2] R. K. Chang and T. E. Furtak, editors. *Surface Enhanced Raman Scattering*. Plenum Press, 1982.

[3] Thorsten Liebermann and Wolfgang Knoll. Surface-plasmon field-enhanced fluorescence spectroscopy. *Colloid Surface A*, **171**(1-3):115–130, 2000.

[4] Koichi Okamoto, Isamu Niki, Alexander Shvartser, Yukio Narukawa, Takashi Mukai, and Axel Scherer. Surface-plasmon-enhanced light emitters based on InGaN quantum wells. *Nature Mater.*, **3**(9):601–605, 2004.

[5] M. Vaupel, A. Eing, K. O. Greulich, J. Roegener, P. Schellenberg, H. M. Striebel, and H. F. Arlinghaus. Marker-free Detection on Microarrays. In D. Nicolau and U. Mueller, editors, *Microarray Technology and Its Applications*. Springer, 2005.

[6] M. Pokinski and H. Arwin. Protein monolayers monitored by internal reflection ellipsometry. *Thin Solid Films*, **455-456**:716–721, 2004.

[7] S. A. Maier, P. G. Kik, H. A. Atwater, S. Meltzer, E. Harel, B. E. Koel, and A. A. G. Requicha. Local detection of electromagnetic energy transport below the diffraction limit in metal nanoparticle plasmon waveguides. *Nature Mater.*, **2**(4):229–232, 2003.

[8] H. J. Lezec, A. Degiron, E. Devaux, R. A. Linke, L. Martin-Moreno, F. J. Garcia-Vidal, and T. W. Ebbesen. Beaming Light from a Subwavelength Aperture. *Science*, **297**(5582):820–822, 2002.

[9] William L. Barnes, Alain Dereux, and Thomas W. Ebbesen. Surface plasmon subwavelength optics. *Nature*, **424**(6950):824–830, 2003.

[10] H. Ditlbacher, J. R. Krenn, G. Schider, A. Leitner, and F. R. Aussenegg. Two-dimensional optics with surface plasmon polaritons. *Appl. Phys. Lett.*, **81**(10):1762–1764, 2002.

[11] T. W. Ebbesen, H. J. Lezec, H. F. Ghaemi, T. Thio, and P. A. Wolff. Extraordinary optical transmission through sub-wavelength hole arrays. *Nature*, **391**(6668):667–669, 1998. ISSN 0028-0836.

[12] J. D. Joannopoulos, R. D. Meade, and J. N. Winn. *Photonic Crystals*. Princeton University Press, 1995.

[13] D. S. Kim, S. C. Hohng, V. Malyarchuk, Y. C. Yoon, Y. H. Ahn, K. J. Yee, J. W. Park, J. Kim, Q. H. Park, and C. Lienau. Microscopic Origin of Surface-Plasmon Radiation in Plasmonic Band-Gap Nanostructures. *Phys. Rev. Lett.*, **91**(14):143901, 2003.

[14] A. Dogariu, T. Thio, L. J. Wang, T. W. Ebbesen, and H. J. Lezec. Delay in light transmission through small apertures. *Opt. Lett.*, **26**:450, 2001.

[15] A. Dogariu, A. Nahata, R. A. Linke, L. J. Wang, and R. Trebino. Optical pulse propagation through metallic nano-apertures. *Appl. Phys. B*, **V74**(0): s69–s73, 2002.

[16] R. Szipocs, C. Ferencz, K. Spielmann, and F. Krausz. Chirped multilayer coatings for broadband dispersion control in femtosecond lasers. *Opt. Lett.*, **19**:201, 1994.

[17] F. X. Kärtner, N. Matuschek, T. Schibli, U. Keller, H. A. Haus, C. Heine, R. Morf, V. Scheuer, M. Tilsch, and T. Tschudi. Design and fabrication of double-chirped mirrors. *Opt. Lett.*, **22**:831, 1997.

[18] N. Matuschek, F.X. Kartner, and U. Keller. Analytical design of double-chirped mirrors with custom-tailoreddispersion characteristics. *IEEE J. Quantum Elect.*, **35**:129, 1999.

[19] D. E. Spence, P. N. Kean, and W. Sibbett. 60-fsec pulse generation from a self-mode-locked Ti:sapphire laser. *Opt. Lett.*, **16**:42, 1991.

[20] U. Keller, G. W. 'tHooft, W. H. Knox, and J. E. Cunningham. Femtosecond pulses from a continuously self-starting passively mode-locked Ti:sapphire laser. *Opt. Lett.*, **16**:1022, 1991.

[21] F. Salin, J. Squier, and M. Piche. Mode locking of Ti:Al_2O_3 lasers and self-focusing: a Gaussian approximation. *Opt. Lett.*, **16**:1674, 1991.

[22] H. A. Haus, J. G. Fujimoto, and E. P. Ippen. Analytic theory of additive pulse and Kerr lens mode locking. *IEEE J. Quantum Elect.*, **28**:2086, 1992.

[23] J.-C. Diels, E. Van Stryland, and G. Benedict. Generation and measurement of 200 femtosecond optical pulses. *Opt. Commun.*, **25**(1):93–95, 1978.

[24] Jean-Claude Diels and Wolfgang Rudolph. *Ultrashort Laser Pulse Phenomena: Fundamentals, Techniques, and Applications on a Femtosecond Time Scale*. Academic Press, 2nd edition, 1996.

[25] G. Stibenz, C. Ropers, Ch. Lienau, Ch. Warmuth, A. S. Wyatt, I. A. Walmsley, and G. Steinmeyer. Advanced methods for the characterization of few-cycle light pulses: a comparison. *Appl. Phys. B*, **83**:511–519, 2006.

[26] H. R. Telle, G. Steinmeyer, A. E. Dunlop, J. Stenger, D. H. Sutter, and U. Keller. Carrier-envelope offset phase control: A novel concept for absolute optical frequency measurement and ultrashort pulse generation. *Appl. Phys. B*, **69**(4):327–332, 1999.

[27] David J. Jones, Scott A. Diddams, Jinendra K. Ranka, Andrew Stentz, Robert S. Windeler, John L. Hall, and Steven T. Cundiff. Carrier-Envelope Phase Control of Femtosecond Mode-Locked Lasers and Direct Optical Frequency Synthesis. *Science*, **288**(5466):635–639, 2000.

[28] R. Trebino. *Frequency-Resolved Optical Gating: The Measurement of Ultrashort Laser Pulses*. Kluwer, 2000.

[29] Ian A. Walmsley. Characterization of Ultrashort Optical Pulses in the Few-Cycle-Regime Using Spectral Phase Interferometry for Direct Electric-field Reconstruction. In F. X. Kärtner, editor, *Few-Cycle Laser Pulse Generation and Its Application*, Topics in Applied Physics 95. Springer, 2004.

[30] J. D. Jackson. *Classical Electrodynamics*. Wiley, 1975.

[31] F. Reynaud, F. Salin, and A. Barthelemy. Measurement of phase shifts introduced by nonlinear optical phenomena on subpicosecond pulses. *Opt. Lett.*, **14**:275, 1989.

[32] E. Hecht and A. Zajac. *Optics*. Addison Wesley, 3rd edition, 1997.

[33] M. Born and E. Wolf. *Principles of Optics: Electromagnetic Theory of Propagation, Interference and Diffraction of Light*. Cambridge University Press, 6th edition, 1997.

[34] B. D. Guenther. *Modern Optics*. Wiley, 1990.

[35] N. Huse. Master's thesis, Fakultät für Physik und Astronomie, Ruprecht-Karls-Universität Heidelberg, 2001.

[36] T. Wilson. *Confocal Microscopy*. Academic Press, 1990.

[37] Stefan Hell and Ernst H. K. Stelzer. Fundamental improvement of resolution with a 4Pi-confocal fluorescence microscope using two-photon excitation. *Opt. Commun.*, **93**(5-6):277–282, 1992.

[38] E. Synge. Suggested method for extending microscopic resolution into the ultra-microscopic region. *Philos. Mag.*, **6**:356, 1928.

[39] D. W. Pohl, W. Denk, and M. Lanz. Optical stethoscopy: Image recording with resolution $\lambda/20$. *Appl. Phys. Lett.*, **44**(7):651–653, 1984.

[40] A. Lewis, M. Isaacson, A. Harootunian, and A. Muray. Development of a 500 A spatial resolution light microscope : I. light is efficiently transmitted through $\lambda/16$ diameter apertures. *Ultramicroscopy*, **13**(3):227–231, 1984.

[41] G. Binnig, H. Rohrer, Ch. Gerber, and E. Weibel. 7×7 Reconstruction on Si(111) Resolved in Real Space. *Phys. Rev. Lett.*, **50**(2):120–123, 1983.

[42] E. Betzig, M. Isaacson, and A. Lewis. Collection Mode Near-Field Scanning Optical Microscopy. *Appl. Phys. Lett.*, **51**(25):2088–2090, 1987.

[43] M. Specht, J. D. Pedarnig, W. M. Heckl, and T. W. Hänsch. Scanning plasmon near-field microscope. *Phys. Rev. Lett.*, **68**(4):476–479, 1992.

[44] N. F. van Hulst, M. H. P. Moers, O. F. J. Noordman, R. G. Tack, F. B. Segerink, and B. Bolger. Near-field optical microscope using a silicon-nitride probe. *Appl. Phys. Lett.*, **62**(5):461–463, 1993.

[45] Y. Inouye and S. Kawata. Near-Field Scanning Optical Microscope with a Metallic Probe Tip. *Opt. Lett.*, **19**(3):159–161, 1994.

[46] L. Novotny and S. J. Stranick. Near-field optical microscopy and spectroscopy with pointed probes. *Annu. Rev. Phys. Chem.*, **57**:303–331, 2006.

[47] K. Matsuda, T. Saiki, S. Nomura, M. Mihara, Y. Aoyagi, S. Nair, and T. Takagahara. Near-Field Optical Mapping of Exciton Wave Functions in a GaAs Quantum Dot. *Phys. Rev. Lett.*, **91**(17):177401, 2003.

[48] T. Kalkbrenner, U. Håkanson, A. Schadle, S. Burger, C. Henkel, and V. Sandoghdar. Optical Microscopy via Spectral Modifications of a Nanoantenna. *Phys. Rev. Lett.*, **95**(20):200801, 2005.

[49] K. G. Lee, H. W. Kihm, J. E. Kihm, W. J. Choi, H. Kim, C. Ropers, D. J. Park, Y. C. Yoon, S. B. Choi, D. H. Woo, J. Kim, B. Lee, Q. H. Park, C. Lienau, and D.S. Kim. Vector field microscopic imaging of light. *Nature Phot.*, **1**:53–56, 2007.

[50] J. Michaelis, C. Hettich, J. Mlynek, and V. Sandoghdar. Optical microscopy using a single-molecule light source. *Nature*, **405**(6784):325–328, 2000.

[51] J. N. Farahani, D. W. Pohl, H.-J. Eisler, and B. Hecht. Single Quantum Dot Coupled to a Scanning Optical Antenna: A Tunable Superemitter. *Phys. Rev. Lett.*, **95**(1):017402, 2005.

[52] Claus Ropers, Tran Quoc Tien, Christoph Lienau, Jens W. Tomm, Peter Brick, Norbert Linder, B. Mayer, S. Tautz, and W. Schmid. Observation of deep level defects within the waveguide of red-emitting high-power diode lasers. *Appl. Phys. Lett.*, **88**:133513, 2006.

[53] R. Pomraenke, C. Ropers, J. Renard, C. Lienau, L. Lüer, D. Polli, and G. Cerullo. Structural phase contrast in polycrystalline organic semiconductor films observed by broadband near-field optical spectroscopy. *Nano Lett.*, **7**:998, 2007.

[54] R. Pomraenke, C. Ropers, J. Renard, C. Lienau, Lüer, D. Polli, and G. Cerullo. Broadband optical near-field microscope for nanoscale absorption spectroscopy of organic materials. *J. Microsc., **in press***, 2007.

[55] C. Lienau. Near-field scanning optical microscopy of semiconductor nanostructures. In J. Jimenez, editor, *Microprobe Characterization of Optoelectronic Materials*. Taylor and Francis, 2003.

[56] E. Betzig, P. L. Finn, and J. S. Weiner. Combined Shear Force and Near-Field Scanning Optical Microscopy. *Appl. Phys. Lett.*, **60**(20):2484–2486, 1992.

[57] Khaled Karrai and Robert D. Grober. Piezoelectric tip-sample distance control for near field optical microscopes. *Appl. Phys. Lett.*, **66**(14):1842–1844, 1995.

[58] Khaled Karrai and Ingo Tiemann. Interfacial shear force microscopy. *Phys. Rev. B*, **62**(19):13174–13181, 2000.

[59] Franz J. Giessibl. Advances in atomic force microscopy. *Rev. Mod. Phys.*, **75**(3):949, 2003.

[60] W. H. J. Rensen, N. F. van Hulst, A. G. T. Ruiter, and P. E. West. Atomic steps with tuning-fork-based noncontact atomic force microscopy. *Appl. Phys. Lett.*, **75**(11):1640–1642, 1999.

[61] C. Durkan and I. V. Shvets. Investigation of the physical mechanisms of shear-force imaging. *J. Appl. Phys.*, **80**(10):5659–5664, 1996.

[62] L. Merz and H. Jaschek. *Grundkurs der Regelungstechnik*. Oldenbourg, 2003.

[63] E. Betzig. In D. Pohl and D. Courjon, editors, *Near Field Optics*, volume **242** of *NATO ASI*. Kluwer, 1993.

[64] B. Hecht, H. Bielefeldt, Y. Inouye, D. W. Pohl, and L. Novotny. Facts and artifacts in near-field optical microscopy. *J. Appl. Phys.*, **81**(6):2492–2498, 1997.

[65] Jean-Jacques Greffet and Remi Carminati. Image formation in near-field optics. *Prog. Surf. Sci.*, **56**(3):133–237, 1997.

[66] Christian Girard and Alain Dereux. Near-field optics theories. *Rep. Prog. Phys.*, **59**(5):657–699, 1996.

[67] M. A. Paesler and P. J. Moyer. *Near-Field Optics: Theory, Instrumentation, and Applications*. Wiley, 1996.

[68] S. Kawata, editor. *Near-Field Optics and Surface Plasmon Polaritons*. Springer, 2001.

[69] M. Ohtsu and K. Kobayahi. *Optical Near Fields*. Springer, 2004.

[70] L. Novotny, B. Hecht, and D. W. Pohl. Interference of locally excited surface plasmons. *J. Appl. Phys.*, **81**(4):1798–1806, 1997.

[71] A. B. Evlyukhin and S. I. Bozhevolnyi. Point-dipole approximation for surface plasmon polariton scattering: Implications and limitations. *Phys. Rev. B*, **71**(13):134304, 2005.

[72] T. Søndergaard and S. I. Bozhevolnyi. Vectorial model for multiple scattering by surface nanoparticles via surface polariton-to-polariton interactions. *Phys. Rev. B*, **67**(16):165405, 2003.

[73] Ole Keller, Mufei Xiao, and Sergey Bozhevolnyi. Configurational resonances in optical near-field microscopy: a rigorous point-dipole approach. *Surf. Sci.*, **280**(1-2):217–230, 1993.

[74] T. Kalkbrenner, U. Håkanson, and V. Sandoghdar. Tomographic Plasmon Spectroscopy of a Single Gold Nanoparticle. *Nano Lett.*, **4**(12):2309–2314, 2004.

[75] Alain Dereux, Christian Girard, and Jean-Claude Weeber. Theoretical principles of near-field optical microscopies and spectroscopies. *J. Chem. Phys.*, **112**(18):7775–7789, 2000.

[76] C. Girard and D. Courjon. Model for scanning tunneling optical microscopy: A microscopic self-consistent approach. *Phys. Rev. B*, **42**(15): 9340–9349, 1990.

[77] Bernhard Knoll and Fritz Keilmann. Enhanced dielectric contrast in scattering-type scanning near-field optical microscopy. *Opt. Commun.*, **182** (4-6):321–328, 2000.

[78] Mufei Xiao, Anatoly Zayats, and Jesús Siqueiros. Scattering of surface-plasmon polaritons by dipoles near a surface: Optical near-field localization. *Phys. Rev. B*, **55**(3):1824–1837, 1997.

[79] L. Novotny. Allowed and forbidden light in near-field optics. I. A single dipolar light source. *J. Opt. Soc. Am. A*, **14**:91, 1997.

[80] L. Novotny. Allowed and forbidden light in near-field optics. II. Interacting dipolar particles. *J. Opt. Soc. Am. A*, **14**:105, 1997.

[81] M. Xiao. Theoretical treatment for scattering scanning near-field optical microscopy. *J. Opt. Soc. Am. A*, **14**:2977, 1997.

[82] A. Madrazo, R. Carminati, M. Nieto-Vesperinas, and Greffet J.-J. Polarization effects in the optical interaction between a nanoparticle and a corrugated surface: implications for apertureless near-field microscopy. *J. Opt. Soc. Am. A*, **15**:109, 1998.

[83] H. C. van de Hulst. *Light Scattering by Small Particles*. Dover, 1981.

[84] C. F. Bohren and D. R. Huffman. *Absorption and Scattering of Light by Small Particles*. Wiley, 1998.

[85] H. A. Bethe. Theory of Diffraction by Small Holes. *Phys. Rev.*, **66**(7-8): 163–182, 1944.

[86] C. J. Bouwkamp. Diffraction Theory. *Rep. Prog. Phys.*, **17**(1):35–100, 1954.

[87] D. van Labeke and D. Barchiesi. Probes for scanning tunneling optical microscopy - a theoretical comparison. *J. Opt. Soc. Am. A*, **10**(10):2193–2201, 1993.

[88] Eloise Devaux, Alain Dereux, Eric Bourillot, Jean-Claude Weeber, Yvon Lacroute, Jean-Pierre Goudonnet, and Christian Girard. Detection of the optical magnetic field by circular symmetry plasmons. *Appl. Surf. Sci.*, **164** (1-4):124–130, 2000.

[89] A. M. Lindenberg, J. Larsson, K. Sokolowski-Tinten, K. J. Gaffney, C. Blome, O. Synnergren, J. Sheppard, C. Caleman, A. G. MacPhee, D. Weinstein, D. P. Lowney, T. K. Allison, T. Matthews, R. W. Falcone, A. L. Cavalieri, D. M. Fritz, S. H. Lee, P. H. Bucksbaum, D. A. Reis, J. Rudati, P. H. Fuoss, C. C. Kao, D. P. Siddons, R. Pahl, J. Als-Nielsen, S. Duesterer, R. Ischebeck, H. Schlarb, H. Schulte-Schrepping, Th. Tschentscher, J. Schneider, D. von der Linde, O. Hignette, F. Sette, H. N. Chapman, R. W. Lee, T. N. Hansen, S. Techert, J. S. Wark, M. Bergh, G. Huldt, D. van der Spoel, N. Timneanu, J. Hajdu, R. A. Akre, E. Bong, P. Krejcik, J. Arthur, S. Brennan, K. Luening, and J. B. Hastings. Atomic-Scale Visualization of Inertial Dynamics. *Science*, **308**:392–395, 2005.

[90] R. H. Ritchie. Plasma Losses by Fast Electrons in Thin Films. *Phys. Rev.*, **106**(5):874–881, 1957.

[91] E. A. Stern and R. A. Ferrell. Surface Plasma Oscillations of a Degenerate Electron Gas. *Phys. Rev.*, **120**(1):130–136, 1960.

[92] C. J. Powell and J. B. Swan. Effect of Oxidation on the Characteristic Loss Spectra of Aluminum and Magnesium. *Phys. Rev.*, **118**(3):640–643, 1960.

[93] R. H. Ritchie, E. T. Arakawa, J. J. Cowan, and R. N. Hamm. Surface-Plasmon Resonance Effect in Grating Diffraction. *Phys. Rev. Lett.*, **21**(22): 1530–1533, 1968.

[94] V. M. Agranovich and D. L. Mills, editors. *Surface Polaritons*. North-Holland, 1982.

[95] H. J. Simon, D. E. Mitchell, and J. G. Watson. Optical Second-Harmonic Generation with Surface Plasmons in Silver Films. *Phys. Rev. Lett.*, **33**(26): 1531–1534, 1974.

[96] J. C. Quail, J. G. Rako, H. J. Simon, and R. T. Deck. Optical Second-Harmonic Generation with Long-Range Surface Plasmons. *Phys. Rev. Lett.*, **50**(25):1987–1989, 1983.

[97] A. L. Moretti, W. M. Robertson, B. Fisher, and Ralph Bray. Surface-enhanced Brillouin scattering on silver films. *Phys. Rev. B*, **31**(6):3361–3368, 1984.

[98] T. Tsang, T. Srinivasan-Rao, and J. Fischer. Surface-plasmon field-enhanced multiphoton photoelectric emission from metal films. *Phys. Rev. B*, **43**(11):8870–8878, 1991.

[99] M. Fleischmann, P. J. Hendra, and A. J. McQuillan. Raman spectra of pyridine adsorbed at a silver electrode. *Chem. Phys. Lett.*, **26**(2):163–166, 1974.

[100] David L. Jeanmaire and Richard P. Van Duyne. Surface Raman spectroelectrochemistry: Part I. Heterocyclic, aromatic, and aliphatic amines adsorbed on the anodized silver electrode. *J. Electroanal. Chem.*, **84**(1):1–20, 1977.

[101] M. Grant Albrecht and J. Alan Creighton. Anomalously intense Raman spectra of pyridine at a silver electrode. *J. Am. Chem. Soc.*, **99**:5215, 1977.

[102] J. A. Creighton, C. G. Blatchford, and M. G. Albrecht. Plasma resonance enhancement of Raman scattering by pyridine adsorbed on silver or gold sol particles of size comparable to the excitation wavelength. *J. Chem. Soc. Farad. T. 2*, **75**:790–798, 1979.

[103] D. W. Lynch and W. R. Hunter. In E. D. Palik, editor, *Handbook of Optical Constants of Solids*. Academic Press, 1998.

[104] L. D. Landau and E. M. Lifshitz. *Electrodynamics of Continuous Media*. Pergamon, 1960.

[105] N. W. Ashcroft and N. D. Mermin. *Festkörperphysik*. Oldenbourg, 2001.

[106] C. Kittel. *Introduction to Solid State Physics*. Wiley, 7th edition, 1996.

[107] J. A. Dionne, L. A. Sweatlock, H. A. Atwater, and A. Polman. Planar metal plasmon waveguides: frequency-dependent dispersion, propagation, localization, and loss beyond the free electron model. *Phys. Rev. B*, **72**(7): 075405, 2005.

[108] P. Winsemius, M. Guerrisi, and R. Rosei. Splitting of the interband absorption edge in Au: Temperature dependence. *Phys. Rev. B*, **12**(10):4570–4572, 1975.

[109] P. B. Johnson and R. W. Christy. Optical Constants of the Noble Metals. *Phys. Rev. B*, **6**(12):4370–4379, 1972.

[110] E. Kretschmann and H. Raether. Radiative decay of non-radiative surface plasmons excited by light. *Z. Naturforsch.*, **A 23**(12):2135, 1968.

[111] E. Kretschmann. Die Bestimmung optischer Konstanten von Metallen durch Anregung von Oberflächenplasmaschwingungen. *Z. Physik A*, **V241** (4):313–324, 1971.

[112] Andreas Otto. Excitation of nonradiative surface plasma waves in silver by the method of frustrated total reflection. *Z. Physik A*, **V216**(4):398–410, 1968.

[113] E. Kretschmann. Die Bestimmung der Oberflächenrauhigkeit dünner Schichten durch Messung der Winkelabhängigkeit der Streustrahlung von Oberflächenplasmaschwingungen. *Opt. Commun.*, **10**(4):353–356, 1974.

[114] E. Schröder. Untersuchungen über den Zusammenhang von Plasmaresonanzstrahlung und Oberflächenrauhigkeit an dünnen Silberschichten. *Z. Physik A*, **V225**(1):26–38, 1969.

[115] A. J. Braundmeier, Jr. and E. T. Arakawa. Effect of surface roughness on surface plasmon resonance absorption. *J. Phys. Chem. Solids*, **35**(4):517–520, 1973.

[116] E. Kroeger and E. Kretschmann. Scattering of light by slightly rough surfaces or thin films including plasma resonance emission. *Z. Physik A*, **237**: 1, 1970.

[117] W. L. Barnes, T. W. Preist, S. C. Kitson, J. R. Sambles, N. P. K. Cotter, and D. J. Nash. Photonic gaps in the dispersion of surface plasmons on gratings. *Phys. Rev. B*, **51**(16):11164–11167, 1995.

[118] W. L. Barnes, T. W. Preist, S. C. Kitson, and J. R. Sambles. Physical origin of photonic energy gaps in the propagation of surface plasmons on gratings. *Phys. Rev. B*, **54**(9):6227–6244, 1996.

[119] H. F. Ghaemi, T. Thio, D. E. Grupp, T. W. Ebbesen, and H. J. Lezec. Surface plasmons enhance optical transmission through subwavelength holes. *Phys. Rev. B*, **58**(11):6779–6782, 1998.

[120] E. Popov, M. Nevière, S. Enoch, and R. Reinisch. Theory of light transmission through subwavelength periodic hole arrays. *Phys. Rev. B*, **62**(23): 16100–16108, 2000.

[121] L. Martín-Moreno, F. J. García-Vidal, H. J. Lezec, K. M. Pellerin, T. Thio, J. B. Pendry, and T. W. Ebbesen. Theory of Extraordinary Optical Transmission through Subwavelength Hole Arrays. *Phys. Rev. Lett.*, **86**(6):1114–1117, 2001.

[122] Qing Cao and Philippe Lalanne. Negative Role of Surface Plasmons in the Transmission of Metallic Gratings with Very Narrow Slits. *Phys. Rev. Lett.*, **88**(5):057403, 2002.

[123] Hugo F. Schouten, Taco D. Visser, Greg Gbur, Daan Lenstra, and Hans Blok. Connection between Phase Singularities and the Radiation Pattern of a Slit in a Metal Plate. *Phys. Rev. Lett.*, **93**(17):173901, 2004.

[124] K. J. Klein Koerkamp, S. Enoch, F. B. Segerink, N. F. van Hulst, and L. Kuipers. Strong Influence of Hole Shape on Extraordinary Transmission through Periodic Arrays of Subwavelength Holes. *Phys. Rev. Lett.*, **92**(18):183901, 2004.

[125] Henri Lezec and Tineke Thio. Diffracted evanescent wave model for enhanced and suppressed optical transmission through subwavelength hole arrays. *Opt. Express*, **12**:3629, 2004.

[126] S. C. Hohng, Y. C. Yoon, D. S. Kim, V. Malyarchuk, R. Muller, Ch. Lienau, J. W. Park, K. H. Yoo, J. Kim, H. Y. Ryu, and Q. H. Park. Light emission from the shadows: Surface plasmon nano-optics at near and far fields. *Appl. Phys. Lett.*, **81**(17):3239–3241, 2002.

[127] C. Ropers, D. J. Park, G. Stibenz, G. Steinmeyer, J. Kim, D. S. Kim, and C. Lienau. Femtosecond Light Transmission and Subradiant Damping in Plasmonic Crystals. *Phys. Rev. Lett.*, **94**(11):113901–4, 2005.

[128] C. Genet and T. W. Ebbesen. Light in tiny holes. *Nature*, **445**(7123):39–46, 2007.

[129] Roland Müller, Viktor Malyarchuk, and Christoph Lienau. Three-dimensional theory on light-induced near-field dynamics in a metal film with a periodic array of nanoholes. *Phys. Rev. B*, **68**(20):205415, 2003.

[130] Hans Lochbihler and Ricardo A. Depine. Characterization of highly conducting wire gratings using an electromagnetic theory of diffraction. *Opt. Commun.*, **100**(1-4):231–239, 1993.

[131] H. Lochbihler and R. Depine. Highly conducting wire gratings in the resonance region. *Appl. Optics*, **32**:3459, 1993.

[132] H. Lochbihler and R. Depine. Diffraction from highly conducting wire gratings of arbitrary cross-section. *J. Mod. Optic.*, **40**:1273, 1993.

[133] Hans Lochbihler. Surface polaritons on gold-wire gratings. *Phys. Rev. B*, **50**(7):4795–4801, 1994.

[134] H. Lochbihler. Field enhancement on metallic wire gratings. *Opt. Commun.*, **111**:417, 1994.

[135] Hans Lochbihler. Surface polaritons on metallic wire gratings studied via power losses. *Phys. Rev. B*, **53**(15):10289–10295, 1996.

[136] R. A. Depine and J. M. Simon. Surface Impedance Boundary-Condition for Metallic Diffraction Gratings in the Optical and Infrared Range. *Opt. Acta*, **30**(3):313–322, 1983.

[137] R. A. Depine. Perfectly conducting diffraction grating formalisms extended to good conductors via the surface impedance boundary condition. *Appl. Optics*, **26**:2348, 1987.

[138] Jin E. Kihm, Y. C. Yoon, D. J. Park, Y. H. Ahn, C. Ropers, C. Lienau, J. Kim, Q. H. Park, and D. S. Kim. Fabry-Perot tuning of the band-gap polarity in plasmonic crystals. *Phys. Rev. B*, **75**(3):035414, 2007.

[139] E. Altewischer, M. P. van Exter, and J. P. Woerdman. Plasmon-assisted transmission of entangled photons. *Nature*, **418**:304, 2002.

[140] E. Altewischer, M. P. van Exter, and J. P. Woerdman. Nonreciprocal reflection of a subwavelength hole array. *Opt. Lett.*, **28**(20):1906, 2003.

[141] Paul N. Stavrinou and Laszlo Solymar. Pulse delay and propagation through subwavelength metallic slits. *Phys. Rev. E*, **68**(6):066604, 2003.

[142] T. Zentgraf, A. Christ, J. Kuhl, and H. Giessen. Tailoring the Ultrafast Dephasing of Quasiparticles in Metallic Photonic Crystals. *Phys. Rev. Lett.*, **93**(24):243901, 2004.

[143] C. Ropers, G. Stibenz, G. Steinmeyer, R. Müller, D. J. Park, K. G. Lee, J. E. Kihm, J. Kim, Q. H. Park, D. S. Kim, and C. Lienau. Ultrafast dynamics of surface plasmon polaritons in plasmonic metamaterials. *Appl. Phys. B*, **84**(1):183–189, 2006.

[144] Michael Sarrazin, Jean-Pol Vigneron, and Jean-Marie Vigoureux. Role of Wood anomalies in optical properties of thin metallic films with a bidimensional array of subwavelength holes. *Phys. Rev. B*, **67**(8):085415, 2003.

[145] C. Genet, M. P. van Exter, and J. P. Woerdman. Fano-type interpretation of red shifts and red tails in hole array transmission spectra. *Opt. Commun.*, **225**(4-6):331–336, 2003.

[146] U. Fano. Zur Theorie der Intensitätsanomalien der Beugung. *Ann. Phys.*, **424**(5):393, 1938.

[147] U. Fano. Effects of Configuration Interaction on Intensities and Phase Shifts. *Phys. Rev.*, **124**(6):1866–1878, 1961.

[148] R. H. Dicke. Coherence in Spontaneous Radiation Processes. *Phys. Rev.*, **93**(1):99, 1954.

[149] R. G. DeVoe and R. G. Brewer. Observation of Superradiant and Subradiant Spontaneous Emission of Two Trapped Ions. *Phys. Rev. Lett.*, **76**(12):2049–2052, 1996.

[150] Dominik Schneble, Yoshio Torii, Micah Boyd, Erik W. Streed, David E. Pritchard, and Wolfgang Ketterle. The Onset of Matter-Wave Amplification in a Superradiant Bose-Einstein Condensate. *Science*, **300**(5618):475–478, 2003.

[151] Sang-Hyun Lim, Thomas G. Bjorklund, Frank C. Spano, and Christopher J. Bardeen. Exciton Delocalization and Superradiance in Tetracene Thin Films and Nanoaggregates. *Phys. Rev. Lett.*, **92**(10):107402, 2004.

[152] F. Meinardi, M. Cerminara, A. Sassella, A. Borghesi, P. Spearman, G. Bongiovanni, A. Mura, and R. Tubino. Intrinsic Excitonic Luminescence in Odd and Even Numbered Oligothiophenes. *Phys. Rev. Lett.*, **89**(15): 157403, 2002.

[153] Y. N. Chen, D. S. Chuu, and T. Brandes. Current Detection of Superradiance and Induced Entanglement of Double Quantum Dot Excitons. *Phys. Rev. Lett.*, **90**(16):166802, 2003.

[154] M. Hübner, J. Kuhl, T. Stroucken, A. Knorr, S. W. Koch, R. Hey, and K. Ploog. Collective Effects of Excitons in Multiple-Quantum-Well Bragg and Anti-Bragg Structures. *Phys. Rev. Lett.*, **76**(22):4199–4202, 1996.

[155] A. Christ, S. G. Tikhodeev, N. A. Gippius, J. Kuhl, and H. Giessen. Waveguide-Plasmon Polaritons: Strong Coupling of Photonic and Electronic Resonances in a Metallic Photonic Crystal Slab. *Phys. Rev. Lett.*, **91** (18):183901, 2003.

[156] P. Paddon and Jeff F. Young. Two-dimensional vector-coupled-mode theory for textured planar waveguides. *Phys. Rev. B*, **61**(3):2090–2101, 2000.

[157] S. G. Tikhodeev, A. L. Yablonskii, E. A. Muljarov, N. A. Gippius, and Teruya Ishihara. Quasiguided modes and optical properties of photonic crystal slabs. *Phys. Rev. B*, **66**(4):045102, 2002.

[158] P. Lalanne, C. Sauvan, J. P. Hugonin, J. C. Rodier, and P. Chavel. Perturbative approach for surface plasmon effects on flat interfaces periodically corrugated by subwavelength apertures. *Phys. Rev. B*, **68**(12):125404, 2003.

[159] Steven G. Johnson, M. Ibanescu, M. A. Skorobogatiy, O. Weisberg, J. D. Joannopoulos, and Y. Fink. Perturbation theory for Maxwell's equations with shifting material boundaries. *Phys. Rev. E*, **65**(6):066611, 2002.

[160] Uzma Akram, Z. Ficek, and S. Swain. Decoherence and coherent population transfer between two coupled systems. *Phys. Rev. A*, **62**(1):013413, 2000.

[161] T. Shih, K. Reimann, M. Woerner, T. Elsaesser, I. Waldmuller, A. Knorr, R. Hey, and K. H. Ploog. Radiative coupling of intersubband transitions in GaAs/AlGaAs multiple quantum wells. *Physica E*, **32**(1-2):262–265, 2006.

[162] Sergey I. Bozhevolnyi and Victor Coello. Elastic scattering of surface plasmon polaritons: Modeling and experiment. *Phys. Rev. B*, **58**(16):10899–10910, 1998.

[163] Sergey I. Bozhevolnyi and Valentyn S. Volkov. Multiple-scattering dipole approach to modeling of surface plasmon polariton band gap structures. *Opt. Commun.*, **198**(4-6):241–245, 2001.

[164] J. Seidel. *Propagation, Scattering and Amplification of Surface Plasmons in Thin Silver Films*. PhD thesis, Institut für Angewandte Physik, Fachrichtung Physik, Fakultät Mathematik und Naturwissenschaften, Technische Universität Dresden, 2005.

[165] H. Ditlbacher, J. R. Krenn, A. Hohenau, A. Leitner, and F. R. Aussenegg. Efficiency of local light-plasmon coupling. *Appl. Phys. Lett.*, **83**(18):3665–3667, 2003.

[166] Jan Renger. *Excitation, Interaction, and Scattering of Localized and Propagating Surface Polaritons*. PhD thesis, Institut für Angewandte Physik, Fachrichtung Physik, Fakultät Mathematik und Naturwissenschaften, Technische Universität Dresden, 2006.

[167] P. Lalanne, J. P. Hugonin, and J. C. Rodier. Theory of Surface Plasmon Generation at Nanoslit Apertures. *Phys. Rev. Lett.*, **95**(26):263902, 2005.

[168] U. Schröter and D. Heitmann. Surface-plasmon-enhanced transmission through metallic gratings. *Phys. Rev. B*, **58**(23):15419–15421, 1998.

[169] J. B. Pendry, L. Martin-Moreno, and F. J. Garcia-Vidal. Mimicking Surface Plasmons with Structured Surfaces. *Science*, **305**(5685):847–848, 2004.

[170] Alastair P. Hibbins, Benjamin R. Evans, and J. Roy Sambles. Experimental Verification of Designer Surface Plasmons. *Science*, **308**(5722):670–672, 2005.

[171] R. Müller, C. Ropers, and C. Lienau. Femtosecond light pulse propagation through metallic nanohole arrays: The role of the dielectric substrate. *Opt. Express*, **12**:5067, 2004.

[172] A. Krishnan, T. Thio, T. J. Kim, H. J. Lezec, T. W. Ebbesen, P. A. Wolff, J. Pendry, L. Martin-Moreno, and F. J. Garcia-Vidal. Evanescently coupled resonance in surface plasmon enhanced transmission. *Opt. Commun.*, **200** (1-6):1–7, 2001.

[173] Yun Suk Jung, Zhijun Sun, Jeff Wuenschell, Hong Koo Kim, Palwinder Kaur, Lei Wang, and David Waldeck. High-sensitivity surface plasmon resonance spectroscopy based on a metal nanoslit array. *Appl. Phys. Lett.*, **88**(24):243105, 2006.

[174] Zhijun Sun and Hong Koo Kim. Refractive transmission of light and beam shaping with metallic nano-optic lenses. *Appl. Phys. Lett.*, **85**(4):642–644, 2004.

[175] D. Nau, A. Schönhardt, C. Bauer, A. Christ, T. Zentgraf, J. Kuhl, and H. Giessen. Disorder issues in metallic photonic crystals. *phys. stat. sol. b*, **243**(10):2331–2343, 2006.

[176] A. S. Vengurlekar, A. Venu Gopal, and T. Ishihara. Femtosecond pulse distortion at surface plasmon resonances in a plasmonic crystal: Effect of surface plasmon lifetime. *Appl. Phys. Lett.*, **89**(18):181927, 2006.

[177] O. Marti, H. Bielefeldt, B. Hecht, S. Herminghaus, P. Leiderer, and J. Mlynek. Near-field optical measurement of the surface plasmon field. *Opt. Commun.*, **96**(4-6):225–228, 1993.

[178] P. M. Adam, L. Salomon, F. de Fornel, and J. P. Goudonnet. Determination of the spatial extension of the surface-plasmon evanescent field of a silver film with a photon scanning tunneling microscope. *Phys. Rev. B*, **48**(4): 2680–2683, 1993.

[179] J. R. Krenn, R. Wolf, A. Leitner, and F. R. Aussenegg. Near-field optical imaging the surface plasmon fields of lithographically designed nanostructures. *Opt. Commun.*, **137**(1-3):46–50, 1997.

[180] J.-C. Weeber, J. R. Krenn, A. Dereux, B. Lamprecht, Y. Lacroute, and J. P. Goudonnet. Near-field observation of surface plasmon polariton propagation on thin metal stripes. *Phys. Rev. B*, **64**(4):045411, 2001.

[181] Sergey I. Bozhevolnyi, John Erland, Kristjan Leosson, Peter M. W. Skovgaard, and Jørn M. Hvam. Waveguiding in Surface Plasmon Polariton Band Gap Structures. *Phys. Rev. Lett.*, **86**(14):3008–3011, 2001.

[182] H. Gao, J. Henzie, and T. W. Odom. Direct Evidence for Surface Plasmon-Mediated Enhanced Light Transmission through Metallic Nanohole Arrays. *Nano Lett.*, **6**(9):2104–2108, 2006.

[183] Remi Carminati and Jean-Jacques Greffet. Two-dimensional numerical simulation of the photon scanning tunneling microscope. Concept of transfer function. *Opt. Commun.*, **116**(4-6):316–321, 1995.

[184] A. Bouhelier, M. Beversluis, A. Hartschuh, and L. Novotny. Near-Field Second-Harmonic Generation Induced by Local Field Enhancement. *Phys. Rev. Lett.*, **90**:013903, 2003.

[185] Catalin C. Neacsu, Georg A. Reider, and Markus B. Raschke. Second-harmonic generation from nanoscopic metal tips: Symmetry selection rules for single asymmetric nanostructures. *Phys. Rev. B*, **71**(20):201402, 2005.

[186] C. C. Neacsu, G. A. Steudle, and M. B. Raschke. Plasmonic light scattering from nanoscopic metal tips. *Appl. Phys. B*, **V80**(3):295–300, 2005.

[187] Bin Ren, Gennaro Picardi, and Bruno Pettinger. Preparation of gold tips suitable for tip-enhanced Raman spectroscopy and light emission by electrochemical etching. *Rev. Sci. Instrum.*, **75**(4):837–841, 2004.

[188] L. Novotny, D. W. Pohl, and B. Hecht. Scanning near-field optical probe with ultrasmall spot size. *Opt. Lett.*, **20**(9):970–972, 1995.

[189] A. Drezet, J. C. Woehl, and S. Huant. Far-field emission of a tapered optical fibre tip: a theoretical analysis. *J. Microsc.*, **202**(2):359–361, 2001.

[190] Christian Obermuller and Khaled Karrai. Far field characterization of diffracting circular apertures. *Appl. Phys. Lett.*, **67**(23):3408–3410, 1995.

[191] S. I. Bozhevolnyi. Near-field mapping of surface polariton fields. *J. Microsc.*, **202**(2):313–319, 2001.

[192] J. P. Kottmann, O. J. F. Martin, D. R. Smith, and S. Schultz. Non-regularly shaped plasmon resonant nanoparticle as localized light source for near-field microscopy. *J. Microsc.*, **202**(1):60–65, 2001.

[193] J. B. Pendry. Negative Refraction Makes a Perfect Lens. *Phys. Rev. Lett.*, **85**(18):3966–3969, 2000.

[194] Michael R. Beversluis, Alexandre Bouhelier, and Lukas Novotny. Continuum generation from single gold nanostructures through near-field mediated intraband transitions. *Phys. Rev. B*, **68**:115433, 2003.

[195] M. Labardi, M. Allegrini, M. Zavelani-Rossi, D. Polli, G. Cerullo, S. De Silvestri, and O. Svelto. Highly efficient second-harmonic nanosource for near-field optics and microscopy. *Opt. Lett.*, **29**:62–64, 2004.

[196] C. Ropers, D. R. Solli, C. P. Schulz, C. Lienau, and T. Elsaesser. Localized Multiphoton Emission of Femtosecond Electron Pulses from Metal Nanotips. *Phys. Rev. Lett.*, **98**(4):043907, 2007.

[197] B. C. Buchler, T. Kalkbrenner, C. Hettich, and V. Sandoghdar. Measuring the Quantum Efficiency of the Optical Emission of Single Radiating Dipoles Using a Scanning Mirror. *Phys. Rev. Lett.*, **95**(6):063003, 2005.

[198] Sergei Kuhn, Ulf Håkanson, Lavinia Rogobete, and Vahid Sandoghdar. Enhancement of Single-Molecule Fluorescence Using a Gold Nanoparticle as an Optical Nanoantenna. *Phys. Rev. Lett.*, **97**(1):017402, 2006.

[199] W. Patrick Ambrose, Peter M. Goodwin, Richard A. Keller, and John C. Martin. Alterations of Single Molecule Fluorescence Lifetimes in Near-Field Optical Microscopy. *Science*, **265**(5170):364–367, 1994.

[200] A. Femius Koenderink, Maria Kafesaki, Ben C. Buchler, and Vahid Sandoghdar. Controlling the Resonance of a Photonic Crystal Microcavity by a Near-Field Probe. *Phys. Rev. Lett.*, **95**(15):153904, 2005.

[201] S. Götzinger, O. Benson, and V. Sandoghdar. Influence of a sharp fiber tip on high-Q modes of a microsphere resonator. *Opt. Lett.*, **27**(2):80–82, 2002.

[202] A. Mazzei, H. Krauter, Oliver Benson, and Stephan Gotzinger. Influence of a controllable scatterer on the lasing properties of an ultralow threshold Raman microlaser. *Appl. Phys. Lett.*, **89**(10):101105, 2006.

[203] A. A. Mikhailovsky, M. A. Petruska, M. I. Stockman, and V. I. Klimov. Broadband near-field interference spectroscopy of metal nanoparticles using a femtosecond white-light continuum. *Opt. Lett.*, **28**, 2003.

[204] A. A. Mikhailovsky, M. A. Petruska, Kuiru Li, M. I. Stockman, and V. I. Klimov. Phase-sensitive spectroscopy of surface plasmons in individual metal nanostructures. *Phys. Rev. B*, **69**(8):085401, 2004.

[205] J. Seidel, S. Grafstrom, Ch. Loppacher, S. Trogisch, F. Schlaphof, and L. M. Eng. Near-field spectroscopy with white-light illumination. *Appl. Phys. Lett.*, **79**(14):2291–2293, 2001.

[206] Achim Hartschuh, Erik J. Sánchez, X. Sunney Xie, and Lukas Novotny. High-Resolution Near-Field Raman Microscopy of Single-Walled Carbon Nanotubes. *Phys. Rev. Lett.*, **90**(9):095503, 2003.

[207] B. Lamprecht, J. R. Krenn, G. Schider, H. Ditlbacher, M. Salerno, N. Felidj, A. Leitner, F. R. Aussenegg, and J. C. Weeber. Surface plasmon propagation in microscale metal stripes. *Appl. Phys. Lett.*, **79**(1):51–53, 2001.

[208] Mark I. Stockman. Nanofocusing of Optical Energy in Tapered Plasmonic Waveguides. *Phys. Rev. Lett.*, **93**(13):137404, 2004.

[209] Hyotcherl Ihee, Vladimir A. Lobastov, Udo M. Gomez, Boyd M. Goodson, Ramesh Srinivasan, Chong-Yu Ruan, and Ahmed H. Zewail. Direct Imaging of Transient Molecular Structures with Ultrafast Diffraction. *Science*, **291**:458–462, 2001.

[210] Bradley J. Siwick, Jason R. Dwyer, Robert E. Jordan, and R. J. Dwayne Miller. An Atomic-Level View of Melting Using Femtosecond Electron Diffraction. *Science*, **302**:1382–1385, 2003.

[211] C.-Y. Ruan, Y. Murooka, R. K. Raman, and R. A. Murdick. Dynamics of Size-Selected Gold Nanoparticles Studied by Ultrafast Electron Nanocrystallography. *Nano Lett.*, 2007. ISSN 1530-6984.

[212] Vladimir A. Lobastov, Ramesh Srinivasan, and Ahmed H. Zewail. Four-dimensional ultrafast electron microscopy. *P. Natl. Acad. Sci. USA*, **102** (20):7069–7073, 2005.

[213] Wayne E. King, Geoffrey H. Campbell, Alan Frank, Bryan Reed, John F. Schmerge, Bradley J. Siwick, Brent C. Stuart, and Peter M. Weber. Ultrafast electron microscopy in materials science, biology, and chemistry. *J. Appl. Phys.*, **97**:111101, 2005.

[214] M. Bargheer, N. Zhavoronkov, Y. Gritsai, J. C. Woo, D. S. Kim, M. Woerner, and T. Elsaesser. Coherent Atomic Motions in a Nanostructure Studied by Femtosecond X-ray Diffraction. *Science*, **306**:1771–1773, 2004.

[215] B. J. Siwick, J. R. Dwyer, R. E. Jordan, and R. J. D. Miller. Ultrafast electron optics: Propagation dynamics of femtosecond electron packets. *J. Appl. Phys.*, **92**:1643–1648, 2002.

[216] C. T. Hebeisen, R. Ernstorfer, M. Harb, T. Dartigalongue, R. E. Jordan, and R. J. D. Miller. Femtosecond electron pulse characterization using laser ponderomotive scattering. *Opt. Lett.*, **31**(23):3517–3519, 2006.

[217] Bradley J. Siwick, Alexander A. Green, Christoph T. Hebeisen, and R. J. Dwayne Miller. Characterization of ultrashort electron pulses by electron-laser pulse cross correlation. *Opt. Lett.*, **30**:1057–1059, 2005.

[218] Ernst Fill, Laszlo Veisz, Alexander Apolonski, and Ferenc Krausz. Sub-fs electron pulses for ultrafast electron diffraction. *New J. Phys.*, **8**(11):272, 2006.

[219] E. W. Müller. Elektronenmikroskopische Beobachtungen von Feldkathoden. *Z. Physik A*, **106**(9):541–550, 1937.

[220] M. Boussoukaya, H. Bergeret, R. Chehab, B. Leblond, and J. Le Duff. High quantum yield from photofield emitters. *Nucl. Instr. Meth. A*, **279**:405–409, 1989.

[221] C. Hernandez-Garcia and C. A. Brau. Electron beams formed by photoelectric field emission. *Nucl. Instr. Meth. A*, **475**:559–563, 2001.

[222] C. Hernandez Garcia and C. A. Brau. Pulsed photoelectric field emission from needle cathodes. *Nucl. Instr. Meth. A*, **483**:273–276, 2002.

[223] S. A. Aseyev, B. N. Mironov, S. V. Chekalin, and V. S. Letokhov. Femtosecond laser source of nanolocalized directed photoelectrons. *Appl. Phys. Lett.*, **89**(11):112513, 2006.

[224] Peter Hommelhoff, Yvan Sortais, Anoush Aghajani Talesh, and Mark A. Kasevich. Field Emission Tip as a Nanometer Source of Free Electron Femtosecond Pulses. *Phys. Rev. Lett.*, **96**:077401, 2006.

[225] A. Einstein. Über einen die Erzeugung und Verwandlung des Lichtes betreffenden heuristischen Gesichtspunkt. *Ann. Phys.*, **17**:132, 1905.

[226] C. N. Berglund and W. E. Spicer. Photoemission Studies of Copper and Silver: Theory. *Phys. Rev.*, **136**(4A):A1030–A1044, 1964.

[227] W. Schattkey and M. A. van Hove, editors. *Solid-State Photoemission and Related Methods: Theory and Experiment*. Wiley, 2003.

[228] M. J. Lisowski. *Elektronen- und Magnetisierungsdynamik in Metallen untersucht mit zeitaufgelöster Photoemission*. PhD thesis, Fachbereich Physik, Freie Universität Berlin, 2005.

[229] R. H. Fowler and L. W. Nordheim. Electron Emission in Intense Electric Fields. *Proc. Roy. Soc. (London) A*, **119**:173, 1928.

[230] S. Gasiorowicz. *Quantum Physics*. Wiley, 3rd edition, 2003.

[231] R. E. Burgess, H. Kroemer, and J. M. Houston. Corrected Values of Fowler-Nordheim Field Emission Functions $v(y)$ and $s(y)$. *Phys. Rev.*, **90**(4):515, 1953.

[232] C. A. Spindt, I. Brodie, L. Humphrey, and E. R. Westerberg. Physical properties of thin-film field emission cathodes with molybdenum cones. *J. Appl. Phys.*, **47**(12):5248–5263, 1976.

[233] A. S. Berdinsky, A. V. Shaporin, J.-B. Yoo, J.-H. Park, P. S. Alegaonkar, J.-H. Han, and G.-H. Son. Field enhancement factor for an array of MWNTs in CNT paste. *Appl. Phys. A*, **38**:377, 2006.

[234] J. H. Bechtel, W. Lee Smith, and N. Bloembergen. Two-photon photoemission from metals induced by picosecond laser pulses. *Phys. Rev. B*, **15**(10): 4557–4563, 1977.

[235] R. Yen, J. Liu, and N. Bloembergen. Thermally assisted multiphoton photoelectric emission from tungsten. *Opt. Commun.*, **35**(2):277–282, 1980.

[236] J. G. Fujimoto, J. M. Liu, E. P. Ippen, and N. Bloembergen. Femtosecond Laser Interaction with Metallic Tungsten and Nonequilibrium Electron and Lattice Temperatures. *Phys. Rev. Lett.*, **53**(19):1837–1840, 1984.

[237] J. Kupersztych and M. Raynaud. Anomalous Multiphoton Photoelectric Effect in Ultrashort Time Scales. *Phys. Rev. Lett.*, **95**(14):147401, 2005.

[238] A. T. Georges. Coherent and incoherent multiple-harmonic generation from metal surfaces. *Phys. Rev. A*, **54**(3):2412–2418, 1996.

[239] A. T. Georges. Theory of the multiphoton photoelectric effect: A stepwise excitation process. *Phys. Rev. B*, **51**(19):13735, 1995.

[240] H. Petek and S. Ogawa. Femtosecond time-resolved two-photon photoemission studies of electron dynamics in metals. *Prog. Surf. Sci.*, **56**(4): 239–310, 1997.

[241] Nicolaas Bloembergen. *Nonlinear Optics*. World Scientific, 4th edition, 1996.

[242] P. Agostini, F. Fabre, G. Mainfray, G. Petite, and N. K. Rahman. Free-Free Transitions Following Six-Photon Ionization of Xenon Atoms. *Phys. Rev. Lett.*, **42**(17):1127–1130, 1979.

[243] L. V. Keldysh. Ionization in field of a strong electromagnetic wave. *Sov. Phys. JETP*, **20**:1307, 1965.

[244] P. B. Corkum, N. H. Burnett, and F. Brunel. Above-threshold ionization in the long-wavelength limit. *Phys. Rev. Lett.*, **62**(11):1259–1262, 1989.

[245] Hiromichi Niikura, F. Legare, R. Hasbani, A. D. Bandrauk, Misha Yu. Ivanov, D. M. Villeneuve, and P. B. Corkum. Sub-laser-cycle electron pulses for probing molecular dynamics. *Nature*, **417**(6892):917–922, 2002.

[246] Hiromichi Niikura, F. Legare, R. Hasbani, Misha Yu Ivanov, D. M. Villeneuve, and P. B. Corkum. Probing molecular dynamics with attosecond resolution using correlated wave packet pairs. *Nature*, **421**(6925):826–829, 2003.

[247] J. Itatani, F. Quéré, G. L. Yudin, M. Yu. Ivanov, F. Krausz, and P. B. Corkum. Attosecond Streak Camera. *Phys. Rev. Lett.*, **88**(17):173903, 2002.

[248] J. Itatani, J. Levesque, D. Zeidler, Hiromichi Niikura, H. Pepin, J. C. Kieffer, P. B. Corkum, and D. M. Villeneuve. Tomographic imaging of molecular orbitals. *Nature*, **432**(7019):867–871, 2004.

[249] M. Drescher, M. Hentschel, R. Kienberger, M. Uiberacker, V. Yakovlev, A. Scrinzi, Th. Westerwalbesloh, U. Kleineberg, U. Heinzmann, and F. Krausz. Time-resolved atomic inner-shell spectroscopy. *Nature*, **419** (6909):803–807, 2002.

[250] M. Hentschel, R. Kienberger, Ch. Spielmann, G. A. Reider, N. Milosevic, T. Brabec, P. Corkum, U. Heinzmann, M. Drescher, and F. Krausz. Attosecond metrology. *Nature*, **414**(6863):509–513, 2001.

[251] Francesco Banfi, Claudio Giannetti, Gabriele Ferrini, Gianluca Galimberti, Stefania Pagliara, Daniele Fausti, and Fulvio Parmigiani. Experimental Evidence of Above-Threshold Photoemission in Solids. *Phys. Rev. Lett.*, **94**(3):037601, 2005.

[252] J. Hohlfeld, S.-S. Wellershoff, J. Gudde, U. Conrad, V. Jahnke, and E. Matthias. Electron and lattice dynamics following optical excitation of metals. *Chem. Phys.*, **251**(1-3):237–258, 2000.

[253] A. Kubo, K. Onda, H. Petek, Z. Sun, Y. S. Jung, and H. K. Kim. Femtosecond Imaging of Surface Plasmon Dynamics in a Nanostructured Silver Film. *Nano Lett.*, **5**(6):1123–1127, 2005.

[254] W. Denk, J. H. Strickler., and W. W. Webb. Two-photon laser scanning fluorescence microscopy. *Science*, **248**(4951):73–76, 1990.

[255] Peter Hommelhoff, Catherine Kealhofer, and Mark A. Kasevich. Ultrafast Electron Pulses from a Tungsten Tip Triggered by Low-Power Femtosecond Laser Pulses. *Phys. Rev. Lett.*, **97**(24):247402, 2006.

[256] Martin Wolf. Femtosecond dynamics of electronic excitations at metal surfaces. *Surf. Sci.*, **377-379**:343–349, 1997.

[257] W. S. Fann, R. Storz, H. W. K. Tom, and J. Bokor. Direct measurement of nonequilibrium electron-energy distributions in subpicosecond laser-heated gold films. *Phys. Rev. Lett.*, **68**(18):2834–2837, 1992.

[258] C. Hernandez-Garcia and C. A. Brau. Photoelectric field emission from needle cathodes. *Nucl. Instr. Meth. A*, **429**:257–263, 1999.

[259] M. Aeschlimann, M. Bauer, and S. Pawlik. Competing nonradiative channels for hot electron induced surface photochemistry. *Chem. Phys.*, **205** (1-2):127–141, 1996.

[260] John J. Quinn. Range of Excited Electrons in Metals. *Phys. Rev.*, **126**(4): 1453–1457, 1962.

[261] A. I. Anisimov, V. A. Benderskii, and G. Farkas. Nonlinear photoelectric emission from metals induced by a laser radiation. *Sov. Phys. Uspekhi*, **20** (6):467, 1977.

[262] Alessandro Tredicucci, Claire Gmachl, Federico Capasso, Albert L. Hutchinson, Deborah L. Sivco, and Alfred Y. Cho. Single-mode surface-plasmon laser. *Appl. Phys. Lett.*, **76**(16):2164–2166, 2000.

[263] P. W. Brumer and M. Shapira. *Coherent Control of Atomic and Molecular Processes*. Wiley, 2003.

[264] Stefan Linden, Christian Enkrich, Martin Wegener, Jiangfeng Zhou, Thomas Koschny, and Costas M. Soukoulis. Magnetic Response of Metamaterials at 100 Terahertz. *Science*, **306**(5700):1351–1353, 2004.

[265] J. Kupersztych, P. Monchicourt, and M. Raynaud. Ponderomotive Acceleration of Photoelectrons in Surface-Plasmon-Assisted Multiphoton Photoelectric Emission. *Phys. Rev. Lett.*, **86**(22):5180–5183, 2001.

[266] S. E. Irvine, A. Dechant, and A. Y. Elezzabi. Generation of 0.4-keV Femtosecond Electron Pulses using Impulsively Excited Surface Plasmons. *Phys. Rev. Lett.*, **93**(18):184801, 2004.

[267] S. E. Irvine and A. Y. Elezzabi. Femtosecond electron pulse gating using surface plasmons. *Opt. Express*, **14**:4115, 2006.

Appendix

A Notations, Abbreviations[3]

$\doteq$	"defined as"
$\simeq$	"almost equal to"
$\approx$	"approximated as"
$\sim$	"roughly equal to"
$\propto$	"proportional to"
AM	air-metal
α	polarizability (scalar)
$\widehat{\alpha}$	polarizability (tensor)
a_0	lattice period
β	polar angle
b	slit width
c	vacuum speed of light (constant)
∂_x	partial derivative with respect to x
E	Energy
$\mathbf{E}$	electric field (vector)
ε	element of
ε_0	vacuum permittivity (constant)
ε	relative material permittivity
FROG	frequency-resolved optical gating
fs	femtosecond (unit)
ϕ	phase
φ	azimuthal angle
Φ	work function
G	lattice vector
$\widehat{G}$	Green's function (tensor)
γ	absorptive decay rate *or* Keldysh parameter
Γ	total decay rate
$\mathbf{H}$	magnetic field (vector)
$\hbar$	Planck's constant
h	film thickness

[3]Only notations and abbreviations appearing in more than one paragraph in the text are listed.

I	Intensity
$\Im(x)$	imaginary part of a variable x
j	electron current density
J	electron current
k	wave number
$\mathbf{k}$	wave vector (vector)
κ	spatial decay constant
MHz	Megahertz (unit)
λ	wavelength
$\mathbf{m}$	magnetic dipole moment
meV	millielectronvolt
μ_0	vacuum permeability (constant)
μ	waveguide propagation constant *or* magnetic polarizability
μm	micrometer (unit)
n	diffraction order *or* nonlinear order *or* refractive index
$\mathbf{n}$	unit length vector along $\mathbf{r}$ (vector)
nm	nanometer (unit)
NSOM	near-field scanning optical microscopy
ω	optical angular frequency
$\mathbf{p}$	electric dipole moment (vector)
P	power
θ	angle of incidence
$\mathbf{r}$	position (vector)
r	length of $\mathbf{r}$
$\Re(x)$	real part of a variable x
SIBC	surface impedance boundary condition
SPIDER	spectral phase interferometry for direct electric field reconstruction
SM	substrate-metal (sapphire-metal)
SPP	surface plasmon polariton
t	time *or* transmissivity
τ	delay
T	transmission *or* tunneling probability
T_1	lifetime
TEM	transverse electromagnetic
TEEM	tip-enhanced electron emission microscopy
TM	transverse magnetic
V	Volts (unit)
x	distance along the surface (perpendicular to slits)
y	distance along the surface (extruded dimension)
z	distance from surface
Z	surface impedance

B NSOM Setup

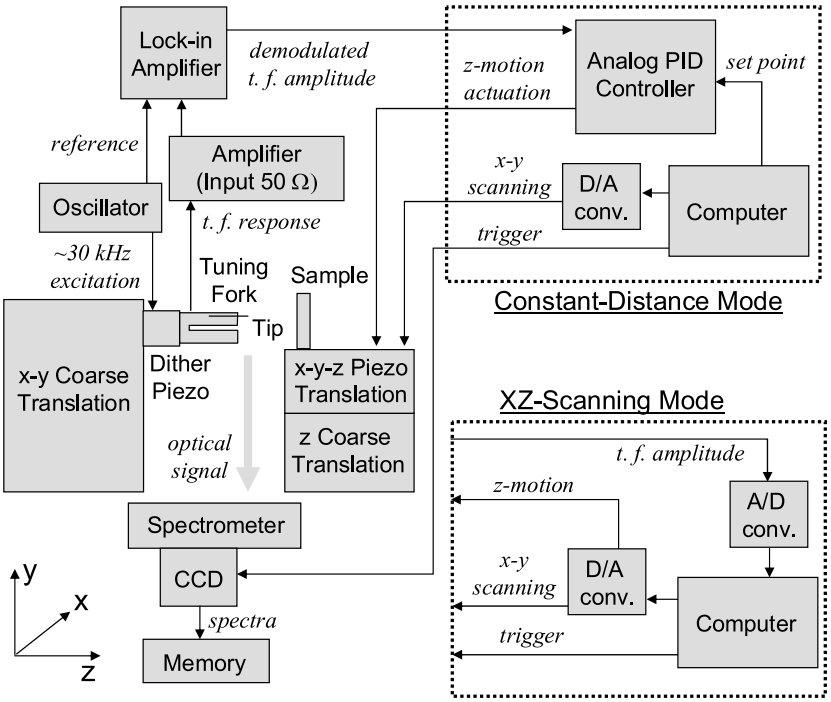

Figure 1: Schematic of the components and the signal paths in the NSOM constructed for this thesis. In the constant-distance imaging mode, a constant oscillation amplitude of the tuning fork and tip are maintained by the PID-controller. For the "*x*-*z*" imaging mode, the dotted box in the top is replaced by that in the bottom. In this mode, the tuning fork amplitude is repeatedly measured as the sample approaches the tip. An optical spectrum is recorded at every scanning point. At the moment of tip-sample contact, the sample is retracted and a lateral scanning step in the *x*-direction is performed, before the next approach curve is measured. The computer control and acquisition software was written in the programming environment LabVIEW, manufactured by National Instruments Corporation.

C Lippmann-Schwinger Equation

In this appendix, we derive the exact integral equation for the electric field in a general scattering scenario, in which the materials can be described in terms of a local and isotropic dielectric function. The derivation and notations are similar to that in [65]. The problem is divided into an unperturbed and perturbed geometry with dielectric functions $\varepsilon_{ref}(\mathbf{r})$ and $\varepsilon(\mathbf{r})$, respectively. For the unperturbed situation, the solution $\mathbf{E}_0(\mathbf{r})$ to the wave equation is assumed to be known[4]:

$$\nabla \times \nabla \times \mathbf{E}_0(\mathbf{r}) - \varepsilon_{ref}(\mathbf{r}) k^2 \, \mathbf{E}_0(\mathbf{r}) = 0. \tag{C.1}$$

We denote as $\mathbf{E}(\mathbf{r})$ the field in the presence of the probe, i.e., the solution to the complete problem given by

$$\nabla \times \nabla \times \mathbf{E}(\mathbf{r}) - \varepsilon(\mathbf{r}) k^2 \, \mathbf{E}(\mathbf{r}) = 0. \tag{C.2}$$

Rewriting the total field $\mathbf{E}(\mathbf{r})$ as a sum of the unperturbed wave plus a scattered wave,

$$\mathbf{E}(\mathbf{r}) = \mathbf{E}_0(\mathbf{r}) + \mathbf{E}_s(\mathbf{r}), \tag{C.3}$$

and taking the difference between (C.2) and (C.1), an equation for the scattered field is obtained (after rearrangement of some terms), in which the complete field acts as the source term:

$$\nabla \times \nabla \times \mathbf{E}_s(\mathbf{r}) - \varepsilon_{ref}(\mathbf{r}) k^2 \, \mathbf{E}_s(\mathbf{r}) = k^2 [\varepsilon(\mathbf{r}) - \varepsilon_{ref}(\mathbf{r})] \mathbf{E}(\mathbf{r}). \tag{C.4}$$

We define a Green's tensor $\widehat{G}(\mathbf{r}, \mathbf{r}')$ satisfying the wave equation for a point source at $\mathbf{r}'$,

$$\nabla \times \nabla \times \widehat{G}(\mathbf{r}, \mathbf{r}') - \varepsilon(\mathbf{r}) k^2 \, \widehat{G}(\mathbf{r}, \mathbf{r}') = \widehat{I} \delta(\mathbf{r} - \mathbf{r}'). \tag{C.5}$$

Here, $\widehat{I}$ is the unit tensor (matrix). With this definition, the formal solution to Eq. (C.4) is written as

$$\mathbf{E}_s(\mathbf{r}) = k^2 \int d\mathbf{r}' \, [\varepsilon(\mathbf{r}') - \varepsilon_{ref}(\mathbf{r}')] \widehat{G}(\mathbf{r}, \mathbf{r}') \mathbf{E}(\mathbf{r}'). \tag{C.6}$$

Addition of the unperturbed field yields the Lippmann-Schwinger equation

$$\mathbf{E}(\mathbf{r}) = \mathbf{E}_0(\mathbf{r}) + k^2 \int d\mathbf{r}' \, [\varepsilon(\mathbf{r}') - \varepsilon_{ref}(\mathbf{r}')] \widehat{G}(\mathbf{r}, \mathbf{r}') \mathbf{E}(\mathbf{r}'). \tag{C.7}$$

[4] A harmonic time dependence $e^{-i\omega t}$ is assumed and left out.

D Fano Lineshape

Equivalence of the Fano Lineshape and a Lorentzian plus a Continuum

The complex transmission amplitude in Sec. (4.2.2) can be written in the form

$$t(\omega) = a_{nr} + \frac{a e^{i\phi}\Gamma}{\omega - \omega_0 + i\Gamma} = a_{nr}\left(1 + \frac{\rho e^{i\phi}}{\varepsilon + i}\right) \tag{D.1}$$

with the definitions

$$\rho = \frac{a}{a_{nr}} \quad \text{and} \quad \varepsilon = \frac{\omega - \omega_0}{\Gamma}.$$

Evaluating $|t(\omega)|^2$ results in:

$$\begin{aligned}
|t(\omega)|^2 &= |a_{nr}|^2 \left(1 + \frac{\rho e^{i\phi}}{\varepsilon + i}\right)\left(1 + \frac{\rho e^{-i\phi}}{\varepsilon - i}\right) \\
&= |a_{nr}|^2 \frac{\varepsilon^2 + 1 + \rho^2 + \varepsilon\rho(e^{i\phi} + e^{-i\phi}) - i\rho(e^{i\phi} - e^{-i\phi})}{\varepsilon^2 + 1} \\
&= |a_{nr}|^2 \frac{\varepsilon^2 + 1 + \rho^2 + 2\varepsilon\rho\cos(\phi) + 2\rho\sin(\phi)}{\varepsilon^2 + 1} \\
&= |a_{nr}|^2 \frac{(\rho\cos(\phi) + \varepsilon)^2 + (\rho\cos(\phi) + 1)^2}{\varepsilon^2 + 1}.
\end{aligned} \tag{D.2}$$

Except for the constant coefficient $|a_{nr}|^2$, this is the same expression as Eq. (17) in Fano's original paper [146].

Resonance Parameter Ambiguity of the Fano Lineshape

Starting from a spectral transmission of the form of Eq. (D.2),

$$T(\omega) = |a_{nr}|^2 \frac{(\rho\cos(\phi)+\varepsilon)^2 + (\rho\cos(\phi)+1)^2}{\varepsilon^2+1}, \tag{D.3}$$

the resonance parameters are re-defined as

$$x + iy \doteq \rho e^{i\phi} \ .$$

Now, the transmissivity is invariant under the replacement

$$\begin{aligned} x' &\to x \\ y' &\to -y-2 \ , \end{aligned} \tag{D.4}$$

because

$$\begin{aligned} T_{\{x,y\}}(\omega) = \ & |a_{nr}|^2 \frac{(x+\varepsilon)^2 + (y+1)^2}{\varepsilon^2+1} \\ = \ & |a_{nr}|^2 \frac{(x+\varepsilon)^2 + (-y-2+1)^2}{\varepsilon^2+1} = T_{\{x',y'\}} \end{aligned} \tag{D.5}$$

Both sets of resonance parameters can be consistent with the Kramers-Kronig relations [30], since ϕ and ρ only define the relative phase and amplitude, respectively, of the resonant and direct transmission amplitudes. They are therefore both physically meaningful, and constitute an ambiguity, which is of particular importance, if there is a considerable amount of direct transmission. An additional phase-resolved measurement is therefore always necessary, if one is interested in the exact resonance parameters or the dispersion of the transmitted light.

Publications

Articles directly relevant to the content of this thesis:

- C. Ropers, C. C. Neacsu, T. Elsässer, M. Albrecht, M. B. Raschke, and C. Lienau, "Grating-coupling of Surface Plasmons onto Metallic Tips: A Nanoconfined Light Source," Nano Lett., *in press* (2007).

- C. Ropers, T. Elsässer, G. Cerullo, M. Zavelani-Rossi, and C. Lienau, "Ultrafast optical excitations of metallic nanostructures: From light confinement to a novel electron source," *submitted* (2007)

- C. Ropers, D. R. Solli, C.-P. Schulz, C. Lienau, and T. Elsässer, "Localized Multiphoton Emission of Femtosecond Electron Pulses from Metal Nanotips," Phys. Rev. Lett. **98,** 043907 (2007).

- J. E. Kihm, Y. C. Yoon, D. J. Park, Y. H. Ahn, C. Ropers, C. Lienau, J. Kim, Q. H. Park, and D. S. Kim, "Fabry-Perot tuning of the band-gap polarity in plasmonic crystals," Phys. Rev. B **75,** 035414 (2007).

- K. G. Lee, H. W. Kihm, J. E. Kihm, W. J. Choi, H. Kim, C. Ropers, D. J. Park, Y. C. Yoon, S. B. Choi, D. H. Woo, J. Kim. B. Lee, Q. H. Park, C. Lienau, and D. S. Kim, "Vector field microscopic imaging of light," Nature Photonics **1,** 53 (2007).

- C. Ropers, D. R. Solli, C.-P. Schulz, C. Lienau, and T. Elsässer, "A Nanometer-sized Femtosecond Electron Source at 80 MHz Repetition Rate," In *Ultrafast Phenomena* **XV,** P. Corkum, D. Jonas, D. Miller, and A. M. Weiner, (Eds.), to appear (2007).

- G. Stibenz, C. Ropers, C. Lienau, C. Warmuth, A. Wyatt, I. Walmsley, and G. Steinmeyer, "Advanced methods for the characterization of few-cycle light pulses: a comparison," Appl. Phys. B **83,** 511 (2006).

- C. Ropers, G. Stibenz, G. Steinmeyer, R. Müller, D. J. Park, K. G. Lee, J. E. Kihm, J. Kim, Q. H. Park, D. S. Kim, and C. Lienau,"Ultrafast dynamics

of surface plasmon polaritons in plasmonic metamaterials," Appl. Phys. B **84,** 183–189 (2006).

- C. Ropers, D. J. Park, G. Stibenz, G. Steinmeyer, J. Kim, D. S. Kim, and C. Lienau, "Femtosecond Light Transmission and Subradiant Damping in Plasmonic Crystals," Phys. Rev. Lett. **94,** 113901 (2005).

- C. Ropers, R. Müller, C. Lienau, G. Stibenz, G. Steinmeyer, D. J. Park, Y. C. Yoon, and D. S. Kim, "Ultrafast dynamics of light transmission through plasmonic crystals," In *Ultrafast Phenomena* **XIV,** T. Kobayashi, T. Okada, T. Kobayashi, K. A. Nelson, and S. De Silvestri, (Eds.), 650–654 (Springer, 2005).

- R. Müller, C. Ropers, and C. Lienau, "Femtosecond light pulse propagation through metallic nanohole arrays: The role of the dielectric substrate," Opt. Express **12,** 5067 (2004).

Other articles:

- D. R. Solli, C. Ropers, P. Koonath, and B. Jalali, "Optical rogue waves," *submitted* (2007).

- R. Pomraenke, C. Ropers, J. Renard, C. Lienau, L. Lüer, D. Polli, and G. Cerullo, "Structural phase contrast in polycrystalline organic semiconductor films observed by broadband near-field optical spectroscopy," Nano Lett. **7,** 998 (2007)

- R. Pomraenke, C. Ropers, J. Renard, C. Lienau, L. Lüer, D. Polli, and G. Cerullo, "Broadband optical near-field microscope for nanoscale absorption spectroscopy of organic materials," J. Microsc., *in press* (2007)

- C. Ropers, M. Wenderoth, L. Winking, T. C. G. Reusch, M. Erdmann, R. G. Ulbrich, M. Grochol, F. Grosse, R. Zimmermann, S. Malzer, and G. H. Döhler, "Atomic scale structure and optical emission of AlGaAs/GaAs quantum wells," Phys. Rev. B **75,** 115317 (2007)

- M. Erdmann, C. Ropers, M. Wenderoth, R. G. Ulbrich, S. Malzer, and G. H. Döhler, "Diamagnetic shift of disorder-localized excitons in narrow GaAs/AlGaAs quantum wells," Phys. Rev. B **74,** 125412 (2006).

- C. Ropers, T. Q. Tien, C. Lienau, J. W. Tomm, P. Brick, N. Linder, B. Mayer, S. Tautz, and W. Schmid, "Observation of deep level defects within

the waveguide of red-emitting high-power diode lasers," Appl. Phys. Lett. **88,** 133513 (2006).

- D. R. Solli, C. F. McCormick, C. Ropers, J. J. Morehead, R. Y. Chiao, and J. M. Hickmann, "Demonstration of superluminal effects in an absorptionless, nonreflective system," Phys. Rev. Lett. **91,** 143906 (2003).

Danksagung

An erster Stelle gilt mein besonderer Dank Herrn Prof. Dr. Thomas Elsässer für seine klare und zielorientierte wissenschaftliche Betreuung dieser Arbeit, für viele anregende Diskussionen und die Unterstützung und Freiheit bei der Verfolgung eigener Ideen.

Prof. Dr. Christoph Lienau danke ich sehr für seine produktive Leitung des Projekts und dafür, daß er durch viel Begeisterungsfähigkeit und persönlichen Einsatz wesentlich zum Gelingen der Arbeit beigetragen hat.

Prof. Dr. Oliver Benson danke ich für seine spontane Bereitschaft, das Zweitgutachten zu verfassen.

I am very grateful to Prof. Dr. Dai-Sik Kim for the productive collaboration over the past three years. I would also like to acknowledge several members of his group, in particular Jin-Eun Kihm, Kwang-Geol Lee and Doo-Jae Park, whose visits to Berlin I enjoy remembering.

I thank Dr. Daniel R. Solli for important help in the initial stage of the electron experiment, his proofreading of large parts of the manuscript and a friendship resulting in exciting physics.

For successful collaborative efforts in recent years, I would like to thank (in alphabetical order): Dr. Martin Albrecht, Prof. Dr. Giulio Cerullo, Dr. Matthias Erdmann, Dr. Frank Grosse, Prof. Dr. B. Jalali, Dr. Larry Lüer, Dr. Roland Müller, C. Catalin Neacsu, Dr. Dario Polli, Dr. Markus B. Raschke, J. Renard, Dr. Thilo C. G. Reusch, Dr. Claus-Peter Schulz, Dr. Günter Steinmeyer, Dr. Gero Stibenz, Dr. Jens Tomm, Prof. Dr. Rainer G. Ulbrich, Dr. Martin Wenderoth, Lars Winking, and Prof. Dr. Roland Zimmermann.

Robert Pomraenke danke ich für seine uneigennützige Hilfsbereitschaft in allen Dingen. Er ist ein Kollege, wie man ihn sich wünscht. Zudem: Ein Dank für das absolut unvergessene Viertelfinale, das ich ohne ihn nicht miterlebt hätte!

Monika Tischer danke ich für die hervorragende Spitzenherstellung und die Einweisung am REM, Wolfgang Goleschny, Peter Scholze und Peter Stolz für ihre schnelle und präzise Hilfe aus der Werkstatt, und Gabriele Kordaß für die Hilfe bei vielen mühsamen Kleinigkeiten.

Besonders hervorheben möchte ich Prof. Dr. Klaus Reimann, seines Zei-

chens geduldiges Lexikon in Sachen Computer, Netzwerk, LateX, Elektronik, Optik...Wie heißt es so schön? Nicht verzagen, Reimann fragen.

Den zahlreichen hier nicht namentlich aufgeführten Mitgliedern des Bereichs C und der Abteilung von Dr. Michael Wörner möchte ich für die freundliche Aufnahme in eine Arbeitsatmosphäre danken, in der ich Spaß am Forschen hatte, und in der ich neue Freunde gefunden habe.

Außerdem möchte ich meinen Freunden und meiner Familie einen Dank aussprechen. Unter ihnen möchte ich besonders meine Schwester für ihre außerordentlich fleißige Korrekturarbeit und Gandalf Lechner für sein gutes Auge hervorheben, sowie Tobias Kampfrath für zahlreiche spannende Physik-Diskussionen.

Meinen Eltern bin ich sehr dankbar für die uneingeschränkte Unterstützung und ihr ungebrochenes Interesse an meiner Arbeit.

Der Liebe und dem Verständnis meiner Frau Meike verdanke ich eine wundervolle Zeit in Berlin und den Sinn für vieles andere außerhalb der Physik.